



POLITECNICO DI TORINO
Repository ISTITUZIONALE

Integration of Active Systems for a Global Chassis Control Design

Original

Integration of Active Systems for a Global Chassis Control Design / Tota, Antonio. - (2017).

Availability:

This version is available at: 11583/2675382 since: 2017-06-30T10:47:37Z

Publisher:

Politecnico di Torino

Published

DOI:10.6092/polito/porto/2675382

Terms of use:

Altro tipo di accesso

This article is made available under terms and conditions as specified in the corresponding bibliographic description in the repository

Publisher copyright

(Article begins on next page)



ScuDo

Scuola di Dottorato ~ Doctoral School

WHAT YOU ARE, TAKES YOU FAR

Doctoral Dissertation

Doctoral Program in Mechanical Engineering (29th cycle)

Integration of Active Systems for a Global Chassis Control Design

By

Antonio Tota

Supervisor(s):

Prof. Mauro Velardocchia, Supervisor

Doctoral Examination Committee:

Prof. Giuseppe Carbone, Referee, Università degli Studi di Cassino

Prof. Alessandro Gasparetto, Referee, Università degli Studi di Udine

Prof. Enrico Ravina, Università degli Studi di Genova

Prof. Giuseppe Quaglia, Politecnico di Torino

Prof. Vladimir Viktorov, Politecnico di Torino

Politecnico di Torino

2017

Declaration

I hereby declare that, the contents and organization of this dissertation constitute my own original work and does not compromise in any way the rights of third parties, including those relating to the security of personal data.

Antonio Tota
2017

* This dissertation is presented in partial fulfillment of the requirements for **Ph.D. degree** in the Graduate School of Politecnico di Torino (ScuDo).

*Ai miei nonni,
Antonio e Michele
e alle mie nonne,
Ida e Rosa*

Acknowledgements

La presente tesi di dottorato rappresenta il risultato finale di un lungo ed impegnativo percorso di ricerca durato tre anni, che non sarebbe stato tale senza il supporto, la collaborazione e l'aiuto di molte persone alle quali vorrei rivolgere i miei più sinceri ringraziamenti.

Il percorso universitario rappresenta per tutti una prova impegnativa e piena di ostacoli durante la quale bisogna imparare a conoscere se stessi ed il mondo che ci circonda, ma le oltre 200 pagine raccolte in questa tesi non basterebbero da sole a descrivere a pieno il sostegno e l'aiuto che ogni figlio/fratello vorrebbe ricevere dalla propria famiglia per il raggiungimento di obbiettivi personali e traguardi fondamentali per la propria vita. Io sono riuscito ad affrontarlo grazie alla presenza delle tre persone più importanti della mia vita: Benedetto, Loredana e Giuseppe Luca. Loro, che mi sono stati vicini anche quando ero lontano migliaia di chilometri dalla nostra amata/odiata Taranto, mi hanno trasmesso la forza per crederci sempre e la volontà di andare avanti senza mai guardare indietro. Mio padre Benedetto mi ha insegnato il rispetto per se stessi e per gli altri aiutandomi nelle scelte più difficili: sono estremamente fortunato di ricevere i suoi consigli. Mia madre Loredana è riuscita a rassicurarmi e a rasserenarmi durante i momenti più tristi e difficili, senza mai stancarsi di ripetere quanto fosse importante non sottovalutare i traguardi già raggiunti e cercando di spronarmi per raggiungerne degli altri. Giuseppe Luca, invece, non è più il fratellino minore da proteggere, ma una persona responsabile ed autonoma capace di gestirsi la vita ed in grado di trasmettere la sua sicurezza anche ad un fratello sbadato e disorganizzato come me, concedendomi talvolta anche le sue note doti culinarie. Spero che i sacrifici fatti e gli obbiettivi raggiunti durante questi anni vi renderanno orgogliosi e fieri di me.

Il lavoro di ricerca non sarebbe stato possibile e realizzabile senza la guida e la supervisione del Prof. Velardocchia che, con grande passione e fiduciosa aspettativa, insieme al Prof. Vigliani e all'Ing. Galvagno, conduce interessanti progetti di ricerca all'avanguardia nell'innovazione scientifica ed in collaborazione con importanti aziende legate al mondo automotive, per rimanere sempre al passo con le realtà industriali.

Un immenso ed impagabile ringraziamento è riservato per la mia amata Agathe che, oltre ad aver sopportato le numerose lamentele durante questi 3 anni di dottorato, ha sempre creduto nelle mie capacità incoraggiando i miei sforzi sia nei momenti di difficoltà che in quelli di felicità e spensieratezza. Neanche un oceano intero è riuscito a tenerti lontana da me: mi hai raggiunto in ogni posto sperduto del mondo in cui andavo a finire, trasformando la distanza in momenti straordinari ed indimenticabili. Merci beaucoup, ma belle!

Inoltre vorrei ringraziare il Prof. Aldo Sorniotti per avermi ospitato all'interno del suo team presso l'University of Surrey (Guildford, UK), e per avermi inserito all'interno di un progetto di ricerca che per me è stato un momento di vero apprendimento nel verificare concetti teorici attraverso prove sperimentali su pista davvero stimolanti oltre che divertenti. Un grazie speciale va anche a tutti gli amici del SAVAG ed i frequentatori di Stoke House che hanno saputo rendere indimenticabile il mio periodo trascorso a Guildford; un particolare grazie a Fabio, Daniele, Basilio, Stefano, Tommaso, Michele, Ilhan, Ventura per le serate trascorse insieme al Wetherspoons.

Sentiti e sinceri ringraziamenti sono dovuti anche agli attuali e vecchi membri del team di meccanica del veicolo (Guido, Pablo, Alberto, Mariangela, Hamid, Sara ed Andrea), con cui ho condiviso momenti di quotidianità al Politecnico di Torino e divertenti cene/pranzi/panzerottate in giro per Torino.

Uno speciale ringraziamento è rivolto anche al Prof. Rizzoni e al Prof. Guvenc per avermi invitato presso il Center for Automotive Research (CAR) dell'Ohio State University (Columbus, OH), concedendomi l'opportunità di passare un'ulteriore esperienza internazionale ed interculturale che mi ha aiutato molto a perfezionare le mie abilità di lavoro di squadra grazie alla collaborazione con i componenti del Automated Driving Lab (ADL) Prof. Bilin Aksun-Guvenc, Santhosh, Nitish, Hongliang e Haoan. Vorrei anche inviare un saluto ed un ringraziamento a Matilde ed a Martin per tutti i momenti di divertimento e svago trascorsi insieme per le vie di Columbus.

Infine, last but not least, vorrei ricordare con un saluto tutti gli amici di Taranto e Torino che mi hanno sempre accompagnato durante i momenti di svago e di totale felicità, rappresentando sempre un punto di riferimento da cui trarre forza e sostegno per superare gli ostacoli della vita.

Grazie!

Turin, December 2016

Antonio Tota

Abstract

Vehicle chassis control active systems (braking, suspension, steering and driveline), from the first ABS/ESC control unit to the current advanced driver assistance systems (ADAS), are progressively revolutionizing the way of thinking and designing the vehicle, improving its interaction with the surrounding world (V2V and V2X) and have led to excellent results in terms of safety and performances (dynamic behavior and drivability). They are usually referred as *intelligent vehicles* due to a software/hardware architecture able to assist the driver for achieving specific safety margin and/or optimal vehicle dynamic behavior. Moreover, industrial and academic communities agree that these technologies will progress till the diffusion of the so called autonomous cars which are able to drive robustly in a wide range of traffic scenarios. Different autonomous vehicles are already available in Europe, Japan and United States and several solutions have been proposed for smart cities and/or small public area like university campus.

In this context, the present research activity aims at improving safety, comfort and performances through the integration of global active chassis control: the purposes are to study, design and implement control strategies to support the driver for achieving one or more final target among safety, comfort and performance. Specifically, the vehicle subsystems that are involved in the present research for active systems development are the steering system, the propulsion system, the transmission and the braking system. The thesis is divided into three sections related to different applications of active systems that, starting from a robust theoretical design procedure, are strongly supported by objective experimental results obtained from Hardware In the Loop (HIL) test rigs and/or proving ground testing sessions.

The first chapter is dedicated to one of the most discussed topic about autonomous driving due to its impact from the social point of view and in terms of human error mitigation when the driver is not prompt enough. In particular, it is here analyzed the automated steering control which is already implemented for automatic parking and that could represent also a key element for conventional passenger car in emergency situation where a braking intervention is not enough for avoiding an imminent collision. The activity is focused on different steering controllers design and their implementation

for an autonomous vehicle; an obstacle collision avoidance adaptation is introduced for future implementations. Three different controllers, Proportional Derivative (PD), PD+Feedforward (FF) e PD+Integral Sliding Mode (ISM), are designed for tracking a reference trajectory that can be modified in real-time for obstacle avoidance purposes. Furthermore, PD+FF and PD+ISM logic are able to improve the tracking performances of automated steering during cornering maneuvers, relevant from the collision avoidance point of view. Path tracking control and its obstacle avoidance enhancement is also shown during experimental tests executed in a proving ground through its implementation for an autonomous vehicle demonstrator. Even if the activity is presented for an autonomous vehicle, the active control can be developed also for a conventional vehicle equipped with an Electronic Power Steering (EPS) or Steer-by-wire architectures.

The second chapter describes a Torque Vectoring (TV) control strategy, applied to a Fully Electric Vehicle (FEV) with four independent electric motor (one for each wheel), that aims to optimize the lateral vehicle behavior by a proper electric motor torque regulation. A yaw rate controller is presented and designed in order to achieve a desired steady-state lateral behaviour of the car (handling task). Furthermore, a sideslip angle controller is also integrated to preserve vehicle stability during emergency situations (safety task). LQR, LQR+FF and ISM strategies are formulated and explained for yaw rate and concurrent yaw rate/sideslip angle control techniques also comparing their advantages and weakness points. The TV strategy is implemented and calibrated on a FEV demonstrator by executing experimental maneuvers (step steer, skid pad, lane change and sequence of step steers) thus proving the efficacy of the proposed controller and the safety contribution guaranteed by the sideslip control. The TV could be also applied for internal combustion engine driven vehicles by installing specific torque vectoring differentials, able to distribute the torque generated by the engine to each wheel independently.

The TV strategy evaluated in the second chapter can be influenced by the presence of a transmission between the motor (or the engine) and wheels (where the torque control is supposed to be designed): in addition to the mechanical delay introduced by transmission components, the presence of gears backlashes can provoke undesired noises and vibrations in presence of torque sign inversion. The last chapter is thus related to a new method for noises and vibration attenuation for a Dual Clutch Transmission (DCT). This is achieved in a new way by integrating the powertrain control with the braking system control, which are historically and conventionally analyzed and designed separately. It is showed that a torsional preload effect can be obtained on transmission components by increasing the wheel torque and concurrently applying a braking wheel torque. For this reason, a pressure following controller is presented and validated through a Hardware In

the Loop (HIL) test rig in order to track a reference value of braking torque thus ensuring the desired preload effect and noises reduction. Experimental results demonstrates the efficacy of the controller, also opening new scenario for global chassis control design.

Finally, some general conclusions are drawn and possible future activities and recommendations are proposed for further investigations or improvements with respect to the results shown in the present work.

Contents

Abstract	vi
List of Figures	xii
List of Tables	xx
1 Autonomous Steering Control	1
1.1 Introduction on Autonomous Steering Driving	1
1.2 Experimental Setup of the Autonomous Vehicle	5
1.3 Single-Track Model	7
1.3.1 Dynamics equations	8
1.3.2 Steady-State behavior	11
1.3.3 Experimental Validation	13
1.3.4 Steering Dynamics Model	21
1.3.5 Lateral Deviation Equations	24
1.4 Path Tracking Control	26
1.4.1 Reference Path Generation	26
1.4.2 Parameter Space Approach: Theory and Application	32
1.4.3 Static Linear Feedforward	51
1.4.4 Integral Sliding Mode: Theory and Application	52
1.4.5 Obstacle Collision Avoidance Path Modification	63
1.5 Experimental Results	66
1.5.1 Close-Loop Path	66

1.5.2	Close-Loop Path for Obstacle Avoidance	72
1.6	Conclusions	74
2	Torque Vectoring Control for Fully-Electric Vehicles	76
2.1	Introduction on Torque Vectoring Theory	76
2.2	Experimental Setup of the FEV demonstrator	81
2.3	Control System Design	83
2.3.1	Control structure	84
2.3.2	Yaw rate and Sideslip references	86
2.3.3	Yaw Moment Controller: Linear Quadratic Regulator Design	93
2.3.4	Yaw Moment Controller: Integral Sliding Mode Design	97
2.4	Simulation Results	103
2.4.1	High friction coefficient step steer	103
2.4.2	Low friction coefficient sequence of step steers	105
2.5	Experimental Results in High Friction Conditions	107
2.5.1	Skid pad	107
2.5.2	Step steer	108
2.5.3	Sequence of step steers	113
2.5.4	Obstacle avoidance test	113
2.6	Sideslip Angle Estimation Analysis	115
2.6.1	Extended Kalman Filter Theory	116
2.6.2	Sideslip angle estimation using EKF and Integral solution	119
2.7	Conclusions	123
3	Integration of Powertrain & Brake System Controls	126
3.1	Introduction	126
3.2	Overview of Dual Clutch Transmissions	130
3.3	NVH Issues	132
3.3.1	NVH Excitations	133
3.4	Braking System Integration: High Level Logic	137

3.4.1	Detection of NVH Sources	138
3.4.2	Simulation concept proof	140
3.5	Braking System Intervention: Low Level Logic	145
3.5.1	Braking Test Rig	147
3.5.2	Hydraulic system model	148
3.5.3	Pressure control design	160
3.6	Experimental Analysis of NVH Reduction Control Strategy	176
3.6.1	Transmission Test Rig	176
3.6.2	Experimental Validation	179
3.7	Conclusions	185
Conclusions and Recommendation for Future Works		187
Bibliography		189

List of Figures

1.1	Vehicle Demonstrator and Sensors/Actuators Platform	5
1.2	Single-Track Model (adapted from [1])	7
1.3	Kinematic diagram of wheel speed (adapted from [1])	10
1.4	Lateral behavior of a vehicle with a single steering axle (adapted from [1])	14
1.5	Ramp steer maneuver: steering angle and vehicle speed	16
1.6	Ramp steer maneuver: sideslip angle β , yaw rate $r = d\psi/dt$ and lateral acceleration a_y	16
1.7	Step steer maneuver: reference and current steering angle for different amplitudes	17
1.8	Step steer maneuver: sideslip angle β , yaw rate $r = d\psi/dt$ and lateral acceleration a_y from experimental test (EXP) and single-track model (STM)	17
1.9	Step steer maneuver: vehicle position for different steering angles from both experimental test (EXP) and single-track model (STM)	18
1.10	Skid Pad: vehicle steering angle δ , gas pedal and speed V	19
1.11	Skid Pad: vehicle longitudinal a_x , lateral acceleration a_y and yaw rate r . .	19
1.12	Skid Pad: vehicle GPS position	20
1.13	Skid Pad handling characteristics: $\delta_F - \delta_{Kin}$ and β vs a_y	20
1.14	Sweep frequency test with constant amplitude of 90	21
1.15	Sweep frequency tests with different steering amplitudes (90 deg, 180 deg and 270 deg) and vehicle operating conditions	22
1.16	System identification: comparison with experimental FRF at 90 deg against different transfer function structures	23

1.17 Experimental validation of system identification: EXP - experimental data, EST - estimated with a transfer function with 4 poles and 2 zeros	24
1.18 Scheme representation of vehicle lateral deviation with respect reference path	25
1.19 Digital map creation: segmentation of real data (right) and comparison of digital map with real data (left)	30
1.20 Control scheme for lateral deviation y regulation: $G(s)$ plant; $C(s)$ controller	32
1.21 Generic single-input single-output (SISO) plant $G(s)$ controlled by a controller $C(s)$	33
1.22 RRB nad CRB stability boundary for the characteristic polynomial of 1.65 .	38
1.23 Example of D-stable Region based on eigenvalues specifications	45
1.24 Hurwitz and Gamma stability design criteria for lateral deviation control: boundaries and stability regions	47
1.25 Γ region for different values of cornering stiffness	50
1.26 D-stable region and dominant poles placement with $K_P = 0.1$ and $K_D = 0.15$	50
1.27 Reference path modification according to the elastic band theory: external (\mathbf{F}_i^{EXT}) and internal ($\mathbf{F}_{i,i-1}^{INT}, \mathbf{F}_{i,i+1}^{INT}$) forces applied to the i -th node N_i provokes a deformation u_i	64
1.28 Force distribution applied to initial path according to the elastic band theory	65
1.29 Initial path deformation for four obstacle positions according to the elastic band theory	66
1.30 Initial path deformation for different values of $T_p = \frac{R_{pr}}{k_e}$ ratios	67
1.31 Controller scheme implemented on the prototype autonomous vehicle for path tracking control with PSA+FF and PSA+ISM strategies	67
1.32 Lateral deviation y and steering angle δ_{Out} during manual path tracking for three different drivers at constant speed of $15km/h$	68
1.33 Global coordinates during manual path tracking for three different drivers at constant speed of $15km/h$	69
1.34 Lateral deviation y and steering angle δ_{Out} during autonomous path tracking with PSA, PSA+FF and PSA+ISM strategies at constant speed of $15km/h$	69
1.35 Global coordinates during autonomous path tracking with PSA, PSA+FF and PSA+ISM strategies at constant speed of $15km/h$	70

1.36	PSA+FF contributions during autonomous path tracking at constant speed of 15 km/h	70
1.37	PSA+ISM contributions during autonomous path tracking at constant speed of 15 km/h	71
1.38	Effect of preview distance l_s on path tracking control with PSA logic at constant speed of 15 km/h	72
1.39	Global coordinates during obstacle collision avoidance maneuver with PSA, PSA+FF and PSA+ISM strategies at constant speed of 5 km/h	72
1.40	Lateral deviation y and steering angle δ_{Out} during obstacle collision avoidance maneuver with PSA, PSA+FF and PSA+ISM strategies at constant speed of 5 km/h	73
1.41	Lateral deviation y , vehicle speed V , yaw rate r and sideslip angle β during obstacle collision avoidance maneuver with PSA strategy	74
2.1	General scheme of Torque Vectoring application for a 4WD FEV with individual on-board electric motors	77
2.2	Understeer characteristic modification through TV control application	78
2.3	Understeer characteristic for the vehicle with TV at $V = 90\text{ km/h}$ and values of a_x ranging from -5 to 5 in step of 2.5 m/s^2 (adapted from [2])	79
2.4	Simulation results for a TV application to a FEV with four on-board electric motors: r -yaw rate, β -sideslip angle, M_z -yaw moment	80
2.5	General scheme of the vehicle demonstrator experimental setup with its electric drivelines (adapted from [3, 4])	82
2.6	Vehicle Dynamics Area (VDA) of Lommel (BE) proving ground with the vehicle demonstrator	83
2.7	Simplified schematic of the vehicle control structure	85
2.8	Definition of Normal mode, Sport mode and Enhanced Sport mode understeer characteristics versus passive vehicle experimental data for $a_x = 0$ and high friction condition	87
2.9	$a_{y,lin}$ and $a_{y,max}$ maximum values that can be selected for the desired understeer characteristic for high friction condition and $V = 100\text{ km/h}$	90
2.10	reference yaw rate map $r_{LUT}(\delta, V, a_x, \mu)$ for a high friction coefficient and $a_x = 0$ at different vehicle speed V in sport mode and enhanced sport mode	91

2.11 Reference yaw rate correction mechanism	93
2.12 Gain scheduled controller $\mathbf{L}(\nu)$	97
2.13 Time history of the disturbance contributions during a sequence of step steers at 90 km/h	102
2.14 Yaw rate and sideslip angle for a step steer maneuver of 100 deg at 100 km/h for the passive and active vehicles	104
2.15 Yaw moment for a step steer maneuver of 100 deg at 100 km/h for LQR and ISM control strategies	104
2.16 Conventional s , integral z and final s sliding variables during ISM control activation	105
2.17 $r(t)$ for the passive and active (ISM control with only yaw rate control and concurrent yaw rate and sideslip control) vehicles during sequences of step steers in low tire-road friction conditions with different sideslip thresholds	106
2.18 $\beta(t)$ for the passive and active (ISM control with only yaw rate control and concurrent yaw rate and sideslip control) vehicles during sequences of step steers in low tire-road friction conditions with different sideslip thresholds	106
2.19 Examples of experimental understeer characteristics for the passive and active vehicles	107
2.20 $r(t)$ during a step steer for the passive (a) and active (LQR (b), LQR+FF (c) and ISM (d)) vehicles	109
2.21 $M_{z,sat}(t)$ during a step steer for the LQR, LQR + FF and ISM controls	110
2.22 ISM yaw moment contributions during a step steer	110
2.23 $r(t)$ during a step steer with the ISM control for different values of ω_F . . .	111
2.24 $\beta(t)$ during step steers with the ISM control in Enhanced Sport mode, with and without the sideslip angle controller (for different sideslip thresholds, -7 deg, -14 deg, and -21 deg)	112
2.25 $r(t)$ during step steers with the ISM control in Enhanced Sport mode, with and without the sideslip angle controller (for different sideslip thresholds, -7 deg, -14 deg, and -21 deg)	113
2.26 $r(t)$ and $\beta(t)$ for the passive and active (ISM control, Normal mode) vehi- cles during sequences of step steers with a sideslip threshold of 15 deg . .	114
2.27 path description according to standard ISO 3888 – 2	114

2.28 $\delta(t)$, $r(t)$ and $\beta(t)$ for the passive and active (in Normal mode) vehicles during an obstacle avoidance maneuver from an initial $V = 51.5$ km/h . . .	115
2.29 Distribution of the successful (indicated by the blank symbols) and unsuccessful indicated by 'x') tests for the passive and active vehicles (in Normal mode), during obstacle avoidance maneuvers	115
2.30 Extended Kalman Filter iterative scheme	118
2.31 Vehicle speed V , torque vectoring yaw moment $M_{z,TV}$ and steering wheel angle δ during a step steer maneuver of 100 deg steering angle at 100 km/h executed in sport mode	122
2.32 Vehicle yaw rate r , lateral acceleration a_y and longitudinal acceleration a_x during a step steer maneuver of 100 deg steering angle at 100 km/h executed in sport mode	123
2.33 Experimental and estimate of sideslip angle β for different selection of matrix R elements	123
2.34 Experimental and estimate of sideslip angle β during a step steer maneuver of 100 deg steering angle at 100 km/h executed in enhanced sport mode . . .	124
3.1 General scheme of a DCT with two secondary shafts architecture and power flow representation	131
3.2 Gear Impact	132
3.3 Tip-out maneuver: engine & clutches torques	134
3.4 Tip-out maneuver: vehicle and transmission speeds	134
3.5 Tip-out maneuver: Angular Position Differences $\Delta\theta$; I: First gears - II: Second gears - FD: Final Drive gears - Diff: Differential gears	136
3.6 Speed-bump maneuver: disturbance longitudinal acceleration and speed	137
3.7 Speed-bump maneuver: vehicle and transmission speeds	138
3.8 Speed-bump maneuver: angular position differences $\Delta\theta$; I: First gears - II: Second gears - FD: Final Drive gears - Diff: Differential gears	139
3.9 Controller Strategy for Noises Reduction	140
3.10 Tip-out maneuver: Torques applied to the Transmission	141
3.11 Tip-out maneuver: Vehicle Speed for Passive and Active configuration . . .	141

3.12 Tip-out maneuver: $\Delta\theta$ on the engaged shaft for active and passive configurations; I: First gears - II: Second gears - FD: Final Drive gears - Diff: Differential gears	142
3.13 Tip-out maneuver: $\Delta\theta$ on the preselected shaft for active and passive configurations; I: First gears - II: Second gears - FD: Final Drive gears . . .	143
3.14 Tip-out maneuver: $\Delta\theta$ for Brake Intervention with and without K2 clutch slip control; I: First gears - II: Second gears - FD: Final Drive gears	143
3.15 Speed-Bump maneuver: vehicle speed for passive and active configurations	144
3.16 Speed-Bump maneuver: $\Delta\theta$ on the engaged shaft for active and passive configurations; I: First gears - II: Second gears - FD: Final Drive gears - Diff: Differential gears	145
3.17 Speed-Bump maneuver: $\Delta\theta$ on the preselected shaft for active and passive configurations; I: First gears - II: Second gears - FD: Final Drive gears . . .	145
3.18 Speed-Bump maneuver: $\Delta\theta$ for brake intervention with and without K2 clutch slip control; I: First gears - II: Second gears - FD: Final Drive gears .	146
3.19 HIL Test Rig 1-TMC 2-customized ESC 3-Brake caliper 4-Brake disk 5-oil tank 6-Data Acquisition System 7-Relay Box	148
3.20 Representation of ABS/ESC hydraulic circuit with input (red) and output (green)	149
3.21 Influence of Bulk modulus on brake pressure trend: experimental (solid black line) vs simulation with constant β (dotted gray line) and with non-linear β (dashed gray line)	154
3.22 'Raising phase': 1= 1° chamber TMC, 2= 2° chamber TMC, b= Rear Right caliper, FL= Front Left caliper, eq= equivalent Front Right+Rear Left caliper, exp=experimental, sim= simulation	155
3.23 Sensitivity analysis on b_2 and F_{f2} : 1= 1 st TMC chamber, 2= 2 nd TMC chamber, b= Rear Right caliper, n = nominal condition	155
3.24 'Falling phase': 1= 1 st TMC chamber, 2= 2 nd TMC chamber, b= Rear Right caliper, a= accumulator, exp=experimental, sim= simulation	156
3.25 Effect of PWM Duty Cycle on pressure trend in the brake caliper: the inlet valve is controlled via a constant frequency and variable Duty Cycle	156

3.26 Raising and falling phases by applying a PWM signal of 40% DC and modulation frequency of 900 Hz to the inlet valve and a PWM signal of 25% DC on 50 Hz to the outlet valve	157
3.27 Static Gain G_s for both inlet (left) and outlet (right) valve	158
3.28 Experimental validation of non-linear model during ABS emergency braking under extremely low road friction conditions: b= Rear Right caliper, exp=experimental, sim= simulation	159
3.29 Experimental Validation of Non-Linear Model under a PWM signal excitation: b= Rear Right caliper, exp=experimental, sim= simulation	159
3.30 Hydraulic scheme for the raising and falling phase in a brake caliper including Inlet/Outlet valves, Motor-pump and Spring accumulator.	161
3.31 Data Acquisition with a sample time of 0.1 ms of TMC (p_T) and Brake (p_b) pressures	163
3.32 PWM signal with different frequencies for both Inlet (DC=30%) and Outlet Valves (DC=70%), p_b = Brake Pressure	164
3.33 PWM frequency influence on brake pressure ripple for both Inlet (blue) and Outlet (green) valves	165
3.34 Brake pressure (up) and its gradient (down) vs time for different values of DC (Inlet valve)	165
3.35 Inlet Open-Loop map: pressure gradient vs pressure drop across Inlet valve for different value of DC	166
3.36 Outlet Open-Loop map: pressure gradient vs pressure drop across Outlet valve for different value of DC	167
3.37 Conversion from open-loop map (left) to inverse map (right) for different values of pressure drop across Inlet valve	170
3.38 Inlet Inverse map: DC vs reference pressure gradient and pressure drop across Inlet valve	170
3.39 Outlet Inverse map: DC vs reference pressure gradient and pressure drop across Outlet valve	170
3.40 Block diagram of FF + PI control strategy	171
3.41 Bode plots for transfer functions $\frac{e(s)}{n_b(s)}$ (left) and $\frac{e(s)}{n_T(s)}$ (right)	173

3.42 System response to a sequence of step changes of the reference pressure (dashed gray)	174
3.43 System response to a triangle wave reference pressure (dashed gray)	175
3.44 System response to a trapezoidal wave reference pressure (dashed gray) .	175
3.45 Transmission Test Rig at Politecnico di Torino	176
3.46 Transmission test bench layout. M1, M2: electric motors; EM1, EM2, ED: speed sensors (encoders); T1, T2, T_{HS} : torque sensors; B: disk (D) brake; SA1, SA2: half shafts.	178
3.47 Example of HIL configuration for longitudinal dynamics analysis.	179
3.48 DCT Test Rig: zoom on the brake caliper mounting	180
3.49 Speed-Bump crossing: M1 - torque applied by 37 kW motor; M2 - torque applied by 11 kW motor; HS - Half shaft torque	181
3.50 Speed-Bump crossing: transmission and motor speeds	182
3.51 Speed-Bump crossing: $\Delta\theta$ on the engaged and preselected shafts	182
3.52 Speed-Bump crossing: $\Delta\theta$ inside the differential	183
3.53 Speed-Bump crossing with different braking pressures: M1 - torque applied by 37 kW motor; M2 - torque applied by 11 kW motor; HS - Half shaft torque	183
3.54 Speed-Bump crossing with different braking pressures: $\Delta\theta$ on the engaged and preselected shafts	184
3.55 Tip-Out Maneuver with and without the control action (brake pressure of 8 bar): M1 - torque applied by 37 kW motor; M2 - torque applied by 11 kW motor; HS - Half shaft torque	185
3.56 Tip-Out Maneuver without (a) and with (b) the control action (brake pres- sure of 8 bar): transmission speeds	185
3.57 Tip-Out Maneuver without (a) and with (b) the control action (brake pres- sure of 8 bar): $\Delta\theta$ on the engaged and preselected shafts	186

List of Tables

1.1	Model parameters for the single-track model of autonomous vehicle . . .	15
1.2	Root Mean Square of lateral deviation y during Close-Loop path tracking control	70
2.1	Main I/O signals for TV controller in the dSPACE® AutoBox system with their discretization times and their availability on vehicle CAN network (Yes:present, No:absent)	82
2.2	Reference yaw rate correction Δr_{ref}	92
2.3	Performance indicators for the step steer test for the passive and controlled vehicles	109
2.4	Performance indicators for the step steers for different values of ω_F	111
3.1	Model parameters for break pressure dynamic non-linear model	153

Chapter 1

Autonomous Steering Control

1.1 Introduction on Autonomous Steering Driving

Autonomous or *Self-Driving* vehicles are nowadays a hot-topic for research and development in both industrial and academic fields, also arousing interest among social and governmental communities, well beyond the automotive engineering. 'Autonomous driving' represents a generic term for identifying a non conventional vehicle that is able to drive in urban and/or highway scenarios without or with a partial human intervention. In order to provide a common terminology, in [5] are considered different levels of driving automation from *no automation* in 'level 0' to *full automation* in 'level 5': the automated driving is distinguished from human driving if specific systems are designed to monitor the driving environment. Each level deals with the execution of steering and acceleration/deceleration tasks, the monitoring of driving environment, the fallback of dynamic driving task and the system capability. An example of self-driving application, with current technologies available on automotive market, is the Conventional Cruise Control (CCC) designed for keeping constant a desired vehicle speed set up by the driver; the 'autonomous' system takes full control of throttle and brake command in order to track the reference speed but with no environment monitoring so that the driver is responsible for control overtaking in emergency situations. This simple technology is now popular enough to be accepted by drivers and its safety benefits/limits have been studied by several authors [6, 7]. An advanced version of CCC is the Adaptive Cruise Control (ACC) [8–11] which elaborates the information coming from specific RADAR for obstacle detection thus enhancing the communication with external environment and providing a warning feedback to the driver which is expected to react in collision risk situations. In the case of Automatic Emergency Braking (AEB) [12, 13], the system is also requested to provide a braking intervention for obstacle avoidance purposes. For

autonomous driving applications, three different layers can be identified as indicated by [14, 15]:

- The *Strategic* layer, for gathering information from the environment surrounding the vehicle, i.e. pedestrian or obstacle recognition, lane and road signals identification;
- The *Tactical* layer, for providing the reference signals for the next layer, i.e. reference path to be followed or reference speed to be reached;
- The *Control* layer, for evaluating the commands for each autonomous or automatic vehicle components and tracking the reference behavior imposed by the Tactical layer;

The present chapter is focused on the analysis and the development of the Control layer in the specific application of an automatic steering control for path tracking and obstacle collision avoidance purposes. The path tracking control is a well-known topic in the robotic control field [16–18] and driver modeling [19–21]. Several experiments were carried out for automatic driving [22, 23] where the reference path is generally provided through inductive cables or magnetic markers, but new technologies about Global Positioning Systems (GPS) have incremented the position accuracy through the use of external global navigation satellite system (GNSS). Different feedback controllers have been designed for automated path tracking control (an extended review is described by [24]) and they can be generally divided into two separate categories.

The first category includes all methods based on simple geometrical relationships by exploiting the vehicle kinematic models (i.e. by approximating a zero slip angle for the front and rear tires) described by the well-known Ackerman steering formula. One example is the *Pure Pursuit* algorithm whose objective is to calculate the curvature of the arc from the vehicle position to the desired position placed at a *look-ahead* distance on the reference path [25, 26]; a different geometric-based approach is designed by Stanford's University during the DARPA Grand Challenge [27], usually referred as *Stanley method*, which elaborates the steering angle as a combination of vehicle yaw angle error and a term based on the lateral deviation of the front axle with respect to the reference path.

The second category deals with all feedback controllers based on the simplified linear single-track model, described in section 1.3, that takes into account a different slip angle for the front and rear axles and provides a second order yaw dynamics with damping and stiffness coefficients variable with vehicle speed. The Proportional Integral Derivative (PID) is the most used control logic adopted for steering angle evaluation: a PD structure

on lateral deviation error added to a P control on heading error is designed by [28] which proves that yaw angle error contribution further improves the tracking performance, as it is also confirmed by [29] where only the lateral position error is taken into account with evident worse results. A more detailed analysis is conducted by [30] based on frequency responses of lateral acceleration and yaw rate with respect steering angle, calculated from the linear single-track model: the effect of the vehicle speed and friction coefficient is studied and consequently a feedforward steering contribution based on reference path curvature is coupled with a feedback yaw rate and lateral acceleration control. Moreover, it is suggested to design the look-ahead distance as an increasing function of vehicle speed. The benefits introduced by a feedforward contribution which avoid the selection of high feedback control gain is shown by [31] thus also demonstrating its importance in terms of tradeoff between stability and tracking performances. In [32] a PID² controller is designed, according to the parameter state approach [33], for the path tracking problem related to an automated bus in order to be robust with respect to the variation of vehicle speed and mass in a specific range. The same state parameter approach is used for autonomous passenger vehicle by [34, 35]. The classical loop-shaping theory is applied in [36] where two different controllers are proposed for achieving alternatively a better ride comfort or a good tracking performance. Linear Quadratic Regulator (LQR) based on optimal control theory is applied by Nissan [29] which makes a comparison against the PD strategy with the final conclusion that the LQR logic is "unable to track the path accurately on curves" due to large model error on the curvature part of reference path. This issue is solved with an additional feedforward (FF) contribution to the LQR control in [9]. A non conventional LQR design is presented in [37–39] for the PATH framework: authors adopt the loop shaping technique for achieving the robustness on measurement noise at high frequencies and introduce a performance index that takes into account the ride quality. The *centers of percussion* concept is shown by [40] for a four-wheel-steering (4WS) through the design of a first order sliding model control meanwhile [41] has implemented a super-twisting version for reducing the chattering problem. More references in the field of sliding mode theory and application are [42–45]. Other controller structures has been analyzed and implemented: H_∞ in [46, 47], back-stepping control [48] and fuzzy logics [49]. Recently, the path tracking control strategies are further improved for being robust at high lateral accelerations [50–52] even with the implementation of model predictive controls now extensively used in simulation and preliminary experimental tests [53–55].

Similar to the difference between CCC and ACC, the path tracking problem can be extended to an Obstacle Collision Avoidance (OCA) algorithm where the reference path is no more fixed but it is changed in real-time by elaborating further information coming from other sensors (Radar, Lidar, Camera) thus enabling the communication

with external environment. The core aspect of OCA control logic is represented by the path planning algorithm that needs to provide the reference path for the lower controller layer (i.e. path tracking control). A 3D virtual dangerous potential field is used for generating the desired trajectory to avoid obstacle in real-time and a Multi-constrained Model Predictive Control (MMPC) problem is formulated in [56]. In [57] a novel algorithm for obstacle avoidance path planning, defined as *navigation circle*, is developed and optimized to provide feasible trajectories in real-time. A decision-making algorithm is presented in [58] where a group of path candidates are generated starting from a global reference path and the local reference trajectory is selected according to safety, smoothness and consistency criteria in presence of static obstacles. The path planning has been experimentally tested during the 2010 Autonomous Vehicle Competition. In 1993 authors from Stanford University [59] proposed for the first time the *Elastic Bands theory* for deforming an initial reference path into a collision-free path which is able to take into account the presence of local obstacles. The same OCA method is applied by [60] with modifications to road vehicle based systems and realistic simulation results are presented using high fidelity vehicle models with several different collision scenarios.

The intent of the present section is to design an automatic steering control for an autonomous vehicle equipped with Electric Power Assist Steering (EPAS) and drive-by-wire technologies. Despite the importance of tires lateral force in path tracking controller, the single-track model is chosen instead of a kinematic/geometric one ([25–27]) and it is further enhanced by introducing the steering actuation (EPAS) dynamics if compared with existing literature. The steering action is calculated to let the vehicle follow a reference path which is stored in a Digital Map properly built to be available in real-time. Furthermore, the contribution described in the following chapter is the enhancement of a Proportional + Derivative (PD) control designed with the Parameter State Approach [33, 35] (PSA) by coupling it with a static Feedforward (FF) or with an integral sliding mode (ISM) for improving the tracking performance in cornering maneuvers: the FF term requires the knowledge of the instantaneous reference path curvature, meanwhile the ISM can be designed to reject external disturbances without the exact evaluation of the path curvature. Experimental tests are carried out for showing and comparing the efficacy of the two controllers against PD control and manual driving behavior. Moreover, an experimental implementation of an obstacle collision avoidance system based on the elastic band method is briefly described with the main objective to show that the method can be implemented in real time and used in actual vehicles.

The present chapter is divided into five sections by including the present introduction and the conclusion: section 2 shows the autonomous vehicle demonstrator with its set-

up; in section 3 the single-track model with steering dynamics is presented; section 4 is focused on path tracking control design and its implementation for an OCA application which are finally experimentally verified with specific tests in a proving ground.

1.2 Experimental Setup of the Autonomous Vehicle

The vehicle demonstrator, shown in Fig. 1.1, used for dynamics model validation and control calibration is a Ford Fusion hybrid which has been converted into an autonomous vehicle through the installation of EPAS module, throttle-by-wire and brake-by-wire Dataspeed interfaces.

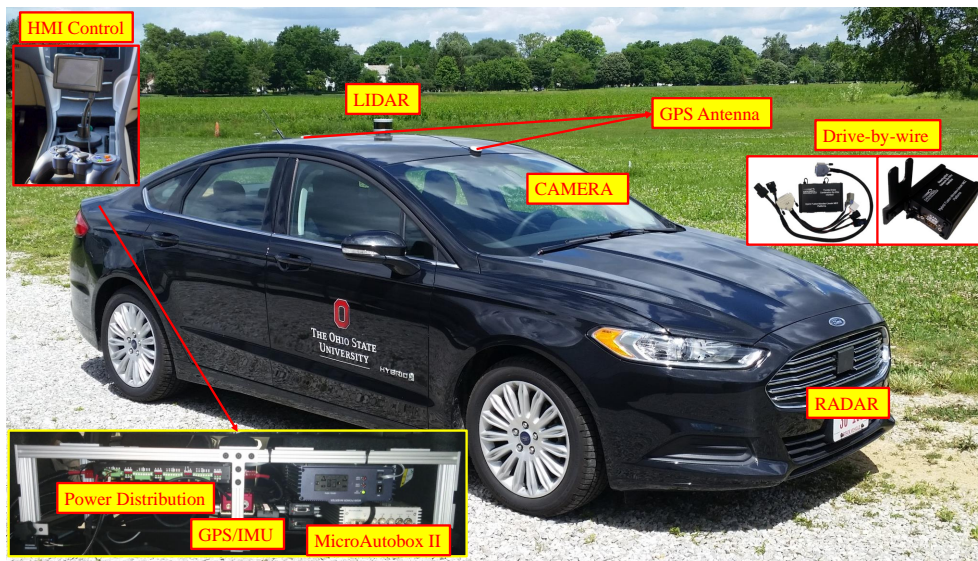


Figure 1.1 Vehicle Demonstrator and Sensors/Actuators Platform

The Dataspeed Inc. [61] EPAS module and Throttle-Brake Combination By-Wire interfaces enable computer control of the steering wheel, the throttle and braking systems in a safe and effective manner. This plug-in ready kit requires no modification to the factory harnessing and can be installed in few minutes. Industry standard CAN and USB networks enable control and monitoring of the steering wheel (angular position), the throttle and braking systems (pedal positions). The Dataspeed modules are connected through CAN bus communication to a dSPACE® MicroAutoBox II electronic unit where controller logic, previously designed in Matlab®/Simulink® environment, is flashed. A range of several sensors are installed on-board vehicle in order to monitoring the external environment and to localizing vehicle position:

- Delphi ESR [62] radar combines a wide field of view at mid-range with long-range coverage to provide two measurement modes simultaneously. Based on Simulta-

neous Transmit and Receive Pulse Doppler (STAR PD) Waveform technology, the ESR provides independent measurements of range and range-rate and superior detection of clustered stationary objects. Mid-range coverage not only allows vehicles cutting in from adjacent lanes to be detected but also identifies vehicles and pedestrians across the width of the equipped vehicle. Long-range coverage provides accurate range and speed data with powerful object discrimination that can identify up to 64 targets in the vehicle's path.

- Velodyne VLP-16 Lidar [63] creates 360°3D images by using 16 laser/detector pairs mounted in a compact housing. The housing rapidly spins to scan the surrounding environment and the lasers fire thousands of times per second, providing a rich, 3D point cloud in real time. Advanced digital signal processing and waveform analysis provide high accuracy, extended distance sensing, and calibrated reflectivity data.
- Mobileye camera 5 [64] uses a smart digital camera located on the front windshield inside the vehicle. Inside the camera, Mobileye's powerful EyeQ2[®] Image Processing Chip provides high-performance real-time image processing, by utilizing the Mobileye vehicle, lane and pedestrian detection technologies to effectively measure and calculate dynamic distances between the vehicle and road objects.
- OXTS xNAV 550 RTK GPS [65] integrates dual L1/L2 GNSS receivers for 2 cm RTK position accuracy and an Inertial Measurement Unit (IMU) with three accelerometers and three angular rate sensors used to smooth the jumps in GNSS and fill in missing data. The improved receivers also mean better heading accuracy. Its communication with MicroAutoBox II is via UDP protocol.

In the present activity, the differential OXTS GPS is the only sensor used for vehicle position localization as feedback input to the path tracking controller meanwhile other sensors are going to be integrated for real-time implementation of obstacle collision avoidance control logic according to which is generally referred as *Sensor-Fusion* technology.

The vehicle demonstrator architecture is also equipped with a power distribution unit for managing the electric energy between vehicle high voltage battery and sensors/actuators.

Finally, A Human Machine Interface (HMI) with touch screen technology provides a control panel for basic command selections (power on/off all devices and switch between manual and autonomous modes).

1.3 Single-Track Model

The present section describes a linearized single-track model used for designing controller strategies that are introduced in next sections. This linear model (see [66, 67] for further details) is also able to describe vehicle dynamics for a lateral acceleration up to $4m/s^2$. The vehicle is considered symmetric with respect its longitudinal direction so that the front and the rear axles can be represented by single wheels as indicated in Fig. 1.2 where an inertial reference system O_E, X_E, Y_E, Z_E and a vehicle reference system O, x, y, z are shown.

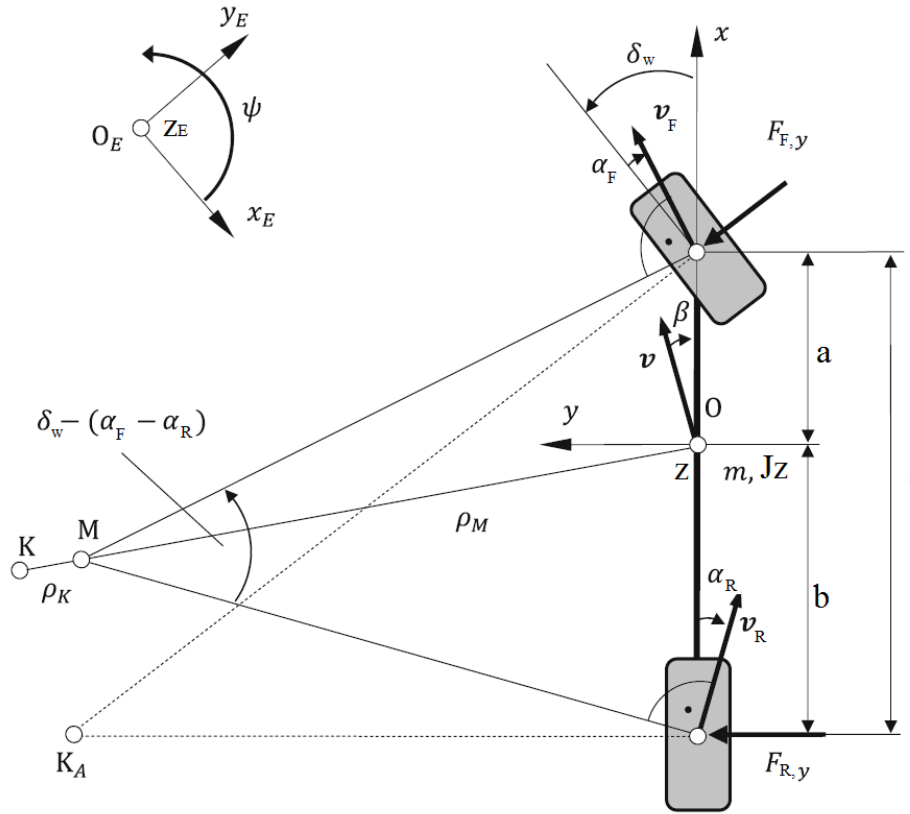


Figure 1.2 Single-Track Model (adapted from [1])

When vehicle speed is very small, and slip angles can be neglected (ideal kinematic steering), all points of vehicle move along a circle with the center of the curvature being K_A which coincides with the instantaneous center of rotation M of the motion. The steering angle required to execute this motion is given as:

$$\tan \delta_w = \frac{l}{\sqrt{R_M^2 - b^2}} \xrightarrow{|\delta_w| \ll 1, b \ll R_M} \delta_w \approx \frac{l}{R_M} \quad (1.1)$$

In a real scenario, slip angles cannot be neglected and the new instantaneous center of rotation is evaluated from the front and rear wheel speed directions. The following assumptions are considered for evaluating the single-track model equations:

- the vehicle is assumed as a rigid body in motion on a 2D plane with mass m and inertia moment J_z
- vehicle speed V is assumed constant and only two degree of freedom (yaw rate $r = \dot{\psi}$ and sideslip angle β) are taken into account
- vehicle sideslip angle β , tires slip angles α_i and yaw rate acceleration \dot{r} are considered small enough to consider the linear part of vehicle dynamics
- Front steering action (small wheel steering angles δ_w)

1.3.1 Dynamics equations

A rigid body in motion on a 2D surface can be described by 3 degrees of freedom: global reference positions X_E , Y_E of vehicle center of gravity and its yaw angle ψ .

$$\begin{cases} m\ddot{X}_E &= F_X \\ m\ddot{Y}_E &= F_Y \\ J_z\ddot{\psi} &= M_Z \end{cases} \quad (1.2)$$

where F_X , F_Y and M_Z are the total forces applied along X_E , Y_E axes and total yaw moment around Z_E axis. In order to have a linearized vehicle model and avoid trigonometric expression of ψ , Eq. 1.2 can be expressed in the vehicle reference frame:

$$\left. \frac{d\vec{V}}{dt} \right|_E = \left. \frac{d\vec{V}}{dt} \right|_v + \vec{\omega} \wedge \vec{V} = \begin{Bmatrix} \dot{u} \\ \dot{v} \\ 0 \end{Bmatrix} + \begin{Bmatrix} -rv \\ ru \\ 0 \end{Bmatrix} \quad (1.3)$$

$$\begin{cases} m(\dot{u} - rv) &= F_x \\ m(\dot{v} + ru) &= F_y \\ J_z\dot{r} &= M_z \end{cases} \quad (1.4)$$

where u and v are the vehicle speed components respectively along x and y axis and F_x , F_y , M_z are the same of Eq. 1.2 but expressed in the vehicle reference frame. Eq. 1.4 are non-linear with respect u , v , and r but, since the sideslip angle β is supposed to be

small, it is possible to linearize the trigonometric functions:

$$\begin{cases} u &= V \cos(\beta) \approx V \\ v &= V \sin(\beta) \approx V\beta \end{cases} \quad (1.5)$$

thus leading to:

$$\begin{cases} m(\dot{V} - rV\beta) &= F_x \\ m(V\dot{\beta} + \beta\dot{V} + rV) &= F_y \\ J_z\dot{r} &= M_z \end{cases} \quad (1.6)$$

If the interaction between longitudinal and lateral tire forces is neglected, the first equation of system 1.6 can be decoupled from the remaining two, thus reducing the degrees of freedom to the sideslip angle β and yaw rate r . Furthermore, if the speed V is considered constant the system 1.6 can be reduced to:

$$\begin{cases} mV(\dot{\beta} + r) &= F_y \\ J_z\dot{r} &= M_z \end{cases} \quad (1.7)$$

F_y and M_z can be related to tires forces:

$$\begin{cases} F_y &= \sum_{\forall i} F_{x_i} \sin(\delta_i) + \sum_{\forall i} F_{y_i} \cos(\delta_i) \approx \sum_{\forall i} F_{x_i} \delta_i + \sum_{\forall i} F_{y_i} \\ M_z &= \sum_{\forall i} F_{x_i} \sin(\delta_i) x_i + \sum_{\forall i} F_{y_i} \cos(\delta_i) x_i \approx \sum_{\forall i} F_{x_i} \delta_i x_i + \sum_{\forall i} F_{y_i} x_i \end{cases} \quad (1.8)$$

where F_{x_i} , F_{y_i} are force components on i_{th} axle and x_i , y_i are the coordinates of its center. In Eq. 1.8, drug forces and self-alignment yaw moments are neglected and trigonometric functions are linearized by considering low values of wheel steering angles δ_i . Furthermore, the products $F_{x_i} \delta_i$ can be also neglected since they are negligible with respect other terms of Eq. 1.8. Tires lateral forces F_{y_i} depends on several variables such as tires slip angles, tires vertical forces, road contact friction coefficients and tires slip ratio. In order to have a linearized model, F_{y_i} can be evaluated as:

$$F_{y_i} = C_i \alpha_i \quad (1.9)$$

where C_i is the cornering stiffness of i_{th} axle and not of an individual wheel: with the single-track model the vehicle is assumed as a rigid body (roll angle neglected) thus compensating the camber forces between right and left wheels. Moreover, even the toe angle influence and lateral load transfer are neglected: this would be correct if a linear relation occurs between cornering stiffness and load transfer since the increase of the cornering stiffens of the most heavily loaded wheel is exactly compensated by the

decreasing of the cornering stiffness of the opposite wheel; This is not generally verified and the load transfer introduces a reduction of axles cornering stiffness eve though this effect is negligible for a lateral acceleration lower than $5m/s^2$. Furthermore, a positive toe angle increases axle cornering stiffness meanwhile a negative value decreases it.

Tires slip angles can be expressed as a function of their correspondent wheel speeds as indicated in Fig. 1.3. The speed V_i of the i_{th} wheel center P_i can be referred to the

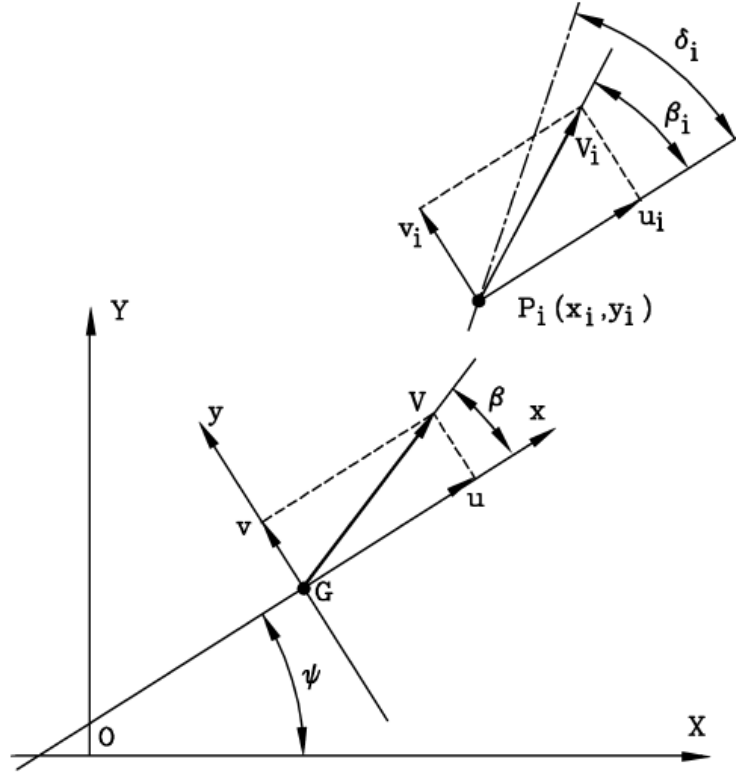


Figure 1.3 Kinematic diagram of wheel speed (adapted from [1])

speed of vehicle center of gravity V :

$$\vec{V}_{P_i} = \vec{V}_G + \dot{\psi} \wedge (P_i - G) = \begin{Bmatrix} u - \dot{\psi} y_i \\ v + \dot{\psi} x_i \end{Bmatrix} \quad (1.10)$$

The angle β_i between the direction of \vec{V}_{P_i} and vehicle x axis is defined as:

$$\beta_i = \arctan\left(\frac{v_i}{u_i}\right) = \arctan\left(\frac{v + \dot{\psi} x_i}{u - \dot{\psi} y_i}\right) \quad (1.11)$$

If the i_{th} tire is rotated by a steering angle of δ_i , its slip angle is:

$$\alpha_i = \delta_i - \beta_i = \delta_i - \arctan\left(\frac{v + \dot{\psi} x_i}{u - \dot{\psi} y_i}\right) \quad (1.12)$$

Eq. 1.12 can be easily linearized by considering that the term ψy_i is negligible with respect vehicle speed V :

$$\alpha_i = \delta_i - \beta \approx \delta_i - \arctan\left(\frac{v + r x_i}{V}\right) = \delta_i - \beta - \frac{x_i}{V} r \quad (1.13)$$

In the linearized expression of α_i , the coordinate y_i doesn't appear with the consequence that if δ_i is the same between right and left wheels also their slip angles are equal as highlighted in Eq. 1.13: this allows to approximate vehicle dynamics with a single track scheme (1.2) thus writing equations in terms of axle instead of single wheels.

Finally, slip angles of front and rear axles are reported respectively in the following equations:

$$\begin{cases} \alpha_F &= \delta_F - \beta - \frac{a}{V} r \\ \alpha_R &= \delta_R - \beta + \frac{b}{V} r \end{cases} \quad (1.14)$$

In most of passenger cars, and even in the vehicle considered in this activity, only the front axle can be steered so that the assumption $\delta_R = 0$ can be used without loss of generality.

The final equation of linearized single-track vehicle model are:

$$\begin{cases} mV(\dot{\beta} + r) &= (-C_F - C_R)\beta + \left(-\frac{C_F a}{V} + \frac{C_R b}{V}\right)r + C_F \delta_F \\ J_z \dot{r} &= (-C_F a + C_R b)\beta + \left(-\frac{C_F a^2}{V} - \frac{C_R b^2}{V}\right)r + (C_F a)\delta_F \end{cases} \quad (1.15)$$

It is a system of two first order differential equations in terms of β and r even though these two variables are dimensionally an angular speed (r) and something related to vehicle speed (β) thus implying that their derivative are accelerations. The steering angle δ_F can be considered an input for the system.

1.3.2 Steady-State behavior

In steady-state conditions ($\dot{\beta} = 0$ and $\dot{r} = 0$), vehicle trajectory is circular with a constant radius equal to:

$$R = Vr \quad (1.16)$$

From Eq. 1.15, the evaluation of steady-state values of sideslip angle β and yaw rate r deals to:

$$\begin{cases} \beta &= \frac{C_F C_R b L - m V^2 C_F a}{C_F C_R L^2 + m V^2 (b C_R - a C_F)} \delta_F \\ r &= \frac{C_F C_R L V}{C_F C_R L^2 + m V^2 (b C_R - a C_F)} \delta_F \end{cases} \quad (1.17)$$

where $L = a + b$ is the vehicle wheelbase. The new parameter named as *Understeer gradient* can be defined as:

$$K = \frac{m}{L} \left(\frac{b}{C_F} - \frac{a}{C_R} \right) \quad (1.18)$$

so that the following steady-state gains are formulated:

- Sideslip angle steady-state gain

$$\frac{\beta}{\delta_F} = \left(1 - \frac{maV^2}{bLC_R} \right) \frac{b}{L + KV^2} \quad (1.19)$$

- Yaw rate steady-state gain

$$\frac{r}{\delta_F} = \frac{V}{L + KV^2} \quad (1.20)$$

- Lateral acceleration steady-state gain

$$\frac{a_y}{\delta_F} = \frac{V^2}{L + KV^2} \quad (1.21)$$

- Curvature steady-state gain

$$\frac{\rho}{\delta_F} = \frac{1}{L + KV^2} \quad (1.22)$$

Eq. 1.1 indicates that the curvature steady-state gain in kinematic condition (Eq. 1.1 with assumption of slip angles negligible) can be corrected by a factor of $\frac{L+KV^2}{L}$ to take into account the important influence of wheel slip angles. If the understeer gradient is null the value of $\frac{1}{R\delta}$ is constant and vehicle response to any steering angle is equal to that one in kinematic condition; This doesn't mean that the vehicle is operating in kinematic condition, since wheel slip angles are not negligible so that its behavior is generally defined as 'neutral condition'.

If $K > 0$, the value of $\frac{1}{R\delta}$ decreases with vehicle speed: for keeping constant the trajectory radius, the steering angle has to be increase when vehicle speed increases. The vehicle is operating in 'understeer condition'. A direct measure of vehicle understeer behavior is the 'characteristic velocity', defined as the speed at which the steering angle required to follow a desired trajectory is double the *Ackerman angle* by means the curvature steady-state gain is equal to $1/2L$:

$$V_{car} = \sqrt{\frac{1}{K}} \quad (1.23)$$

If $K < 0$, the value of $\frac{1}{R\delta}$ increases with vehicle speed until it reaches the values of the 'critical velocity':

$$V_{cri} = \sqrt{\frac{1}{-K}} \quad (1.24)$$

where vehicle response tends to infinity and the vehicle becomes unstable. A vehicle that presents such a behavior is operating in 'oversteer condition': for this configuration the critical velocity must be greater than the vehicle max speed.

The value of sideslip angle steady-state gain β/δ_F decreases when speed increases until it becomes null for the velocity:

$$V_{\beta=0} = \sqrt{\frac{bLC_R}{am}} \quad (1.25)$$

For higher vehicle speeds its value becomes negative and tends to infinity when speed tends to critical velocity for an oversteer condition; In case of understeer condition its value tends to:

$$\frac{\beta}{\delta_F} = \frac{aC_F}{aC_F - bC_R} \quad (1.26)$$

In case of neutral condition, the slip angles of front and rear axles are equal. For oversteering vehicles, slip angle of rear axle is higher (in absolute value) than the front axle one meanwhile the opposite situation occurs for understeering vehicles. Fig. 1.4 shows a graphic description of vehicle behavior during different conditions. The vehicle presents a front steering axle A and a fixed rear axle B. For low values of vehicle speed, the kinematic condition is almost verified: the slip angles are null and the trajectory center is placed in O. In the condition $\alpha_F = \alpha_R$ the angle BO'A is still equal to δ_F and the point O' leads on the same circle identified by points A, B and O: the vehicle is operating in neutral condition. If $|\alpha_F| > |\alpha_R|$ the curvature center is moved to point O'' and radius R'' is higher than R thus leading to an understeering behavior. If $|\alpha_F| < |\alpha_R|$ the curvature center is O''' and the radius R''' is lower than R thus leading to an oversteering behavior. These considerations are verified only if the understeer gradient K is constant and doesn't depend on vehicle speed; in a real scenario, the value of K is influenced by vehicle speed that can modify its understeering behavior.

1.3.3 Experimental Validation

The present section aims to describe the single-track model and to validate it with experimental test carried out with the prototypal vehicle equipped with drive-by-wire technology. Most of the single-track model parameters (m, J_z, a and b) are obtained

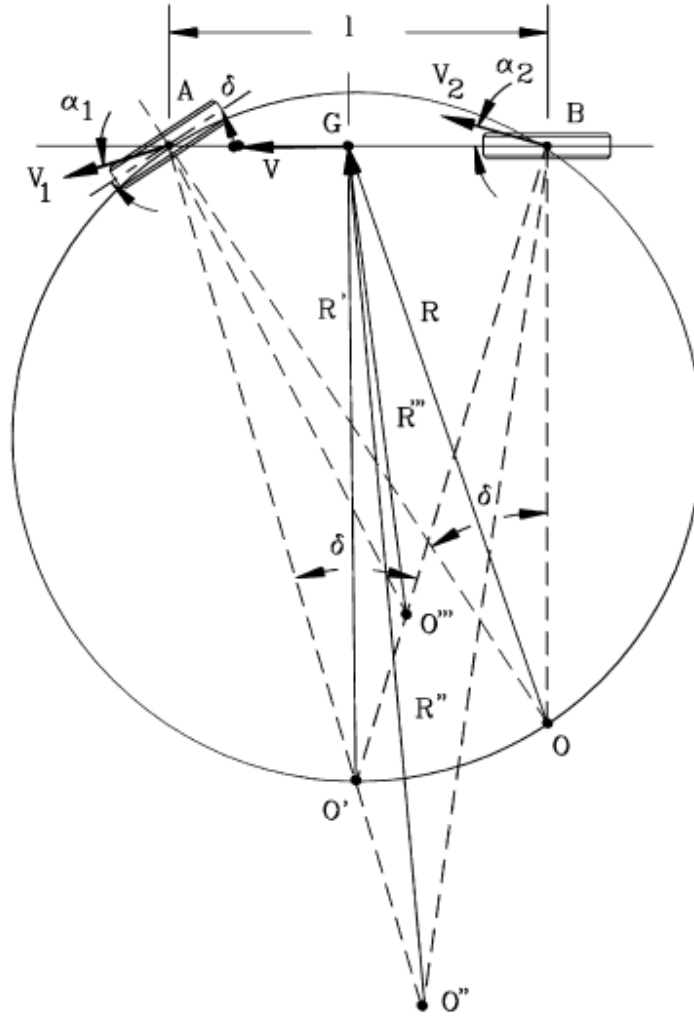


Figure 1.4 Lateral behavior of a vehicle with a single steering axle (adapted from [1])

through specific measurements on the vehicle meanwhile the front and rear cornering stiffness values are evaluated and proper tuned in order to get the best fit between model and experimental data. All single-track parameters are reported in Table 1.1. Three specific experimental test are here presented in order to show the efficacy and limits of a single-track model:

1. Ramp steer at constant speed
2. Step steer at constant speed
3. Skid pad

Table 1.1 Model parameters for the single-track model of autonomous vehicle

Symbol	Description	Value
m	Vehicle mass with 4 passengers	1997.6 <i>kg</i>
J_z	Inertia moment around vehicle z axle	3728 <i>kgm</i> ²
a	Front semi-wheelbase	1.3008 <i>m</i>
b	Rear semi-wheelbase	1.5453 <i>m</i>
L	Wheelbase	2.84607 <i>m</i>
C_F	Front Cornering Stiffness	1.3e ⁵ <i>N/rad</i>
C_R	Rear Cornering Stiffness	15.9e ⁵ <i>N/rad</i>
R_s	Steering ratio	14.6
l_s	Preview Distance	0.5 <i>m</i>
$[n_2 \ n_1 \ n_0]$	Numerator of steering dynamics	[74.45 – 1001 53760]
$[d_4 \ d_3 \ d_2 \ d_1 \ d_0]$	Denominator of steering dynamics	[1 36.33 1205 12950 53760]

All these maneuvers are executed on a flat surface (no bank angle) and in high friction conditions. The single-track model receives as input the experimental steering angle measured during each test in order to have coherent comparison.

Ramp steer at constant speed

The ramp steer maneuver can be described with the following steps:

- set the cruise control at a specific speed
- when the desired speed is reached, the steering angle is gradually increased from 0 to 400 deg with a slope of 14 deg/s
- the vehicle is stopped when lateral acceleration saturates

These steps can be identified in Fig. 1.5 where input steering angle and speed are shown. The vehicle speed can be considered constantly equal to 30 *km/h* for the whole application of the ramp steering action. The variables analyzed during the maneuvers are the sideslip angle β , the yaw rate r (output of single-track model) and the lateral acceleration a_y reported in Fig. 1.6. This test is useful to observe the quasi-static lateral behavior of the vehicle in the whole range of lateral acceleration thus allowing to validate the single-track model in the linear part of vehicle dynamics and to detect the limit beyond which the model is not enough accurate to describe tires forces saturation. It is possible

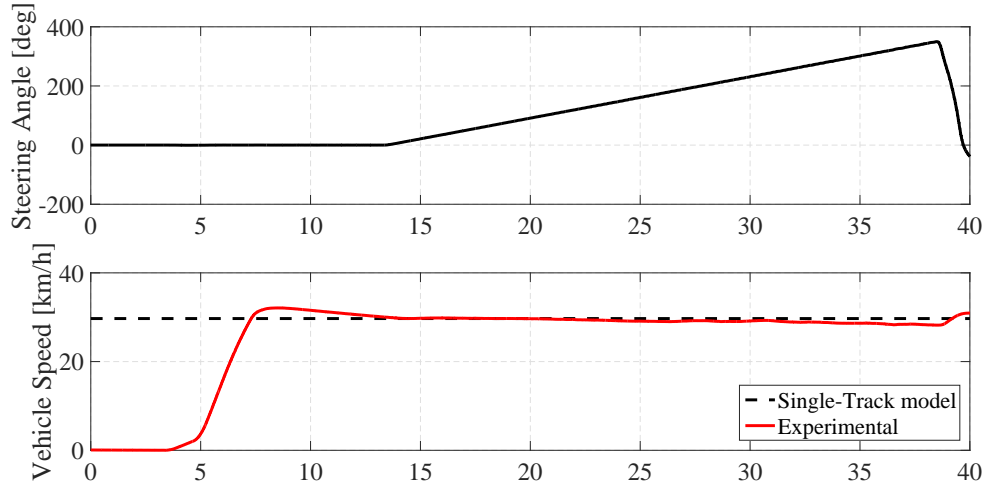


Figure 1.5 Ramp steer maneuver: steering angle and vehicle speed

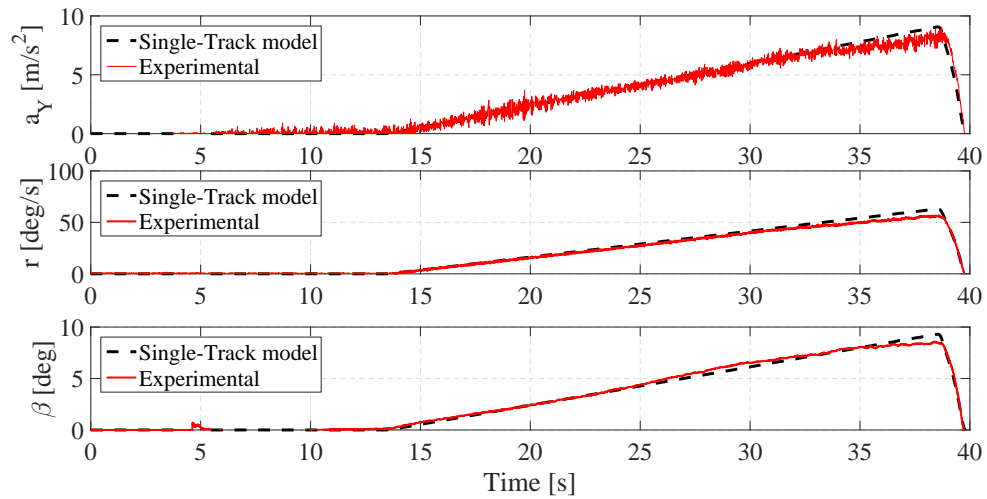


Figure 1.6 Ramp steer maneuver: sideslip angle β , yaw rate $r = d\psi/dt$ and lateral acceleration a_y

to appreciate that the linear single-track model is able to give a good matching with respect experimental values for lateral acceleration up to 5 m/s².

Step steer at constant speed

The step steer maneuver can be described with the following steps:

- set the cruise control at a specific speed
- when the desired speed is reached, an instantaneous step steering action is applied and kept constant to a desired value

- the vehicle is stopped when the vehicle trajectory is stabilized

Different step steer amplitudes are selected in order to verify the single-track model in different operating conditions, as indicated in Fig. 1.7. All the tests are executed by using

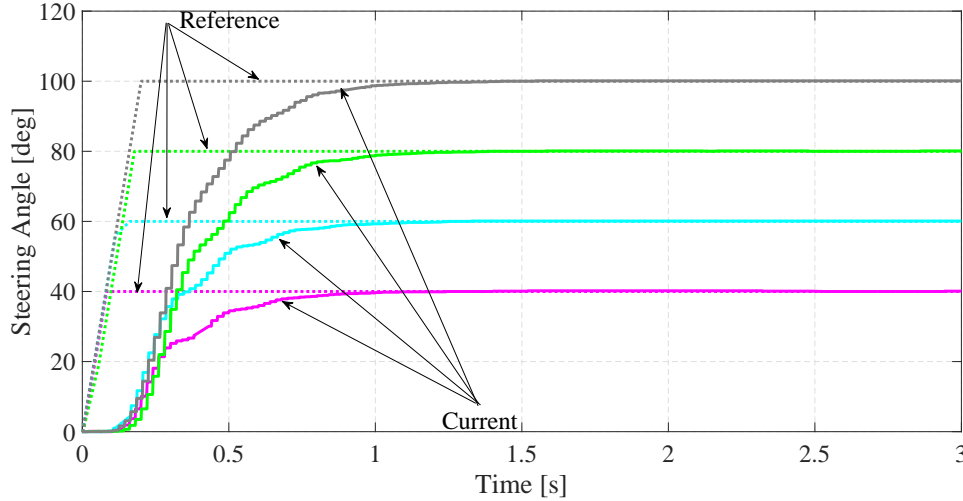


Figure 1.7 Step steer maneuver: reference and current steering angle for different amplitudes

the cruise control to keep the speed equal to 30 km/h . Fig. 1.7 also shows the comparison between the steering angle set for the EPAS system and its response: the dynamics of the steering reaction must be taken into account and a model will be proposed in next section. Step steer test are usually adopted for analyzing the transient vehicle behavior

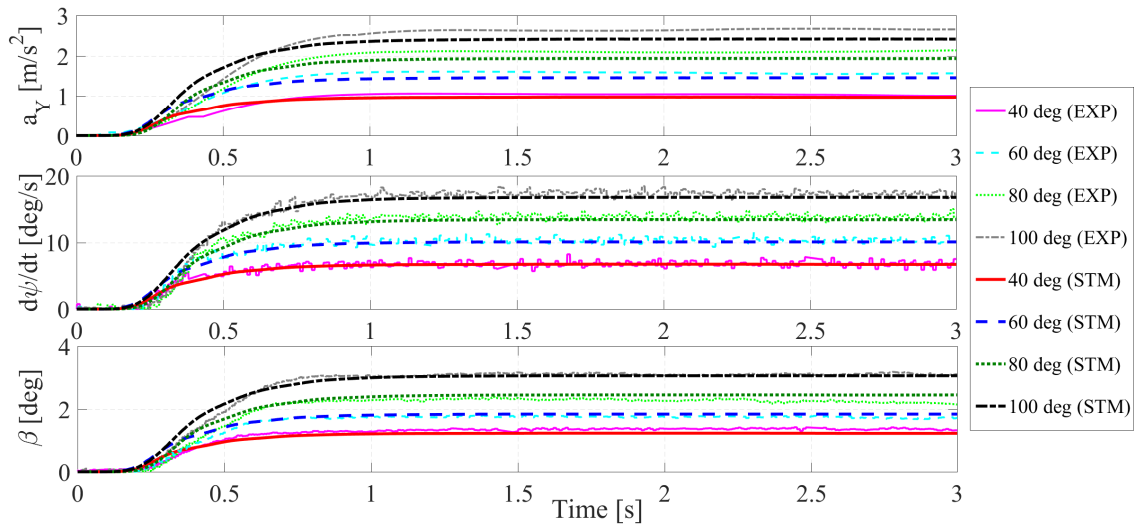


Figure 1.8 Step steer maneuver: sideslip angle β , yaw rate $r = d\psi/dt$ and lateral acceleration a_y from experimental test (EXP) and single-track model (STM)

and to have a double check on its steady-state response. In Fig. 1.8 the steady-state

values of lateral acceleration a_y , yaw rate r and sideslip angle β are well described by the single-track model meanwhile the transient response of a_y seems to be different from experimental data: this aspect is related to the hypothesis of single-track model according which $\dot{\beta} \ll r$ thus leading to $a_y = V(r + \dot{\beta}) \cos(\beta) \approx Vr$; Since the final purpose of the single-track model is for vehicle position control design, a further experimental validation can be carried out by comparing GPS position. In the single-track model, vehicle global position is evaluated from yaw rate, sideslip angle and speed:

$$\begin{cases} \psi &= \int_{\psi_0} r dt \\ X_G &= \int_{X_0} (V \cos \beta \cos \psi - V \sin \beta \sin \psi) dt \\ Y_G &= \int_{Y_0} (V \cos \beta \sin \psi + V \sin \beta \cos \psi) dt \end{cases} \quad (1.27)$$

where X_G and Y_G are the east and north global vehicle coordinate and ψ the yaw angle with respect the X axis. Values of ψ_0 , X_0 and Y_0 are obtained from experimental data in order to make the comparison shown in Fig. 1.9.

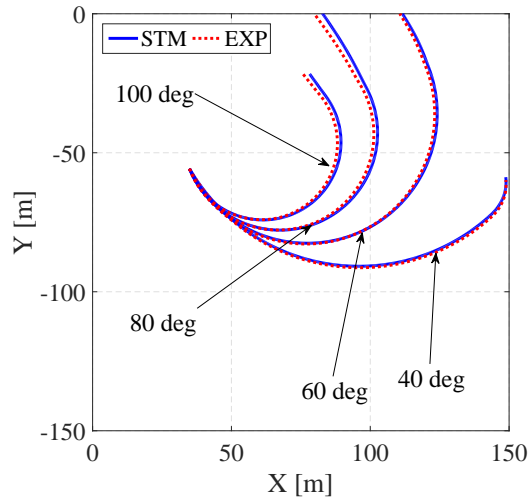


Figure 1.9 Step steer maneuver: vehicle position for different steering angles from both experimental test (EXP) and single-track model (STM)

Finally, the single-track model here presented is able to catch the linear part of vehicle dynamic for a lateral acceleration up to 5 m/s^2 and to well predict the vehicle global position.

Skid Pad

The Skid Pad test is generally used to evaluate the understeer/handling characteristic of the vehicle by means the vehicle sensitivity to a steering input. The test consists

of following a reference trajectory with constant radius while the gas pedal is slowly increased up to the max possible value: increasing the vehicle speed and so the lateral acceleration, forces the driver to adjust the steering angle to increase lateral forces for following the desired constant radius path. The reference path here used has a constant radius of 30 m and the most important variable are plotted in Fig. 1.10, 1.11 and 1.12.

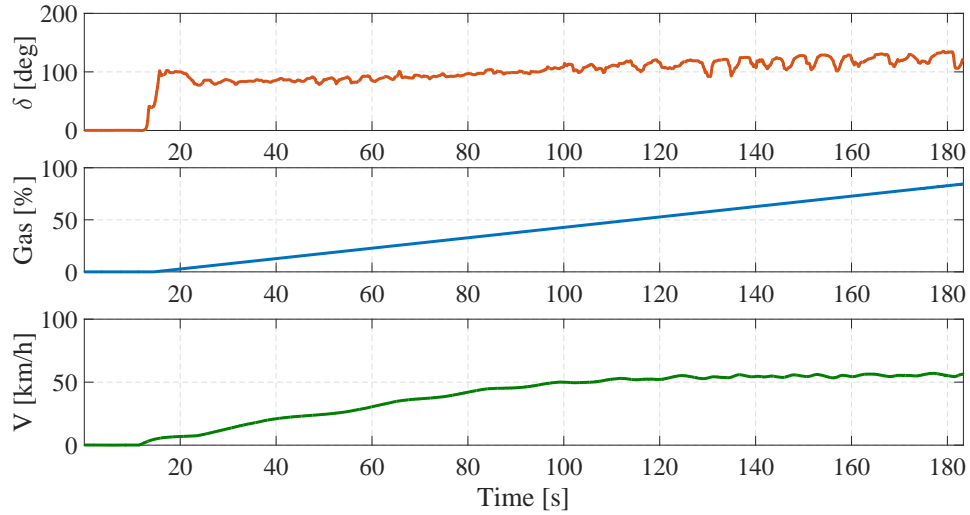


Figure 1.10 Skid Pad: vehicle steering angle δ , gas pedal and speed V

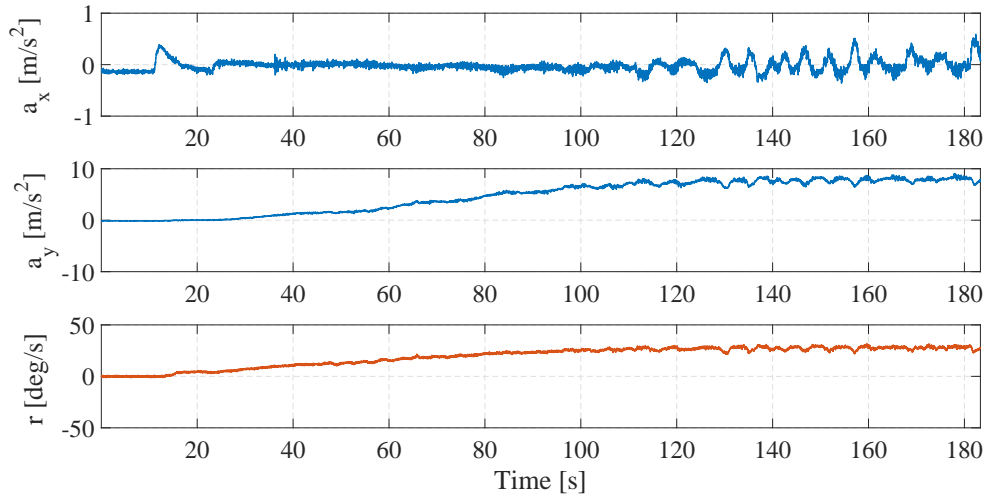


Figure 1.11 Skid Pad: vehicle longitudinal a_x , lateral acceleration a_y and yaw rate r

It is worth noting that the vehicle speed doesn't overpass 50 km/h even if the gas pedal is further increased as a consequence of the tire forces saturation (also highlighted by lateral acceleration and yaw rate). The handling characteristic can be evaluated based on the driver steering correction with respect the kinematic steering ($\delta_F - \delta_{Kin}$) as function of lateral acceleration as shown in Fig. 1.13. The upper subplot of Fig. 1.13 is usually

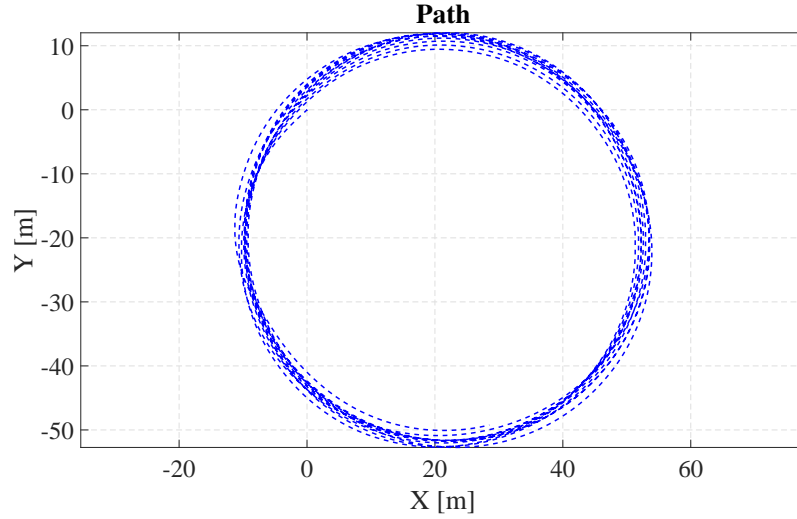
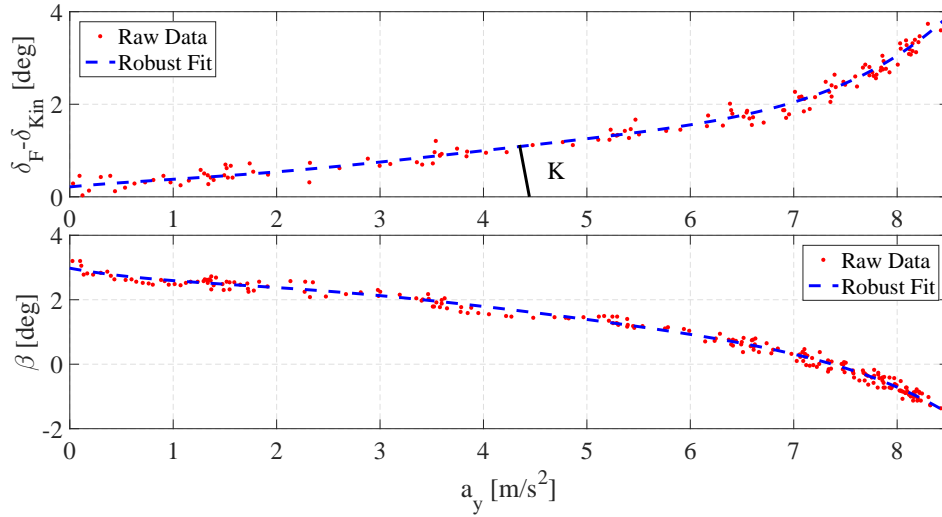


Figure 1.12 Skid Pad: vehicle GPS position

Figure 1.13 Skid Pad handling characteristics: $\delta_F - \delta_{Kin}$ and β vs a_y

adopted for calculating the understeer gradient K defined in Eq. 1.18: it is geometrically equal to the slope of its linear part. The value of K calculated from single-track model by using Eq. 1.18 is $0.006 \text{ rad s}^2/\text{m}$: it is sufficient close to the slope of the handling characteristic ($0.004 \text{ rad s}^2/\text{m}$). The sideslip angle decreases with lateral acceleration until it changes its sign and tends to an asymptotic behavior; the speed value at which sideslip angle becomes equal to 0 is 51 km/h which is the same calculated by Eq. 1.25 using single-track parameters. It is also evident the saturation in both the subplots: when lateral acceleration increases, the driver correction increases until any driver correction is not sufficient to follow the reference path.

1.3.4 Steering Dynamics Model

Fig. 1.7 has proved that the dynamic behavior of EPAS system needs to be analyzed and integrated with the single-track model. Due to a lack of knowledge about mechanical and electrical parameters for building a mathematical model, a system identification of steering actuation is carried out since the input (desired steering command δ_{In}) and output (measured steering angular position δ_{Out}) signals are available in real-time. For a complete and detailed description of it, a sweep frequency test (SFT) is carried out in order to plot the frequency response function (FRF) of the steering actuation. The SFT consists of applying a sinusoidal steering command with a constant amplitude and variable frequency (linear time-variant):

$$\begin{cases} \delta_{In} &= \delta_0 \sin(2\pi f(t) t) \\ f(t) &= f_0 + \frac{f_T - f_0}{T} t \end{cases} \quad (1.28)$$

where f_0 is the frequency at initial time t_0 and f_T the frequency at time T . One example of sweep frequency test with constant amplitude of 90 deg is shown in Fig. 1.14. Under the assumption of uncorrelated noise on the output signal and negligible noise

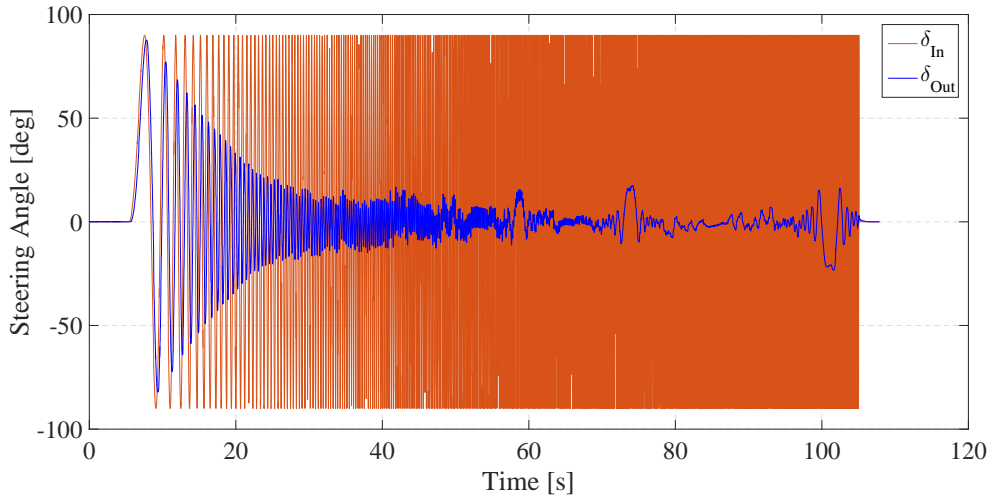


Figure 1.14 Sweep frequency test with constant amplitude of 90

contamination on the input, the so called $H_2(f)$ estimator of FRF can be used:

$$H_2(f) = \frac{P_{yy}(f)}{P_{yx}(f)} \quad (1.29)$$

where P_{yy} is the auto power spectral density of the output and P_{yx} is the cross power spectral density between output (δ_{Out}) and input (δ_{In}). To evaluate the quality of the

estimated FRF the coherence function is also computed:

$$C_{xy}(f) = \frac{|P_{yx}(f)|^2}{P_{xx}(f)P_{yy}(f)} \quad (1.30)$$

where P_{xx} is the auto power spectral density of the input and P_{xy} is the cross power spectral density between input and output. The algorithm for finding the transfer function and coherence function estimates given experimental input and output signal vectors uses the Welch's averaged periodogram method. The input parameters for the transfer function estimation algorithm are: Hamming window type; 8 second window length; 90% overlap between segment and 1000 Hz sampling frequency.

Five different configurations are selected for evaluating the FRF diagram:

- stationary vehicle and a steering amplitude of 90, 180 and 270 deg
- constant pedal gas (7%) and a steering amplitude of 90, 180 deg

For each configuration, the following parameters are selected:

$$f_0 = 0.001 \text{ Hz}$$

$$f_T = 5 \text{ Hz}$$

$$T = 100 \text{ s}$$

The estimated FRF plot are shown in Fig. 1.15 by reporting magnitude and phase delay as function of frequency. The first important observation is that the cut-off frequency of the

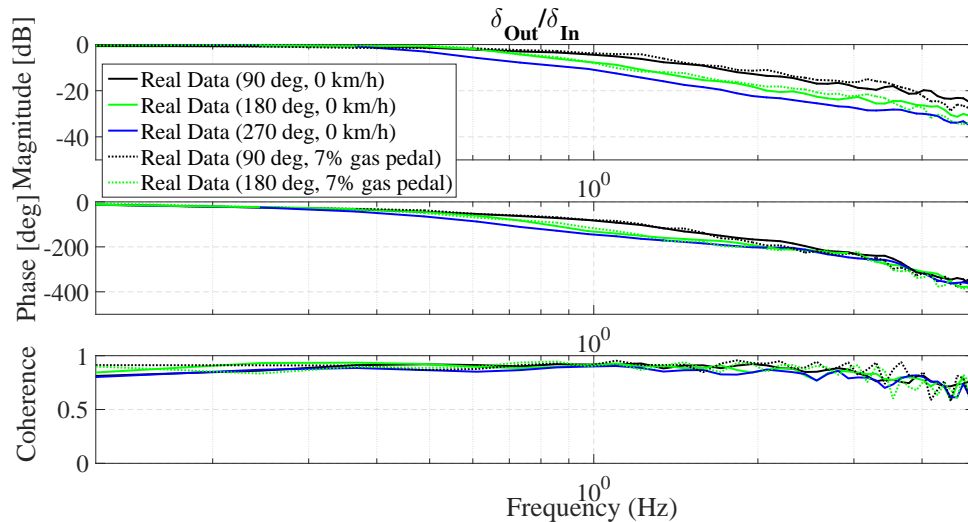


Figure 1.15 Sweep frequency tests with different steering amplitudes (90 deg, 180 deg and 270 deg) and vehicle operating conditions

system depends on the command amplitude thus implying a non-linearity that cannot be taken into account by a linear model: the higher the sweep frequency amplitude, the lower the cut-off frequency. This non-linear effect is more evident for the magnitude than for the phase delay. Furthermore, the operating condition at 7% of gas pedal doesn't modify the FRF response obtained with a stationary vehicle test: at low vehicle speed, the steering dynamic can be approximated with stationary vehicle condition (worst case scenario). By using the System Identification Toolbox of Matlab®, different transfer function structures are taken into consideration: the magnitude shape depicts the dynamics of an over-damped system meanwhile the phase delay becomes extremely greater for high frequency values thus suggesting the adoption of additional zeros. A comparison among different transfer function structures in terms of number of poles and zeros is shown in Fig. 1.16. A first order transfer function is not able to match magnitude

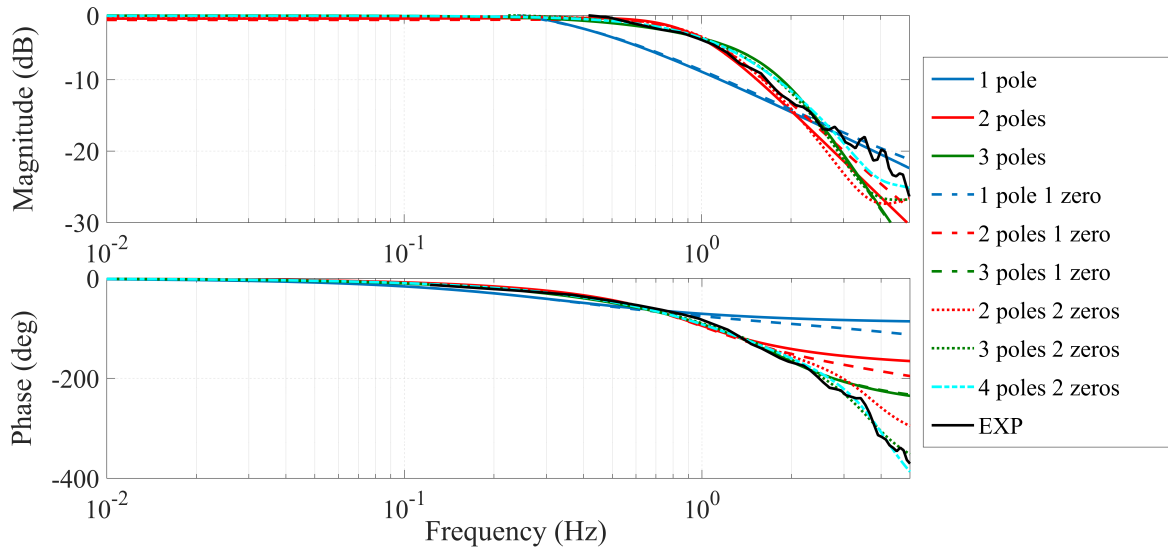


Figure 1.16 System identification: comparison with experimental FRF at 90 deg against different transfer function structures

neither phase lag of experimental FRF even with the adoption of one zero properly designed; a second order transfer function can better describe system response up to a maximum frequency of 2 Hz and the introduction of 2 zeros improves the phase delay identification but with a negative influence on the magnitude for high frequency values. A 4th order transfer function with 2 zeros (coefficient values are shown in Table 1.1) is finally selected as a good linear model for describing the real system up to a maximum operating frequency condition of 5 Hz:

$$\frac{\delta_{Out}}{\delta_{In}} = \frac{n_2 s^2 + n_1 s + n_0}{n_4 s^4 + n_3 s^3 + n_2 s^2 + n_1 s + n_0} \quad (1.31)$$

A comparison with a realistic experimental time history is used as validation test finally obtaining a verification of the linear model selected as shown in Fig. 1.17.

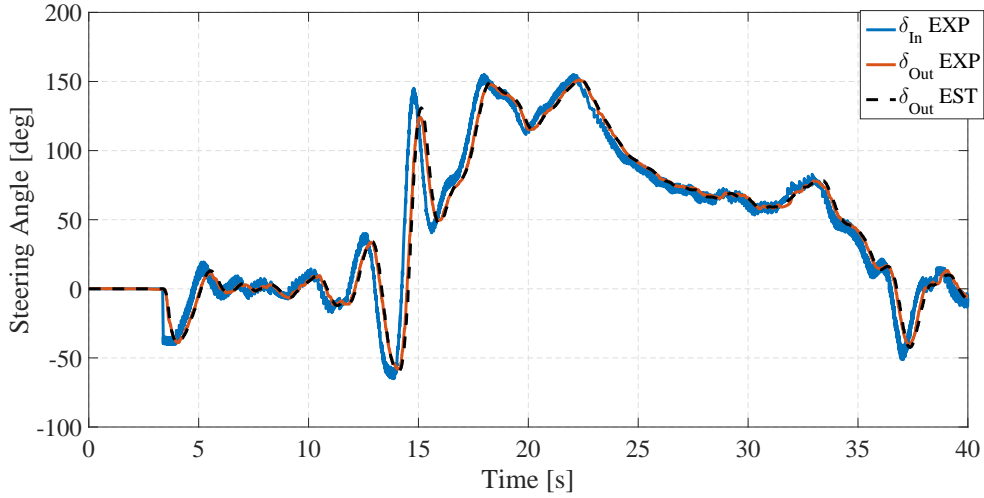


Figure 1.17 Experimental validation of system identification: EXP - experimental data, EST - estimated with a transfer function with 4 poles and 2 zeros

1.3.5 Lateral Deviation Equations

In autonomous driving applications, a key factor is the calculation of wheel steering angle to follow a desired path selected by the driver or passengers. In order to analyze this aspect, the steering model must be extended including not only velocities (β and r) but also the vehicle heading and its lateral position with respect to the reference path. Such a reference may be provided by a guiding wire in the center of the lane or by processing the images from a car-mounted video camera. In this section it is assumed that reference path is provided offline and that vehicle position is obtained from an accurate GPS sensor (1 cm accuracy and 100 Hz sampling rate). Fig. 1.18 shows an inertial coordinate frame x_0, y_0 and a vehicle body fixed coordinate frame x, y , which is rotated by the yaw angle ψ . The tangent to the path in the closest point to the vehicle, indicated by vector V_t , is rotated by an angle ψ_t with respect to x_0 . The component of the vehicle speed V perpendicular to V_t is equal to the rate change of y_{CG} . The perpendicular component is expressed by $V \sin(\beta + \Delta\psi)$, where β is the vehicle sideslip angle and $\Delta\psi = \psi - \psi_t$ is the angle between the tangent to the path and the x axis of the vehicle. With the linearization $\sin(\beta + \Delta\psi) \approx \beta + \Delta\psi$, the lateral deviation in the center of gravity y_{CG} changes according to:

$$\dot{y}_{CG} = V(\beta + \Delta\psi) \quad (1.32)$$

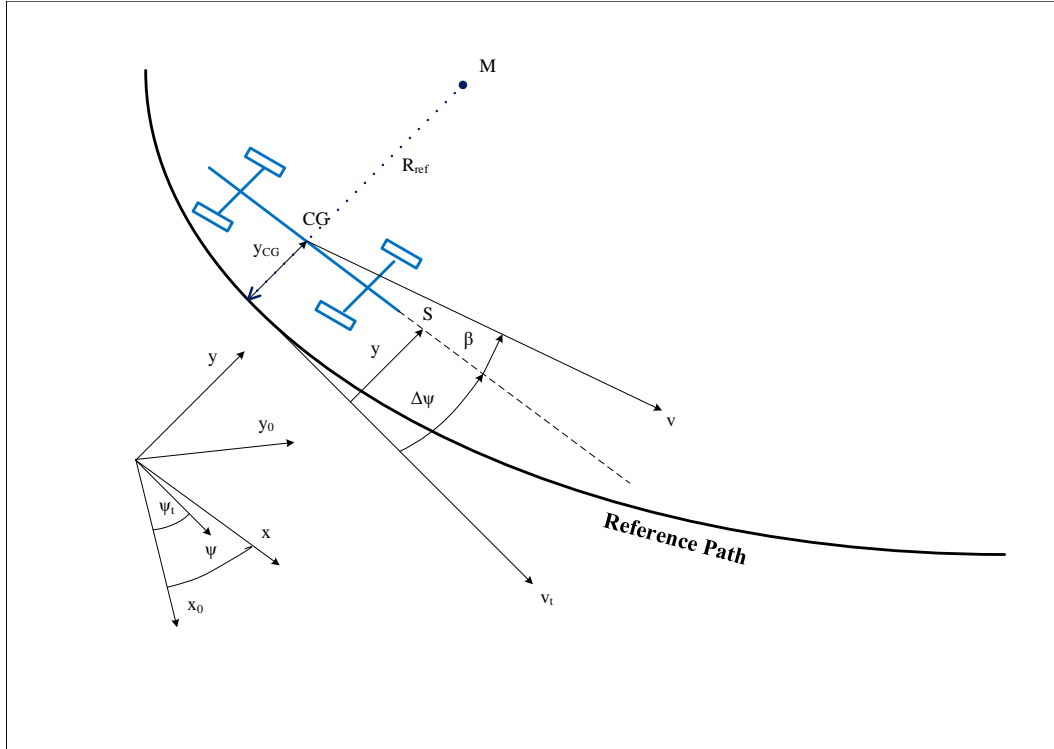


Figure 1.18 Scheme representation of vehicle lateral deviation with respect reference path

The distance y at the so called *preview distance* l_s is here considered as controller input instead of y_{CG} since it constitutes a prediction variable thus enhancing the promptness of path tracking control strategy. The preview lateral deviation can be expressed as:

$$y = y_{CG} + l_s \sin(\Delta\psi) \approx y_{CG} + l_s \Delta\psi \quad (1.33)$$

changes both with \dot{y}_{CG} and under the influence of vehicle yaw rate $r = \dot{\psi}$, and the rate change of the new displacement y is:

$$\dot{y} = V(\beta + \Delta\psi) + l_s \Delta\dot{\psi} = V(\beta + \Delta\psi) + l_s r - l_s \dot{\psi}_t \quad (1.34)$$

where $\dot{\psi}_t = V/R_{ref} = V\rho_{ref}$ is the yaw rate of the path tangent in stationary circular cornering. Finally, the extended lateral deviation model can be obtained by combining Eq. 1.34 with the single-track and steering response equations (Eqs. 1.15 and 1.31). With the introduction of Eq. 1.34, the reference curvature ρ_{ref} appears as a second input to the system in addition to the steering angle δ_{In} and from the controller point of view it can be treated as an external disturbance or as a known information. This observation will be further discussed in following section.

1.4 Path Tracking Control

In the previous section a vehicle lateral dynamics model is presented and its lateral deviation with respect a reference path is introduced. The purpose of the present section is to describe a methodology to pre-process offline the desired path, how to make it available online and how to design the steering angle δ_{In} by using the Parameter Space Approach (PSA) with a static Feedforward (FF) or with the Integral Sliding Mode (ISM) technique.

1.4.1 Reference Path Generation

In conventional navigation systems already presented in all passenger cars, the driver is requested to select the destination point and an optimized trajectory (i.e. the fastest or shorter one) is calculated on demand. In this contest, it is assumed that the reference trajectory is already available by means as a cloud of points from the initial position to the final destination. This set of data points can be obtained directly from GPS sensor by moving the autonomous car along a specific path at low speed (this is the case when the vehicle needs to repeat always the same paths) or it can be provided by an high-level control strategy that calculate the vehicle positions from a point A to a point B. Both situations usually requires a number of data which is directly connected with the length of the reference path (longer it is more data points are needed) thus eventually compromising the memory hardware available on-board. In this section a methodology to create an offline digital map from original data set is presented and it is described how to elaborate in real time the lateral deviation of the vehicle with respect of it.

The procedure of building the digital map consists of dividing the reference path into a predetermined number of segments and each of this segments is approximated by a parametric polynomial of the distance parameter γ . The aforementioned number of segments can be chosen to contain an equal number of data points or can selected with the purpose of having more segments where the curvature of reference path becomes smaller (it requires an higher accuracy with respect a straight line). The third order polynomials that can fit each segment can be evaluated as follows:

$$\begin{cases} X_i(\gamma) = a_{Xi}\gamma^3 + b_{Xi}\gamma^2 + c_{Xi}\gamma + d_{Xi} \\ Y_i(\gamma) = a_{Yi}\gamma^3 + b_{Yi}\gamma^2 + c_{Yi}\gamma + d_{Yi} \end{cases} \quad (1.35)$$

where γ is the trajectory parameter and its value changes from 0 to 1 for the I segment, from 1 to 2 for the II segment and so on until the last segment. $a_{Xi}, b_{Xi}, c_{Xi}, d_{Xi}$ and

$a_{Yi}, b_{Yi}, c_{Yi}, d_{Yi}$ are the polynomial coefficients of the X and Y components respectively of i_{th} segment. The determination of polynomial coefficients is a constrained least squares problem. Before solving this problem, the unconstrained least square problem is defined as follow:

$$\begin{cases} X_{exp} = \Gamma p_x \\ Y_{exp} = \Gamma p_y \end{cases} \quad (1.36)$$

where

$$\Gamma = \begin{bmatrix} \overline{\gamma_1^3} & \overline{\gamma_1^2} & \overline{\gamma_1} & 1 & 0 & 0 & 0 & 0 & \dots \\ 0 & 0 & 0 & 0 & \overline{\gamma_2^3} & \overline{\gamma_2^2} & \overline{\gamma_2} & 1 & \dots \\ \vdots & \vdots & \vdots & \vdots & \vdots & \vdots & \vdots & \vdots & \ddots \end{bmatrix} \quad (1.37)$$

is the *parameter matrix* where $\overline{\gamma_i}$ represents the entire array of γ_i ranging from its initial value γ'_i to the final one γ''_i corresponding to the i_{th} segment. p_x and p_y contain all the best fitted polynomial coefficients for all n segments and X_{exp} , Y_{exp} are X and Y global coordinates of initial data set points. The unconstrained least square problem solution does not guarantee a continuous and smooth solution at the segment boundaries. To improve this aspect, the boundary conditions below are added to the unconstrained least square problem solution:

$$\begin{cases} X_i(\gamma''_i) &= X_{i+1}(\gamma'_{i+1}) \\ Y_i(\gamma''_i) &= Y_{i+1}(\gamma'_{i+1}) \\ \frac{dX_i}{d\gamma}(\gamma''_i) &= \frac{dX_{i+1}}{d\gamma}(\gamma'_{i+1}) \\ \frac{dY_i}{d\gamma}(\gamma''_i) &= \frac{dY_{i+1}}{d\gamma}(\gamma'_{i+1}) \\ \frac{d^2X_i}{d\gamma^2}(\gamma''_i) &= \frac{d^2X_{i+1}}{d\gamma^2}(\gamma'_{i+1}) \\ \frac{d^2Y_i}{d\gamma^2}(\gamma''_i) &= \frac{d^2Y_{i+1}}{d\gamma^2}(\gamma'_{i+1}) \end{cases} \quad (1.38)$$

The conditions shown in Eq. 1.38 can be expressed with the following linear relations among polynomial coefficients:

$$\begin{cases} a_{Xi}(\gamma''_i)^3 + b_{Xi}(\gamma''_i)^2 + c_{Xi}(\gamma''_i) + d_{Xi} &= a_{Xi+1}(\gamma'_{i+1})^3 + b_{Xi+1}(\gamma'_{i+1})^2 + c_{Xi+1}(\gamma'_{i+1}) + d_{Xi+1} \\ a_{Yi}(\gamma''_i)^3 + b_{Yi}(\gamma''_i)^2 + c_{Yi}(\gamma''_i) + d_{Yi} &= a_{Yi+1}(\gamma'_{i+1})^3 + b_{Yi+1}(\gamma'_{i+1})^2 + c_{Yi+1}(\gamma'_{i+1}) + d_{Yi+1} \\ 3a_{Xi}(\gamma''_i)^2 + 2b_{Xi}(\gamma''_i) + c_{Xi} &= 3a_{Xi+1}(\gamma'_{i+1})^2 + 2b_{Xi+1}(\gamma'_{i+1}) + c_{Xi+1} \\ 3a_{Yi}(\gamma''_i)^2 + 2b_{Yi}(\gamma''_i) + c_{Yi} &= 3a_{Yi+1}(\gamma'_{i+1})^2 + 2b_{Yi+1}(\gamma'_{i+1}) + c_{Yi+1} \\ 6a_{Xi}(\gamma''_i) + 2b_{Xi} &= 6a_{Xi+1}(\gamma'_{i+1}) + 2b_{Xi+1} \\ 6a_{Yi}(\gamma''_i) + 2b_{Yi} &= 6a_{Yi+1}(\gamma'_{i+1}) + 2b_{Yi+1} \end{cases} \quad (1.39)$$

for $i = 2$ to $i = n - 1$, meanwhile for the first node $i = 1$ and last node $i = n$ they are given by:

$$\begin{cases} d_{X1} & = X_{exp}(1) \\ d_{Y1} & = Y_{exp}(1) \\ a_{Xn}(\gamma''_n)^3 + b_{Xn}(\gamma''_n)^2 + c_{Xn}(\gamma''_n) + d_{Xn} & = X_{exp}(n) \\ a_{Yn}(\gamma''_n)^3 + b_{Yn}(\gamma''_n)^2 + c_{Yn}(\gamma''_n) + d_{Yn} & = Y_{exp}(n) \end{cases} \quad (1.40)$$

The unconstrained problem 1.38 together with constraint equations 1.39 and 1.40 are solved by using the Matlab[®] command *lsqlin* that solves the least-squares with equality constraints problem:

$$\begin{cases} kx_{opt} & = \min(0.5(\|\Gamma p(x) - X_{exp}\|)^2) \quad \text{subject to } A_{eq}p(x) = b_{eq,x} \\ ky_{opt} & = \min(0.5(\|\Gamma p(y) - Y_{exp}\|)^2) \quad \text{subject to } A_{eq}p(y) = b_{eq,y} \end{cases} \quad (1.41)$$

where the matrices A_{eq} , $b_{eq,x}$ and $b_{eq,y}$ are defined as:

(1.42)

$$b_{eq,x} = \begin{bmatrix} \text{zeros}(n-1,1) \\ X_{exp}(n) \\ X_{exp}(1) \end{bmatrix}$$

$$b_{eq,y} = \begin{bmatrix} \text{zeros}(n-1, 1) \\ Y_{exp}(n) \\ Y_{exp}(1) \end{bmatrix}$$

In order to evaluate the accuracy of the methodology presented, Fig. 1.19 shows an example of the path segmentation and its comparison with respect the original set of data points. The digital map well describes the real data set with the advantage of using

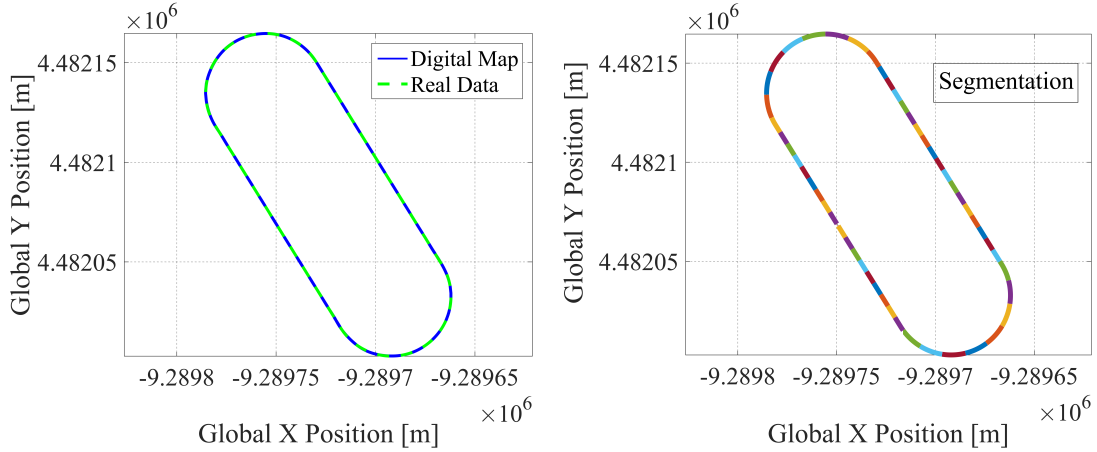


Figure 1.19 Digital map creation: segmentation of real data (right) and comparison of digital map with real data (left)

a considerably smaller amount of data whose quantity depends only on the number of segments chosen and no more linked to the number of original data points.

Lateral deviation real-time calculation

When polynomial coefficients kx_{opt} and ky_{opt} are calculated offline, they are stored to be used for the online calculation of lateral deviation y that depends on the center of gravity deviation from reference path and the heading error between the autonomous vehicle and the desired trajectory (1.33). The matlab[®] function *fminsearch* elaborates the vehicle GPS latitude and longitude to evaluate which is the closest segment i to vehicle position and to calculate the value of $\gamma_i(p)$ (i_{th} segment at point p) for identifying the point of the digital map in proximity of the car. Segment switching condition is also taken into account on the hypothesis that the vehicle is always moving forward: when $\gamma_i(p)$ reaches the γ''_i value of i_{th} segment, the strategy detects the switching condition and provides the upgraded segment number. The number of segment is required to evaluate the correspondent 8 polynomial coefficients (4 for X coordinate and 4 for Y)

stored in kx_{opt} and ky_{opt} , meanwhile the $\gamma_i(p)$ value is important for evaluating the X_p and Y_p coordinates of reference path:

$$\begin{cases} X_p(\gamma_i(p)) &= kx_{opt}(j)\gamma_i(p)^3 + kx_{opt}(j+1)\gamma_i(p)^2 + kx_{opt}(j+2)\gamma_i(p) + kx_{opt}(j+3) \\ Y_p(\gamma_i(p)) &= ky_{opt}(j)\gamma_i(p)^3 + ky_{opt}(j+1)\gamma_i(p)^2 + ky_{opt}(j+2)\gamma_i(p) + ky_{opt}(j+3) \end{cases} \quad (1.43)$$

where $j = 4(i-1) + 1$. By calculating the derivative of X_p and Y_p with respect γ_i , the value of its slope with respect X at the point p ($Tg_\Gamma(p)$) is given by:

$$\begin{cases} X'_p(\gamma_i(p)) &= 3kx_{opt}(j)\gamma_i(p)^2 + 2kx_{opt}(j+1)\gamma_i(p) + kx_{opt}(j+2) \\ Y'_p(\gamma_i(p)) &= 3ky_{opt}(j)\gamma_i(p)^2 + 2ky_{opt}(j+1)\gamma_i(p) + ky_{opt}(j+2) \\ Tg_\Gamma(p) &= \arctan\left(\frac{Y'_p(\gamma_i(p))}{X'_p(\gamma_i(p))}\right) \end{cases} \quad (1.44)$$

and the curvature in that specific point ($\rho_\Gamma(p)$):

$$\begin{cases} X''_p(\gamma_i(p)) &= 6kx_{opt}(j)\gamma_i(p) + 2kx_{opt}(j+1) \\ Y''_p(\gamma_i(p)) &= 6ky_{opt}(j)\gamma_i(p) + 2ky_{opt}(j+1) \\ \rho_\Gamma(p) &= \frac{X'_p Y''_p - Y'_p X''_p}{(X'_p X'_p + Y'_p Y'_p)^{3/2}} \end{cases} \quad (1.45)$$

All these information are needed for calculating the vehicle CoG (Center of Gravity) deviation with respect the reference path y_{CG} and its heading error $\Delta\psi$:

$$\begin{cases} y_{CG} &= \text{sign}(\vec{D}(k)) \sqrt{(X_p(\gamma_i(p)) - X_G)^2 + (Y_p(\gamma_i(p)) - Y_G)^2} \\ \Delta\psi &= \psi - Tg_\Gamma(p) \end{cases} \quad (1.46)$$

where X_G , Y_G and ψ are respectively vehicle global east coordinate, global north coordinate and yaw angle. The sign of y_{CG} is calculated based on the cross product of the vectors between the vehicle's position relative to the path and the slope of the digital map:

$$\vec{D} = ((X_p(\gamma_i(p)) - X_G), (Y_p(\gamma_i(p)) - Y_G), 0) \times (X'_p(\gamma_i(p)), Y'_p(\gamma_i(p)), 0) \quad (1.47)$$

The third dimension of this product gives the direction of the lateral deviation y_{CG} : if y_{CG} is positive the vehicle is on the inner side of a closed path and if y_{CG} is negative the vehicle is moving outside of that path. Finally, the preview lateral deviation y is calculated in real-time as follow:

$$y = y_{CG} + l_s \sin(\Delta\psi) \quad (1.48)$$

and it will be used as feedback for PSA+FF and PSA+ISM control logics as shown in Fig. 1.20.

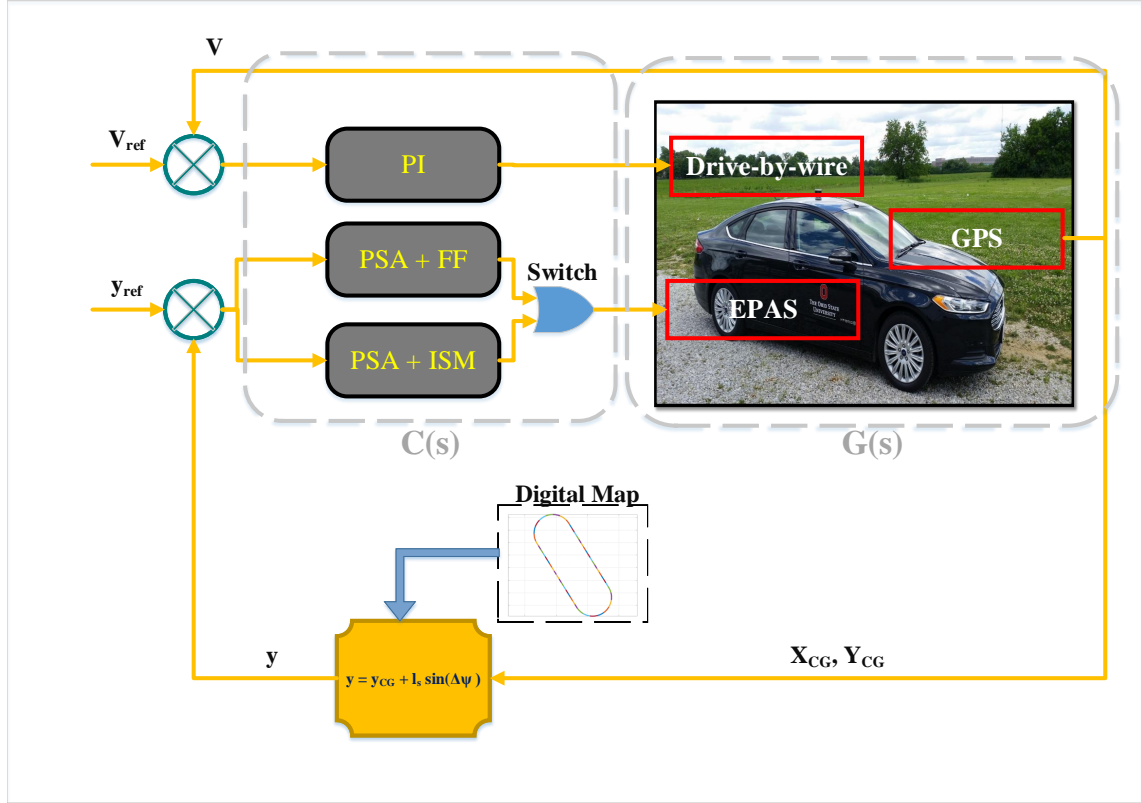


Figure 1.20 Control scheme for lateral deviation y regulation: $G(s)$ plant; $C(s)$ controller

1.4.2 Parameter Space Approach: Theory and Application

The aim of path tracking control is to keep the preview lateral deviation as small as possible even in presence of reference curvature changing ρ_{ref} or disturbance yaw moments M_{zD} and lateral forces F_{zD} . The present section intent is to describe the parameter space approach (PSA) as one possible solution to design the feedback controller for preview lateral deviation y with the purpose of satisfying specific requirements. Before that, some basic concepts related to the PSA theoretical background are presented and subsequently applied to the specific case of autonomous vehicle path tracking control.

Hurwitz-stability criteria

Hurwitz stability is connected to the close-loop transfer function; consider a generic single-input single-output (SISO) plant $G(s)$ that can be controlled by a controller $C(s)$

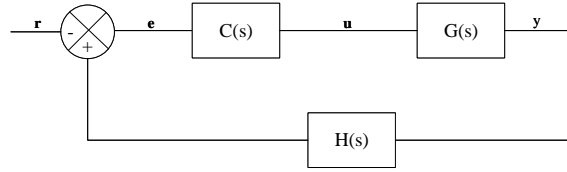


Figure 1.21 Generic single-input single-output (SISO) plant $G(s)$ controlled by a controller $C(s)$

as shown in Fig. 1.21. Let's assume without loss of generality that the denominator of close-loop transfer function can be expressed as follow:

$$p(s) = a_0 + a_1 s + a_2 s^2 + \cdots + a_n s^n, \quad a_n > 0 \quad (1.49)$$

where s is the Laplace transform. Hurwitz has linked the stability of the $n - th$ order polynomial to a set of determinants $\Delta_i = \det \mathbf{H}_i$. The determinants come from the following so called *Hurwitz matrices*:

$$\begin{aligned} \mathbf{H}_1 &= \begin{bmatrix} a_{n-1} \end{bmatrix} \\ \mathbf{H}_2 &= \begin{bmatrix} a_{n-1} & a_{n-3} \\ a_n & a_{n-2} \end{bmatrix} \\ \mathbf{H}_3 &= \begin{bmatrix} a_{n-1} & a_{n-3} & a_{n-5} \\ a_n & a_{n-2} & a_{n-4} \\ 0 & a_{n-1} & a_{n-3} \end{bmatrix} \\ &\vdots \end{aligned} \quad (1.50)$$

This pattern continues until an $n \times n$ matrix is obtained. For n even, the last matrix \mathbf{H}_n has the form:

$$\mathbf{H}_n = \begin{bmatrix} a_{n-1} & a_{n-3} & a_{n-5} & \cdots & a_1 & 0 & 0 & 0 & \cdots & 0 \\ a_n & a_{n-2} & a_{n-4} & \cdots & a_2 & a_0 & 0 & 0 & \cdots & 0 \\ 0 & a_{n-1} & a_{n-3} & \cdots & a_3 & a_1 & 0 & 0 & \cdots & 0 \\ 0 & a_n & a_{n-2} & \cdots & a_4 & a_2 & a_0 & 0 & \cdots & 0 \\ \vdots & \vdots & \vdots & \vdots & \vdots & \vdots & \vdots & \vdots & \vdots & \vdots \\ 0 & \cdots & 0 & a_{n-1} & a_{n-3} & a_{n-5} & \cdots & a_3 & a_1 & 0 \\ 0 & \cdots & 0 & a_n & a_{n-2} & a_{n-4} & \cdots & a_4 & a_2 & a_0 \end{bmatrix} \quad (1.51)$$

while for n odd, it has the form:

$$\mathbf{H}_n = \begin{bmatrix} a_{n-1} & a_{n-3} & a_{n-5} & \cdots & a_0 & 0 & 0 & \cdots & 0 \\ a_n & a_{n-2} & a_{n-4} & \cdots & a_1 & 0 & 0 & \cdots & 0 \\ 0 & a_{n-1} & a_{n-3} & \cdots & a_2 & a_0 & 0 & \cdots & 0 \\ 0 & a_n & a_{n-2} & \cdots & a_3 & a_1 & 0 & \cdots & 0 \\ \vdots & \vdots & a_n & a_{n-2} & \vdots & \vdots & \vdots & a_1 & 0 \\ 0 & \cdots & 0 & a_{n-1} & a_{n-3} & a_{n-5} & \cdots & a_2 & a_0 \end{bmatrix} \quad (1.52)$$

The relation of these matrices to stability is given in the following theorem.

Theorem 1.1 (Hurwitz). *An n – th order polynomial 1.49 is stable if and only if*

$$\det \mathbf{H}_i > 0 \quad \text{for all } i = 1, 2, \dots, n \quad (1.53)$$

It is also important to notice that for both n even and n odd, it follows from expanding $\det \mathbf{H}_n$ by its last column that

$$\det \mathbf{H}_n = a_0 \det \mathbf{H}_{n-1} \quad (1.54)$$

Thus, the stability condition 1.53 is equivalent to $\det \mathbf{H}_i > 0$ for $i = 1, 2, \dots, n-1$ and $a_0 > 0$. If the polynomial coefficients $a_0, a_1 \dots$ are known, the Hurwitz stability represents an easy stability criteria to be verified. If the coefficients are not constant but they contain some uncertainties or are dependent on controller gains, Hurwitz stability becomes a strong tool for robustness properties evaluation (uncertainties) or for control design purposes (gains selection). A further necessary condition is the positivity of all coefficients a_i .

Theorem 1.2 (Hurwitz-positive coefficients criteria). *A stable polynomial 1.49 of degree n satisfies*

$$a_i > 0 \quad \text{for all } i = 1, 2, \dots, n \quad (1.55)$$

The positive coefficient criteria is usually used for reducing the number of determinant criteria in Theorem 1.53. This simplification is due to Liénard and Chipart [68]:

Theorem 1.3 (Hurwitz-Liénard and Chipart). *Necessary and sufficient conditions for a polynomial*

$$p(s) = a_0 + a_1 s + a_2 s^2 + \cdots + a_n s^n, \quad a_n > 0$$

to be stable can be given in one of the four following forms:

$$\begin{aligned}
 LC1 \quad & a_0 > 0, a_2 > 0, \dots; \Delta_1 > 0, \Delta_3 > 0, \dots, \\
 LC2 \quad & a_0 > 0, a_2 > 0, \dots; \Delta_2 > 0, \Delta_4 > 0, \dots, \\
 LC3 \quad & a_0 > 0, a_1 > 0, a_3 > 0, \dots; \Delta_1 > 0, \Delta_3 > 0, \dots, \\
 LC4 \quad & a_0 > 0, a_1 > 0, a_3 > 0, \dots; \Delta_2 > 0, \Delta_4 > 0, \dots,
 \end{aligned} \tag{1.56}$$

where $\Delta_i = \det \mathbf{H}_i$.

Critical Stability Conditions

In the previous paragraph it is mentioned that the Hurwitz criteria becomes a useful tools when the polynomial coefficients of 1.49 are function of unknown parameters z related to model uncertainties or controller gains:

$$p(s, Z) = a_0(z) + a_1(z)s + a_2(z)s^2 + \dots + a_n(z)s^n, \quad a_n(z) > 0 \tag{1.57}$$

The *Critical Stability Conditions* assumes that if real coefficients of $p(s, Z)$ are continuous function of z also the roots of $p(s, Z)$ are continuous with respect the parameter z , since they cannot jump from the left half plane of Nyquist diagram to the right one without crossing the imaginary axis. If $p(s = z_0)$ represents a stable characteristic polynomial, the stable neighborhood of z_0 is bounded by the values of z where one or more eigenvalues cross the imaginary axes under a continuous variation of z . Three different conditions can cause the eigenvalues cross of imaginary axis: at $s = 0$ *real root boundary* (RRB), at $s = \infty$ *infinite root boundary* (IRB) and at $s = \pm j\omega$ *imaginary root boundary* (CRB). The IRB is characterized by the condition $a_n(z) = 0$, mean while the RRB and CRB conditions can be detected by Frazer and Duncan [69]:

Theorem 1.4 (Frazer-Duncan). *The family of polynomials*

$$P(s, Z) = a_0(z) + a_1(z)s + \dots + a_n(z)s^n | z \in Z \tag{1.58}$$

with continuous real coefficient functions $a_i(z)$ is robustly Hurwitz-stable, is and only if:

- *There exists a stable polynomial $p(s, z) \in P(s, Z)$*
- *$a_n(z) \neq 0$ for all $z \in Z$*
- *$\det \mathbf{H}_n(z) \neq 0$ for all $z \in Z$*

Note that $\det \mathbf{H}_n = a_0 \det \mathbf{H}_{n-1}$ the three conditions of previous theorem may be replaced by the following ones:

1. There exists a stable polynomial $p(s, z) \in P(s, Z)$
2. $a_n(z) \neq 0$ for all $z \in Z$
3. $a_0(z) \neq 0$ for all $z \in Z$
4. $\det \mathbf{H}_{n-1}(z) \neq 0$ for all $z \in Z$

Fictitious and Non-active Boundaries An $n - th$ order polynomial can be factorized as:

$$p(s) = a_n \prod_{i=1}^n (s - s_i), \quad s_i = \sigma_i + j\omega_i \quad (1.59)$$

Orlando's formula represents a straightforward relationship between $\det \mathbf{H}_{n-1}$ and the root of $p(s)$:

$$\det \mathbf{H}_{n-1} = (-1)^{n(n+1)/2} a_n^{n-1} \prod_{i,k=1}^n (s_i + s_k) \quad (1.60)$$

If the polynomial has a pair of roots on the imaginary axis at $\sigma_1 = \sigma_2 = 0, \omega_1 = -\omega_2$, then the product term $s_2 + s_1$ is zero and hence $\det \mathbf{H}_{n-1}$ also equals zero. The condition $\det \mathbf{H}_{n-1} = 0$ is also verified for a real symmetric pair $\sigma_1 = -\sigma_2, \omega_1 = \omega_2 = 0$ or for two complex symmetric pairs $s_{1/2} = \sigma_1 \pm j\omega, s_{3/4} = -\sigma_1 \pm j\omega$. Thus, the condition $\det \mathbf{H}_{n-1}(z) = 0$ not only generates the boundary where a root on the imaginary axis occurs but also so called *fictitious boundaries* at complex frequencies. They cannot, however, intersect the stable neighborhood around z_0 because one or more eigenvalues have to cross the imaginary axis first before reaching a symmetric pattern with respect the imaginary axis with unstable eigenvalues. The condition $\det \mathbf{H}_n(z) = 0$ is also verified for a polynomial with unstable roots plus a pair of roots on the imaginary axis thus bringing to a *non-active boundary*.

The Parameter Space Approach

Critical stability conditions represents a good approach to be used for simple systems with a low number of states because the condition $\Delta_{n-1}(z) = \det \mathbf{H}_{n-1}(z) = 0$ leads to complicated symbolic expressions for large values of n . Furthermore, the above condition generates fictitious boundaries since complex values of ω are also included in the boundary $\det \mathbf{H}_n(z) = 0$. The *parameter space approach* has been introduced to restrict ω to real non-negative values and stability boundaries in a two-dimensional

z -space are evaluated by a sweep over ω . The polynomial of 1.58 with real coefficients may be rewritten as:

$$p(s, z) = p_e(s^2, z) + sp_o(s^2, z) \quad (1.61)$$

where

$$\begin{cases} p_e(s^2, z) &= a_0(z) + a_2(z)s^2 + a_4(z)s^4 + \dots \\ p_o(s^2, z) &= a_1(z) + a_3(z)s^2 + a_5(z)s^4 + \dots \end{cases} \quad (1.62)$$

The polynomial $p(s, z)$ has a root at $s = \pm j\omega$ if and only if both the real and the imaginary part of

$$p(\pm j\omega, z) = p_e(-\omega^2, z) \pm j\omega p_o(-\omega^2, z) \quad (1.63)$$

vanish:

$$\begin{cases} \Re[p(j\omega, z)] &= a_0(z) - a_2(z)\omega^2 + a_4(z)\omega^4 - \dots = 0 \\ \Im[p(j\omega, z)] &= \omega[a_1(z) - a_3(z)\omega^2 + a_5(z)\omega^4 - \dots] = 0 \end{cases} \quad (1.64)$$

The boundary crossing concept may now be formulated as:

Theorem 1.5 (boundary crossing). *The family of polynomials $P(s, Z)$ is robustly stable, if and only if:*

- *There exists a stable polynomial $p(s, z) \in P(s, Z)$*
- *$j\omega \notin \text{Roots}[P(s, Z)]$ for all $\omega \geq 0$*

where $\text{Roots}[P(s, Z)]$ represents the set of all roots of $p(s, z)$ for all $z \in Z$. The PSA is usually adopted for a pragmatic controller design of a system with model uncertainties z :

1. identify an operating domain with specific boundaries in Z space where the parameters z are supposed to changed
2. by fixing the z at the vertices of the operating domain in Z , use the robust state approach to find controller gains that simultaneously satisfies eigenvalue specifications for all the vertices (design step)
3. by fixing the control gains, use the robust state approach to map the eigenvalues boundaries in the Z space to check if the entire continuum of operating domain meet the eigenvalue specifications (robust analysis step)

Example Let's consider a polynomial of a closed loop transfer function with the following coefficients as function of controller gains (k_1, k_2):

$$\begin{aligned}
a_0 &= 10k_1 \\
a_1 &= 10k_2 \\
a_2 &= 90 + 2k_1 \\
a_3 &= 2k_2 - 1 \\
a_4 &= 10
\end{aligned} \tag{1.65}$$

The RRB condition is straightforward obtained for $s = 0$ thus leading to the first boundary $k_1 = 0$ in the $k_2 - k_1$ plane. The CRB is described by considering the real and imaginary part of the polynomial for $s = j\omega$:

$$\begin{cases} \Re[p(j\omega, k_1, k_2)] &= 10k_1 - (90 + 2k_1)\omega^2 + 10\omega^4 = 0 \\ \Im[p(j\omega, k_1, k_2)] &= \omega[10k_2 - (2k_2 - 1)\omega^2] = 0 \end{cases} \tag{1.66}$$

thus leading to the CRB boundary:

$$\begin{cases} k_1(\omega^2) &= \frac{5\omega^2(\omega^2-9)}{\omega^2-5} \\ k_2(\omega^2) &= \frac{\omega^2}{2(\omega^2-5)} \end{cases} \tag{1.67}$$

Fig. 1.22 shows the parametric boundary in the $k_1 - k_2$ plane. In $\omega = 0$ the CRB branches

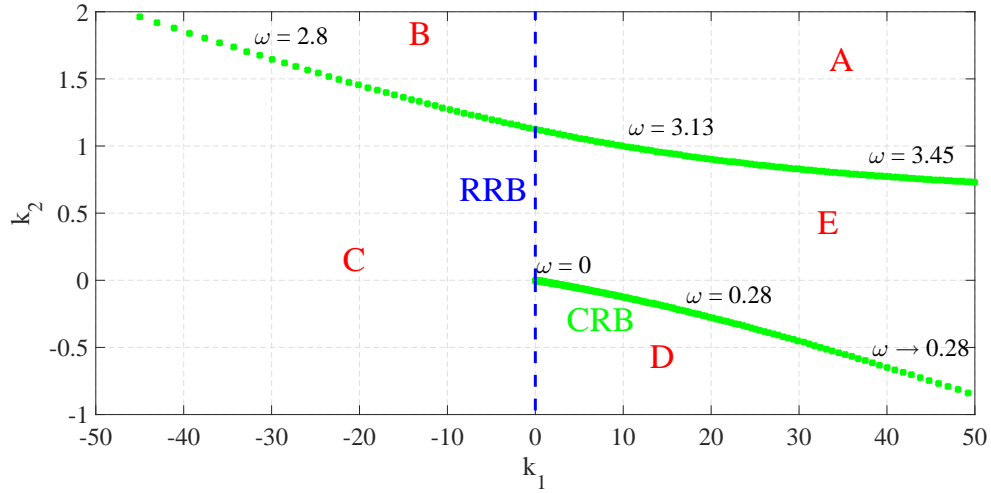


Figure 1.22 RRB nad CRB stability boundary for the characteristic polynomial of 1.65

off from the RRB and then it passes through infinity at $\omega = \sqrt{5}$ and intersects the RRB a second time for $\omega = 3$ at $k_1 = 0$ and $k_2 = 1.125$. The boundaries splits the $k_1 - k_2$ plane into five regions from A to E: A is the only stable region, B has an unstable real root, C has three roots in the right half plane, D has four unstable eigenvalues, and E has two of them.

Singular Frequencies

In the previous example, the CRB boundary is generated by a frequency sweep but there are some special cases where singular frequencies can create an entire branch of the stability boundary. In order to show this phenomena, a simple case is here considered where the characteristic polynomial depends on two parameters z_1 and z_2 (that may be plant or controller parameters):

$$p(s, z_1, z_2) = p_0(s) + z_1 p_1(s) + z_2 p_2(s) \quad (1.68)$$

where $p_0(s)$, $p_1(s)$, $p_2(s)$ are known polynomials. For $s = j\omega$, they can be formulated as:

$$\begin{aligned} p_0(j\omega) &= R_0(\omega) + jI_0(\omega) \\ p_1(j\omega) &= R_1(\omega) + jI_1(\omega) \\ p_2(j\omega) &= R_2(\omega) + jI_2(\omega) \end{aligned} \quad (1.69)$$

meanwhile the real and imaginary part of:

$$p(j\omega, z_1, z_2) = R_p(\omega, z_1, z_2) + jI_p(\omega, z_1, z_2) \quad (1.70)$$

vanishes for

$$\begin{aligned} R_p(\omega, z_1, z_2) &= R_0(\omega) + z_1 R_1(\omega) + z_2 R_2(\omega) = 0 \\ I_p(\omega, z_1, z_2) &= I_0(\omega) + z_1 I_1(\omega) + z_2 I_2(\omega) = 0 \end{aligned} \quad (1.71)$$

In matrix notation:

$$\begin{bmatrix} R_1(\omega) & R_2(\omega) \\ I_1(\omega) & I_2(\omega) \end{bmatrix} \begin{bmatrix} z_1 \\ z_2 \end{bmatrix} + \begin{bmatrix} R_0(\omega) \\ I_0(\omega) \end{bmatrix} = \begin{bmatrix} 0 \\ 0 \end{bmatrix} \quad (1.72)$$

A singularity is present at a frequency ω for which the determinant of the first matrix vanishes:

$$R_1(\omega)I_2(\omega) - R_2(\omega)I_1(\omega) = 0 \quad (1.73)$$

If this condition is verified, the two lines represented by Eq. 1.72 are parallel in the $z_1 - z_2$ plane and the only possible solution is that they become identical:

$$R_1(\omega)I_0(\omega) - R_0(\omega)I_1(\omega) = 0 \quad (1.74)$$

The real frequency that both Eq. 1.73 and 1.74 are called *singular frequencies* where the solution in the $z_1 - z_2$ plane is not just an intersection point (like for non-singular frequencies) but an entire straight line. Since the real parts R_0 , R_1 , R_2 are polynomials in ω^2 ($R(\omega) = \bar{R}(\omega^2)$) meanwhile the imaginary parts I_0 , I_1 , I_2 can be expressed as $I(\omega) = \omega \bar{I}(\omega^2)$. The RRB condition is obtained with $\omega = 0$. For the CRB ($\omega \neq 0$), Eq. 1.73 and 1.74

needs to be divided by ω thus obtaining:

$$\begin{cases} d(\omega^2) = \bar{R}_1(\omega^2)\bar{I}_2(\omega^2) - \bar{R}_2(\omega^2)\bar{I}_1(\omega^2) = 0 \\ d_1(\omega^2) = \bar{R}_1(\omega^2)\bar{I}_0(\omega^2) - \bar{R}_0(\omega^2)\bar{I}_1(\omega^2) = 0 \end{cases} \quad (1.75)$$

A real positive solution ω_k^2 of $d(\omega^2) = 0$ can represent good candidates for singular frequencies. By substituting ω_k in $d_1(\omega^2) = 0$:

$$d_1(\omega_k^2) = \bar{R}_1(\omega_k^2)\bar{I}_0(\omega_k^2) - \bar{R}_0(\omega_k^2)\bar{I}_1(\omega_k^2) = 0 \quad (1.76)$$

If this condition is verified, then ω_k is a singular frequency.

Hurwitz stability for PID design

The problem presented in this section is related to the design of a conventional PID controller by adopting Hurwitz stability approach. A conventional PID controller, designed for a specific plant $G(s)$ (refer to Fig. 1.21 with $H = 1$), can be defined by the following transfer function:

$$C(s) = \frac{K_I + K_P s + K_D s^2}{s(1 + T_R s)} \quad (1.77)$$

where K_P , K_I and K_D are proportional, integral and derivative gains meanwhile T_R is used for the realizability of the final controller. It is of interest to evaluate the set of all stabilizing PID-controllers by representing the stable region in a $K_P - K_D$ plane for a grid of K_I values; in each plane, the intersection of stable regions for N operating conditions is calculated to find the set of simultaneous stabilizers. The parameter space approach is applied to the problem and it will be first developed for one operating condition

$$\begin{aligned} A(s) &= numG(s) = a_0 + a_1 s + \dots + a_k s^k, \quad a_k \neq 0 \\ B(s) &= s(1 + T_R s)denG(s) = b_0 + b_1 s + \dots + b_m s^m, \quad b_m \neq 0 \end{aligned} \quad (1.78)$$

The characteristics polynomial of the close-loop system is given as:

$$P(s, K_I, K_P, K_D) = A(s)(K_I + K_P s + K_D s^2) + B(s) \quad (1.79)$$

and it has a root at $s = j\omega$ if and only if:

$$\begin{aligned} R_P &= \Re[P(j\omega, K_I, K_P, K_D)] = 0 \\ I_P &= \Im[P(j\omega, K_I, K_P, K_D)] = 0 \end{aligned} \quad (1.80)$$

By separating the real part from the imaginary one:

$$\begin{aligned} A(s) &= R_A + jI_A \\ B(s) &= R_B + jI_B \end{aligned} \quad (1.81)$$

and considering K_P as fixed parameter:

$$\begin{bmatrix} R_P \\ I_P \end{bmatrix} \begin{bmatrix} R_A & -R_A\omega^2 \\ I_A & -I_A\omega^2 \end{bmatrix} \begin{bmatrix} K_I \\ K_D \end{bmatrix} + \begin{bmatrix} -K_P I_A \omega + R_B \\ K_P R_A \omega + I_B \end{bmatrix} = \begin{bmatrix} 0 \\ 0 \end{bmatrix} \quad (1.82)$$

Since the matrix multiplying $[K_I K_D]^T$ is always singular, the Eq. 1.82 represent two parallel lines. A solution exists, if and only if the two parallel lines are identical:

$$\begin{aligned} g(\omega) &= \det \begin{bmatrix} R_A & -K_P I_A \omega + R_B \\ I_A & K_P R_A \omega + I_B \end{bmatrix} \\ &= \omega K_P (R_A^2 + I_A^2) + R_A I_B - I_A R_B = 0 \end{aligned} \quad (1.83)$$

Only a positive real solution ω_k^2 lead to real frequencies ω_k ($k = 0, 1, 2 \dots K$) that represent *singular frequencies*. The meaning of the condition 1.83 is that the root of $P(s, K_I, K_D)$ can cross the imaginary axis only at the singular frequencies ω_k . Three different possibilities are here identified on how a root of Eq. 1.79 can cross the imaginary axis by a variation of K_D and K_I :

1. The RRB can be identified by the condition $s = 0$:

$$\begin{cases} I_P(\omega) &= 0 \\ R_P(\omega) &= a_0 K_I + b_0 \end{cases} \quad (1.84)$$

thus finally leading to:

$$K_I = -b_0/a_0 \quad (1.85)$$

2. The IRB can be identified by the condition $s = \infty$ which is obtained by $p_n = 0$ if the polynomial in Eq. 1.79 is written as $P(s) = p_0 + p_1 s + \dots + p_n s^n$:

$$p_n = \begin{cases} a_k K_D & \text{for } m < k+2 \\ a_k K_D + b_m & \text{for } m = k+2 \\ b_m & \text{for } m > k+2 \end{cases} \quad (1.86)$$

thus finally leading to:

$$K_D = \begin{cases} 0 & \text{for } m < k+2 \\ -b_m/a_k & \text{for } m = k+2 \\ \text{none} & \text{for } m > k+2 \end{cases} \quad (1.87)$$

3. The CRB boundary is obtained by substituting ω_k calculated from Eq. 1.82 into one of the equations expressed by Eq. 1.83:

$$\begin{aligned} K_I - K_D \omega_k^2 &= -[R_B(\omega_k) - I_A(\omega_k) \omega_k K_P] / R_A(\omega_k) \quad \text{if } R_A \neq 0 \\ \text{or} \\ K_I - K_D \omega_k^2 &= -[I_B(\omega_k) - R_A(\omega_k) \omega_k K_P] / I_A(\omega_k) \quad \text{if } I_A \neq 0 \end{aligned} \quad (1.88)$$

Equations 1.88 represent straight lines for each ω_k with positive slope ω_k^2 in the $K_D - K_I$ plane.

All these boundaries generates some regions in the $K_D - K_I$ plane (with also some vertex placed at infinity) thus separating the unstable set of gains from the stable one. The final straightforward part of design procedure consists of identifying which region represents the stable one just simply checking one point in each area.

Gamma Stability

In previous sections, the PSA method is introduced and used for designing a controller that stabilizes a generic plant system and it constitutes a useful tool for all system with model uncertainties. In this section, the performance of close loop system dynamics is taken into account and the PSA method is extended to the so called *Gamma Stability* concept: the half-left plane adopted by Hurwitz stability is replaced by the Γ region that guarantee both stability and controller performances (damping effect, settling time, rising time, etc...). Controller performances can be evaluated by considering the poles and the zeros of the close-loop system transfer function that can be placed by a feasible selection of control gains. Some general tips about time-domain response can be listed as follow:

- If the transient time response presents oscillations that decay slowly, a complex pair of eigenvalues with low damping needs to be modified.
- High overshoot values may be due to some poles placed further from zero with respect to zeros.

- A slow settling time with respect the stationary value is probably due to real eigenvalues too close to the origin. They requires to be moved toward the half-left plane.
- Undesired high-frequency content in the actuator signal, may be fixed by increasing the relative degree of the controller and by placing far eigenvalues closer to the origin. Another solution is the design of an anti-aliasing filter in case of sampled-data systems.
- The closer poles to the origin (dominant poles) influences steady-state system response meanwhile the furthest poles characterized the initial part of time response and they have a strong impact on initial actuator signal.
- Zeros in the left half plane provokes the same effect of a reduced damping but they can be canceled by a proper compensator; Zeros in the right half plane can be moved but not removed.

Definition 1.1 (Γ stability). *A generic polynomial $p(s)$ is called Γ stable if all its roots $s_i \in \Gamma$. The area Γ has a boundary $\delta\Gamma$ that is built based on controller design and eigenvalues specifications.*

Theorem 1.6 (boundary crossing for Γ stability). *The family of polynomials $P(s, Z)$ is robustly Γ stable, if and only if:*

- *exists a Γ stable polynomial $p(s) \in P(s, Z)$*
- $\sigma(\alpha) + j\omega(\alpha) \notin \text{Roots}[P(s, Z)] \forall \alpha \in [\alpha^-; \alpha^+]$

where α is the parameter that describes the boundary $\delta\Gamma$ around Γ region. The difference between Hurwitz stability is that $s = \sigma(\alpha) + j\omega(\alpha)$ is taken into account instead of $s = j\omega$. RRB, IRB, and CRB equations can be obtained with less or more difficulty depending on the complexity of relations $\sigma(\alpha)$ and $\omega(\alpha)$:

- RRB is verified every time the $\delta\Gamma$ intersects with real axis ($s = \sigma_0$):

$$p(\sigma_0, z) = 0 \quad (1.89)$$

- IRB is obtained by the following condition:

$$\lim_{\alpha \rightarrow \infty} p(\sigma(\alpha) + j\omega(\alpha), z) = 0 \quad (1.90)$$

- CRB can be mapped by using the following theorem

Theorem 1.7 (CRB mapping). *Consider the family of parameter z :*

$$Z_{CRB}(\alpha) := \{z | p(\sigma(\alpha) + j\omega(\alpha), z) = 0, \alpha \in [\alpha^-; \alpha^+]\} \quad (1.91)$$

if a polynomial family $p(s, z) = [1s \cdots s^n] \mathbf{a}(z)$ has a real continuous coefficient function $\mathbf{a}(z)$, $z \in Z_{CRB}(\alpha)$ if and only if

$$\begin{bmatrix} d_0(\alpha) & d_1(\alpha) & \cdots & d_n(\alpha) \\ 0 & d_0(\alpha) & \cdots & d_{n-1}(\alpha) \end{bmatrix} \mathbf{a}(z) = \begin{bmatrix} 0 \\ 0 \end{bmatrix} \quad (1.92)$$

where

$$\begin{aligned} d_0(\alpha) &= 1 \\ d_1(\alpha) &= 2\sigma(\alpha) \\ d_{i+1}(\alpha) &= 2\sigma(\alpha)d_i(\alpha) - [\sigma^2(\alpha) + \omega^2(\alpha)]d_{i-1}(\alpha), \quad i = 1, 2, \dots, n-1 \end{aligned} \quad (1.93)$$

The ω sweep on the imaginary axis shown for the Hurwitz stability is here replaced by an α sweep on $\delta\Gamma$. The *pole placement* technique ([70]) is a conventional logic design that starts from a nominal value of $z_0 \in Z$ for controller gains selection based on desired eigenvalues. This method loses accuracy when the system contains model uncertainties that could lead to a not desired close-loop performances. The PSA procedure applied to a Γ stability problem can satisfy the controller requirements in presence of model with uncertainties since the target is to place eigenvalues in a region Γ instead of a single point. In this case, this procedure is called *pole region assignment*. A good Γ region shape for controller design is the D-stable region shown in Fig. 1.23 where the bandwidth is bounded by a circular line (radius R_b) and its damping by a hyperbola according to its asymptotes (α) and its real part is bounded by the apex of hyperbola (σ_0). The value of σ_0 imposes a minimum limit on the raising time to reach the steady-state value thus influencing the speed of controller action; The α value imposes a minimum level of damping effect on system response thus reducing oscillations in reaching stationary behavior; The bandwidth limit, identified by R_b , is required in all situations where high frequency control actions may be affected by actuators dynamics.

Generalized Singular Frequencies

The concept of singular frequencies ω_k has been introduced in section 1.4.2 for the specific case of Hurwitz stability. Here the concept is extended to generalized singular frequency α_k on the Γ stability boundary $s = \sigma(\alpha) + j\omega(\alpha)$, $\alpha \in [\alpha^-; \alpha^+]$. Consider a

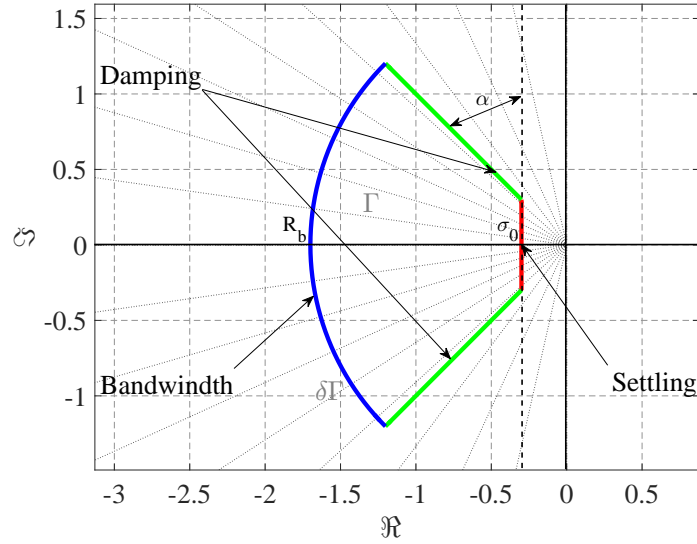


Figure 1.23 Example of D-stable Region based on eigenvalues specifications

polynomial linearly dependent to z_1 and z_2 :

$$p(s, z_1, z - 2) = p_0(s) + z_1 p_1(s) + z_2 p_2(s) \quad (1.94)$$

Let's assume $s = \sigma(\alpha) + j\omega(\alpha)$ and by substituting $\mathbf{a}(z_1, z_2) = \mathbf{a}_0 + z_1 \mathbf{a}_1 + z_2 \mathbf{a}_2$ in Eq. 1.92 two linear equations as function of z_1 and z_2 are obtained:

$$\begin{bmatrix} c_{11}(\alpha) & c_{12}(\alpha) \\ c_{21}(\alpha) & c_{22}(\alpha) \end{bmatrix} \begin{bmatrix} z_1 \\ z_2 \end{bmatrix} + \begin{bmatrix} c_{10}(\alpha) \\ c_{20}(\alpha) \end{bmatrix} = \begin{bmatrix} 0 \\ 0 \end{bmatrix} \quad (1.95)$$

and finally a generalized singular frequency α_k is guaranteed by the condition:

$$\text{rank} \begin{bmatrix} c_{11}(\alpha) & c_{12}(\alpha) & c_{10}(\alpha) \\ c_{21}(\alpha) & c_{22}(\alpha) & c_{20}(\alpha) \end{bmatrix} = 1 \quad (1.96)$$

PSA applied to Lateral Deviation Control

This section intent is to show how to exploit the PSA method with Hurwitz and Gamma stability concepts for designing a conventional PD logic for controlling the vehicle lateral

deviation. The Laplace transform of Eq. 1.34, 1.15 and 1.31 are given by:

$$\begin{aligned}
 y(s) &= \frac{V}{s}\beta(s) + \left(\frac{l_s}{s} + \frac{V}{s^2}\right)r(s) - \left(\frac{l_s V}{s} + \frac{V^2}{s^2}\right)\rho_{ref}(s) \\
 \beta(s) &= \frac{C_F J_z V s + C_F C_R b l - m V^2 C_F a}{Den(s)} \delta_{Out}(s) \\
 r(s) &= \frac{C_F a m V^2 s + C_F C_R l V}{Den(s)} \delta_{Out}(s) \\
 \delta_{Out}(s) &= \frac{n_2 s^2 + n_1 s + n_0}{d_4 s^4 + d_3 s^3 + d_2 s^2 + d_1 s + d_0} \delta_{In}(s)
 \end{aligned} \tag{1.97}$$

where

$$Den(s) = m V^2 J_z s^2 + (C_F V J_z + C_R V J_z + C_F a^2 m V + C_R b^2 m V) s + C_F C_R l^2 + m V^2 b C_R - m V^2 a C_F$$

thus obtaining the transfer function between the preview lateral deviation y and the two input: the required steering angle δ_{In} and ρ_{ref} .

$$\begin{aligned}
 \frac{y(s)}{\delta_{In}(s)} &= G(s) \\
 &= \frac{[(C_F J_z V^2 + l_s C_F a m V^2) s^2 + (C_F C_R V b l + l_s V C_F C_R l) s + V^2 C_F C_R l][n_2 s^2 + n_1 s + n_0]}{s^2 Den(s)(d_4 s^4 + d_3 s^3 + d_2 s^2 + d_1 s + d_0)} \\
 \frac{y(s)}{\rho_{ref}(s)} &= -\left(\frac{l_s V}{s} + \frac{V^2}{s^2}\right)
 \end{aligned} \tag{1.98}$$

As controller structure, a conventional proportional derivative (PD) logic is selected:

$$C(s) = K_P + K_D s \tag{1.99}$$

The polynomial of the closed loop transfer function between the reference lateral deviation y_{ref} and the actual lateral deviation y (see Fig. 1.20) can be expressed as a function of controller gains K_P and K_D , by considering the nominal parameters identified in Table 1.1 and a constant vehicle speed of 15 km/h :

$$\begin{aligned}
 p(s, K_P, K_D) &= num(1 + G(s)C(s)) = a_0 K_P + (a_{1,1} K_D + a_{1,2} K_P) s + \\
 &+ (a_{2,0} + a_{2,1} K_D + a_{2,2} K_P) s^2 + (a_{3,0} + a_{3,1} K_D + a_{3,2} K_P) s^3 + \\
 &+ (a_{4,0} + a_{4,1} K_D + a_{4,2} K_P) s^4 + (a_{5,0} + a_{5,1} K_D) s^5 + \\
 &+ a_6 s^6 + a_7 s^7 + a_8 s^8
 \end{aligned} \tag{1.100}$$

The Hurwitz stability boundaries RRB, IRB, CRB are calculated as indicated in the following list:

- RRB condition ($s = 0$) consists of $a_0 K_P = 0$ thus leading to the line $K_P = 0$ in the plane $K_D - K_P$.
- IRB condition is not present with this controller structure since $a_8 \neq 0$ for all K_P, K_D selection.
- the CRB is evaluated by substituting s with $j\omega$ and by consider its real and imaginary part:

$$\begin{cases} \Re(p(j\omega, K_P, K_D)) = 0; \\ \Im(p(j\omega, K_P, K_D)) = 0; \end{cases} \quad (1.101)$$

thus leading to a unique solution dependent on ω that can led to an acceptable solution for real positive values of ω .

A graphical solution is plot in Fig. 1.24 in the plane $K_D - K_P$ where all boundaries are shown. The RRB and CRB boundaries according to Hurwitz stability are marked with

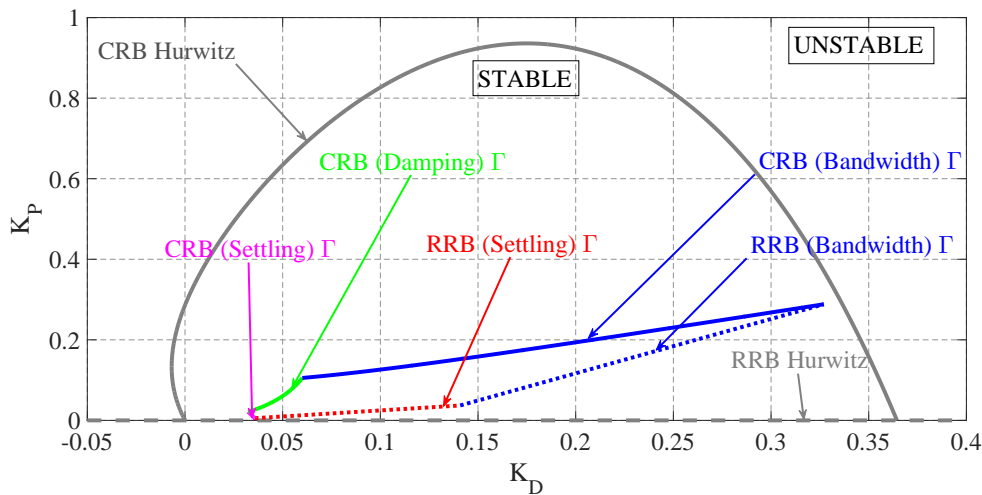


Figure 1.24 Hurwitz and Gamma stability design criteria for lateral deviation control: boundaries and stability regions

gray line thus separating the stable regions (left-half section of Argand-Gauss plane) from the unstable one: with this method a conservative selection of controller gains may be adopted if the task is only the close-loop system stability. In many controller design, the guarantee of stability is not sufficient for the specific application since more performances factor must be satisfied. In this sense, the gamma stability concept can contribute to satisfy eigenvalues specifications in terms of settling time, damping factor and bandwidth selection; the D-stable region, shown in Fig. 1.24 represents a good selection for PD gains design. The following parameters are used for the definition of the

D-stable region in the left-half section of Argand-Gauss plane:

$$\begin{aligned}\sigma_0 &= 0.3 \\ \alpha &= 30 \text{ deg} \\ R_b &= 1.3\end{aligned}\tag{1.102}$$

The most critical parameter is the bandwidth constraint since the EPAS system has a cut-frequency almost equal to 1 Hz , meanwhile the other two requirements σ_0 and α can be selected with a greater margin. The RRB and CRB boundaries (since no IRB boundaries are presents), are evaluated for each segment of D-stable region:

- CRB condition of settling time constraint is obtained with the substitution $s = -\sigma_0 + j\omega$ in Eq. 1.100, solving the following system:

$$\begin{cases} \Re(p(-\sigma_0 + j\omega, K_P, K_D)) = 0; \\ \Im(p(-\sigma_0 + j\omega, K_P, K_D)) = 0; \end{cases}\tag{1.103}$$

and expressing the control gains K_P and K_D as function of ω ($0 \leq \omega \leq \sigma_0 \tan(\pi/2 - \alpha)$).

- CRB condition of damping constraint is obtained with the substitution $s = r_b e^{j\alpha}$ in Eq. 1.100, solving the following system:

$$\begin{cases} \Re(p(r_b e^{j\alpha}, K_P, K_D)) = 0; \\ \Im(p(r_b e^{j\alpha}, K_P, K_D)) = 0; \end{cases}\tag{1.104}$$

and expressing the control gains K_P and K_D as function of r_b ($\sigma / \cos(\pi/2 - \alpha) \leq r_b \leq R_b$).

- CRB condition of bandwidth constraint is obtained with the substitution $s = R_b e^{j\vartheta}$ in Eq. 1.100, solving the following system:

$$\begin{cases} \Re(p(R_b e^{j\vartheta}, K_P, K_D)) = 0; \\ \Im(p(R_b e^{j\vartheta}, K_P, K_D)) = 0; \end{cases}\tag{1.105}$$

and expressing the control gains K_P and K_D as function of ϑ ($\pi/2 + \alpha \leq \vartheta \leq \pi$).

- RRB condition of settling time constraint is obtained with the substitution $s = -\sigma_0$ in Eq. 1.100 and expressing the control gains K_P as function of K_D .

- RRB condition of damping constraint is not present since this segment doesn't intersect the Real axis.
- RRB condition of bandwidth constraint is obtained with the substitution $s = -R_b$ in Eq. 1.100 and expressing the control gains K_P as function of K_D .

The resulting Γ region is shown in Fig. 1.24 and compared with the Hurwitz stability region: Γ region is encapsulated in Hurwitz one since gamma stability adds more constraints on desired eigenvalues placement. Each pairs of K_P and K_D values inside the Γ region satisfies the lateral deviation control requirements indicated in Eq. 1.102 if and only if the system parameters assume the nominal values reported in Table 1.1.

Gamma stability robust analysis and design A more strict gain selection in terms of gamma stability design may be extended by considering the effect of model parameters uncertainties. The values of the mass m , inertia moment J_z and COG position (a, b) are measured with a specific test bench by loading the vehicle with four passenger and full fuel; nominal values of cornering stiffness C_F and C_R are evaluated by a system identification procedure against the experimental step steer test. In particular, cornering stiffness represents a model uncertainty that changes in a wide range of values which depends mainly on friction coefficients between tires and road, load transfer among tires and their slip ratio. Four conditions are here listed for considering the cornering stiffness variation on the selection of K_P and K_D gains:

1. *nominal* condition: nominal values of C_F and C_R
2. *worst* condition: low values of C_F and C_R (i.e. 1/10 of nominal value)
3. C_F *nominal* condition: low value of C_R and nominal value of C_F
4. C_R *nominal* condition: low value of C_F and nominal value of C_R

The Γ stability procedure is repeated for each condition and the correspondent Γ regions are overlapped and shown in Fig. 1.25. The *worst* condition replicate a low-friction situation where cornering stiffness values collapse at the same time on front and rear axles, meanwhile the C_R *nominal* and C_F *nominal* conditions represent respectively an understeer and an oversteer vehicle behaviors. The final selection of gains must be restricted to the dashed region (for example the red point) thus satisfying all the four conditions. The placement of the two dominant close-loop poles (i.e. the closest to the imaginary axis) in the Argand-Gauss plane is shown in the Fig. 1.26, thus providing a proof of the requirements commitment. It is important to point out that the robust de-

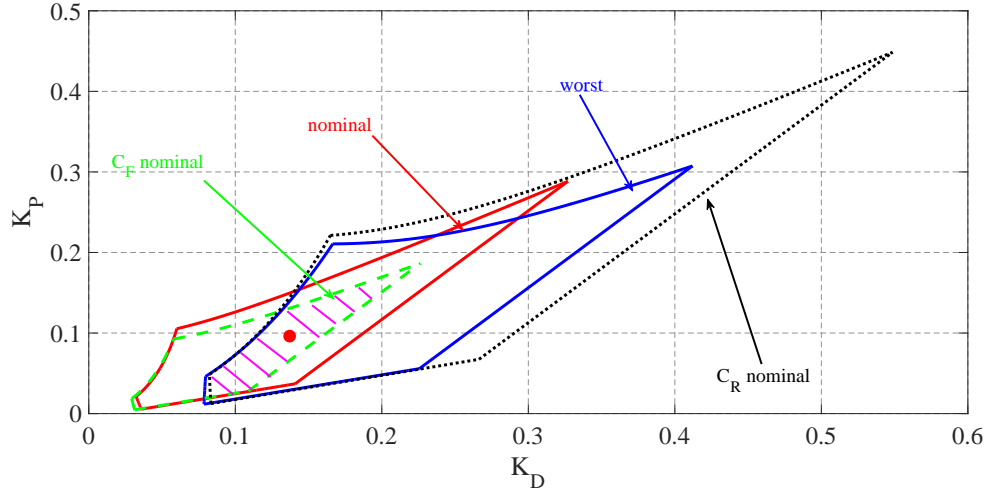


Figure 1.25 Γ region for different values of cornering stiffness

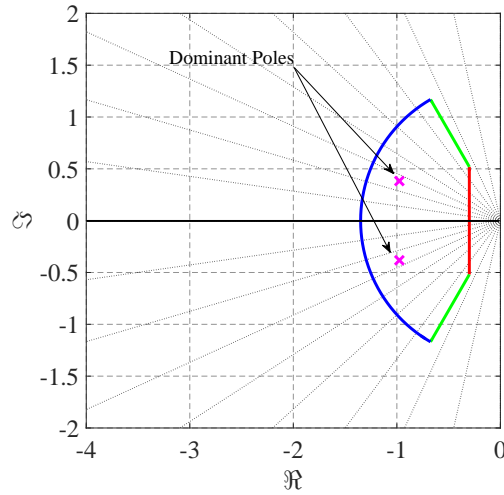


Figure 1.26 D-stable region and dominant poles placement with $K_P = 0.1$ and $K_D = 0.15$

sign procedure shown in this paragraph guarantees the desired PD control performances only for the four conditions here considered but it does not ensure the requirements satisfaction for a continuous variation of cornering stiffness among the these conditions. In order to reach this task, the polynomial in Eq. 1.100 has to be parametrized as function of model uncertainties (C_F and C_R) meanwhile the gain K_P and K_D are fixed to a specific value (i.e. the red point in Fig. 1.25); by applying the gamma stability procedure, the D-stable region is reported in the $C_F - C_R$ plane thus proving the continuum robustness of the PD logic designed for all operating condition. Unfortunately, even if this method represents a reliable and elegant design requirements, such robustness analysis is not always trivial in particular in all situations where a non-linear dependence of the poly-

nomial coefficients with physical plan parameters is present as it happens for C_F and C_R .

1.4.3 Static Linear Feedforward

The preview lateral deviation, whose dynamics is expressed by Eq. 1.98, is influenced by two input: the steering angle δ_{In} and the curvature of the reference path ρ_{ref} . The PD control logic has been designed by considering only the transfer function $G(s)$ between δ_{In} and y and it requires a further improvement to take into account the curvature ρ_{ref} . Two different methodologies are here presented based on vehicle actual configuration:

1. the value of the curvature ρ_{ref} is available in real-time: it can be used as an input for a Static Linear Feedforward (SLF) which is added to the PD output.
2. the value of the curvature ρ_{ref} is not available in real-time: an integral sliding mode (ISM) is used as disturbance observer.

In the present section the SLF method is introduced and designed meanwhile the ISM control is presented in the next section. The starting point for the SLF design is the online evaluation of ρ_{ref} which can be easily obtained by the digital map, since segments of reference path are approximated by a third order polynomial and the value of curvature is expressed by Eq. 1.45:

$$\rho_{ref}(p) = \frac{X'_p Y''_p - Y'_p X''_p}{(X'_p X'_p + Y'_p Y'_p)^{3/2}}$$

where X'_p , Y'_p are the first derivative and X''_p , Y''_p the second derivative respectively of X_p and Y_p with respect γ_i . The SLF is an open-loop control designed in order to provide a value of δ_{FF} based on the current value of $\rho_{ref}(p)$ and this can be obtaining by inverting the steady-state relation between steering angle and vehicle curvature expressed by Eq. 1.22:

$$\delta_{FF} = (L + KV^2)\rho_{ref}(p) \quad (1.106)$$

This represents a static design since it takes into account only the steady-state behavior and it is also affected by model uncertainties because the value K is influenced by cornering stiffness, loading condition and suspension kinematics. Experimental results prove that even a simple and fast feedforward design is effective if it works in collaboration with the PD control as it will shown in the experimental results section.

1.4.4 Integral Sliding Mode: Theory and Application

The Integral Sliding Mode (ISM) represents a sub-case of the sliding mode controllers since it is mainly used as a disturbance observer to be integrated with a nominal control strategy. A short introduction about sliding mode concept is here presented followed by the design procedure for ISM control according to [71, 72].

Conventional Sliding Mode

Consider a general non-linear affine system identified by the following equation:

$$\dot{\mathbf{x}} = \mathbf{f}(\mathbf{x}) + \mathbf{B}u + \mathbf{h}(\mathbf{x}) \quad (1.107)$$

where \mathbf{x} is the $n \times 1$ state vector, u the control output, \mathbf{f} , \mathbf{B} respectively the non-linear function with respect \mathbf{x} and the linear function with respect u and $\mathbf{h}(\mathbf{x})$ is an unknown term or external disturbance that is bounded. Let's assume that the desired dynamical behavior of close-loop system can be expressed by the following relation:

$$\sum_{i=1}^n c_i x_i = 0, \quad c_i > 0 \quad (1.108)$$

which implies an exponential transient behavior, dependent on c_i selection, before approaching to the stationary state. The problem statement of sliding mode control is to find the controller action u for converging the system behavior towards the desired dynamics expressed by Eq. 1.108, even in presence of external disturbances. The first step is to introduce a new variable, called sliding variable s_0 , that is a linear function of system states:

$$s_0 = \sum_{i=1}^n c_i x_i, \quad c_i > 0 \quad (1.109)$$

In order to have the desired behavior of Eq. 1.108, the control output u needs to drive the sliding variable s_0 to zero in a finite time and in presence of external disturbances. The task is achieved by satisfying the Lyapunov Theorem:

Theorem 1.8 (Lyapunov asymptotic and finite-time stability). *For the general non-linear affine system in Eq. 1.107, suppose there exists a differentiable function $V(s) : \mathbb{R}^n \rightarrow \mathbb{R}$ which is radially unbounded and positive definite such that:*

$$\dot{V}(s) < 0 \text{ for } s \neq 0$$

Then the system is asymptotically stable. If

$$\dot{V}(s) \leq -\alpha V(s)^{1/2} \text{ for } s \neq 0 \text{ and } \alpha > 0$$

Then the system is finite-time stable and by integrating the inequality over the time interval $0 \leq \tau \leq t$:

$$V^{1/2}(t) \leq -\frac{1}{2}\alpha t + V^{1/2}(t_0)$$

thus driving the variable V in a finite time t_f :

$$t_f \leq \frac{2V^{1/2}(t_0)}{\alpha}$$

the larger α , the shorter is the reaching time.

A candidate Lyapunov function can be selected as a function of sliding variable since s_0 is a linear function of system states:

$$V = \frac{1}{2}s_0^2 \quad (1.110)$$

whose derivative is given by:

$$\dot{V} = s_0 \dot{s}_0 = s_0(\mathbf{C}\mathbf{f}(\mathbf{x}) + \mathbf{C}\mathbf{B}u + \mathbf{C}\mathbf{h}(\mathbf{x})) \quad (1.111)$$

where $\mathbf{C} = [c_1, c_2, \dots, c_n]$. Assuming a control action

$$u = -(\mathbf{C}\mathbf{B})^{-1}\mathbf{C}\mathbf{f}(\mathbf{x}) - \rho \operatorname{sign}(s_0) \quad (1.112)$$

and substituting in Eq. 1.111:

$$\dot{V} = s_0(-\mathbf{C}\mathbf{B}\rho \operatorname{sign}(s_0) + \mathbf{C}\mathbf{h}(\mathbf{x})) = -s_0\mathbf{C}\mathbf{B}\rho \operatorname{sign}(s_0) + s_0\mathbf{C}\mathbf{h}(\mathbf{x}) \quad (1.113)$$

and since $\mathbf{h}(\mathbf{x})$ is bounded $|\mathbf{C}\mathbf{h}(\mathbf{x})| \leq H$:

$$\dot{V} \leq |s_0| H - |s_0| |\mathbf{C}\mathbf{B}| \rho = -|s_0| (|\mathbf{C}\mathbf{B}| \rho - H) \quad (1.114)$$

Finally by choosing $\rho > (\mathbf{C}\mathbf{B})^{-1}H$, the sliding variable s_0 is driven to zero and the desired dynamical behavior of Eq. 1.108 is achieved.

Definition 1.2 (Sliding surface). *The following equation:*

$$c_1 + c_2 + \dots + c_n = 0$$

represents a straight line in state space plane of the system in Eq. 1.107 and it is called *sliding surface*.

The condition $s_0 \dot{s}_0 \leq 0$ is often defined as *reachability condition* and its existence guarantees that the system is driven towards the sliding surface and keeps staying on it. The phase when the state trajectory is driven towards the sliding surface is called *reaching phase* meanwhile the *sliding phase* is when states are moving on the sliding surface. The control logic in Eq. 1.112 that drives the system states \mathbf{x} to the sliding surface and forces them to lay on it even in presence of disturbances \mathbf{h} is called as *sliding mode controller*. When the states are laying on the sliding surface, they exhibit an high frequency behavior with small amplitudes called *chattering* and it is caused by the switching function introduced by the controller in Eq. 1.112; in ideal sliding mode the frequency is supposed to approach infinity and the amplitude to zero. Different solutions to solve the chattering problem are discussed in [71].

Equivalent Control & Sliding Mode Equations

Assume that the sliding surface is reached and the system states are forced by the sliding mode controller u to stay on it. This means that $s_0 = \dot{s}_0 = 0$ and the condition $\dot{s}_0 = 0$ gives:

$$\dot{s}_0 = \frac{\partial s_0}{\partial \mathbf{x}} \frac{\partial \mathbf{x}}{\partial t} = \mathbf{C}(\mathbf{f}(\mathbf{x}) + \mathbf{B}u + \mathbf{h}(\mathbf{x})) = 0 \quad (1.115)$$

A direct analytical controller solution of Eq. 1.115 can be expressed by:

$$u_{eq} = -(\mathbf{CB})^{-1}[\mathbf{Cf}(\mathbf{x}) - \mathbf{Ch}(\mathbf{x})] \quad (1.116)$$

Definition 1.3 (Equivalent Control). *The controller equation calculated by Eq. 1.116 to ensure that the system trajectory lays on the sliding surface is called equivalent control*

The equivalent control is not the sliding mode control expressed by Eq. 1.112 and it cannot be implemented since it is dependent on the disturbance term $\mathbf{h}(\mathbf{x})$ which is not commonly available in real-time. The equivalent control represents the "average" value of the high-frequency switching controller 1.112 whose filtered value \hat{u}_{eq} can be an estimation of u_{eq} :

$$\begin{aligned} \hat{u}_{eq} &= -(\mathbf{CB})^{-1} \mathbf{Cf}(\mathbf{x}) - \rho s_f \\ \tau \dot{s}_f &= -s_f + \text{sign}(s_0) \end{aligned} \quad (1.117)$$

where τ is the time constant of the filter applied to the signal $\text{sign}(s_0)$. The equivalent control can be also used to estimate the disturbance or unknown term $\mathbf{h}(\mathbf{x})$ since the

comparison between equations [Eq. 1.117](#) and [1.116](#) leads to:

$$(\mathbf{CB})^{-1} \mathbf{Ch}(\mathbf{x}) = \rho s_f \quad (1.118)$$

The close-loop response is given by substituting [Eq. 1.116](#) in [Eq. 1.107](#):

$$\dot{\mathbf{x}} = (\mathbf{I} - \mathbf{B}(\mathbf{CB})^{-1} \mathbf{C}) \mathbf{f}(\mathbf{x}) + (\mathbf{I} - \mathbf{B}(\mathbf{CB})^{-1} \mathbf{C}) \mathbf{h}(\mathbf{x}) \quad (1.119)$$

An important property of sliding mode control is its robustness or invariance to specific class of uncertainty. Suppose that the unknown term $\mathbf{h}(\mathbf{x})$ has the following structure:

$$\mathbf{h} = \mathbf{B}\xi \quad (1.120)$$

where ξ is an unknown signal, thus obtaining:

$$\begin{aligned} (\mathbf{I} - \mathbf{B}(\mathbf{CB})^{-1} \mathbf{C}) \mathbf{h} &= (\mathbf{I} - \mathbf{B}(\mathbf{CB})^{-1} \mathbf{C}) \mathbf{B}\xi = \\ &= \mathbf{B}\xi - \mathbf{B}\xi = \\ &= 0 \end{aligned}$$

finally reducing [Eq. 1.119](#) into:

$$\dot{\mathbf{x}} = (\mathbf{I} - \mathbf{B}(\mathbf{CB})^{-1} \mathbf{C}) \mathbf{f}(\mathbf{x}) \quad (1.121)$$

The close-loop is completely independent on the disturbance ξ , which is called *matched disturbance* since it represents uncertainties which act on the channel of the controller input.

when the system reaches the sliding surface, the system dynamics is described by [Eq. 1.108](#) thus leading to the following conclusions:

- The order of the system dynamics is reduced since the sliding mode control drives the system from a first order dynamics ([Eq. 1.107](#)) to a states linear relation ([Eq. 1.108](#))
- When the system is moving on sliding surface, its dynamics is not influenced by the matched disturbances $\mathbf{h}(\mathbf{x})$ ([Eq. 1.121](#))
- The equivalent sliding mode control u_{eq} , is not the real control action u applied to the system and it can be seen as an abstract concept used to evaluate the reduced-order system expressed by [Eq. 1.119](#)

- The choice of sliding surface affects the dynamics of the reduced order motion, so that it constitutes a key point for control system design. (in [71] some design examples are shown in order to reduce the effects of unmatched disturbances)

Example Consider the Multi-Input Multi-Output (MIMO) system:

$$\dot{x}_1 = x_1 + x_2 + x_3 + u_2 + h_2$$

$$\dot{x}_2 = x_2 + 3x_3 + u_1 - u_2 + h_1 - h_2$$

$$\dot{x}_3 = x_1 + x_3 - u_1 - h_1$$

thus obtaining that:

$$\mathbf{B} = \begin{bmatrix} 0 & 1 \\ 1 & -1 \\ -1 & 0 \end{bmatrix}$$

and the following sliding surfaces are selected:

$$s_{0,1} = x_1 + c_1 x_3$$

$$s_{0,2} = x_2 + x_3$$

thus leading to:

$$\mathbf{C} = \begin{bmatrix} 1 & 0 & c_1 \\ 0 & 1 & 1 \end{bmatrix}$$

The equivalent control can be evaluated by vanishing $\dot{s}_{0,1} = 0$ and $\dot{s}_{0,2} = 0$:

$$\dot{s}_{0,1} = (1 + c_1)x_1 + x_2 + (1 + c_1)x_3 - c_1 u_1 + u_2 - c_1 h_1 + h_2 = 0$$

$$\dot{s}_{0,2} = x_1 + x_2 + 4x_3 - u_2 - h_2 = 0$$

$$u_{1eq} = \frac{2 + c_1}{c_1} x_1 + \frac{2}{c_1} x_2 + \frac{5 + c_1}{c_1} x_3 - h_1$$

$$u_{2eq} = x_1 + x_2 + 4x_3 - h_2$$

and the reduced dynamics of the original system is given by:

$$x_1 = -c_1 x_3$$

$$x_2 = -x_3$$

$$\dot{x}_3 = \frac{2c_1 - 3}{c_1} x_3$$

In order to have a stable solution $0 < c_1 < 3/2$. It is evident that close-loop dynamics has a reduce-order than original system and it is invariant with respect h_1 and h_2 that are matched disturbances.

Finally, the sliding mode controller is selected as stated in Eq. 1.112:

$$\begin{aligned} u_1 &= \frac{2+c_1}{c_1}x_1 + \frac{2}{c_1}x_2 + \frac{5+c_1}{c_1}x_3 - \rho_1 \text{sign}(s_{0,1}) \\ u_2 &= x_1 + x_2 + 4x_3 - \rho_2 \text{sign}(s_{0,2}) \end{aligned}$$

where ρ_1 and ρ_2 have to be designed by applying the Lyapunov theorem based on the maximum value of disturbances h_1 and h_2 . The filtered values of $\rho_1 \text{sign}(s_{0,1})$ and $\rho_2 \text{sign}(s_{0,2})$ can be also used as estimators of respectively h_1 and h_2 .

Relative degree approach

The sliding surface design can be carried out based on the *relative degree* definition.

Definition 1.4 (Relative Degree). *Consider a Single-Input Single-Output system (SISO) with output $y \in \mathbb{R}$, state vector $\mathbf{x} \in \mathbb{R}^n$ and $u \in \mathbb{R}$. If the i_{th} derivative $y^{(i)}$ is independent on u for all $i = 1, 2, \dots, k-1$ and $y^{(k)}$ is proportional to u , then k is called the relative degree.*

The sliding surface can be defined conventionally as a linear differential equation of order equal to $k-1$ with respect the error between the output variable and its reference value.

Example Consider the following system:

$$\begin{cases} \dot{x}_1 &= x_2 \\ \dot{x}_2 &= u + h(x_1, x_2, t) \\ y &= x_1 \end{cases}$$

The problem statement is to design a sliding mode control u that makes the output y follow a reference profile $y_r(t)$ thus driving the tracking error $e = y_r - y$ to zero even in presence of the external disturbance $h(x_1, x_2, t)$. In this case the relative degree is equal to 2 and the sliding variable can be chosen as:

$$s_0 = \dot{e} + ce, \quad c > 0$$

As soon as the sliding variable s_0 reaches the zero, the sliding motion starts and the tracking error e will respect the reduced order differential equation:

$$\dot{e} + ce = 0, \quad c > 0$$

The sliding variable dynamics is expressed by:

$$\dot{s}_0 = \ddot{y}_r + c\dot{y}_r - \underbrace{h(x_1, x_2, t) - c\dot{y}}_{\phi(y, \dot{y}, t)} - u$$

and it is assumed that $\phi(y, \dot{y}, t)$ is bounded $|\phi(y, \dot{y}, t)| \leq M$. The sliding mode control u can be designed by using the Lyapunov theorem:

$$s_0 \dot{s}_0 = s_0(\phi(y, \dot{y}, t) - u) \leq |s_0| M - s_0 u$$

and choosing the control as:

$$u = \rho \operatorname{sign}(s_0)$$

thus obtaining that:

$$s_0 \dot{s}_0 \leq |s_0| (M - \rho) \leq 0$$

finally selecting the controller gain ρ as:

$$\rho > M$$

Integral sliding mode

The invariance property (robustness) of conventional sliding mode with respect external disturbances can occur only when the system is operating in the sliding phase. During the reaching phase, the robustness property is not guaranteed. The ISM control aims to eliminate the reaching phase and let the sliding phase occurs from the beginning of controller action thus preserving the robustness property throughout the entire system response. As additional effect of ISM, the order of the motion equation in integral sliding mode is equal to the order of the original system. Moreover, the integral sliding mode control can be extended to build a new type of perturbation estimator which solves the chattering problem characteristic of conventional sliding mode controllers (see [73, 72] for further information).

Consider a dynamic system represented by the following state space equation:

$$\dot{\mathbf{x}} = \mathbf{f}(\mathbf{x}) + \mathbf{B}(\mathbf{x})\mathbf{u} \quad (1.122)$$

where $\mathbf{x} \in \mathbb{R}^n$ is the state vector and $u \in \mathbb{R}^m$ is the control input vector. Suppose that a nominal controller $u = u_0(\mathbf{x})$ stabilizes the system in Eq. 1.122 in a desired way.

$$\dot{\mathbf{x}}_0 = \mathbf{f}(\mathbf{x}_0) + \mathbf{B}(\mathbf{x}_0)\mathbf{u}_0 \quad (1.123)$$

However, in real situations system in Eq. 1.122 is influenced by parameter variation, unmodelled dynamics and external disturbances and the states trajectory is modified:

$$\dot{\mathbf{x}} = \mathbf{f}(\mathbf{x}) + \mathbf{B}(\mathbf{x})\mathbf{u} + \mathbf{h}(\mathbf{x}) \quad (1.124)$$

where the $\mathbf{h}(\mathbf{x})$ comprise all the unknown terms that influence the states dynamics. Assume that the unknown term fulfill the *matching condition*:

$$\mathbf{h}(\mathbf{x}) = \mathbf{B}(\mathbf{x})\mathbf{u}_h \quad (1.125)$$

which means that the controller u is able to influence all components of $\mathbf{h}(\mathbf{x})$ through the matrix $\mathbf{B}(\mathbf{x})$. Finally, the unknown term $\mathbf{h}(\mathbf{x})$ is supposed to be bounded:

$$|h_i(\mathbf{x})| \leq h_i^+(\mathbf{x}) \quad i = 1, \dots, n \quad (1.126)$$

where $h_i^+(\mathbf{x})$ is a positive scalar function. The objective of the ISM is to find a control logic u such that the trajectory of real system in Eq. 1.126 satisfy $x(t) = x_0(t)$. The first step is to split the control logic u into two sub-controllers:

$$u = u_0 + u_1 \quad (1.127)$$

where $u_0 \in \mathbb{R}^m$ is the *ideal control* defined in Eq. 1.123 and $u_1 \in \mathbb{R}^m$ will be designed to reject the perturbation term $\mathbf{h}(\mathbf{x})$. The substitution of control logic of Eq. 1.127 into Eq. 1.124 yields to:

$$\dot{\mathbf{x}} = \mathbf{f}(\mathbf{x}) + \mathbf{B}(\mathbf{x})\mathbf{u}_0 + \mathbf{B}(\mathbf{x})\mathbf{u}_1 + \mathbf{h}(\mathbf{x}) \quad (1.128)$$

Introduce a new sliding variable s :

$$s = s_0 + z \quad (1.129)$$

which is composed by two parts: the first sliding variable s_0 may be designed as a linear combination of the system states, as it happens for conventional sliding mode controllers; the second sliding variables z introduce an integral term that will be designed below. The control logic $u_1 = \text{Sign}(s)$ is designed as conventional sliding mode such as its equivalent expression to reach the sliding surface $s = 0$ is:

$$\mathbf{B}(\mathbf{x})\mathbf{u}_{1eq} = -\mathbf{h}(\mathbf{x}) \quad (1.130)$$

By imposing the time derivative of s to be equal to zero:

$$\dot{s} = \dot{s}_0 + \dot{z} = \frac{\partial s_0}{\partial x} [\mathbf{f}(\mathbf{x}) + \mathbf{B}(\mathbf{x})\mathbf{u}_0 + \mathbf{B}(\mathbf{x})\mathbf{u}_{1eq} + \mathbf{h}(\mathbf{x})] + \dot{z} = 0 \quad (1.131)$$

in order to ensure Eq. 1.130 the second sliding variable z must be selected by integrating the following expression:

$$\dot{z} = -\frac{\partial s_0}{\partial x} [\mathbf{f}(\mathbf{x}) + \mathbf{B}(\mathbf{x})\mathbf{u}_0] \quad z(0) = -s_0(\mathbf{x}_0) \quad (1.132)$$

The initial condition $z(0) = -s_0(\mathbf{x}_0)$ imposes that the sliding phase occurs starting from the initial time instance. With this design methodology, the Eq. 1.130 is satisfied and the system behaves in a similar way to the ideal system trajectory:

$$\dot{\mathbf{x}} = \mathbf{f}(\mathbf{x}) + \mathbf{B}(\mathbf{x})\mathbf{u}_0 \quad (1.133)$$

Perturbation estimation A crucial problem that afflicts the nature of conventional sliding mode is the control discontinuity. The switching effect of control action results in high-frequency oscillations which can excite system fast dynamics, like those of actuators and sensors. This phenomenon is commonly referred as *chattering*, and several methods are presented in the literature to limit the controller gain or bandwidth. The paragraph intent is to describe how design the IMS as a disturbance estimator and rejecting disturbance without causing chattering. Instead of Eq. 1.127, the control output is selected as:

$$u = u_0 + u_{1eq} \quad (1.134)$$

but since the equivalent control depends on unknown term $\mathbf{h}(\mathbf{x})$ and it cannot practically implemented. The equivalent control is thus evaluated by applying a first-order linear filter to the discontinuous control u_1 . The time constant of the filter should be sufficiently fast such that the plant and disturbance dynamics are allowed to pass through the filter without significant phase lag. Even if the discontinuous control u_1 is shifted from the plant input to the input of the filter, the sliding mode can still be generated and the perturbation is still canceled. Here is the explanation by redesigning the sliding variable as follow:

$$s = s_0 + z \quad (1.135)$$

with z defined as

$$\dot{z} = -\frac{\partial s_0}{\partial x} [\mathbf{f}(\mathbf{x}) + \mathbf{B}(\mathbf{x})\mathbf{u} - \mathbf{B}(\mathbf{x})\mathbf{u}_1] \quad z(0) = -s_0(\mathbf{x}_0) \quad (1.136)$$

the derivative of sliding variable s can be calculated as:

$$\begin{aligned}\dot{s} &= -\frac{\partial s_0}{\partial x} [\mathbf{f}(\mathbf{x}) + \mathbf{B}(\mathbf{x})\mathbf{u} + \mathbf{h}(\mathbf{x})] - \frac{\partial s_0}{\partial x} [\mathbf{f}(\mathbf{x}) + \mathbf{B}(\mathbf{x})\mathbf{u} - \mathbf{B}(\mathbf{x})\mathbf{u}_1] = \\ &= \frac{\partial s_0}{\partial x} \mathbf{h}(\mathbf{x}) + \frac{\partial s_0}{\partial x} \mathbf{B}(\mathbf{x})\mathbf{u}_1\end{aligned}\quad (1.137)$$

so that when the sliding phase is reached, the equivalent control of u_1 is able to estimate and reject the disturbance $\mathbf{h}(\mathbf{x})$. The Eq. 1.136 can be seen as an internal process for generating the sliding mode; discontinuity appears only in the internal process thus no chattering is excited in the real control path. Moreover, the redesign control logic in Eq. 1.134 cancels the *matched disturbance* $\mathbf{h}(\mathbf{x})$ without a precise knowledge of the system model and its parameters thus ensuring an high degree of robustness. The unique information needed for designing the ISM control is the upper bound of the perturbation. In conclusion, the ISM is used for estimating the system perturbation rather than for the purpose of control since the control action to the real plant will be continuous and enhanced by the perturbation compensator.

ISM applied to Lateral Deviation Control

The present section intent is to apply the ISM technique as disturbance observer contribution, coupled with the PSA as nominal controller, for lateral deviation regulation. The starting point for designing the ISM is the state space representation of the lateral deviation dynamics expressed by Eq. 1.134 in section 1.3.5 and defined by the following four differential equations:

$$\begin{cases} \dot{\beta} &= a_{11}\beta + a_{12}r + b_{11}\delta_F \\ \dot{r} &= a_{21}\beta + a_{22}r + b_{21}\delta_F \\ \Delta\dot{\psi} &= r - V\rho_{ref} \\ \dot{y} &= V\beta + l_s r + V\Delta\psi - Vl_s\rho_{ref} \end{cases}\quad (1.138)$$

where $a_{11} = -(C_F + C_R)/(mV)$, $a_{12} = -1 - (C_F a - C_R b)/(mV^2)$, $a_{21} = -(C_F a - C_R b)/(J_z)$, $a_{22} = -(C_F a^2 + C_R b^2)/(VJ_z)$, $b_{11} = C_F/mV$, $b_{21} = C_F a/J_z$. The state space representation can be obtained as follows:

$$\dot{\mathbf{x}} = \underbrace{\begin{bmatrix} a_{11} & a_{12} & 0 & 0 \\ a_{21} & a_{22} & 0 & 0 \\ 0 & 1 & 0 & 0 \\ V & l_s & V & 0 \end{bmatrix}}_{\mathbf{A}} \mathbf{x} + \underbrace{\begin{bmatrix} b_{11} \\ b_{21} \\ 0 \\ 0 \end{bmatrix}}_{\mathbf{B}} \delta_F + \underbrace{\begin{bmatrix} 0 \\ 0 \\ -V \\ -Vl_s \end{bmatrix}}_{\mathbf{E}} \rho_{ref} + \underbrace{\begin{bmatrix} h_\beta \\ h_r \\ h_{\Delta\psi} \\ h_y \end{bmatrix}}_{\mathbf{H}(\mathbf{x})}\quad (1.139)$$

The sliding variable s for ISM design is selected as:

$$s = s_0 + z \quad (1.140)$$

Since the relative degree with respect the lateral deviation y is equal to 2, the conventional sliding variable s_0 can be selected as:

$$s_0 = \dot{y} + cy \quad (1.141)$$

and by choosing the controller action δ_F as sum of nominal controller (PSA) δ_0 and the equivalent value δ_{1eq} of sliding mode controller δ_1 ($\delta_{1eq} = \delta_1 \frac{\omega_F}{p+\omega_F}$):

$$\delta_F = \delta_0 + \delta_{1eq} \quad (1.142)$$

it is possible to evaluate the time derivative of sliding variable:

$$\dot{s} = \frac{\partial s_0}{\partial \mathbf{x}} [\mathbf{Ax} + \mathbf{B}\delta_F + \mathbf{E}\rho_{ref} + \mathbf{H} + \mathbf{H}_s] + \dot{z} \quad (1.143)$$

where $\frac{\partial s_0}{\partial \mathbf{x}} = [V \ l_s \ V \ c]$ and $\mathbf{H}_s = [0 \ V\dot{\rho}_{ref} \ 0 \ \dot{h}_y/c]'$. The second sliding variable z is thus designed as:

$$\dot{z} = -\frac{\partial s_0}{\partial \mathbf{x}} [\mathbf{Ax} + \mathbf{B}\delta_F - \mathbf{B}\delta_1] \quad z(0) = -s_0(0) = -cy(t = t_0) \quad (1.144)$$

where t_0 is the time at which the path tracking control is activated. With the above selection of z dynamics, the sliding phase starts as soon as the controller is activated and the dynamics of the sliding variable s is defined by the following equation:

$$\begin{aligned} \dot{s} &= -\frac{\partial s_0}{\partial \mathbf{x}} [\mathbf{Ax} + \mathbf{B}\delta_F + \mathbf{E}\rho_{ref} + \mathbf{H} + \mathbf{H}_s] - \frac{\partial s_0}{\partial \mathbf{x}} [\mathbf{Ax} + \mathbf{B}\delta_F - \mathbf{B}\delta_1] = \\ &= \frac{\partial s_0}{\partial \mathbf{x}} [\underbrace{\mathbf{E}\rho_{ref} + \mathbf{H} + \mathbf{H}_s}_{\mathbf{H}_2}] + \frac{\partial s_0}{\partial \mathbf{x}} \mathbf{B}\delta_1 \end{aligned} \quad (1.145)$$

so that when the sliding phase is reached, the control action δ_1 is able to reject the unknown terms identified by $\mathbf{H}_2 = \mathbf{E}\rho_{ref} + \mathbf{H} + \mathbf{H}_s$ (the curvature of reference path ρ_{ref} is supposed to be unknown for ISM formulation). Finally, the discontinuous control action $\delta_1 = -K \text{sign}(s)$ must be properly designed according to the Lyapunov Theorem based on the max value of unknown terms $\left| \frac{\partial s_0}{\partial \mathbf{x}} \mathbf{H}_2 \right| \leq N$:

$$\dot{V} = s\dot{s} \leq |s| \left| \frac{\partial s_0}{\partial \mathbf{x}} \mathbf{H}_2 - \frac{\partial s_0}{\partial \mathbf{x}} \mathbf{B}K \text{sign}(s) \right| \leq |s| \left[\left| \frac{\partial s_0}{\partial \mathbf{x}} \mathbf{H}_2 \right| - K(Vb_{11} + l_s b_{21}) \right] \leq 0 \quad (1.146)$$

where $V = 1/2s^2$ is the candidate Lyapunov function and K is the controller gain to be designed for keeping negative the value of \dot{V} :

$$K \geq \frac{N(V, l_s)}{(Vb_{11} + l_sb_{21})} \quad (1.147)$$

The final gains K depends on the vehicle speed V , preview distance l_s and on maximum value N . In the present case it is supposed to decouple the longitudinal dynamics by considering a constant speed (15km/h) and for a fixed value of preview distance l_s meanwhile the value of N has been evaluated by considering an high value of reference curvature ($1/\rho_{ref} = 5m$) and by neglecting the effect of four coefficients h_β , h_r , $h_{\Delta\psi}$ and h_y since the simulation model is not be able to capture such uncertainties. The experimental tuning of the gain K will slightly correct the value obtained by simulation results.

1.4.5 Obstacle Collision Avoidance Path Modification

In section 1.4.1 a method for reference path segmentation and digital map implementation in real-time application is described with the hypothesis that a high-level path planning strategy (not designed in the present work) provides a global way-points trajectory, defined by global coordinates X_{exp} and Y_{exp} , without considering the presence of external obstacles. The present section aims to show how the elastic band theory [59, 60] can be applied for autonomous steering control and its effect in terms of reference path modification when an obstacle is detected (object detection and/or recognition is not the final purpose of the present thesis). The method consists in comparing the initial reference path to a series of springs that can be deformed by internal and external forces

obstacles are detected and, consequently, the static balance of internal forces acting on each node N_i can be calculated as:

$$\mathbf{F}_{i,i-1}^{INT} + \mathbf{F}_{i,i+1}^{INT} = k_s(\mathbf{r}_{i-1} - \mathbf{r}_i) + k_s(\mathbf{r}_{i+1} - \mathbf{r}_i) = 0 \quad (1.148)$$

where k_s is the spring stiffness, \mathbf{r}_i is the position vector of i -th node and $\mathbf{F}_{i,i-1}^{INT}$ is the internal force between N_i and N_{i-1} .

When an obstacle is detected, an external force \mathbf{F}_i^{EXT} is applied thus modifying the static relation expressed by Eq. 1.148:

$$\begin{aligned} \mathbf{F}_{i,i-1}^{INT} + \mathbf{F}_{i,i+1}^{INT} + \mathbf{F}_i^{EXT} &= k_s(\mathbf{r}_{i-1}^* - \mathbf{r}_i^*) + k_s(\mathbf{r}_{i+1}^* - \mathbf{r}_i^*) + \mathbf{F}_i^{EXT} = \\ &= k_s(\mathbf{r}_{i-1} + \mathbf{u}_{i-1} - \mathbf{r}_i - \mathbf{u}_i) + k_s(\mathbf{r}_{i+1} + \mathbf{u}_{i+1} - \mathbf{r}_i - \mathbf{u}_i) + \mathbf{F}_i^{EXT} = 0 \end{aligned} \quad (1.149)$$

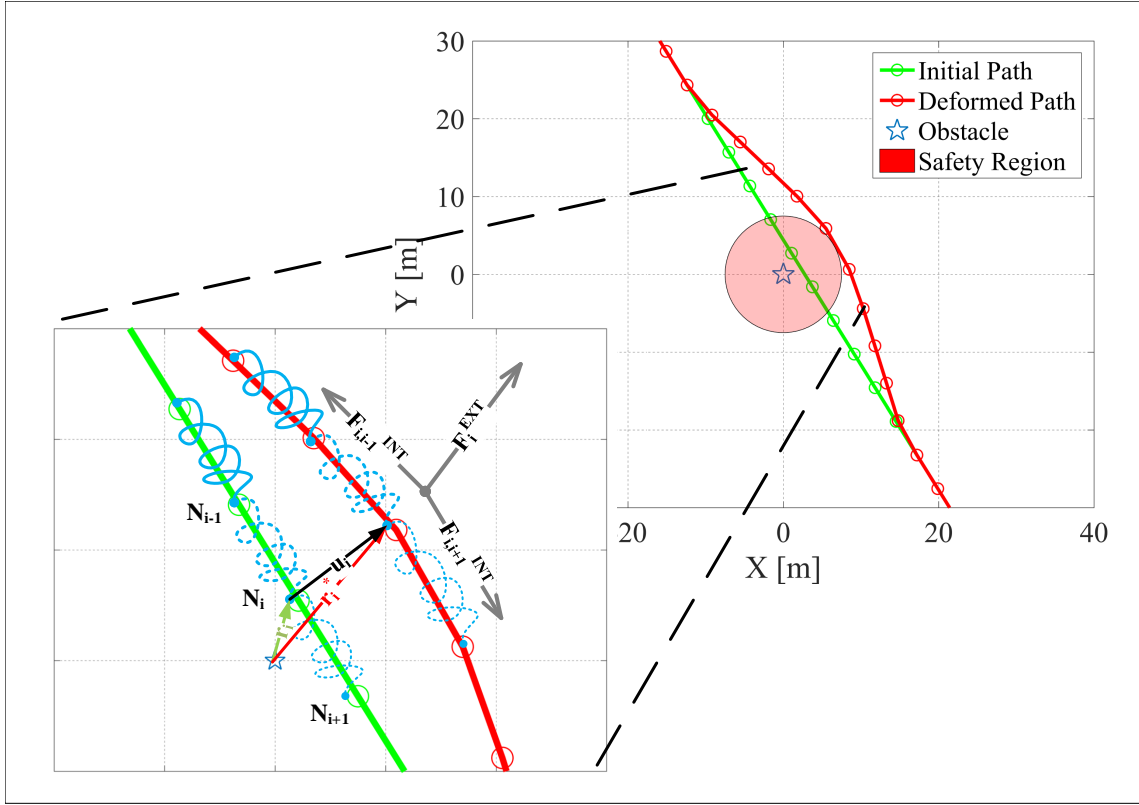


Figure 1.27 Reference path modification according to the elastic band theory: external (\mathbf{F}_i^{EXT}) and internal ($\mathbf{F}_{i,i-1}^{INT}, \mathbf{F}_{i,i+1}^{INT}$) forces applied to the i -th node N_i provokes a deformation u_i

where \mathbf{r}_i^* is the vector position of node N_i after the application of the external force \mathbf{F}_i^{EXT} . By substituting Eq. 1.148 in Eq. 1.149 the following relation is obtained:

$$\mathbf{F}_i^{EXT} = -[k_s(\mathbf{u}_{i-1} - \mathbf{u}_i) + k_s(\mathbf{u}_{i+1} - \mathbf{u}_i)] = -k_s(\mathbf{u}_{i-1} - 2\mathbf{u}_i + \mathbf{u}_{i+1}) \quad (1.150)$$

The elastic band method is not applied to all n nodes that constitutes the initial path, but it is limited to $q < n$ nodes that are located within a desired circle with radius R_{pr} defined as preview radius. The external force \mathbf{F}_i^{EXT} is selected according to the relative position between the obstacle and the initial path:

$$\mathbf{F}_i^{EXT} = \begin{cases} -k_e(\|\mathbf{r}_i\| - r_{max}) \frac{\mathbf{r}_{i,min}}{\|\mathbf{r}_{i,min}\|}, & \|\mathbf{r}_i\| \leq r_{max} \\ 0, & \|\mathbf{r}_i\| > r_{max} \end{cases} \quad (1.151)$$

where $\mathbf{r}_{i,min}$ is the minimum vector position \mathbf{r}_i between the obstacle and initial path. If the obstacle is detected beyond a safety margin expressed by r_{max} , no external forces are applied thus locally limiting the path deformation. An example of the external force distribution is shown in Fig. 1.28 as function of the initial path X and Y global coordinates. Eq. 1.150 can be reformulated into a matrix equation:

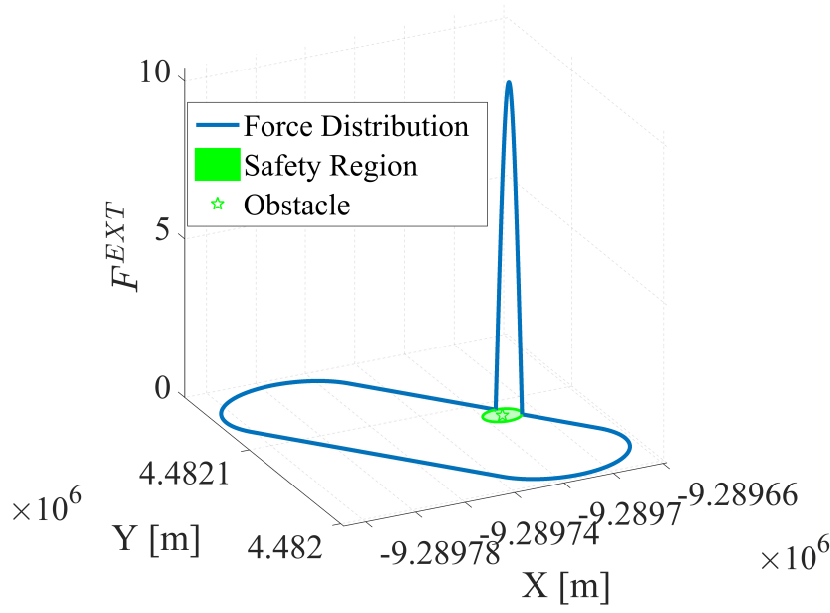


Figure 1.28 Force distribution applied to initial path according to the elastic band theory

$$\mathbf{F}^{EXT} = k_s \mathbf{K} \mathbf{u} \quad (1.152)$$

where \mathbf{F}^{EXT} , \mathbf{u} and \mathbf{K} have respectively $q \times 2$, $q \times 2$ and $q \times q$ dimensions:

$$\mathbf{K} = \begin{bmatrix} 2 & -1 & 0 & 0 & 0 & \cdots & 0 \\ -1 & 2 & -1 & 0 & 0 & \cdots & 0 \\ \vdots & \vdots & \vdots & \vdots & \vdots & \cdots & \vdots \\ 0 & 0 & 0 & \cdots & 0 & -1 & 2 \end{bmatrix}, \mathbf{u} = \begin{bmatrix} u_{1,x} & u_{1,y} \\ \vdots & \vdots \\ u_{i,x} & u_{i,y} \\ \vdots & \vdots \\ u_{q,x} & u_{q,y} \end{bmatrix}, \mathbf{F}^{EXT} = \begin{bmatrix} F_{1,x}^{EXT} & F_{1,y}^{EXT} \\ \vdots & \vdots \\ F_{i,x}^{EXT} & F_{i,y}^{EXT} \\ \vdots & \vdots \\ F_{q,x}^{EXT} & F_{q,y}^{EXT} \end{bmatrix}$$

$F_{i,x}^{EXT}$ and $F_{i,y}^{EXT}$ are X and Y axis components of \mathbf{F}_i^{EXT} meanwhile $u_{i,x}$ and $u_{i,y}$ are the same components of \mathbf{u}_i . The deformation vector \mathbf{u} can be obtained by inverting the matrix \mathbf{K} :

$$\mathbf{u} = \frac{1}{k_s} \text{inv}(\mathbf{K}) \mathbf{F}^{EXT} \quad (1.153)$$

thus generating the modified reference path defined by X_{exp}^* and Y_{exp}^* coordinates:

$$[X_{exp}^* \ Y_{exp}^*] = [X_{exp} \ Y_{exp}] + [\mathbf{0} \ \mathbf{0}; \mathbf{u} \ \mathbf{0}] \quad (1.154)$$

An example of reference path deformation as a consequence of different obstacle positions is reported in Fig. 1.29 by adopting the following parameters:

- $R_{pr} = 25 \text{ m}$
- $r_{max} = 7.5 \text{ m}$
- $k_s = 520000 \text{ N/m}$
- $k_e = 3 \text{ N/m}$

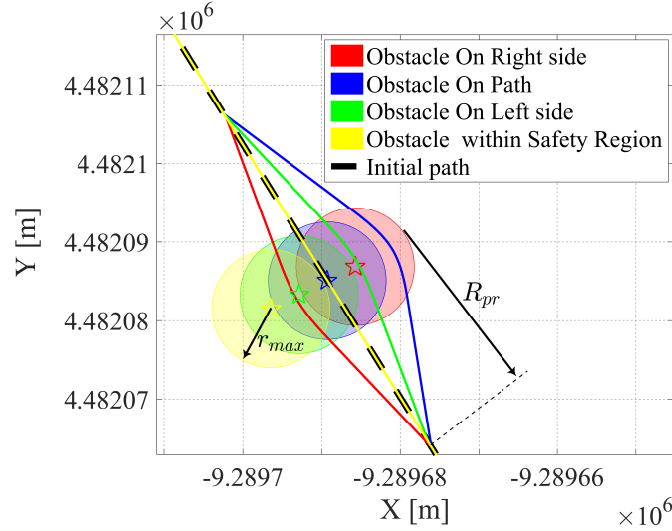


Figure 1.29 Initial path deformation for four obstacle positions according to the elastic band theory

When the obstacle is closer to the initial path a larger deformation is requested in order to overtake the safety region. Moreover, the deformation of the elastic band can change its sign when the obstacle changes its relative position with respect the reference path. In the present activity, the safety region bounded by r_{max} is selected by assuming only static obstacles. The value of maximum external force amplitude k_e and the preview radius R_{pr} are properly designed in order to have a smooth curvature change when the initial path deformation occurs. In particular, Fig. 1.30 shows the effect of different ratios $T_p = \frac{R_{pr}}{k_e}$ on the path deformation: a high T_p value provokes a smoother deformation thus requiring a less aggressive steering action when the vehicle begins and completes the obstacle avoidance maneuver.

1.5 Experimental Results

1.5.1 Close-Loop Path

The PSA+FF and PSA+ISM strategies explained in previous sections are here implemented on the vehicle prototype platform introduced in section 1.2 and described by

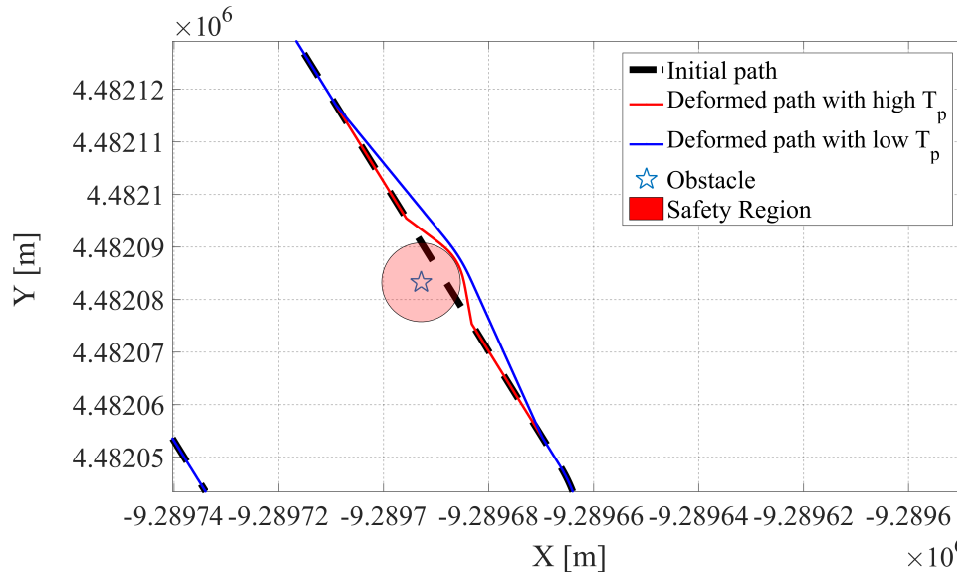


Figure 1.30 Initial path deformation for different values of $T_p = \frac{R_{pr}}{k_e}$ ratios

the control scheme shown in Fig. 1.31. The vehicle speed is kept constant at 15 km/h by

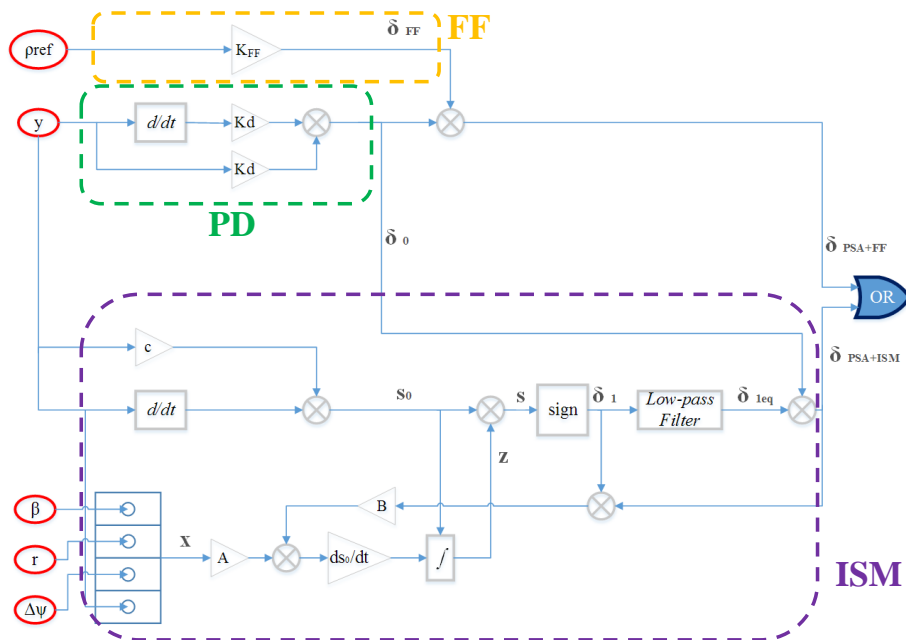


Figure 1.31 Controller scheme implemented on the prototype autonomous vehicle for path tracking control with PSA+FF and PSA+ISM strategies

using a PI cruise control experimentally tuned. The reference path adopted for experimental test is a close loop path shown in Fig. 1.18 which is composed by two semicircles with a radius of 30 m and two straight lines of 120 m and it is divided into 51 segments. For a benchmark comparison, two different modes can be selected for experimental tests:

1. **Manual mode:** the driver is requested to follow the reference path meanwhile the PI cruise control is responsible for keeping constant the speed (the autonomous system is disabled)
2. **Autonomous mode:** the vehicle is responsible for both path tracking and cruise control (the driver can take over only during emergency situations)

The manual mode is executed with three different drivers who are asked to track the reference path which has been previously marked on the street meanwhile cruise control keeps constant the speed at 15km/h ; results are shown in Figures 1.32 and 1.33.

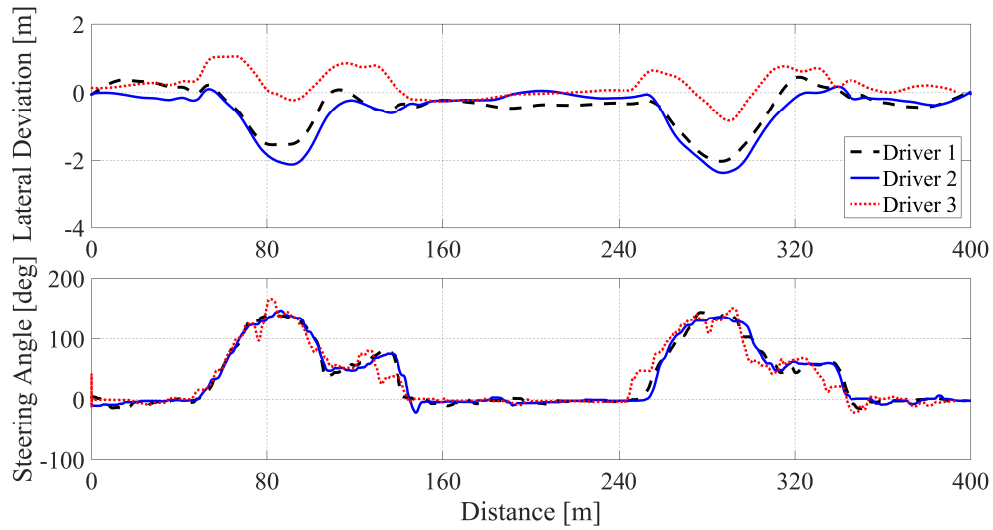


Figure 1.32 Lateral deviation y and steering angle δ_{Out} during manual path tracking for three different drivers at constant speed of 15km/h

The vehicle always starts from the same position and all variables are plotted as function of distance coordinate (with respect starting point) instead of time thus obtaining a comparison not influenced by vehicle speed. When the vehicle approaches the two semicircles, the driver are forced to increase the steering angle in order to keep the vehicle trajectory as close as possible to the reference path. The driver 3 is able to keep the lateral deviation smaller than the other two drivers but it results as an increase in steering oscillations. The same test is repeated in autonomous mode in order to compare the results with the manual mode and to show the effects introduced by the PSA+FF and PSA+ISM strategies. The results are reported in Figures 1.34 and 1.35.

The first noticeable observation is that lateral deviation responses clearly prove the efficacy of PSA+FF and especially PSA+ISM controllers if compared to the manual driving test. The root mean square value of lateral deviation is shown by Tab. 1.2 in order to quantify the comparison among experimental tests. It is quite visible that the

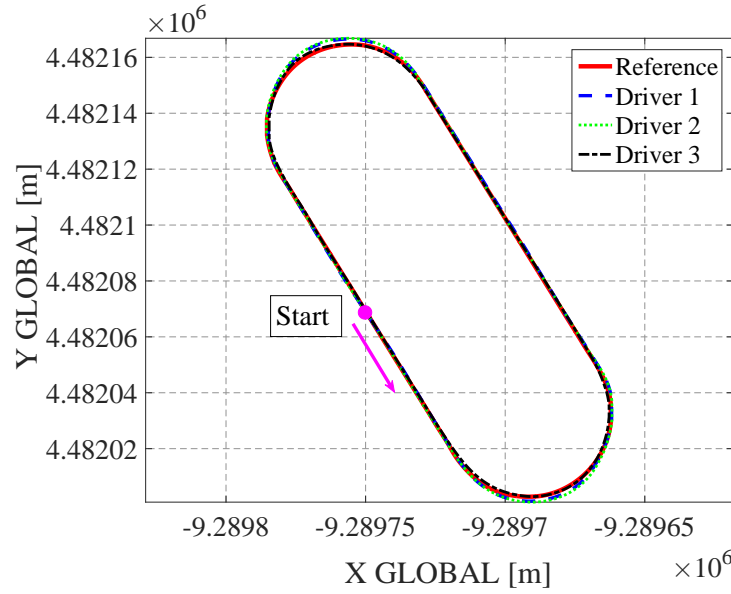


Figure 1.33 Global coordinates during manual path tracking for three different drivers at constant speed of 15 km/h

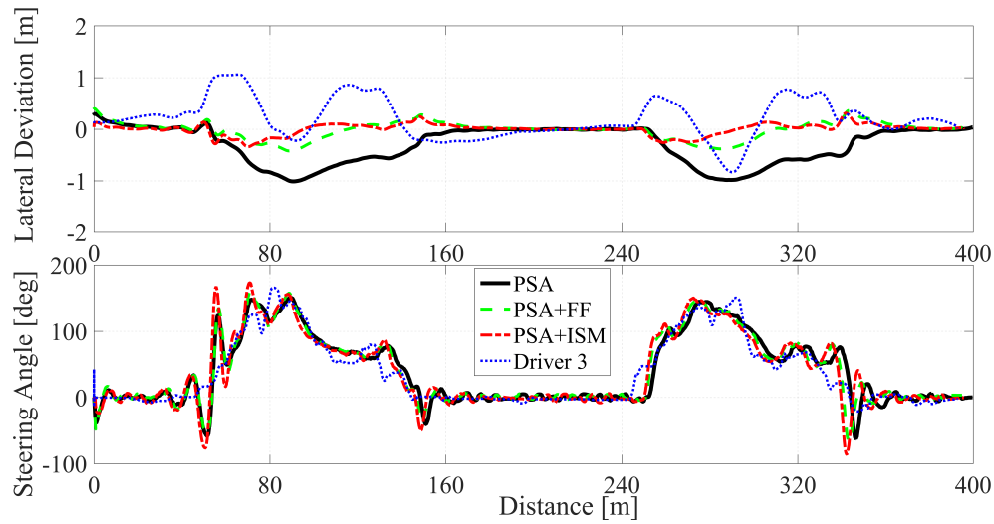


Figure 1.34 Lateral deviation y and steering angle δ_{Out} during autonomous path tracking with PSA, PSA+FF and PSA+ISM strategies at constant speed of 15 km/h

PSA+FF and PSA+ISM provides better results if compared to the PSA logic and to the best driver behavior: the PSA logic is designed based on transfer function between the lateral deviation y and the steering angle δ_{In} without taking into account the influence of ρ_{ref} as stated by Eq. 1.28; the FF contribution provides a steering additional contribution based on the calculation of reference curvature ρ_{ref} meanwhile the ISM additional contribution is able to reject external disturbances (in this case ρ_{ref}) that can affect the PSA performances (just requiring the maximum value of the disturbance).

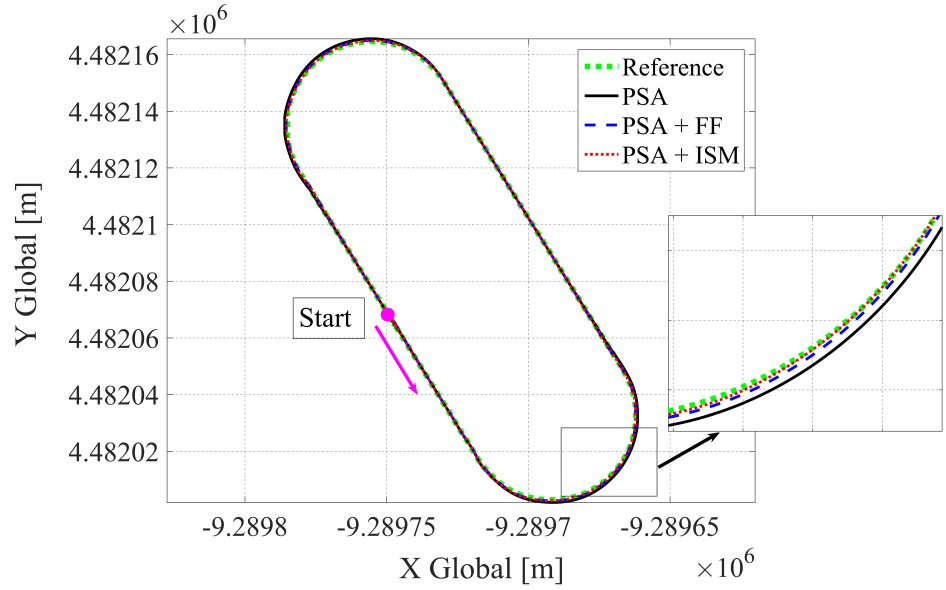


Figure 1.35 Global coordinates during autonomous path tracking with PSA, PSA+FF and PSA+ISM strategies at constant speed of 15 km/h

Root Mean Square of lateral deviation y				
	PSA	PSA+FF	PSA+ISM	Driver 4
$y_{RMS}[m]$	0.4682	0.1870	0.1079	0.4102

Table 1.2 Root Mean Square of lateral deviation y during Close-Loop path tracking control

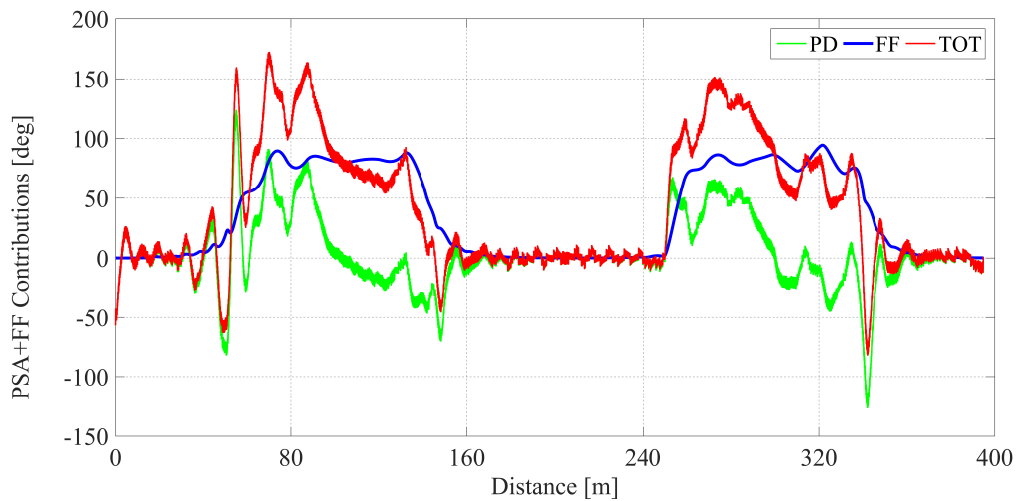


Figure 1.36 PSA+FF contributions during autonomous path tracking at constant speed of 15 km/h

Figures 1.36 and 1.37 show that both contributions FF and ISM are effective during the two semicircles in order to enhance the PSA robust properties. By considering that FF contribution is proportional to the ρ_{ref} as highlighted by Eq. 1.106, it is visible

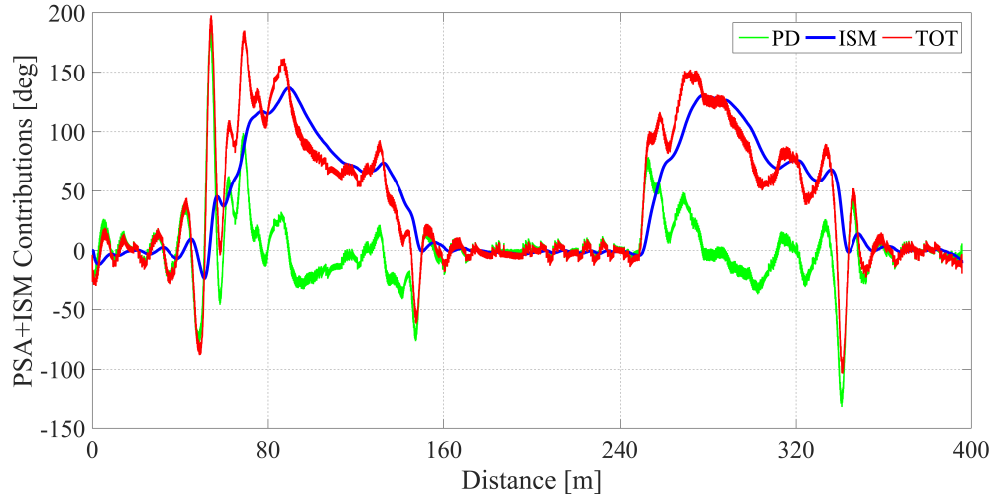


Figure 1.37 PSA+ISM contributions during autonomous path tracking at constant speed of 15 km/h

that the curvature presents some oscillations and it is not a discontinuous function as intended by original path: this effect is introduced by the digital map approximation and it could be improved by increasing the number of segments or by adopting a greater order of polynomial function. The PSA+FF and PSA+ISM are two path tracking strategies that perfectly suit the controller tasks: keep the lateral deviation as small as possible in all possible conditions. The discrimination between the two strategies can be evaluated based on the reference curvature availability in real-time since it constitutes the input for FF term; the PSA+ISM control can be designed also for different external disturbances just keeping in mind that at least the max value of the disturbances is required.

Moreover, in Eq. 1.33 the preview distance has been introduced by enhancing the promptness of the path tracking control; in order to analyze the effect of the preview distance l_s , three experimental tests are repeated on the same reference path by adopting only the PSA logic. Results for three different l_s values ($l_s = 6.5, l_s = 0.5$ and $l_s = -1.5$) are shown in Fig. 1.38. A higher value of preview distance increases the controller action intervention: the controller with $l_s = 6.5$ is able to detect in advance the change of curvature but with the negative aspect of triggering undesired oscillations. As a counterpart, a negative value of l_s can provoke during straight line maneuvers some issues related to steering oscillations. By gathering all these aspects, a nominal value of $l_s = 0.5$ represents a good tradeoff between controller promptness and steering oscillations.

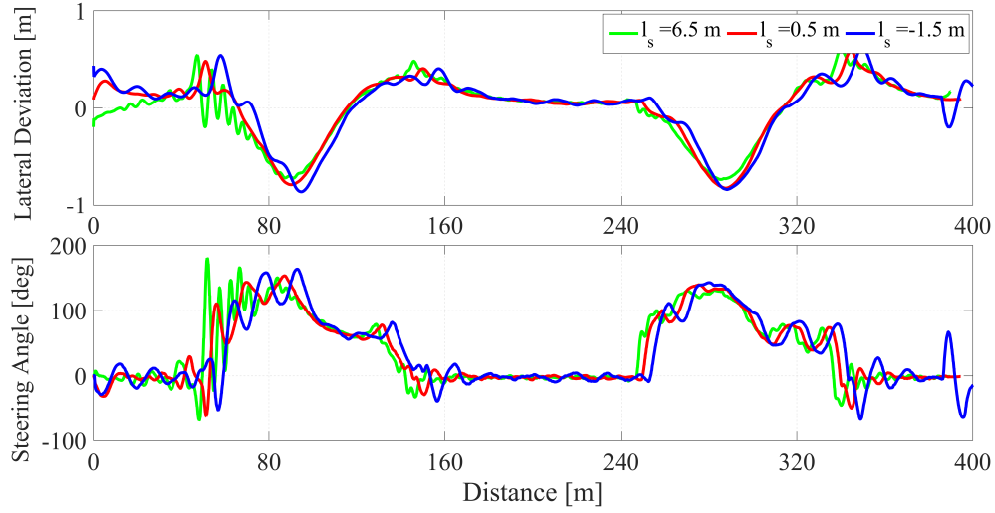


Figure 1.38 Effect of preview distance l_s on path tracking control with PSA logic at constant speed of 15 km/h

1.5.2 Close-Loop Path for Obstacle Avoidance

In order to verify the elastic-band theory described in section 1.4.5, it is supposed that a static obstacle is detected by on-board sensors and its position is evaluated for modifying the reference path thus overtaking it within a specific safety region. The safety limit is defined by a circular region with a radius of 7.5 m and the initial path would cross it if no collision avoidance algorithm is applied as shown in Fig. 1.39. The modified reference

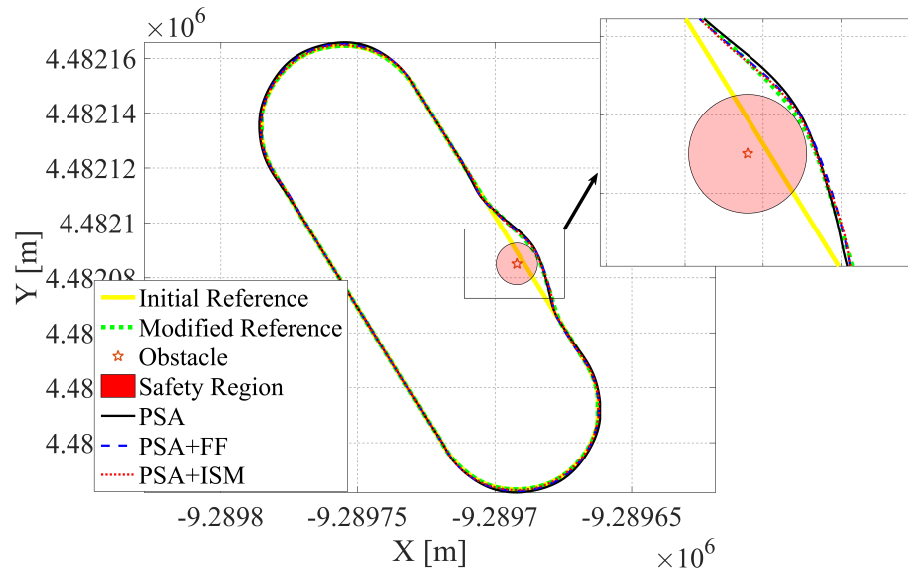


Figure 1.39 Global coordinates during obstacle collision avoidance maneuver with PSA, PSA+FF and PSA+ISM strategies at constant speed of 5 km/h

path is used as input for generating the steering angle according to PSA, PSA+FF and

PSA+ISM strategies meanwhile the speed is kept constant at 5 km/h by the cruise control. Results in terms of lateral deviation and steering angle are reported in Fig. 1.40 where it is also indicated where the two semicircular turning and the obstacle occurs. The obstacle

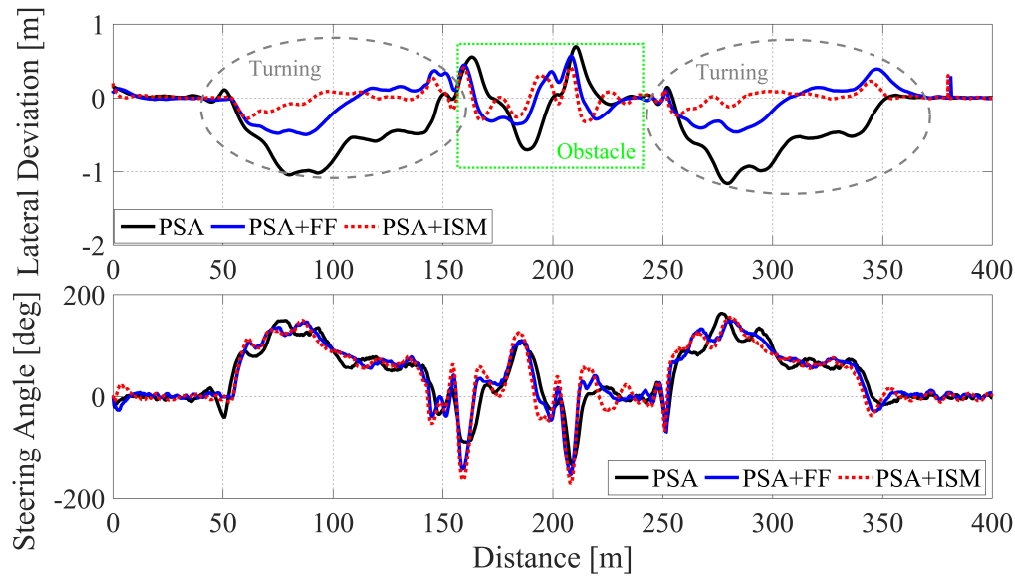


Figure 1.40 Lateral deviation y and steering angle δ_{Out} during obstacle collision avoidance maneuver with PSA, PSA+FF and PSA+ISM strategies at constant speed of 5 km/h

avoidance maneuver requires a faster steering intervention (which could be a weakness point for the steering control frequency bandwidth) with respect the remaining part of the path due to a larger curvature needed for obstacle overtaking. It is evident the benefit introduced by the Feedforward and further enhanced by the ISM term for keeping the lateral deviation as close as possible to zero in all conditions. Furthermore, PSA+FF and PSA+ISM strategies yield to a faster steering intervention, with respect PSA strategy, during the initial and final part of obstacle avoidance maneuver thus improving the safety margin.

An important aspect that can be further analyzed is the passenger comfort during the obstacle overtaking maneuver. In particular the same close-loop path is executed twice at two different vehicle speed (5 and 15 km/h) by activating the PSA logic for steering path tracking control. The most important variables are shown in Fig. 1.41 where an orange point indicates when the starting point is crossing for the second time. From the point of view of lateral deviation, not a large difference is present when the speed increases from 5 to 15 km/h: a slight reduction of lateral deviation is perceived at 15 km/h since the PSA control strategy has been design for this specific vehicle speed. An important evidence is the yaw rate and sideslip angle aggressiveness in terms of peak values and frequency content: at 5 km/h the steering intervention is perceived by passengers as a smooth maneuver differently from the second loop at 15 km/h where it

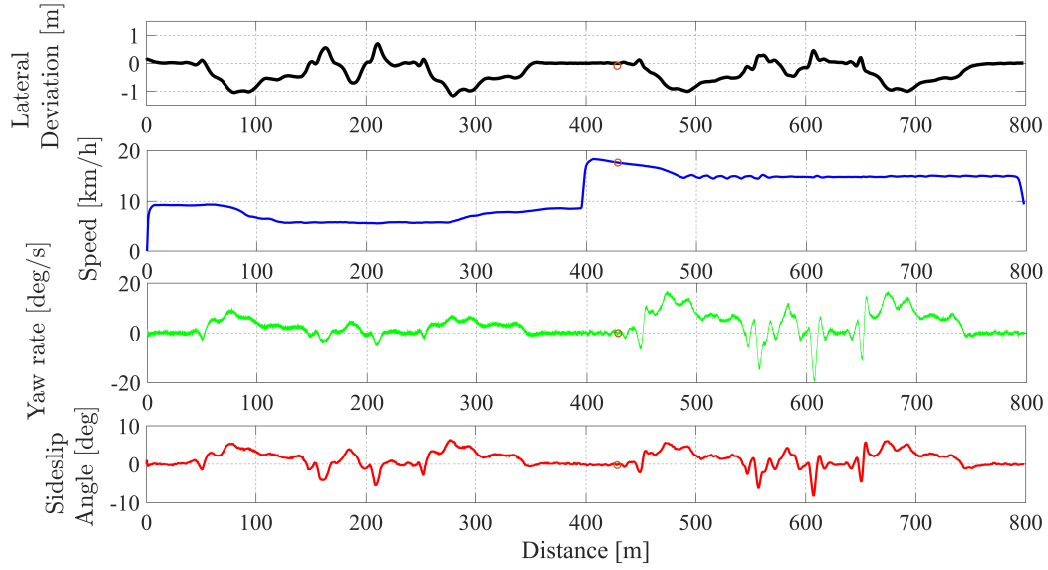


Figure 1.41 Lateral deviation y , vehicle speed V , yaw rate r and sideslip angle β during obstacle collision avoidance maneuver with PSA strategy

seems an aggressive intervention. Furthermore, the sideslip angle (and its derivative) reaches high values during the obstacle avoidance part of the second loop at 15 km/h thus representing a weak point from the safety point of view. Finally, the primary task of path tracking controller is to keep the lateral deviation as close as possible to zero (performance achievement) without any concern to the comfort or safety part of it. The importance of having a yaw rate or sideslip angle control will be discussed in the next chapter where the tradeoff between performance and safety is designed and obtained.

1.6 Conclusions

The present chapter describes some solutions about autonomous steering design and implementations on a prototypical vehicle properly converted into a self-driving car. A linear single-track model is used for lateral deviation dynamics and it is extended for introducing the steering actuation influence. The model is experimentally validated through specific maneuvers on a professional proving ground. The reference path, assumed known, is approximated by a digital map in order to reduce the size of stored data during steering controller activation. Moreover, a PD logic for path tracking is designed based on the PSA approach applied to the single-track model and steering dynamics. The control strategy is enhanced with a FF term and an innovative ISM contribution in order to reduce the reference curvature effect on lateral deviation regulation during cornering maneuvers. A solution is presented for modifying the reference path

when an obstacle is detected by adopting the elastic band theory. Finally, the path tracking and the obstacle collision avoidance controls are implemented on the vehicle demonstrator and are tested during close-loop maneuvers to verify their efficacy and to compare PSA, PSA+FF and PSA+ISM strategies. In conclusion, ideas presented in this chapter represent a perfect integration between known technologies and new innovative methodologies also providing an easy solution for converting a conventional vehicle into an autonomous car that can be enhanced by future investigations especially in the obstacle detection/recognition field. Moreover, the steering control designed for tracking a reference path could imply to undesirable behavior from the point of view of comfort and/or safety. A possible solution to this topic will be illustrated in the following chapter.

Chapter 2

Torque Vectoring Control for Fully-Electric Vehicles

2.1 Introduction on Torque Vectoring Theory

During last years, there has been an increasing attention to alternative energy sources for automotive propulsion systems. A particular interest has been headed to fully-electric vehicles (FEV) due to their *zero emissions* mobility solution and for their advantages in energy storage and electric motor with high power density [74]. From the point of view of vehicle dynamics, the control of longitudinal and lateral behavior is enhanced by the possibility of controlling directly the torque applied to each wheel thus modifying the vehicle steady-state and transient attitudes.

In this wide contest, torque vectoring control (TV) has been studied and developed with the aim of modifying the vehicle lateral dynamics by generating a yaw moment through the redistribution of individual electric motors torques. Several TV architectures for FEV have been studied and developed for both industrial and research purposes (i.e. the adoption of an active or semi-active *torque vectoring differentials* [75, 76]) but the most flexible solution is the one with individual wheel electric motors: if a single or double speed gearbox is placed between the electric motor and the wheel, the configuration is commonly define as *on-board motors* architecture; if the motors are mounted directly inside the wheels, it is referred as *in-wheel motors* configuration which further increases the driveline packaging effect with respect to conventional one. An example of Torque Vectoring application for a 4WD FEV with individual on-board electric motors is shown in Fig. 2.1 where the same torque Δ_T is removed from the left side and added to the right one.

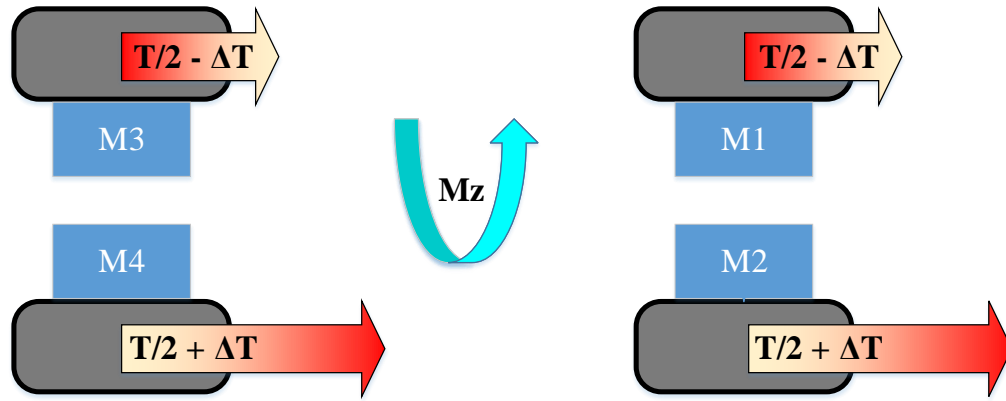


Figure 2.1 General scheme of Torque Vectoring application for a 4WD FEV with individual on-board electric motors

The classic electronic stability control (ESC, [9]), which creates a vehicle yaw moment with individual brake torque distribution, can be seen as a TV logic designed for stability control system with the drawback of generating only braking actions thus leading to vehicle speed reduction; an important advantage of TV through individual electric motors is the generation of a yaw moment without compromising the desired vehicle speed (in Fig. 2.1 the total wheel torque is not influenced by Δ_T) since it can deal with both braking and driving torques. In this respect, [77] compares the transient response of the same direct yaw moment controller actuated through the electric drivetrains and the friction brakes, and shows that significantly increased yaw damping is achieved by the continuous, precise and fast modulation of the electric motor torques. This was experimentally demonstrated in extreme transient conditions on a vehicle demonstrator with on-board electric drivetrains.

The performance improvement due to the development of a TV methodology can be split into the steady state and the transient behavior analysis.

Steady-State behavior analysis One important advantage of TV control is the active modification of the vehicle *understeer characteristic* without any mechanical chassis manipulation but just selecting the desired dynamics mode through the software. [78] defines several driving modes, selectable by the driver, each of them corresponding to a different set of understeer characteristics, thus providing a systematic approach to the specification of the objectives of torque-vectoring control (which is essential according to [79]). The understeer characteristic expresses the relation between the wheel steering correction with respect the kinematic angle $\delta_{\omega, dyn} = \delta_{\omega} - \delta_{\omega, Kin}$ and the

lateral acceleration a_y as shown in Fig. 2.2; this is conventionally identified by three parameters: the understeer gradient K_{US} corresponding to the slope of the characteristic in the linear region ($a_y = 0 - 0.4 g$), the max value of the lateral acceleration in the linear part $a_{y,lin}$ and its asymptotic value $a_{y,max}$. The TV strategy is able to increase the vehicle

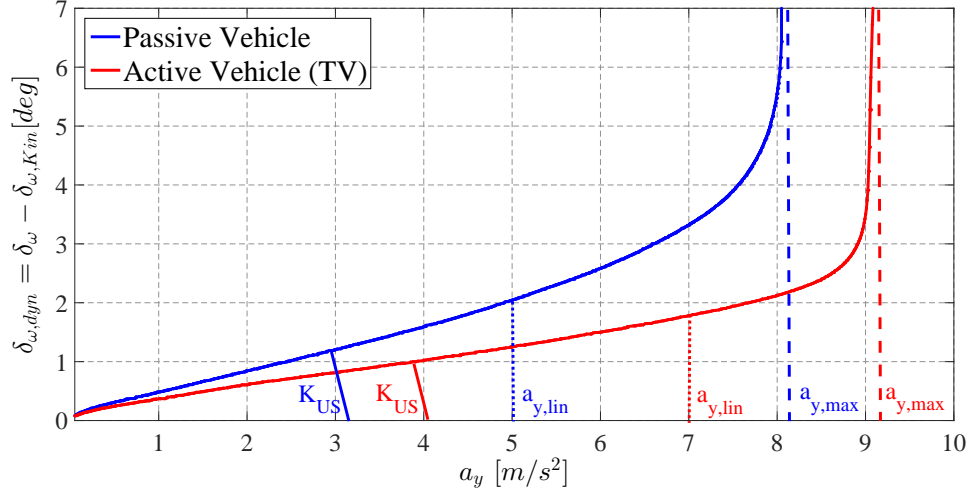


Figure 2.2 Understeer characteristic modification through TV control application

sportive asset by reducing the understeer gradient K_{US} , by extending the linear region and increasing the max value $a_{y,max}$.

Furthermore, the understeer characteristic is also influenced by the longitudinal acceleration a_x as highlighted in [80] where it is shown that a longitudinal acceleration reduces the linear region by also increasing the understeering behavior meanwhile a braking action provokes an oversteer asset. The variation of the cornering behavior for acceleration or braking conditions is drastically reduced through different TV strategies applied to a four-wheel-drive (4WD) vehicle in [2] where an optimal wheel torque distribution is developed to minimize several objective functions. One result achieved by [2] is shown in Fig. 2.3 where an optimal yaw moment calculation is adopted for a TV strategy applied to a 4WD FEV with two on-board motors (one for each axle) and two torque vectoring differentials.

Transient behavior analysis The TV strategy entails also important advantages in terms of transient response. The authors of [81] have developed an analysis procedure called *β -Method* which shows the influence of the sideslip angle on the stabilizing yaw moment $M_{z,Fy}$ (by means the yaw moment generated by tires lateral forces and self-alignment moments) that is representative for all transient conditions: the yaw moment M_z can be proportionally regulated by the steering angle only for low values of sideslip

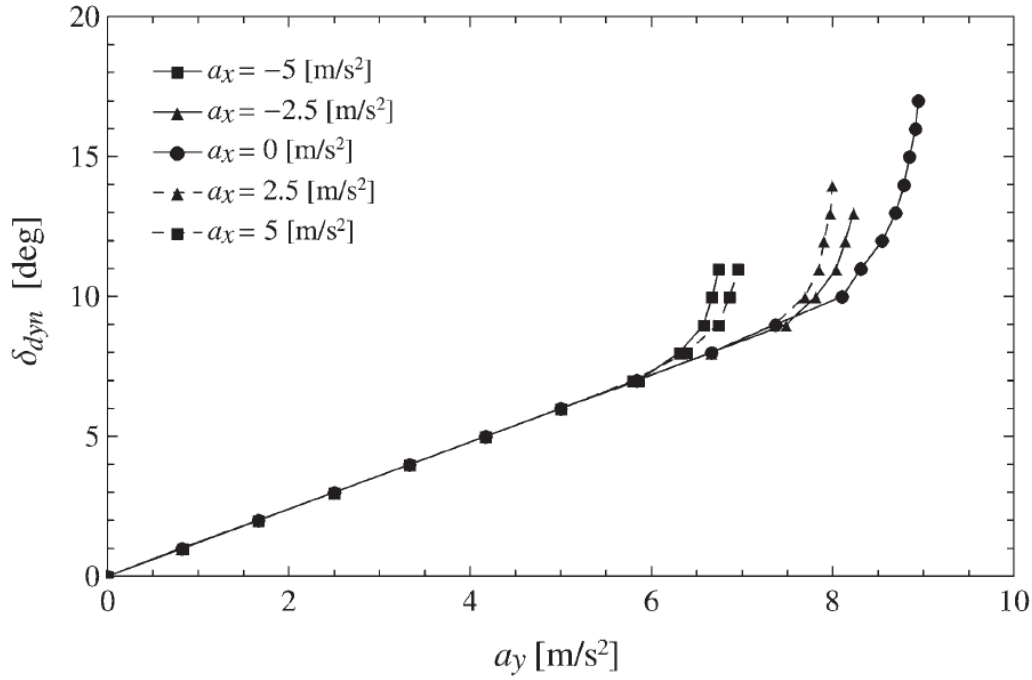


Figure 2.3 Understeer characteristic for the vehicle with TV at $V = 90 \text{ km/h}$ and values of a_x ranging from -5 to 5 in step of 2.5 m/s^2 (adapted from [2])

angle meanwhile this relation is drastically compromised for high values of β thus reducing the driver ability to control the vehicle in emergency situations. The TV strategy can be designed to generate an additional yaw moment $M_{z,Fx}$ due to the modification of longitudinal tire forces through the torque control of individual electric motors. It is proved in [82] that the overall yaw moment $M_z = M_{z,Fy} + M_{z,Fx}$, generated at high values of sideslip angle, is enlarged by a rear-wheel TV control which is also able to drastically reduce the lateral dynamics modification induced by a longitudinal acceleration or by a braking intervention. In order to better appreciate the TV intervention, an aggressive step steer of 100 deg at 100 km/h is simulated for a FEV equipped with four individual on-board electric motors and results are reported in Fig. 2.4 The aggressive maneuver, which is executed at constant wheel torque, shows that the TV strategy is able to control the total yaw moment applied to the vehicle by introducing a $M_{z,Fx}$ term able to increase the vehicle response reaction and to damp the yaw rate and sideslip angle oscillations thus providing a safer condition with respect to the passive (without TV) situation. Furthermore, the TV strategy can better exploit tires saturation limits by a proper distribution of forces for generating a target yaw moment: the $M_{z,Fy}$ for the passive vehicle reaches suddenly the saturation limit of lateral forces thus triggering oscillations in yaw rate; the term $M_{z,Fx}$ generated by the TV provides an additional contribution that enhances and improves lateral dynamics thus letting the term $M_{z,Fy}$ gradually tend to its steady-state value.

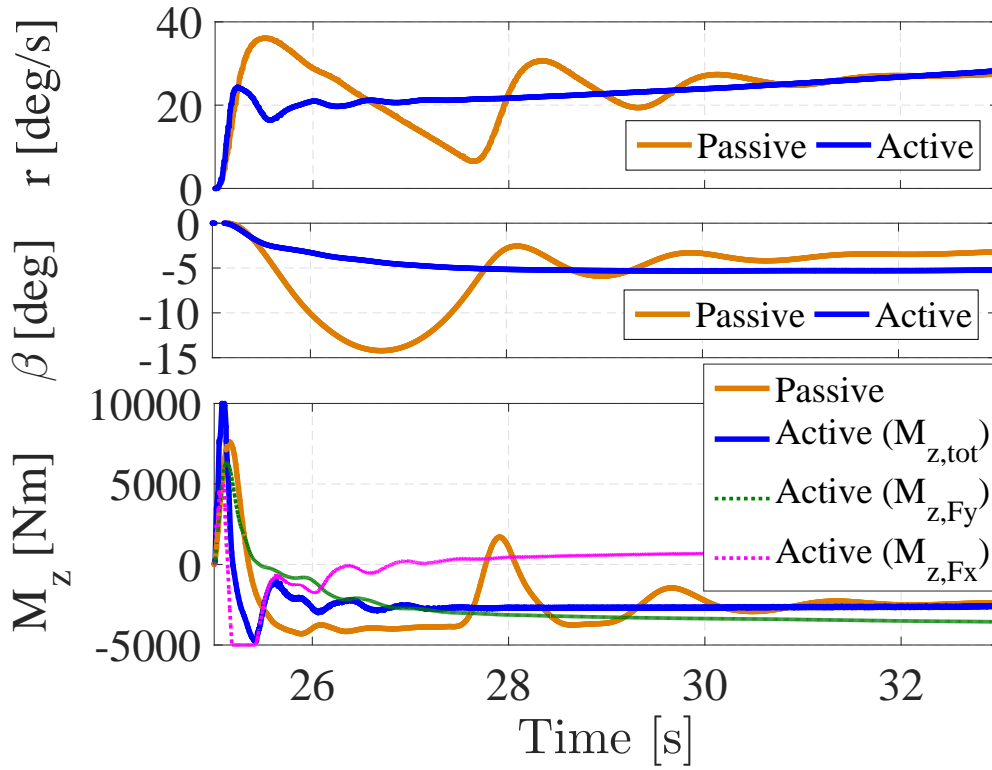


Figure 2.4 Simulation results for a TV application to a FEV with four on-board electric motors: r -yaw rate, β -sideslip angle, M_z -yaw moment

In order to achieve the benefits of torque-vectoring, specific control formulations are required, which are capable of providing continuous and smooth control action in order to shape vehicle cornering response even at low lateral acceleration levels. [83–90, 4, 91–106] include a selection of different controllers potentially applicable to the problem of yaw rate and sideslip control of electric vehicles with multiple motors. The control structures can be based on Proportional Integral Derivative (PID) controllers ([77], [84, 85] and [105]), linear quadratic regulators ([86–89]), sliding mode controllers [90, 4, 91–95], H_∞ controllers [96, 97], linear parameter varying controllers [98], robust controllers [99] and model predictive controllers [100, 101], with the possibility of including fuzzy components [87] or adaptive schemes [102]. Linear or non-linear feedforward contributions can also be included in the control structure ([77], [88]) to reduce the interventions of the feedback component, thus allowing reduced sensitivity with respect to measurement errors, noise and disturbances, and better drivability. Importantly, only a few studies [103, 104] assess the performance of controllers with varying levels of complexity through vehicle simulations.

The objectives of the study presented in following chapters are:

- formulation of an Integral Sliding Mode Control (ISMC) algorithm, based on the known ISMC theory [72], for the concurrent control of yaw rate and sideslip angle on electric vehicles with multiple motors
- demonstration, based on simulations, that a feedback multivariable direct yaw moment controller based on yaw rate and sideslip angle, with the sideslip contribution activated only for constraining sideslip angle at the cornering limit, allows safe vehicle operation even in absence of any form of tire-road friction coefficient estimation
- experimental demonstration of the performance benefit of the ISMC compared to a controller based on LQR with and without a non-linear feedforward contribution
- experimental testing of a new driving mode, i.e., the Enhanced Sport mode, purposely inducing high values of sideslip angle for increasing the 'fun-to-drive', and then constraining sideslip angle at the desired threshold

The chapter consists of 7 sections by including the previous introduction: the second section deals with the experimental setup of the FEV demonstrator followed by the description of TV controller design in the third section; simulation results of the proposed controller are shown in fourth section meanwhile its experimental validation is reported in the fifth section; furthermore, the sixth section introduces a sideslip angle estimation analysis for future implementations; finally, some conclusions are drawn in the last section.

2.2 Experimental Setup of the FEV demonstrator

The TV control strategy designed in this chapter is related to a research activity that involves a FEV vehicle demonstrator within the framework of the European FP7 project iCOMPOSE whose main task is the enchantment of systems integration for electric vehicle. The general scheme of the vehicle demonstrator is shown in Fig. 2.5 where a four-wheel-drive (4WD) with individual on-board electric motors architecture is adopted in order to have the best torque control configuration as it is proved in [107]. The on-board electric drivetrain consists of a single-speed double-stage transmission, half-shafts and constant velocity joints that connects electric motors M_i with their correspondent inverters I_i to the wheels. An electro-hydraulic braking system is added for an individual control of friction brake pressures independent of the brake pedal force applied by the driver. The TV control logic is deployed on a dSPACE® Autobox system as indicated by the vehicle control unit (VCU) which also receives as input the data coming from a

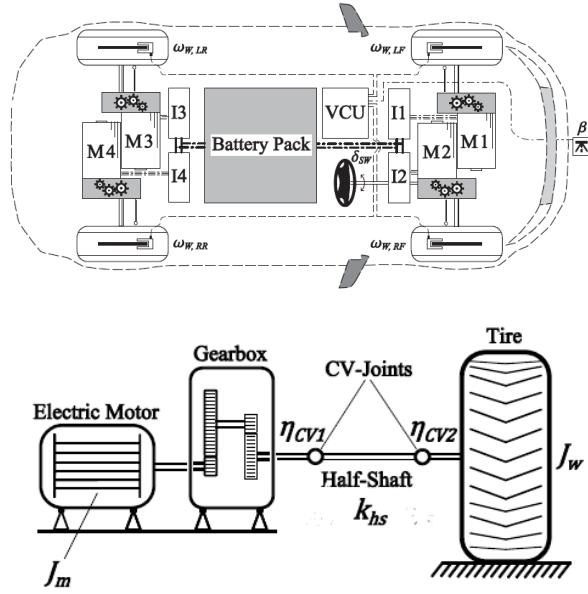


Figure 2.5 General scheme of the vehicle demonstrator experimental setup with its electric drivelines (adapted from [3, 4])

sideslip angle and vehicle speed sensor, from an Inertial Measurement Unit (IMU) and from wheel speed encoders (see Table 2.1). All experimental tests are executed in the

Table 2.1 Main I/O signals for TV controller in the dSPACE® AutoBox system with their discretization times and their availability on vehicle CAN network (Yes:present, No:absent)

Symbol	Signal	Discretization time [ms]	CAN bus	I/O
δ	Steering wheel angle	10	Yes	I
r	Yaw rate	10	No	I
a_x	Longitudinal acceleration	10	No	I
a_y	Lateral acceleration	10	No	I
$\omega_{W,i}$	Wheel speed	2	Yes	I
$T_{M,MAX,i}$	Maximum motor torque	10	Yes	I
$T_{M,dem,i}$	Motor torque demand	2	Yes	O
$p_{b,dem,i}$	Brake pressure demand	2	Yes	O
u	Longitudinal vehicle speed	2	No	I
v	Lateral vehicle speed	2	No	I
β	Vehicle sideslip angle	2	No	I

professional proving ground of Lommel (BE) within the flat surface of Vehicle Dynamics Area (VDA) as shown in Fig. 2.6.

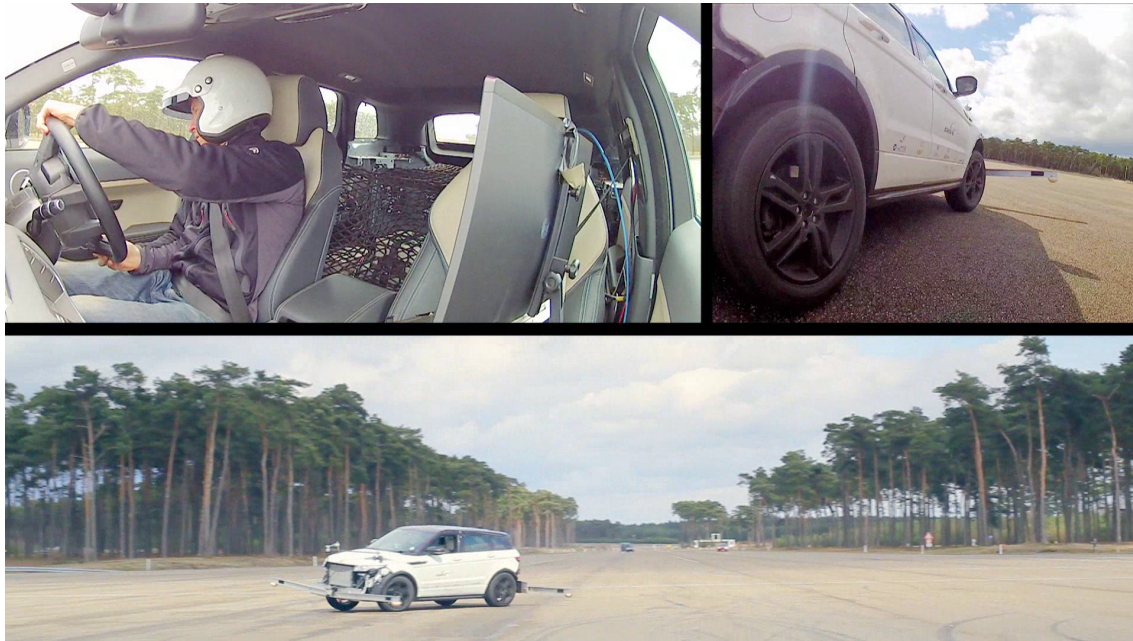


Figure 2.6 Vehicle Dynamics Area (VDA) of Lommel (BE) proving ground with the vehicle demonstrator

2.3 Control System Design

The steady-state and transient cornering responses with a TV strategy can be designed based on high-level reference targets, and implemented through the continuous torque control of individual wheels. This section presents a controller for concurrent yaw rate and sideslip control to enhance vehicle responsiveness and safety. The controller permits the selection of different driving modes, each of them corresponding to a set of reference understeer characteristics. A new driving mode, the Enhanced Sport mode, is proposed, inducing high values of sideslip angle, which can be safely limited to a specified threshold set within the controller. For vehicles without active steering or four-wheel-steering capability, three main control concepts are proposed in the literature: i) yaw rate control; ii) continuous yaw rate and sideslip angle control; and iii) continuous yaw rate control with sideslip angle used as a constraint only in emergency conditions. In this respect, [98] states that "lateral velocity or sideslip angle are not considered as controlled outputs because it is not possible to control the yaw rate and the sideslip angle independently, using only the yaw moment. Trying to control both properties leads to a functionally uncontrollable system with uncontrollable directions. Controlling the lateral velocity (or the sideslip angle) and the yaw rate is possible only by including an additional device like an active steering system." This analysis is in accordance with the definition of functional controllability provided in [108], based on the singular value decomposition of the plant model (see [3] for the details): "An m -input l -output

system $G(s)$ is functionally controllable if the normal rank of $G(s)$, denoted r , is equal to the number of outputs, l , that is, if $G(s)$ has full row rank. A system is functionally uncontrollable if $r < l$. From a physical viewpoint, the functional uncontrollability of the specific system of this study is caused by the fact that the number of inputs (i.e., the yaw moment) is smaller than the number of outputs (i.e., yaw rate and sideslip angle). Even many of the papers including a sideslip term in their continuous yaw moment controller formulation are not clear regarding the actual benefit of the corresponding contribution. These elements would suggest the selection of control concept i). On the other hand, yaw rate control alone can be a risky option, as it could lead to vehicle instability in the case of incorrect or delayed tire-road friction coefficient estimation. Hence, in this paper control concept iii) is chosen. As sideslip estimation is simpler and faster than tire-road friction estimation [109, 110], a control structure is proposed for continuous yaw rate control, capable of constraining sideslip angle when specified threshold values are reached. Integral sliding mode control (ISM) as a perturbation estimator is selected for its ease of implementation, computational efficiency (e.g., with respect to model predictive control), tunability (i.e., each control parameter provokes a predictable effect and can be modified during a vehicle testing session without significant off-line calculations), robustness (i.e., compensation of matched disturbances), lack of chattering (in comparison with first order sliding mode), and the fact that it represents a disturbance observer added to a more conventional and known controller.

2.3.1 Control structure

Fig. 2.7 shows the simplified schematic of the vehicle control structure, consisting of:

- a set of state estimators, mainly providing the values of vehicle speed, V , sideslip angle, β , and tire-road friction coefficient, μ (more details are provided in [77]). The friction estimation is based on the computation of the acceleration vector at the center of gravity. The filtered value of the ratio between the vehicle inertial force and the vertical load provides the instantaneous estimation of the average tire-road friction coefficient. This is used as estimated value of the tire-road friction capability only when the sideslip angle exceeds critical thresholds. For low sideslip angle values, the system is considered to operate in constant high tire-road friction conditions. This means that the proposed friction estimator is effective only at the cornering limit, similarly to the typical friction estimation algorithms of conventional stability control systems based on the actuation of the friction brakes. Useful references on the subject of friction estimation are [109, 110]. The estimation of additional yet important variables, such as the road angles and

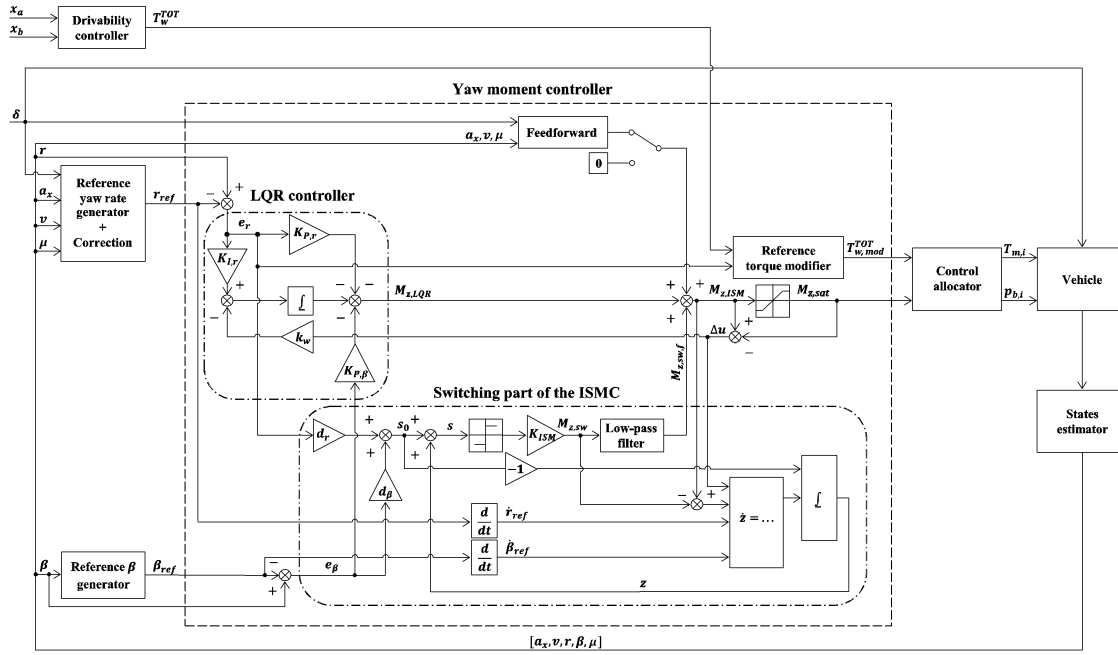


Figure 2.7 Simplified schematic of the vehicle control structure

actual vehicle mass, is not considered in this study, which is focused on the proof of concept of the multi-variable integral sliding mode control formulation. The detailed aspects of state estimation will have to be further analyzed during the industrial implementation of the algorithm, at a higher technology readiness level.

- a high-level controller, generating the reference values of yaw rate and sideslip angle, respectively r_{ref} and β_{ref} , based on steering wheel angle, δ , vehicle speed, V , vehicle longitudinal acceleration, a_x , and μ
- a drivability controller, generating the overall reference wheel torque, T_w^{TOT} , for traction and braking conditions, mainly based on accelerator and brake pedal positions (respectively x_a and x_b) and V
- a yaw moment controller, generating the reference yaw moment, $M_{z,sat}$, in order to continuously track r_{ref} , and constrain β at the values specified by the high-level controller. In the case of significant yaw rate or sideslip errors, indicators of safety-critical conditions, this controller also modifies T_w^{TOT} (for example, for reducing V), which becomes $T_{w,mod}^{TOT}$
- a control allocation algorithm that defines the motor torque demands, $T_{m,i}$, and friction brake pressure demands, $p_{b,i}$, for the i -th vehicle corner. Examples of energy-efficient control allocation are described in [111, 112]

With respect to Fig. 2.7, the novel contribution of this research activity is focused on the gain-scheduled Linear Quadratic Regulator (LQR) and Integral Sliding Mode (ISM) controller design for the yaw moment controller. Details will also be provided regarding the generation of the reference yaw rate and sideslip angle, with special focus on the implementation of the Enhanced Sport Mode. Finally, some indications for the state estimator design will be proposed for future implementations.

2.3.2 Yaw rate and Sideslip references

Continuous TV control enables to reach a desired vehicle behavior through different software-enabled driving modes that can be selected by the driver. For instance, the understeer characteristic of a generic vehicle can be modified to improve the 'fun-to-drive' asset or to increase the overall efficiency.

Reference Yaw Rate

The steady-state value of r_{ref} is generated in order to achieve a reference set of understeer characteristics. The same vehicle includes multiple driving modes selectable by the driver, each of them corresponding to different understeer characteristics:

- *Normal Mode*: understeer gradient K_{US} similar to the passive vehicle, slightly extended linear region (greater $a_{y,lin}$) and the same value of maximum lateral acceleration $a_{y,max}$
- *Sport Mode*: considerably reduced understeer gradient K_{US} with respect to passive vehicle, extended linear region (greater $a_{y,lin}$) and increased value of maximum lateral acceleration $a_{y,max}$ consistent with the available tire-road friction coefficient
- *Enhanced Sport Mode*: the reference understeer characteristic in the linear region is the same designed for the sport mode, but the value of $a_{y,max}$ is purposely increased in order to induce high values of sideslip angle thus increasing the fun-to-drive vehicle asset

The three understeer characteristics selected for the TV strategy here designed are shown in Fig. 2.8 where an understeer gradient of $0.5 \text{ deg s}^2/\text{m}$ is chosen for the sport and enhanced sport modes. In order to mathematically handle the desired understeer

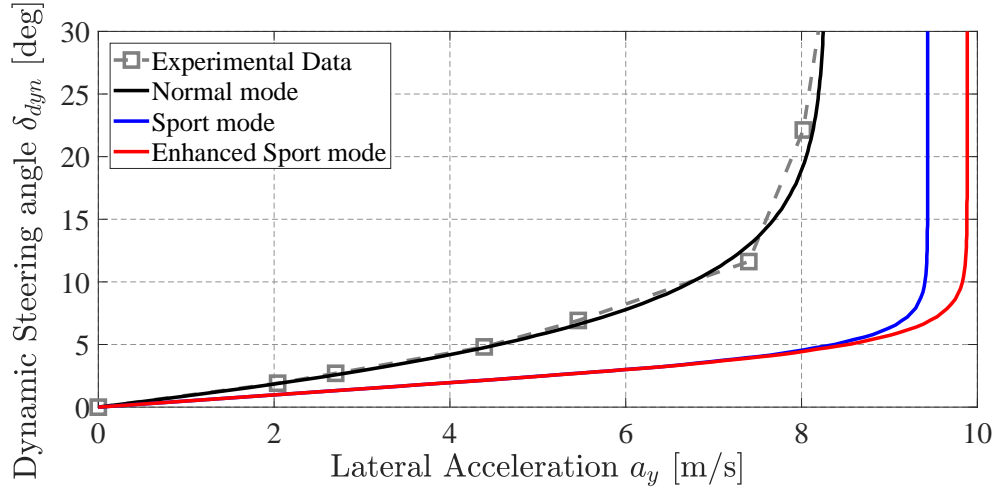


Figure 2.8 Definition of Normal mode, Sport mode and Enhanced Sport mode understeer characteristics versus passive vehicle experimental data for $a_x = 0$ and high friction condition

characteristics, an analytical expression is required as function of K_{US} , $a_{y,lin}$ and $a_{y,max}$:

$$a_y = \begin{cases} \frac{1}{K_{US}} \delta_{dyn} & \text{if } \delta_{dyn} < a_{y,lin} K_{US} \\ a_{y,max} + (a_{y,lin} - a_{y,max}) e^{\frac{a_{y,lin} K_{US} - \delta_{dyn}}{(a_{y,max} - a_{y,lin}) K_{US}}} & \text{if } \delta_{dyn} \geq a_{y,lin} K_{US} \end{cases} \quad (2.1)$$

where δ_{dyn} is the dynamic steering angle equal to the difference between current steering angle δ and the kinematic steering angle δ_{kin} which is connected, through the steering column kinematics, to the kinematic steering wheel angle $\delta_{\omega,kin} = L/R$ being L the vehicle wheel-base and R the trajectory radius of its center of gravity. A part from K_{US} that can be chosen based on TV design requirements, the values of $a_{y,lin}$ and $a_{y,max}$ have to be selected by taking into account the tires saturation limits since they are heavily influenced by the longitudinal acceleration a_x , vehicle speed V and by the available tire-road friction coefficient μ . An offline optimization procedure can be carried out to evaluate the maps $a_{y,lin}(a_x, V, \mu)$ and $a_{y,max}(a_x, V, \mu)$ by adopting the so called *quasi-static* model [113] to purposely reduce the computational cost. The quasi-static principle is applied to an eight-degree-of-freedom (longitudinal, lateral, yaw, roll motions together with the four tires rotations) model and it is based on the following hypothesis:

$$\begin{cases} \dot{\beta} = 0 \\ \dot{r} = 0 \\ \dot{\phi} = 0 \end{cases} \quad (2.2)$$

where β is the sideslip angle, r is the yaw rate and ϕ the roll angle. Assuming a flat surface, the body dynamics is described by the longitudinal and lateral forces balance

equations:

$$\begin{aligned} \sum_{i=1}^4 F_{x_i} \cos \delta_{\omega_i} + \sum_{i=1}^4 F_{y_i} \sin \delta_{\omega_i} - F_{drag} &= m(\dot{u} - rV\beta) \\ \sum_{i=1}^4 F_{x_i} \sin \delta_{\omega_i} + \sum_{i=1}^4 F_{y_i} \cos \delta_{\omega_i} &= m(\dot{V}\beta + ur) \end{aligned} \quad (2.3)$$

the yaw moment balance equation:

$$\begin{aligned} \sum_{i=1}^4 F_{x_i} \cos \delta_{\omega_i} y_i + \sum_{i=1}^4 F_{x_i} \sin \delta_{\omega_i} x_i + \\ + \sum_{i=1}^4 F_{y_i} \cos \delta_{\omega_i} x_i + \sum_{i=1}^4 F_{y_i} \sin \delta_{\omega_i} y_i + \sum_{i=1}^4 M_{z_i} &= 0 \end{aligned} \quad (2.4)$$

and the roll moment balance equation

$$\begin{aligned} m(\dot{V}\beta + ur)(h_{CG} - d_{CG}) \cos \phi + mg(h_{CG} - d_{CG}) \sin \phi + \\ - \left(\sum_{i=1}^2 F_{x_{iF}} \sin \delta_{\omega_{iF}} + \sum_{i=1}^2 F_{y_{iF}} \cos \delta_{\omega_{iF}} \right) (d_F - d_{CG}) + \\ - \left(\sum_{i=1}^2 F_{x_{iR}} \sin \delta_{\omega_{iR}} + \sum_{i=1}^2 F_{y_{iR}} \cos \delta_{\omega_{iR}} \right) (d_R - d_{CG}) = \\ = M_{\phi F} + M_{\phi R} \end{aligned} \quad (2.5)$$

where u is the longitudinal component of vehicle speed V , m its mass, F_{x_i} and F_{y_i} respectively the longitudinal and lateral component of i -th tire force, F_{drag} the aerodynamic drag force, δ_{ω_i} the steering angle of i -th wheel, M_{z_i} the self-aligning of i -th wheel, x_i and y_i respectively the front/rear wheelbase and the front/rear track width, h_{CG} is the vehicle center of gravity height, d_{CG} , d_F and d_R are the height of the roll axis measured respectively at vehicle center of gravity, front and rear axle. The front and rear anti-roll moments $M_{\phi F}$, $M_{\phi R}$ are implemented as look-up tables by taking into account only the stiffness contribution since the roll rate is set to zero for the quasi-static approach ($\dot{\phi} = 0$). Tire forces F_{x_i} , F_{y_i} and the self-aligning moment M_{z_i} are expressed through the Pacejka '96 formulation as a function of slip ratio $\sigma_i = f_{\sigma}(V, \omega_i, \delta_{\omega_i}, r)$, slip angle $\alpha_i = f_{\alpha}(\beta, \delta_{\omega_i}, r)$, camber angle γ_i , tire-road friction coefficient μ and vertical forces F_{z_i} :

$$\begin{aligned} F_{z_i} &= F_{z_{0i}} + \epsilon_1 [F_{drag} + m(\dot{u} - rV\beta)] \frac{h_{CG}}{2L} \\ &+ \epsilon_2 \frac{\sum_{j=1}^2 F_{x_{jF/R}} \sin \delta_{\omega_{jF/R}} + \sum_{j=1}^2 F_{y_{jF/R}} \cos \delta_{\omega_{jF/R}}}{\sum_{j=1}^2 |y_{jF/R}|} d_{F/R} \\ &+ \epsilon_2 \frac{M_{\phi F/R}}{\sum_{j=1}^2 |y_{jF/R}|} \end{aligned} \quad (2.6)$$

where \sum_j refers to the two wheels of the same axle, $F_{z_{0i}}$ is the static vertical load on i -th wheel, L the vehicle wheel-base, $\epsilon_1 = \pm 1$ depending on the axle, and $\epsilon_2 = \pm 1$ depending on which vehicle side (left or right) is inside the curve. The camber angle γ_i is expressed as a non-linear look-up table of roll angle ϕ . The wheels moment balance equations are formulated by considering individual wheel drivetrains with on-board electric motor, two stage single speed transmission and half-shaft with constant-velocity joints:

$$\begin{cases} T_i - T_{Bi} - F_{x_i} R_i - F_{z_i} R_i \left(f_0 + f_1 \omega_i R_{roll_i} + f_2 \omega_i^2 R_{roll_i}^2 \right) - J_{W_i} \dot{\omega}_i = 0 \\ \dot{\omega}_i = \frac{d}{dt} \left[\frac{V_{xi}}{R_{roll_i}} (\sigma_i + 1) \right] = \frac{a_{xi}}{R_{roll_i}} (\sigma_i + 1) + \frac{V_{xi}}{R_{roll_i}} \dot{\sigma}_i \end{cases} \quad (2.7)$$

where T_i and T_{Bi} are respectively the electric wheel torque and the friction brake torque, R_i and R_{roll_i} are the laden and rolling radius respectively of the tire and J_{W_i} is the inertia of the wheel. f_0 , f_1 and f_2 represents the rolling resistance coefficients and ω_i is the wheel angular speed. $\dot{\sigma}_i$ can be neglected due to the quasi-static approach.

The quasi-static model is validated against a more detailed vehicle model that is built in the vehicle dynamics simulation software IPG CarMaker and through specific experimental tests obtained with the FEV vehicle demonstrator described in section 2.2. Some validation proof of the quasi-static model are reported in [77, 78, 2] showing a good match with experimental and IPG results thus confirming its adoption as predictive tool for a FEV handling response.

The maps $a_{y,lin}(a_x, V, \mu)$ and $a_{y,max}(a_x, V, \mu)$ are obtained by solving an optimization problem where a suitable objective function has to be maximized in presence of the equations of quasi-static model (equality constraints) and physical constraints (inequality constraints) in terms of maximum electric motor torque $T_{m_i,MAX}$ and speed $\omega_{m_i,MAX}$, friction brake torque $T_{Bi,MAX}$ and peak power of the battery pack $P_{Batt,MAX}$:

$$\begin{cases} T_{m_i} = \frac{T_i}{\tau_1 \tau_2 \eta_1 \eta_2 \eta_{CV1} \eta_{CV2}} + J_{eq} \dot{\omega}_{m_i} < T_{m_i,MAX}(\omega_{m_i}) \\ T_{Bi} < T_{Bi,MAX} \\ \omega_{m_i} = \omega_i \tau_1 \tau_2 < \omega_{m_i,MAX} \\ \sum_{i=1}^4 T_{m_i} \omega_{m_i} < P_{Batt,MAX} \end{cases} \quad (2.8)$$

where T_{m_i} and ω_{m_i} are respectively the electric motor torque and angular speed, τ_1 and τ_2 the gear ratio of each stage of the transmission, η_1 and η_2 their correspondent efficiencies, η_{CV1} and η_{CV2} are the efficiencies of the constant-velocity joints and J_{eq} the equivalent inertia of electric drivetrain:

$$J_{eq} = J_m + J_1 + \frac{J_2}{\tau_1^2 \eta_1} + \frac{J_3}{\tau_1^2 \tau_2^2 \eta_1 \eta_2} + \frac{J_{HS}}{\tau_1^2 \tau_2^2 \eta_1 \eta_2 \eta_{CV1} \eta_{CV2}} \quad (2.9)$$

where J_m is the electric motor inertia, J_1 , J_2 and J_3 are the inertia of the primary, the secondary and the output shafts and J_{HS} is the inertia of the half-shaft.

In particular for the selection of $a_{y,lin}(a_x, V, \mu)$ and $a_{y,max}(a_x, V, \mu)$ the following objective function must be maximized:

$$J = \sum_{i=1}^4 F_{x_i} \sin \delta_{\omega_i} + \sum_{i=1}^4 F_{y_i} \cos \delta_{\omega_i} \quad (2.10)$$

with the additional equality constraint only for the calculation of $a_{y,lin}(a_x, V, \mu)$ in order to consider only the linear region:

$$a_y = \frac{1}{K_{US}} \delta_{dyn} \quad (2.11)$$

An example of the maximum values of $a_{y,lin}$ and $a_{y,max}$ for a high friction coefficient and for a vehicle speed $V = 100$ km/h is reported in Fig. 2.9 as a function of longitudinal acceleration a_x . Once the desired understeer characteristic expressed by Eq. 2.1 is

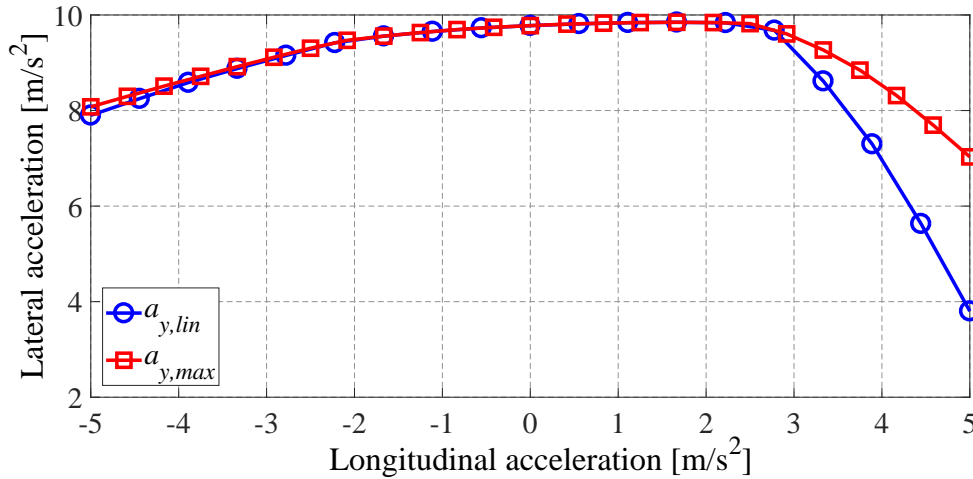


Figure 2.9 $a_{y,lin}$ and $a_{y,max}$ maximum values that can be selected for the desired understeer characteristic for high friction condition and $V = 100$ km/h

designed, the reference yaw rate r_{ref} can be calculated by the following procedure:

- for a specific value of a_y and V : $r_{ref} = a_y/V$ (steady-state hypothesis of $\dot{\beta} = 0$)
- for the same value of a_y , the dynamics steering angle can be determined by Eq. 2.1
 $\delta_{dyn} = \delta_{dyn}(a_y, a_x, \mu)$
- the kinematic steering angle δ_{Kin} is evaluated through the non-linear relationship ρ of the steering column kinematics: $\delta_{Kin} = \rho(\delta_{\omega, Kin}) = \rho(Lr_{ref}/V)$

- the final steering angle corresponding to the selected value of a_y and V is calculated as follow:

$$\delta(a_y, V, a_x, \mu) = \delta_{dyn}(a_y, a_x, \mu) + \delta_{Kin} = \delta_{dyn}(r_{ref} V, a_x, \mu) + \rho(Lr_{ref}/V) \quad (2.12)$$

Finally, the reference yaw rate map $r_{LUT} = r_{LUT}(\delta, V, a_x, \mu)$ is used as input for the yaw moment controller as indicated in Fig. 2.7. An example of the reference yaw rate map for a high friction coefficient and $a_x = 0$ is shown in Fig. 2.10 at different vehicle speed V in sport mode and enhanced sport mode.

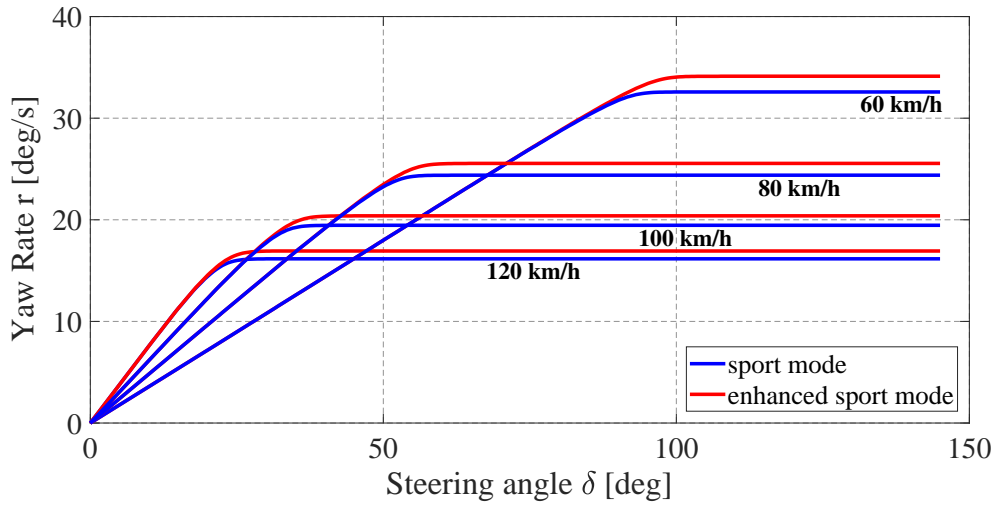


Figure 2.10 reference yaw rate map $r_{LUT}(\delta, V, a_x, \mu)$ for a high friction coefficient and $a_x = 0$ at different vehicle speed V in sport mode and enhanced sport mode

Reference Sideslip Angle

The reference sideslip angle, β_{ref} , is obtained by filtering $\beta_{ref,steady-state}$ defined as follows:

$$\begin{cases} \beta_{ref,steady-state} = \beta & \text{if } |\beta| < \beta_{th} \\ \beta_{ref,steady-state} = \beta_{th} & \text{if } |\beta| \geq \beta_{th} \end{cases} \quad (2.13)$$

Based on Eq. 2.13, the sideslip angle contribution is always aimed at reducing $|\beta|$. In fact, when $|\beta| < \beta_{th}$, i.e., in normal driving conditions, the reference sideslip angle is coincident with the estimated sideslip angle, and only the yaw rate controller is active, while the sideslip-related yaw moment contribution is zero. In extreme maneuvering, when $|\beta| \geq \beta_{th}$, $\beta_{ref,steady-state} - \beta$ becomes non-zero, thus activating the sideslip controller. The threshold β_{th} needs to be carefully selected, for example by using the phase-plane-based criteria proposed in [104, 3], which include consideration of the

estimated sideslip rate. The performance of the sideslip-related contribution depends on the quality of the available sideslip estimation. Based on the literature and their experience (for example, see [77, 109, 110]), a better sideslip estimation (in terms of percentage error with respect to the actual sideslip angle) is achievable in extreme driving conditions, rather than in normal driving conditions. Extreme driving conditions are actually the situations requiring the contribution of the sideslip terms of the proposed controllers.

In general, the sideslip-related yaw moment contribution can interfere with the yaw rate contribution, for example if the sideslip contribution is stabilizing and $|r_{LUT}(t)| \geq |r(t)|$, yielding ineffective control action. In fact, the presence of integral control on the yaw rate error creates a wind-up effect when concurrent yaw rate and sideslip angle control actions are requested. This implies the need for a correction method of the reference yaw rate in order to support sideslip angle control. To this purpose, the reference yaw rate is corrected according to the criteria in Tab. 2.2. In particular, when

Table 2.2 Reference yaw rate correction Δr_{ref}

#	β control active	$ \Delta r_{ref} > \Delta r_{ref,lim}$	Δr_{ref}
1	True	True	$K_{corr} \int \frac{M_{z,\beta}}{J_z} dt + \Delta r_{ref,initial}$
2	True	False	$K_{corr} \int \frac{M_{z,\beta}}{J_z} dt + \Delta r_{ref,initial}$
3	False	True	$\int -k_{ramp} \text{sign}(\Delta r_{ref}) dt + \Delta r_{ref,initial}$
4	False	False	0

the sideslip controller is active, $|r_{LUT}(t)|$ is varied proportionally to the integral of the sideslip-related yaw moment contribution, $M_{z,\beta}$. In fact, $M_{z,\beta}/J_z$ corresponds to the yaw acceleration caused by the sideslip controller, and its integral is the respective yaw rate variation. Overall, r_{ref} is applied as follows:

$$r_{ref} = (r_{LUT}(\delta, V, a_x, \mu) + \Delta r_{ref}) \frac{\omega_r}{p + \omega_r} \quad (2.14)$$

where the first order filter with corner frequency ω_r (p is the Laplace operator) is used to tune vehicle responsiveness for the different driving modes. The presence of integral actions on yaw rate error in both LQR and ISM controller structures creates a windup effect when a concurrent yaw rate and sideslip angle control is requested. This implies the necessity of design a correction factor for the reference yaw rate in order to better support the sideslip angle control thus providing an anti-windup effect. In order to illustrate the concept, the typical qualitative behavior of the reference yaw rate generator with the sideslip correction is shown in Fig. 2.11 during a step steer test (i.e., a test with a

very fast steering wheel angle application). At the beginning of the maneuver $|\beta(t)|$ is

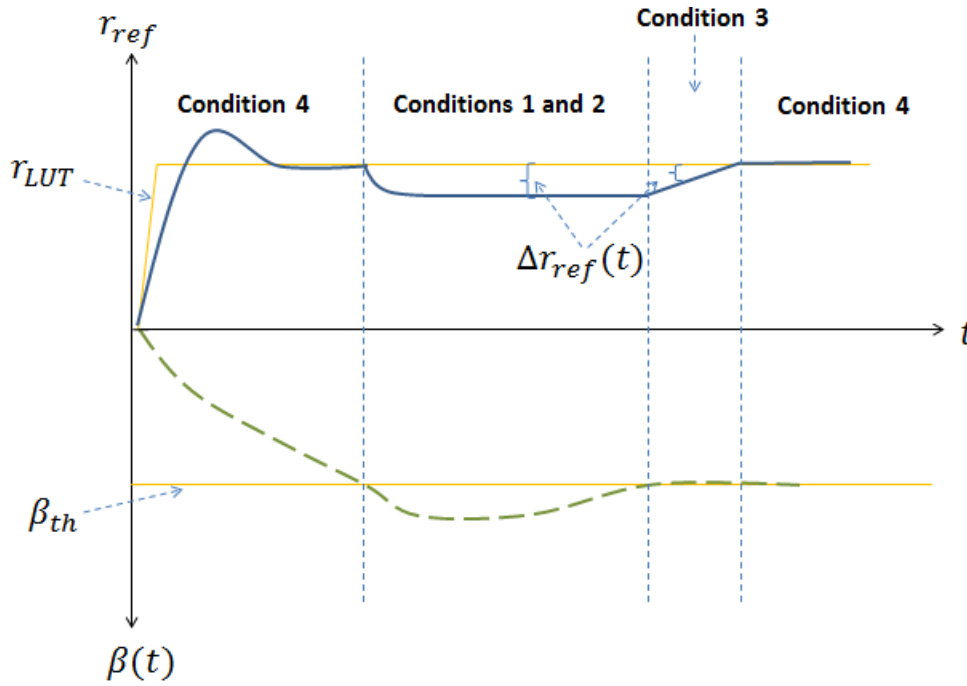


Figure 2.11 Reference yaw rate correction mechanism

smaller than $\beta_{th}(t)$ and the sideslip controller is not active, so no correction is applied (i.e., $\Delta r_{ref}(t) = 0$) according to condition 4. When $|\beta(t)|$ exceeds $\beta_{th}(t)$, the sideslip controller is activated and $\Delta r_{ref}(t)$ is applied based on conditions 1 and 2. When the sideslip controller becomes inactive because $|\beta(t)|$ returns back within acceptable limits, r_{ref} is ramped back to the original value specified by the yaw rate controller, with an initial condition $\Delta r_{ref,initial}$ (see condition 3). This is set not to provoke discontinuities in the reference yaw rate. Thereafter, when $r(t)$ converges to $r_{ref}(t)$ closely enough, no correction is applied any more (condition 4). K_{corr} and k_{ramp} in Tab. 2.2 are used as tuning parameters to obtain the desired response. Also, saturation functions are adopted on in the practical implementation of the algorithm.

2.3.3 Yaw Moment Controller: Linear Quadratic Regulator Design

A linearized single-track vehicle model [67] is used for the design of a linear quadratic regulator (LQR) as yaw moment controller. The model, that is described in section 1.3, is usually adopted to represent cornering response for control system design and it is characterized by the following hypothesis:

1. The vehicle is a rigid body with a single front wheel and a single rear wheel moving on the road plane

2. Vehicle sideslip angle β and tires slip angles α_i are assumed small enough to consider the linear part of vehicle dynamics
3. Longitudinal vehicle speed is assumed constant and only 2 degrees of freedom (yaw rate and sideslip angle) are taken into account
4. Small steering angles are generated exclusively on the front axle

The control problem is formulated into a multivariable control framework, with one input (i.e., the yaw moment) and two outputs (i.e., yaw rate and sideslip angle) of the controlled plant. Kalman's controllability condition is satisfied, i.e., the determinant of the controllability matrix is different from zero, allowing the application of LQR control [114]. The model is represented in state-space form to facilitate the design of the LQR, under the assumption that the states are obtained via measurements (yaw rate and sideslip angle). The state-space formulation of single-track model equations (see section 1.3) is:

$$\dot{\mathbf{x}} = \mathbf{A}\mathbf{x} + \mathbf{B}M_{z,LQR} + \mathbf{E}\delta_\omega + \mathbf{d} \quad (2.15)$$

where the state vector is $\mathbf{x} = [\beta \quad r]^T$, and the matrices \mathbf{A} , \mathbf{B} , \mathbf{C} and \mathbf{E} are:

$$\begin{aligned} \mathbf{A} &= \begin{bmatrix} -\frac{1}{mV}(C_f + C_r) & -1 - \frac{1}{mV^2}(aC_f + bC_r) \\ -\frac{1}{J_z}(aC_f + bC_r) & -\frac{1}{VJ_z}(a^2C_f + b^2C_r) \end{bmatrix} \\ \mathbf{B} &= \begin{bmatrix} 0 \\ \frac{1}{J_z} \end{bmatrix}, \quad \mathbf{C} = [I_{2 \times 2}], \quad \mathbf{E} = \begin{bmatrix} \frac{1}{mV}C_f \\ \frac{a}{J_z}C_f \end{bmatrix} \end{aligned} \quad (2.16)$$

$M_{z,LQR}$ is the reference yaw moment contribution of the LQR, and δ_ω is the steering angle (at the wheel). \mathbf{d} represents model uncertainties and exogenous disturbances. Starting from Eq. 2.15, the error dynamics are expressed by:

$$\dot{\mathbf{e}} = \mathbf{A}\mathbf{e} + \mathbf{B}M_{z,LQR} + U_d \quad (2.17)$$

where:

$$\mathbf{e} = \mathbf{x} - \mathbf{x}_{ref} = \begin{bmatrix} e_\beta \\ e_r \end{bmatrix} = \begin{bmatrix} \beta - \beta_{ref} \\ r - r_{ref} \end{bmatrix} \quad (2.18)$$

$$U_d = \mathbf{A}\mathbf{x}_{ref} - \dot{\mathbf{x}}_{ref} + \mathbf{E}\delta_\omega + \mathbf{d} \quad (2.19)$$

$$\mathbf{x}_{ref} = [\beta_{ref} \quad r_{ref}]^T \quad (2.20)$$

e_r and e_β are the yaw rate and sideslip angle errors, respectively, while the references β_{ref} and r_{ref} are continuous differentiable functions. To reduce the steady-state yaw rate error, an augmented state, η , is introduced such that $\dot{\eta} = e_r$. By grouping η together

with the two error states describing the plant, the augmented system is obtained:

$$\begin{cases} \dot{\mathbf{x}}_a = \mathbf{A}_a \mathbf{x}_a + \mathbf{B}_a M_{z,LQR} + U_{d,a} \\ \mathbf{e} = \mathbf{C}_a \mathbf{x}_a \end{cases} \quad (2.21)$$

$\mathbf{x}_a = [\mathbf{e} \quad \eta]^T$ is the augmented state vector, and \mathbf{A}_a , \mathbf{B}_a and \mathbf{C}_a are the state-space matrices of the augmented system:

$$\mathbf{A}_a = \begin{bmatrix} \mathbf{A} & \mathbf{0} \\ \mathbf{F} & \mathbf{0} \end{bmatrix}, \mathbf{B}_a = \begin{bmatrix} \mathbf{B} \\ \mathbf{0} \end{bmatrix}, \mathbf{C}_a = \begin{bmatrix} \mathbf{C} & \mathbf{0} \\ \mathbf{0} & \mathbf{0} \end{bmatrix}, \mathbf{F} = \begin{bmatrix} 0 & 1 \end{bmatrix}, \quad (2.22)$$

From Eqns. 2.17 and. 2.19, the disturbance term of the augmented system becomes:

$$\mathbf{U}_{d,a} = \mathbf{A}_r \mathbf{x}_{ref,a} - \mathbf{I}_a (\dot{\mathbf{x}}_{ref,a} + \mathbf{d}) + \mathbf{E}_a \delta_\omega \quad (2.23)$$

with $\mathbf{x}_{ref,a} = [\mathbf{x}_{ref} \quad 0]$. \mathbf{A}_r , \mathbf{I}_a and \mathbf{E}_a are defined as follows:

$$\mathbf{A}_r = \begin{bmatrix} \mathbf{A} & \mathbf{0} \\ \mathbf{0} & \mathbf{0} \end{bmatrix}, \mathbf{I}_a = \begin{bmatrix} \mathbf{I}_{2 \times 2} & \mathbf{0} \\ \mathbf{0} & \mathbf{0} \end{bmatrix}, \mathbf{E}_a = \begin{bmatrix} \mathbf{E} \\ \mathbf{0} \end{bmatrix}, \quad (2.24)$$

The performance index J used in the LQR control system design is:

$$J = \frac{1}{2} \int_0^\infty [\mathbf{x}_a^T \mathbf{Q} \mathbf{x}_a + R M_{z,LQR}^2] dt \quad (2.25)$$

with \mathbf{Q} and R being the weighting factors related to the control tracking performance and control effort, respectively. The feedback control gain, L , is obtained from:

$$L = R^{-1} \mathbf{B}_a^T \mathbf{P} = \begin{bmatrix} K_{P,\beta} & K_{P,r} & K_{I,r} \end{bmatrix} = \begin{bmatrix} \frac{p_{21}}{RJ_z} & \frac{p_{22}}{RJ_z} & \frac{p_{23}}{RJ_z} \end{bmatrix} \quad (2.26)$$

where P is the unique positive semi-definite solution of an algebraic Riccati equation [114] and p_{ij} is the element in the i -th row and j -th column of P . Hence $M_{z,LQR}$ is:

$$M_{z,LQR} = -K_{P,\beta} \mathbf{e}_\beta - K_{P,r} \mathbf{e}_r - \int (K_{I,r} \mathbf{e}_r - k_\omega \Delta u) dt \quad (2.27)$$

$K_{P,r}$ and $K_{I,r}$ are the proportional and integral yaw rate gains, respectively, and $K_{P,\beta}$ is the proportional sideslip gain. k_ω is the anti-windup gain, which is multiplied by the difference, Δu , between the demanded yaw moment and the saturated yaw moment, $M_{z,sat}$, according to the anti-windup approach in [115, 116].

LQR stability

The vehicle yaw dynamics are described by second order transfer functions, all of them with the same denominator (e.g., r/δ_ω , β/δ_ω and r/M_z , where M_z is the yaw moment caused by the torque-vectoring controller). The damping ratio of the transfer functions significantly decreases with vehicle speed, V , which is a parameter in Eq. 2.21. This effect justifies a gain scheduling design of the LQR as a function of V (see [89] for a similar application, without consideration of stability requirements). To ensure the stability of the gain scheduled controller, an advanced interpolation method, namely stability preserving interpolation, is applied to the gain scheduling design. This approach can be used for arbitrary linear time invariant (LTI) controllers, providing a sufficient condition on their placement on the scheduling space, such that a stability preserving interpolated controller always exists. The mathematical formulation is given in the following theorem, adapted from [117].

Theorem 2.1 (Stability preserving interpolation). *Consider a set of state-feedback controllers \mathbf{L}_i ($i = 1, \dots, n$) synthesized for the vehicle plant at different fixed vehicle speeds, i.e., $V_1 < V_2 < \dots < V_n \in \Gamma$, where Γ covers the range of possible vehicle speeds. If there exist symmetric positive-definite matrices \mathbf{W}_i and $\gamma > 1$ such that:*

$$\mathbf{W}_i(\mathbf{A}_n(V) + \mathbf{B}_n\mathbf{L}_i)^T + (\mathbf{A}_n(V) + \mathbf{B}_n\mathbf{L}_i)\mathbf{W}_i \leq -\gamma\mathbf{I} \quad (2.28)$$

where $V \in U_i$, and $\Gamma \subseteq \bigcup_{i=1}^n U_i$ (stability covering condition), then there exist intervals $[V_i, V_{i+1}] \subset U_i \cap U_{i+1}$, $i = 1, \dots, n-1$, and continuous controller gains $\mathbf{L}(V)$ defined as:

$$\mathbf{L}(V) = \left(\frac{V_{i+1} - V}{V_{i+1} - V_i} \mathbf{L}_i \mathbf{W}_i + \frac{V - V_i}{V_{i+1} - V_i} \mathbf{L}_{i+1} \mathbf{W}_{i+1} \right) \mathbf{W}^{-1}(V) \quad (2.29)$$

where $V \in [V_i, V_{i+1}]$ and

$$\mathbf{W}(V) = \frac{V_{i+1} - V}{V_{i+1} - V_i} \mathbf{W}_i + \frac{V - V_i}{V_{i+1} - V_i} \mathbf{W}_{i+1} \quad (2.30)$$

is stability preserving. The proof of this theorem is given in [117].

A set of LTI controllers \mathbf{L}_i ($i = 1, \dots, n$) needs to be firstly designed based on the fixed values of the scheduling parameter (i.e., vehicle speed). The parameter values need to be carefully selected in order to meet the stability covering condition.

Definition 2.1 (Stability covering condition). *i) If there exist open neighborhoods U_i , containing V_i and for which \mathbf{L}_i is designed such that \mathbf{L}_i stabilizes the system for all $V_i \in U_i$, $i = 1, \dots, n$; and ii) if the scheduling space Γ meets the condition $\Gamma \subset \bigcup_{i=1}^n U_i$, then the state feedback gains satisfy the stability covering condition.*

To satisfy the stability covering condition, in this study six vehicle speeds (i.e., 40 km/h, 60 km/h, 80 km/h, 100 km/h, 120 km/h and 140 km/h) are selected for designing the LTI controllers $L_i, i = 1, \dots, 6$, which guarantees stability for the speed range 0-170 km/h. Symmetric positive definite matrices $W_i, i = 1, \dots, 6$ are solved for each LTI controller, satisfying condition 2.28. The interpolations are implemented based on Eqns. 2.29 and 2.30 along the LTI controllers for the interval 40-140 km/h. Below 40 km/h, the constant LTI controller L_1 is used, while above 140 km/h the constant LTI controller L_6 is adopted. The scheduled gain $L(v)$ is plotted in Fig. 2.12 and compared

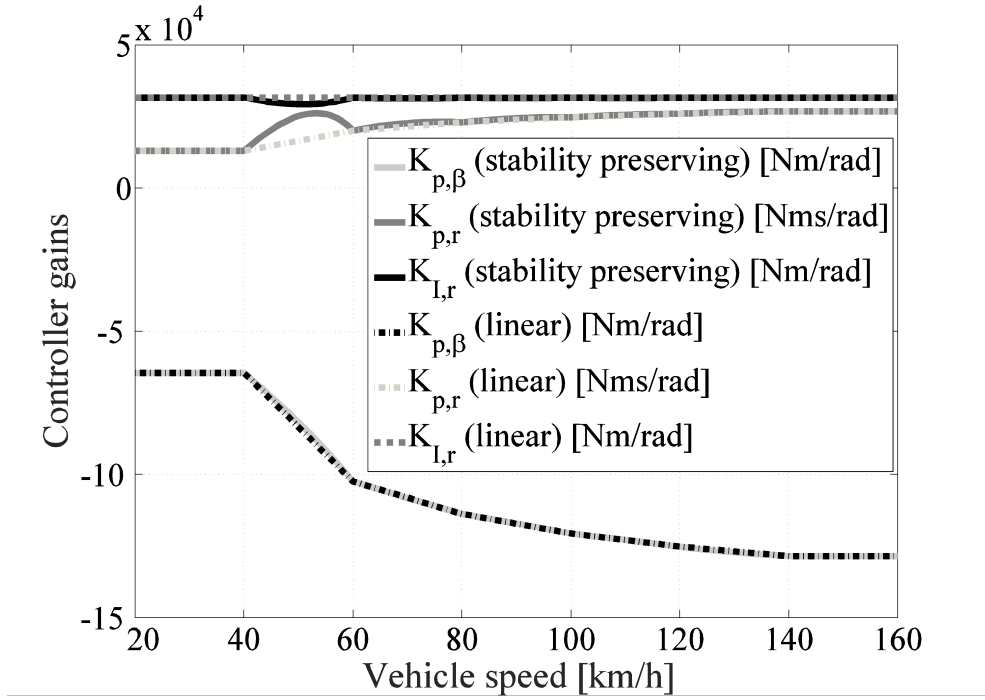


Figure 2.12 Gain scheduled controller $L(v)$

with the gain obtained from the linear interpolation method. The gains obtained from the two interpolation methods are very close to each other, especially in the high speed range. However, it cannot be concluded that the linear interpolation is also stability preserving since the computed matrices $W_i, i = 1, \dots, 6$ are not all equal. The simulation-based assessment and practical implementation of the LQR controller has confirmed the stability of the proposed gain scheduling design.

2.3.4 Yaw Moment Controller: Integral Sliding Mode Design

The Integral Sliding Mode (ISM) control is formulated in terms of perturbation estimation, according to the approach discussed by Utkin in [73, 72]. This was selected after careful consideration. In fact, to use Utkin's words, in this special case of ISMC "the

equivalent control is generated, guaranteeing chattering alleviation and maintaining the robustness properties typical of classical sliding mode... discontinuity appears only in the internal process, thus no chatters are excited in the real control path. Another advantage of this perturbation estimation scheme over the traditional methods is that the time derivative of the state vector is not necessary; the only information needed here is the upper bound of the perturbation ... From the concept point of view Integral Sliding Mode is utilized here only for the estimation of the system perturbation rather than for the purpose of control. The control action to the real controlled system will be continuously enhanced by the perturbation compensator." The ISM implementation of this research is based on the controller in [4], presenting an ISM structure for yaw rate control only (and thus not sufficient for the whole range of vehicle conditions), with a PID nominal controller. In this section the ISM approach is extended to provide continuous and robust yaw rate control, and sideslip angle control when required. The gain scheduled LQR controller of Section 2.3.3 is used as nominal controller. For designing the disturbance rejection part of ISMC, a non-linear model has been selected in order to have the best estimation of upper bound of the perturbation, meanwhile for the design of nominal controller (scheduled LQR) the linearized system is considered as shown in Section 2.3.3. The ISM formulation is based on the non-linear lateral force and yaw moment balance equations of the vehicle:

$$\begin{cases} \dot{\beta} &= -r - \beta \frac{\dot{V}}{V} + \frac{F_y}{mV} + \frac{F_{y,d}}{mV} \\ \dot{r} &= \frac{M_{z,Fy} + M_{z,al}}{J_z} + \frac{M_{z,Fx}}{J_z} + \frac{M_{z,d}}{J_z} \end{cases} \quad (2.31)$$

The model in Eq. 2.31 accounts for the variation of tire cornering stiffness as a function of the operating condition of the vehicle, which is the main limitation of the model used for LQR design. [118] analyzes in detail the variation of cornering stiffness in quasi-static and extreme transient conditions. In a first approximation, the lateral tire force contribution in the vehicle reference system, F_y , is given by:

$$F_y = (F_{x,1} + F_{x,2}) \sin(\delta_\omega) + (F_{y,1} + F_{y,2}) \cos(\delta_\omega) + F_{y,3} + F_{y,4} \quad (2.32)$$

The subscripts '1', '2', '3' and '4' refer to the front left, front right, rear left and rear right wheels. The yaw moment contribution caused by the lateral tire forces, $M_{z,Fy}$, is:

$$M_{z,Fy} = (F_{y,1} + F_{y,2})a \cos(\delta_\omega) - F_{y,3}b - F_{y,4}b + \left(F_{y,1} \frac{T_F}{2} - F_{y,2} \frac{T_F}{2} \right) \sin(\delta_\omega) \quad (2.33)$$

Hence the system can be re-written in the following error form:

$$\dot{\mathbf{e}} = \mathbf{g}(t) + \mathbf{B}M_{z,ISM}(t, \mathbf{e}) + \mathbf{h}(t, \mathbf{e}) \quad (2.34)$$

where \mathbf{g} is the known part of the system, $M_{z,ISM}$ is the control yaw moment, and \mathbf{h} is the unknown part. For simplicity and generality, it is assumed here that no state estimator is present, and therefore it is:

$$\mathbf{g}(t) = \begin{bmatrix} -\dot{\beta}_{ref}(t) \\ -\dot{r}_{ref}(t) \end{bmatrix} \quad (2.35)$$

For the computation of the time derivatives of the reference sideslip angle and yaw rate, an incremental ratio formulation with a time step of 0.1 s and a sampling time of 0.002 s has been adopted. The time step has been selected such that the relevant system dynamics are allowed to pass through the derivative calculation without significant phase lag. The effectiveness of this tuning has been verified during the experimental tests on the case study vehicle demonstrator. \mathbf{h} is defined as:

$$\mathbf{h} = \begin{bmatrix} h_{\beta} \\ h_r \end{bmatrix} = \begin{bmatrix} -r - \beta \frac{\dot{V}}{V} + \frac{F_y}{mV} + \frac{F_{y,d}}{mV} \\ \frac{M_{z,Fy} + M_{z,al} + M_{z,d}}{J_z} \end{bmatrix} \quad (2.36)$$

which includes the lateral force and yaw moment contributions due to the lateral tire forces and aligning moments. Formulation. 2.34-. 2.36 implies a conservative selection of the gains (i.e., higher values of the gains) of the switching part of the ISMC. In fact, if the controller designed for the case of absence of tire force and aligning moment state estimators is effective, the same controller will be effective also for the case of state estimation. In this respect, [119] compares the performance of three yaw rate-based ISM formulations for different levels of state estimation. $M_{z,ISM}$ consists of the sum of the nominal contribution, $M_{z,LQR}$, related to the LQR, and the switching contribution, $M_{z,sw,f}$:

$$M_{z,ISM} = M_{z,LQR} + M_{z,sw,f} \quad (2.37)$$

$M_{z,sw,f}$ is the filtered value of a discontinuous term, $M_{z,sw}$, calculated as a function of the sliding variable s :

$$s = s_0 + z \quad (2.38)$$

where s_0 is the conventional part of the sliding variable, corresponding to a linear combination (with multiplicative factors d_r and d_{β}) of the yaw rate error and sideslip angle error:

$$s_0 = d_r e_r + d_{\beta} e_{\beta} \quad (2.39)$$

The e_{β} contribution, defined according to the formulation in Section 2.3.2, has the peculiarity that it starts from an initial condition equal to zero any time the sideslip contribution switches on. This is a necessary condition for guaranteeing the effectiveness of the ISM design. According to the ISM formulation in terms of perturbation estimator,

z is calculated through the integration of \dot{z} defined as in [72]:

$$\begin{aligned}\dot{z} &= -\frac{\partial s_0}{\partial \mathbf{e}} [\mathbf{g} + \mathbf{B}(M_{z,ISM C} - M_{z,sw} - \Delta u)] = \begin{bmatrix} -d_\beta & -d_r \end{bmatrix} \begin{bmatrix} -\dot{\beta}_{ref} \\ -\dot{r}_{ref} + \frac{M_{z,ISM C} - M_{z,sw} - \Delta u}{J_z} \end{bmatrix} = \\ &= d_\beta \dot{\beta}_{ref} + d_r \dot{r}_{ref} - d_r \frac{M_{z,ISM C} - M_{z,sw} - \Delta u}{J_z}\end{aligned}\quad (2.40)$$

with $z(0) = -s_0(\mathbf{e}(0))$ and $\Delta u = M_{z,ISM C} - M_{z,sat}$. [72] demonstrates that Eq. 2.40, together with the indicated initial condition, allows to achieve sliding motion since the initial instant, without a reaching phase. Through the term Δu in Eq. 2.40, this ISM formulation includes the anti-windup contribution according to the approach defined in [120]. $M_{z,sw,f}$ in Eq. 2.37 is given by:

$$M_{z,sw,f} = M_{z,sw} \frac{\omega_F}{p + \omega_F} = -K_{ISM C} \text{sign}(s) \frac{\omega_F}{p + \omega_F} \quad (2.41)$$

where ω_F is the corner frequency of the first order filter, and $K_{ISM C}$ is the gain of the switching contribution. In [72] Utkin shows that by considering the switching function $s = s_0 + z$, with z defined as $\dot{z} = -\frac{\partial s_0}{\partial \mathbf{x}} (\mathbf{g}(\mathbf{x}) + \mathbf{B}u - \mathbf{B}u_1)$, $z(0) = -s_0(x(0))$, the time derivative of the new sliding variable can be calculated as $\dot{s} = \frac{\partial s_0}{\partial \mathbf{x}} (\mathbf{g}(\mathbf{x}) + \mathbf{B}u + \mathbf{B}u_h) - \frac{\partial s_0}{\partial \mathbf{x}} [\mathbf{g}(\mathbf{x}) + \mathbf{B}u - \mathbf{B}u_1] = \frac{\partial s_0}{\partial \mathbf{x}} \mathbf{B}u_h + \frac{\partial s_0}{\partial \mathbf{x}} \mathbf{B}u_1$. If the discontinuous control law is $u_1 = -K_{ISM} \text{sign}(s)$ and the matrix $\frac{\partial s_0}{\partial \mathbf{x}} \mathbf{B}$ is non-singular during the entire system response, setting $\dot{s} = 0$ reveals that $u_{1,fil t} = -u_h$ holds as well, implying that $u_{1,fil t} = u_{1,eq}$ is indeed an estimate of the perturbation term u_h . Moreover, the previous formulas show the computational efficiency of the ISM control. In fact, the computation of the control action consists of:

- a few algebraic operations for calculating \dot{z} through Eq. 2.40
- an integration for calculating z starting from \dot{z}
- trivial algebraic calculations for obtaining $s = s_0 + z$
- algebraic calculations and a first order filter for calculating $M_{z,sw,f}$
- a summation for calculating $M_{z,ISM C} = M_{z,LQR} + M_{z,sw,f}$

No computationally demanding iterative procedure is needed for the off-line or on-line computation of the gains or the control action. No large look-up table requiring significant memory specifications for the controller hardware is needed.

ISM stability

The stability of the close-loop system with the ISM controller is guaranteed by the following theorem about Lyapunov asymptotic stability which is also used to design the ISM gain K_{ISM} :

Theorem 2.2 (Lyapunov asymptotic stability). *For the general non-linear affine system:*

$$\dot{\mathbf{x}} = \mathbf{f}(\mathbf{x}) + \mathbf{B}u(\mathbf{x})$$

With $\mathbf{x} \in \mathbb{R}^n$ being the state vector and $u \in \mathbb{R}^m$ being the control input vector. Consider a sliding variable $s(\mathbf{x})$ such that when $s(\mathbf{x}) = \dot{s}(\mathbf{x}) = 0$ the system is on the sliding surface and it is forced to behave as the desired dynamic system. Suppose there exists a differentiable function $V(s) : \mathbb{R}^n \rightarrow \mathbb{R}$ which is radially unbounded and positive definite such that:

$$\dot{V}(s) < 0 \text{ for } s \neq 0$$

Then the system is asymptotically stable.

K_{ISM} must be selected to provide system stability. To this purpose, the Lyapunov function $V_{ISM} = 1/2s^2$ is chosen. It can be shown that:

$$\dot{s} = \frac{\partial s_0}{\partial \mathbf{e}} \mathbf{h} - \frac{\partial s_0}{\partial \mathbf{e}} \mathbf{B} K_{ISM} \text{sign}(s) + \frac{\partial s_0}{\partial \mathbf{e}} \mathbf{B} \Delta u = d_\beta h_\beta + d_r h_r - \frac{d_r}{J_z} K_{ISM} \text{sign}(s) + \frac{d_r}{J_z} \Delta u \quad (2.42)$$

Hence, it follows that:

$$\dot{V}_{ISM} = s\dot{s} \leq |s| \left(\left| d_\beta h_\beta + d_r h_r + \frac{d_r}{J_z} \Delta u \right| - \frac{d_r}{J_z} K_{ISM} \right) \quad (2.43)$$

If the uncertainty is constrained, i.e., if $h^* = \left| d_\beta h_\beta + d_r h_r + \frac{d_r}{J_z} \Delta u \right| < N$, with $N > 0$, then in order to have $\dot{V}_{ISM} < 0$ for $s \neq 0$ it must be:

$$K_{ISM} > N \frac{J_z}{d_r} \quad (2.44)$$

As in the practical implementation of the controller high values of K_{ISM} can bring an uncomfortable vehicle behavior in non-critical conditions, a scheduling of K_{ISM} is carried out as a function of $|e_r|$; i.e., $K_{ISM} = K_{ISM}(|e_r|)$. In conditions of low $|e_r|$, the value of the uncertain terms can be assumed to be low; therefore a low value of K_{ISM} is sufficient to provide system stability. The value of N is calculated from vehicle simulation results (based on an experimentally validated vehicle model in CarMaker) obtained during extreme maneuvers. For example, the time histories of the three components of

h^* divided by d_r are shown in Fig. 2.13, together with $J_z h^* / d_r$, during a sequence of step steers. Based on similar analyses, the same test is repeated for different values of J_z and

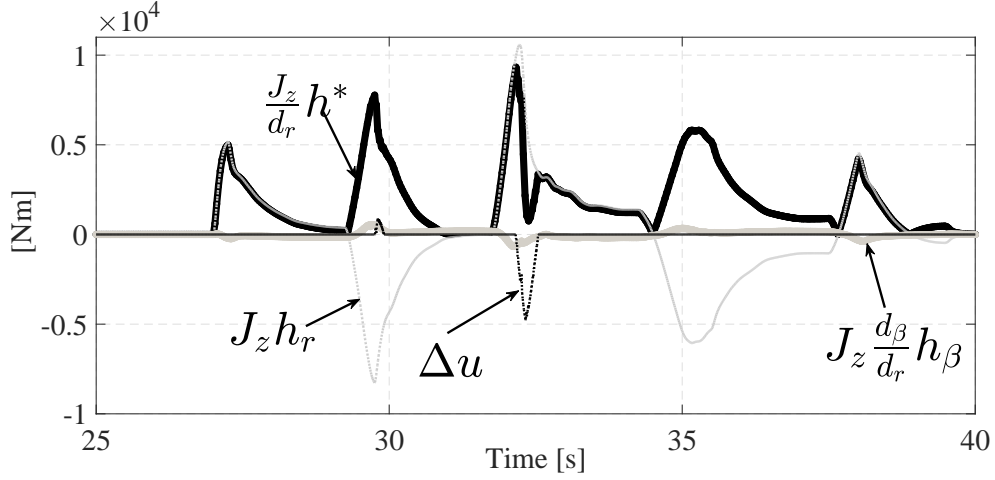


Figure 2.13 Time history of the disturbance contributions during a sequence of step steers at 90 km/h

m and the maximum value of K_{ISMC} for the worst case scenario is set to 10 kNm/rad. Note that the non-linear model formulation of Eq. 2.40 has been used to design the value of K_{ISMC} , through the definition of the upper bound of the possible perturbation. However, in the specific case the non-linear model does not have any practical effect on the controller formulation. The only consequence of the model selection is on the value of the gain, depending on the upper bound of the perturbation, which is better estimated by using a higher-fidelity model than the linear model for LQR control system design. Furthermore, condition. 2.44 ensures stability of the ISM control as a whole, including its LQR contribution.

By imposing $\dot{s} = 0$, the equivalent control action can be obtained:

$$u_{1,eq} = - \left(\frac{\partial s_0}{\partial \mathbf{e}} \mathbf{B} \right)^{-1} \frac{\partial s_0}{\partial \mathbf{e}} \mathbf{h} - \left(\frac{\partial s_0}{\partial \mathbf{e}} \mathbf{B} \right)^{-1} \frac{\partial s_0}{\partial \mathbf{e}} \mathbf{B} \Delta u \quad (2.45)$$

which brings the following system dynamics on the sliding surface:

$$\dot{\mathbf{e}} = \mathbf{g} + \mathbf{B} \mathbf{M}_{z,LQR} + \mathbf{h}' \quad (2.46)$$

with $\mathbf{h}' = \left[h_\beta \quad -h_\beta \frac{d_\beta}{d_r} - \frac{\Delta u}{J_z} \right]^T$. This means that during the sliding motion, h_r (matched disturbance) will be rejected by the ISM control. In the case of concurrent yaw rate and sideslip control (i.e., for incorrect r_{ref} or during extreme cornering with the Enhanced Sport mode), through a specific tuning of d_β / d_r the effect of h_β (unmatched disturbance) on yaw rate control can be tuned. Methods for the compensation of unmatched

disturbances through sliding mode control are proposed in [71]. Their application to this problem will be the topic of future investigations. During the sliding mode the system dynamics is switched from Eq. 2.34 to Eq. 2.46 where the control stability is ensured by the LQR design through the theorem of stability preserving interpolation.

2.4 Simulation Results

In order to evaluate and compare the previous yaw moment control logic (LQR and ISM), specific simulations are carried out by adopting the IPG CarMaker experimentally validated model. The simulation hypothesis is that both yaw rate r and sideslip angle β are measured during controller activation and the torque distribution to provide the reference yaw moment is equally computed for each electric motor:

$$\begin{cases} T_i &= \frac{T_{\omega,mod}^{TOT}}{4} \pm \frac{M_{z,sat} R_i}{T_F} \\ T_{m_i} &= \frac{T_i}{\tau_1 \tau_2 \eta_1 \eta_2 \eta_{CV1} \eta_{CV2}} \end{cases} \quad (2.47)$$

where the sign \pm depends on the sign of δ_ω and the position of the i -th wheel.

2.4.1 High friction coefficient step steer

The sport driving mode is analyzed during a step steer maneuver of 100 deg at initial speed of 100 km/h and high friction coefficient meanwhile T_ω^{TOT} is kept constant to the value needed for compensating the rolling and aerodynamics resistances at 100 km/h. The variables monitored are the yaw rate and the sideslip angle shown in Fig. 2.14. It is possible to appreciate how the active vehicle with LQR and ISM control logic shows a lower level of oscillations around the steady-state value of yaw rate and a faster response in terms of rising time. The ISM is also able to reduce considerably the overshoot and the settling time thus aiming to obtain the desired lateral behavior described by the Sport mode understeer characteristic. The passive vehicle presents an initial unstable behavior since the sideslip angle reaches very high values (almost 15 deg) thus leading to an out-of-control condition for a non professional driver who can better handle a sideslip angle of 5 deg in presence of the torque vectoring control. Furthermore, yaw moment components for LQR and ISM controllers are reported respectively in Fig. 2.15 where it is possible to compare how the LQR and ISM apply their torque vectoring strategies. The LQR total yaw moment is composed by its three components identified by the yaw rate proportional term $M_{z,Pr}$ (main contribution), the yaw rate integral term $M_{z,Ir}$ (for reducing steady-state error) and the sideslip angle proportional term $M_{z,P\beta}$ (which is

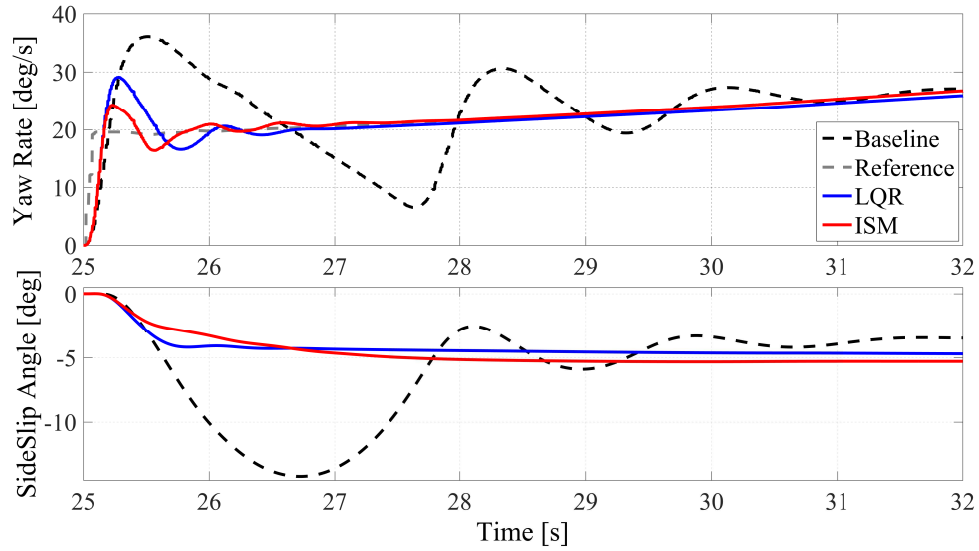


Figure 2.14 Yaw rate and sideslip angle for a step steer maneuver of 100 deg at 100 km/h for the passive and active vehicles

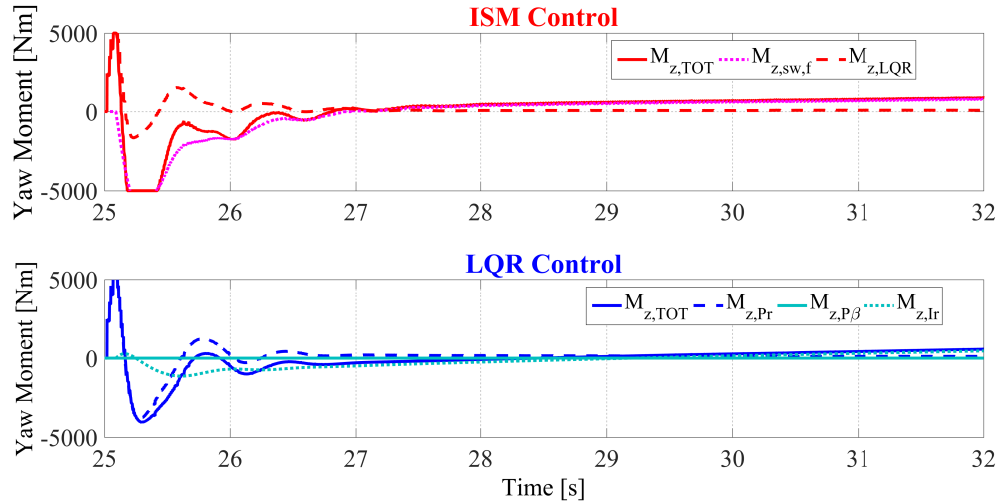


Figure 2.15 Yaw moment for a step steer maneuver of 100 deg at 100 km/h for LQR and ISM control strategies

equal to zero in this scenario since the sport driving mode is designed to avoid wind-up effect of sideslip angle). The ISM yaw moment is composed by the nominal controller term $M_{z,LQR}$ and the switching term $M_{z,sw,f}$ that is able provide a faster and greater yaw moment reaction with respect a simple LQR control thus improving the tracking performance of yaw rate control. Finally, Fig. 2.16 shows how the final sliding variable s , composed by the conventional s_0 and the integral z sliding variables, reaches the null value in almost 0.2 seconds thus forcing the system to move on the sliding surface with the positive benefit obtained by robust properties against matched disturbances described in section 1.4.4.

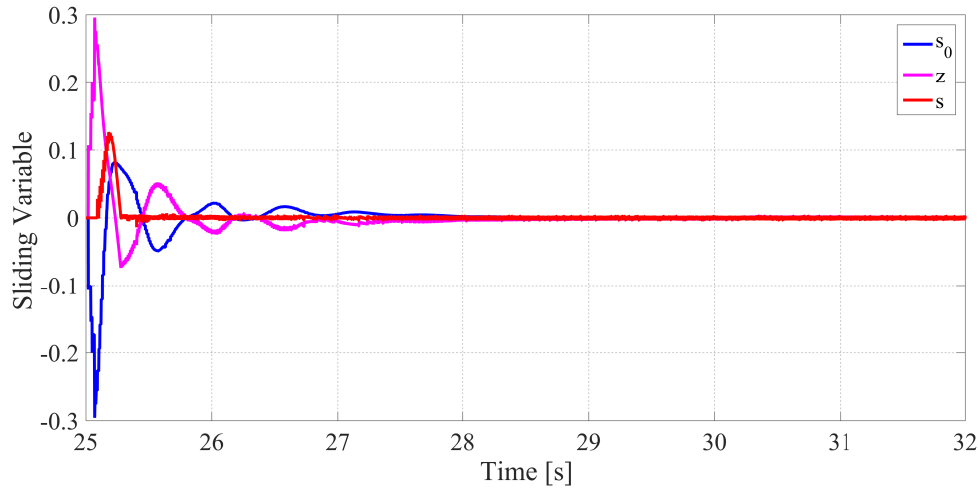


Figure 2.16 Conventional s , integral z and final s sliding variables during ISM control activation

2.4.2 Low friction coefficient sequence of step steers

This section shows that the proposed controller formulation is robust even in absence of tire-road friction coefficient estimation. The adopted electric vehicle simulation model is implemented in CarMaker, and was experimentally validated in [77] with experimental results from the same vehicle demonstrator adopted in Section 2.2. Figs. 2.17 and 2.18 report the simulation results for a sequence of step steers on a low friction surface ($\mu = 0.5$), and a constant wheel torque demand of 500 Nm, from an initial speed of 100 km/h. The test consists of a fast steering input (at a rate of 400 deg/s), followed by an input of equal amplitude and opposite direction, and a final input to bring the steering wheel angle back to zero. The graphs include the comparison of: i) the passive vehicle; ii) the active vehicle with the only yaw rate controller; and iii) the active vehicle with the concurrent control of yaw rate and sideslip angle, with different thresholds for the intervention of the sideslip contribution. In the legends 'Threshold 1', 'Threshold 2' and 'Threshold 3' are characterized by progressively relaxed interventions of the sideslip-related terms. For all cases with the controlled vehicle the reference yaw rate profile is the one calculated for a tire-road friction coefficient of 1, without any friction-related correction. The passive vehicle ('Baseline' in the legends) has an unstable behavior, since after 30 s its sideslip angle profile exhibits a progressive increase towards values exceeding 30 deg. The active vehicle with the only yaw rate controller is stable, but its peak values of sideslip angle in Fig. 2.18 are beyond the typical range a normal driver would be able to govern through the steering wheel. The concurrent control of yaw rate and sideslip angle generates lower peak values of sideslip angle, consistent with the respective sideslip-related thresholds, and thus ensures a higher degree of safety. The

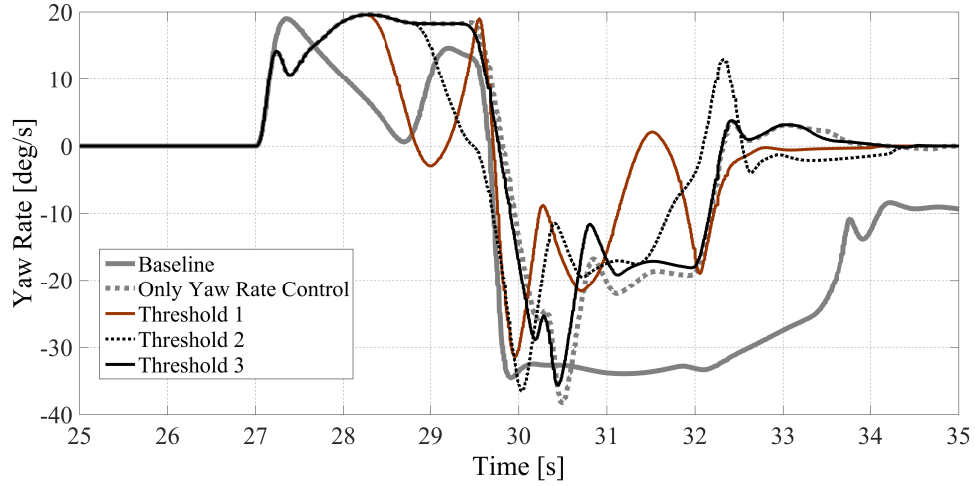


Figure 2.17 $r(t)$ for the passive and active (ISM control with only yaw rate control and concurrent yaw rate and sideslip control) vehicles during sequences of step steers in low tire-road friction conditions with different sideslip thresholds

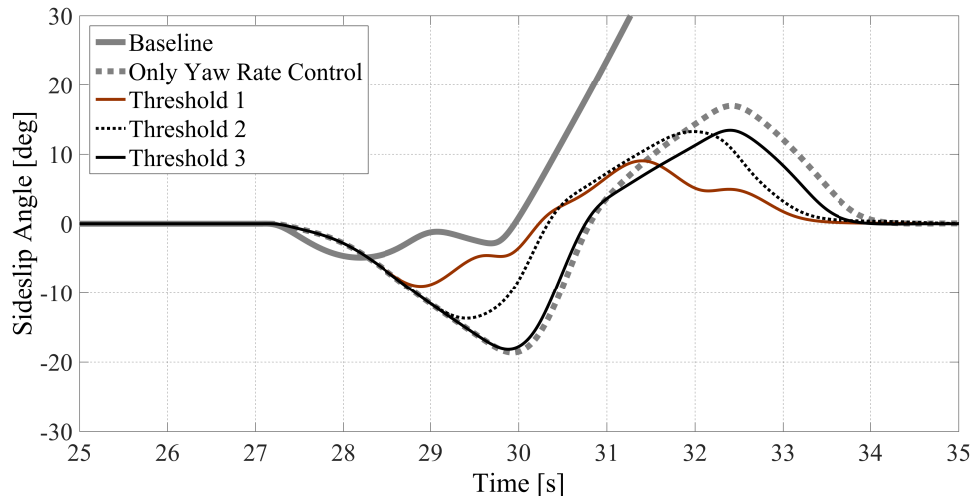


Figure 2.18 $\beta(t)$ for the passive and active (ISM control with only yaw rate control and concurrent yaw rate and sideslip control) vehicles during sequences of step steers in low tire-road friction conditions with different sideslip thresholds

valuable conclusion of the analysis is that a properly tuned concurrent controller of yaw rate and sideslip is sufficient to effectively stabilize the vehicle, even in absence of any form of tire-road friction coefficient estimation. Given the under-actuated nature of the system, the safer sideslip response implies worse yaw rate tracking performance, but this does not actually matter, as the reference yaw rate is not suitable for the specific tire-road friction conditions.

2.5 Experimental Results in High Friction Conditions

This section presents a selection of the test results obtained with the electric vehicle demonstrator of the European Union-funded projects E VECTOORC [121] and iCOMPOSE [122] (described in section 2.2) at the Lommel proving ground (Belgium). The vehicle has four electric drivetrains, each comprising a switched reluctance on-board motor, which is connected to the wheels through a single-speed transmission system, constant velocity joints and a half-shaft. The controller presented in section 2.3 is implemented on a dSPACE® AutoBox system installed on the vehicle. Four maneuvers are analyzed in the following sub-sections.

2.5.1 Skid pad

For the skid pad test the driver slowly accelerates the vehicle and adjusts the steering wheel angle in order to keep the vehicle on a specified circular trajectory; a radius of 60 m is used here. The test is continued until the vehicle reaches its maximum lateral acceleration-cornering limit. Fig. 2.19 compares the understeer characteristics for the

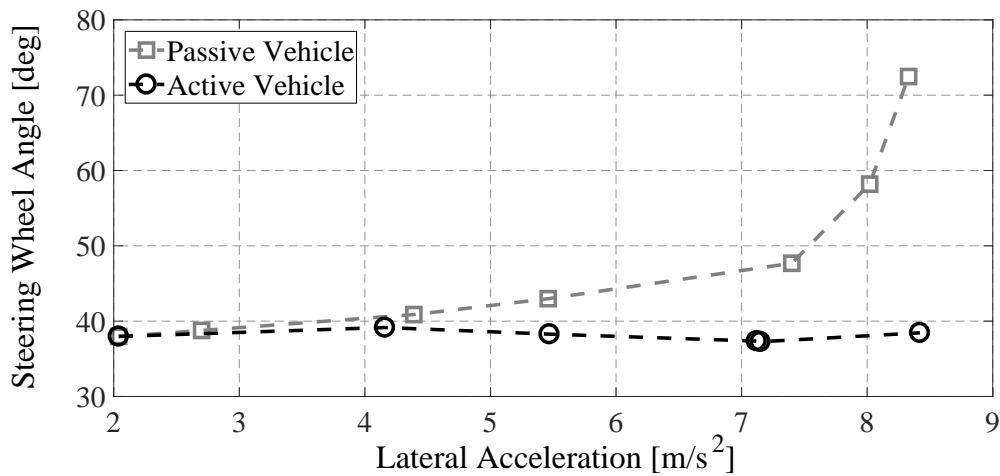


Figure 2.19 Examples of experimental understeer characteristics for the passive and active vehicles

passive vehicle (i.e., the vehicle without any controller) and the vehicle with the ISM control in the Sport mode. The passive vehicle shows a typical non-linear cornering behavior, with an increase of the understeer gradient (i.e., the slope of the diagram) starting from lateral acceleration values of approximately 4 m/s^2 . On the contrary, the vehicle with the ISM control is in a condition of neutral steering throughout the whole test, consistently with the reference understeer characteristic for the selected driving

mode. In the case (not shown here) of the Enhanced Sport mode, the maximum value of lateral acceleration is further increased with respect to that of the Sport mode.

2.5.2 Step steer

Control system performance comparison

Figs. 2.20 - 2.22 show the results for an extreme step steer test executed with the Sport driving mode and different controllers. The step steer test is started from a constant speed of 100 km/h and with the corresponding wheel torque demand fixed ($T_{\omega}^{TOT} = 700 Nm$) within the dSPACE® system to avoid driver input on the accelerator pedal during the maneuver. Then, the driver turns the steering wheel at a rate of ≈ 400 deg/s up to a final value of 100 deg, which is kept during the rest of the maneuver. Following the steering wheel input, the car decelerates because of the increase of tire slip power losses, yielding a reduction of V and, hence, an increase of r .

Fig. 2.20 shows the time histories of vehicle yaw rate for: a) the passive vehicle; b) the vehicle controlled only with the LQR (with the same gains used in the LQR within the ISM); c) the vehicle with the same LQR as in b) and the non-linear static feedforward contribution designed based on the quasi-static model according to the approach presented in [2] (LQR + FF); and d) the vehicle with the ISM control. As indicated by Fig. 2.20, all controllers decrease the duration of the yaw rate oscillations following the steering wheel input. The performance of the ISM control is particularly effective in reducing the first yaw rate overshoots and undershoots, which are 16.8 deg/s and 24.5 deg/s in a), 10.1 deg/s and 8.4 deg/s in b), 11.1 deg/s and 7.0 deg/s in c), and 3.5 deg/s and 4.1 deg/s in d). Table 2.3 includes the values of the three performance indicators adopted to assess the controllers along the maneuver; in particular:

- (i) The root mean square value of the yaw rate error, $RMSE$, calculated during the 3 s following the application of the steering wheel input. The ISM control is able to reduce the $RMSE$ by 77%, 49%, and 42%, in comparison with the cases a), b), and c), respectively
- (ii) The integral of the absolute value of the control action, ν , normalized with time, defined as:

$$IACA = \frac{1}{t_{man,fin} - t_{man,in}} \int_{t_{man,in}}^{t_{man,fin}} |M_{z,sat}(t)| dt \quad (2.48)$$

and calculated during the relevant part of the maneuver, between the times $t_{man,in}$ and $t_{man,fin}$ (in this case the 3 s following the steering application). The significantly improved performance of the ISM control corresponds to a marginal in-

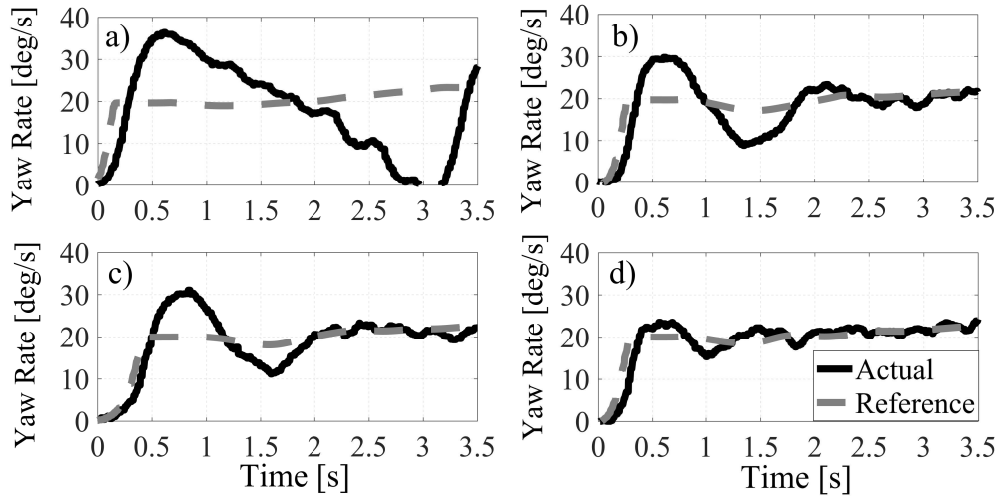


Figure 2.20 $r(t)$ during a step steer for the passive (a) and active (LQR (b), LQR+FF (c) and ISM (d)) vehicles

crease of the control effort, 13% and 6% higher than for the LQR and LQR+FF controllers, respectively

- (iii) The delay between the reference yaw rate and the actual yaw rate, t_d , evaluated for $r_{ref} = 15$ deg/s. This indicator is approximately 30% lower for all controlled vehicles indicating enhanced vehicle responsiveness during transients. t_d can be effectively designed by tuning the filter providing the reference yaw rate

Table 2.3 Performance indicators for the step steer test for the passive and controlled vehicles

	$RMSE$ [deg/s]	$IACA$ [Nm]	t_d [s]
Baseline	11.45	-	0.12
LQR	5.175	1578	0.09
LQR + FF	4.545	1675	0.09
ISM	2.634	1780	0.09

Fig. 2.21 shows $M_{z,sat}(t)$ for the three controllers during the step steer maneuver. For all tests the maximum yaw moment is limited to 4000 Nm. The results indicate that the ISM control generates the first negative (stabilizing) peak of yaw moment earlier and for a longer duration than the other two controllers. In doing so, the ISM control is able to reduce the first yaw rate overshoot as mentioned above. Fig. 2.22 reports the time histories of the yaw moment contributions of the ISM control; in particular the proportional term of the LQR (LQR_{Pr} in the figure), the integral term of the LQR (LQR_{Ir}), the switching contribution, ($Switching ISMC$), and their sum ($Total$). The

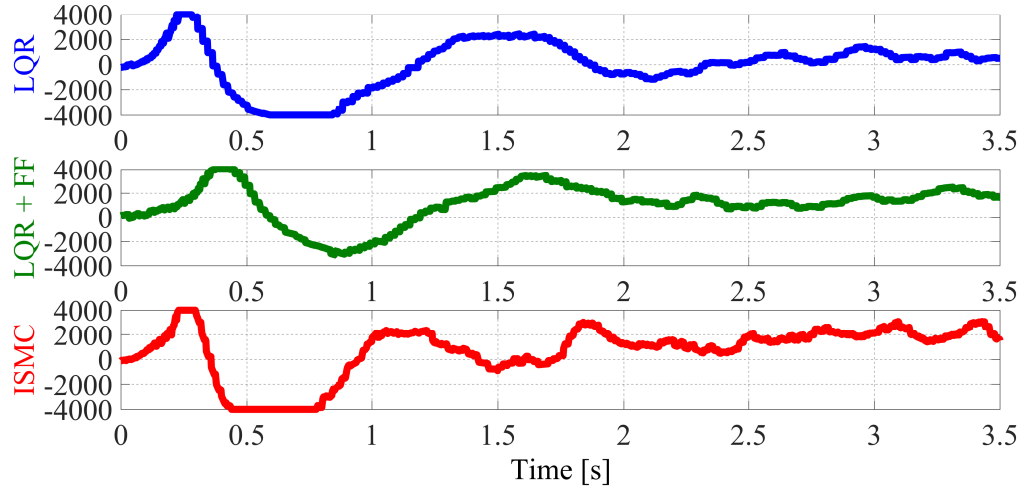


Figure 2.21 $M_{z,sat}(t)$ during a step steer for the LQR, LQR + FF and ISM controls

proportional term is the main contributor for the reduction of the time delay in the initial yaw rate build-up phase, while the switching contribution is primarily responsible for vehicle stabilization between 0.4 s and 0.8 s. As during this test the sideslip angle remains consistently low, the sideslip contribution is inactive.

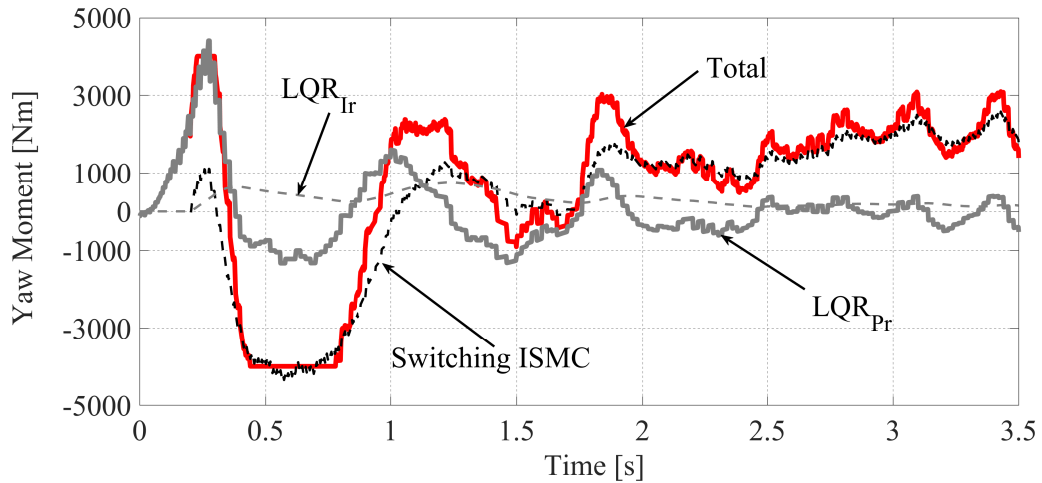


Figure 2.22 ISM yaw moment contributions during a step steer

ISM control tunability

Sliding mode controllers have the significant advantage of providing robustness with very simple formulations of their control laws. For the specific case of the ISM control, the control system tuning is mainly based on the physically meaningful values of the gain K_{ISM} (or its look-up table) and the corner frequency ω_F . With the restricted number of

parameters, the controller can be tuned using the conventional industrial procedures of automotive stability control systems based on trial-and-error sessions on proving grounds, after an initial controller set-up in simulation. For example, Fig. 2.23 reports the variation of yaw rate response for different values of ω_F , while Table 2.4 includes the respective values of *RMSE* and *IACA*. Higher values of ω_F increase the 'aggressiveness' of the controller, thus originating better tracking performance, increased control effort and increased sensitivity to measurement noise. In any case, the tuning procedure of the ISM control is not more complex than for a typical automotive PID or LQR controller, and can be performed by a vehicle engineer without a specific know-how in robust control theory.

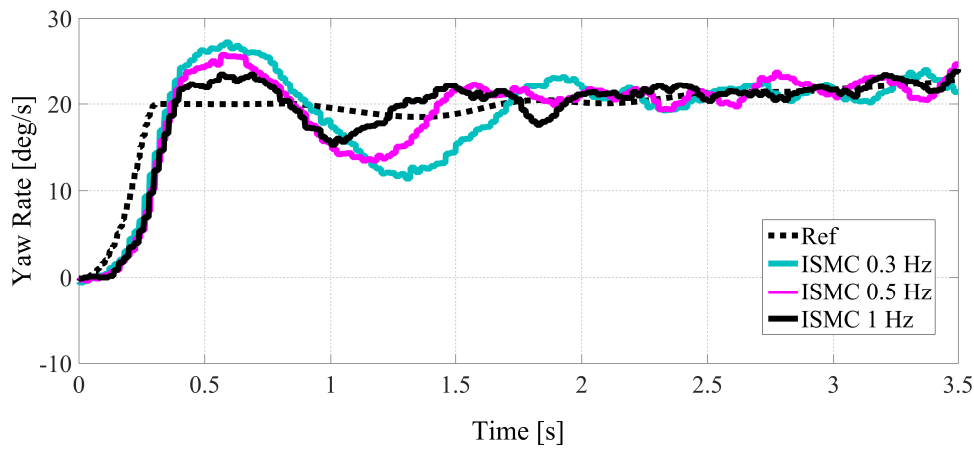


Figure 2.23 $r(t)$ during a step steer with the ISM control for different values of ω_F

Table 2.4 Performance indicators for the step steers for different values of ω_F

	<i>RMSE</i> [deg/s]	<i>IACA</i> [Nm]
ISM 0.3 Hz	3.803	1654
ISM 0.5 Hz	3.307	1617
ISM 1 Hz	2.634	1780

Enhanced Sport mode

Fig. 2.24 shows the results for a step steer test executed in the Enhanced Sport mode with the ISM controlling only the yaw rate, or both yaw rate and sideslip angle. The high value of yaw rate reference at the completion of the steering wheel input (in excess of the

friction limits between the tires and the road surface) provokes a sideslip angle build-up. β reaches values beyond -30 deg when only the yaw rate controller is used. The sideslip contribution limits sideslip to predefined thresholds (i.e, 'Threshold 1', 'Threshold 2', 'Threshold 3' in Fig. 2.24). Fig. 2.25 presents $r(t)$ and $r_{ref}(t)$ for the yaw rate controller

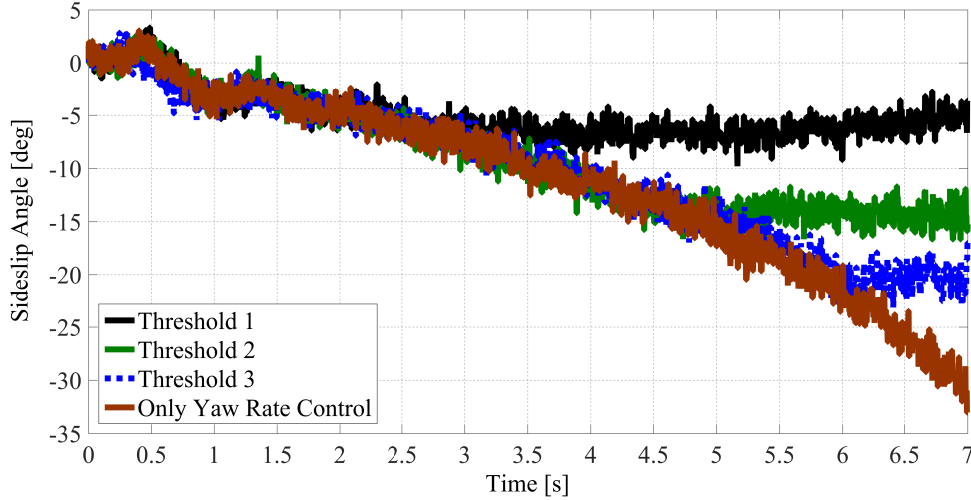


Figure 2.24 $\beta(t)$ during step steers with the ISM control in Enhanced Sport mode, with and without the sideslip angle controller (for different sideslip thresholds, -7 deg, -14 deg, and -21 deg)

only and the 'Threshold 2' case of the yaw rate and sideslip controller. The intervention of the sideslip contribution is associated with a reduced yaw rate (noticeable from ≈ 4 s onwards) compared to the vehicle with the yaw rate controller only. The reduction is caused by the concurrent effect of the yaw moment required for the actuation of sideslip angle control, the higher value of V due to lower tire slip angles, and the reference yaw rate reduction corresponding to Eq. 2.14. These results demonstrate the benefit of sideslip control for 'fun-to-drive' enhancement or, conversely, for enhancing active safety by allowing controlled vehicle operation at the cornering limit. For example, by constraining β at the values specified by the high-level controller the vehicle could be more easily controlled by an unskilled driver during emergency maneuvers in low friction conditions, especially if these are not identified for the generation of $r_{ref}(t)$. The experiments also show that a relatively simple control structure can be used to constrain sideslip angle, without having to use computationally expensive controllers, such as model predictive controllers.

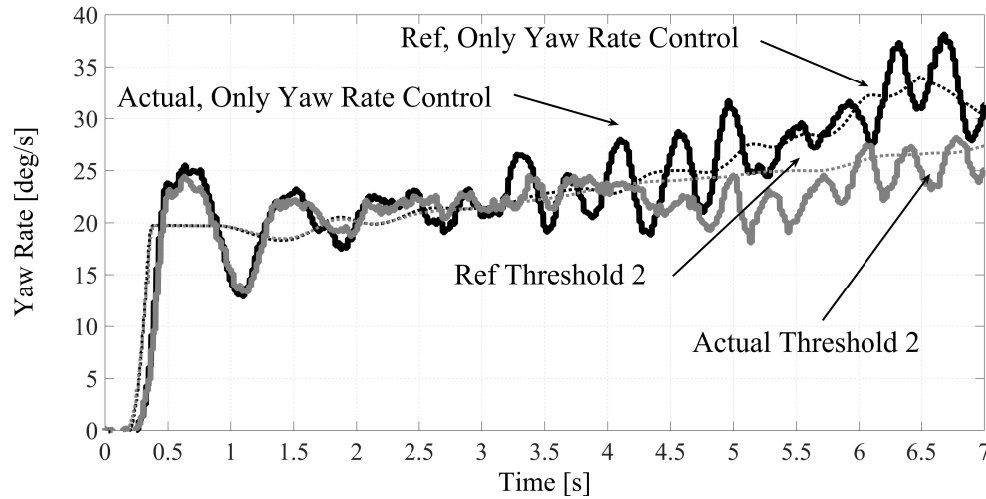


Figure 2.25 $r(t)$ during step steers with the ISM control in Enhanced Sport mode, with and without the sideslip angle controller (for different sideslip thresholds, -7 deg, -14 deg, and -21 deg)

2.5.3 Sequence of step steers

A sequence of step steers was carried out to assess the transient yaw response of the vehicle in extreme conditions (Fig. 2.26). The maneuver was executed for increasing values of steering wheel angle amplitude (with increments of 10 deg), from an initial V of 100 km/h and constant wheel torque demand. The test was considered successful when the sideslip angle peak remained below 10 deg during the whole maneuver. In particular, the passive vehicle reaches this condition for a steering wheel angle amplitude of 70 deg, while the active vehicle is still within the specified sideslip boundary with an amplitude of 150 deg.

2.5.4 Obstacle avoidance test

To assess the ISM control effectiveness on a variety of test cases, the obstacle avoidance test is carried out according to the standard ISO 3888 – 2 (see Fig. 2.27 and [123]) to (subjectively) investigate the road-holding ability of the vehicle. After the initial stabilization of the vehicle at the speed set for the specific test, a constant total wheel torque demand is imposed by the software running on the dSPACE® unit, independently from the driver accelerator pedal position (200 Nm for the test in Fig. 2.28). This procedure allowed high repeatability of the test results, with increased focus of the driver on the steering action. Fig. 2.28 shows that the controlled vehicle requires a significantly reduced steering correction after the first lane change maneuver, when the driver has to stabilize the vehicle to keep it within the second lane without hitting the

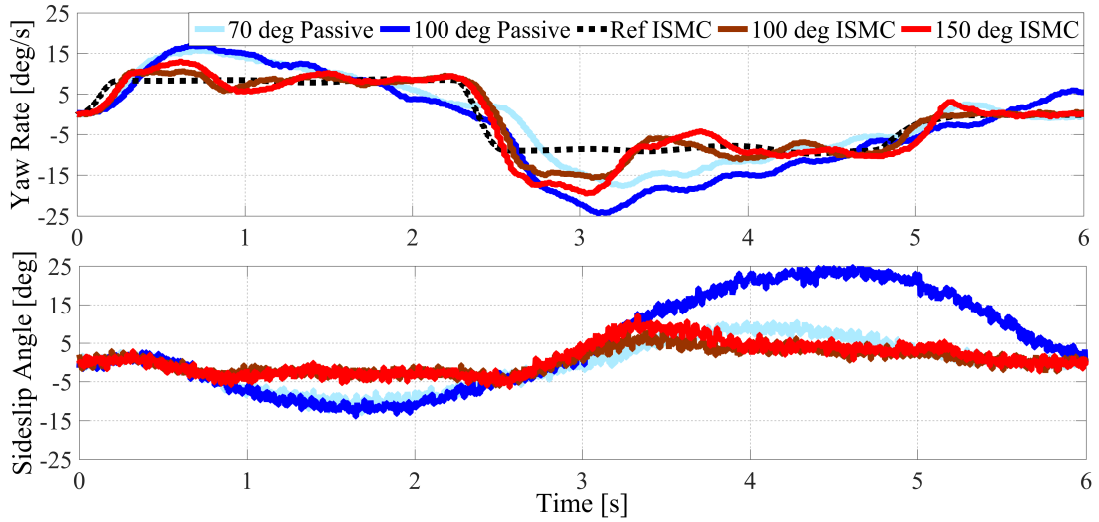


Figure 2.26 $r(t)$ and $\beta(t)$ for the passive and active (ISM control, Normal mode) vehicles during sequences of step steers with a sideslip threshold of 15 deg

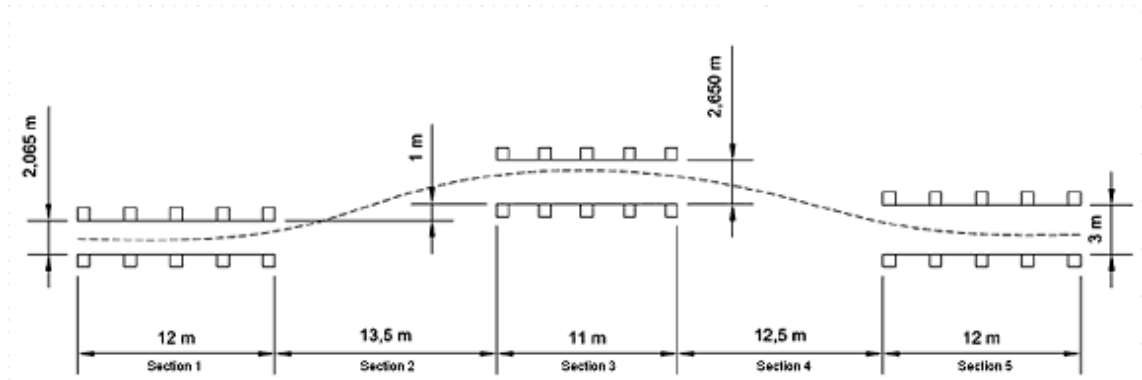


Figure 2.27 path description according to standard ISO 3888 – 2

cones. Correspondingly the yaw rate and sideslip angle oscillations are reduced, and thereby the vehicle exhibits a better performance and driving experience. Also, owing to the lower values of $|\beta(t)|$, the controlled vehicle maintains a higher speed during the maneuver. Fig. 2.29 reports a sample of the tests, executed on dry tarmac with zero road gradient and bank angle. The figure indicates the corresponding initial speed, i.e, the speed at the entrance of the first lane, and whether the test was successful or unsuccessful. The test is considered successful when the vehicle performs the maneuver without hitting any cone placed along the boundaries of the obstacle avoidance track. The results show a 7% increase of the maximum initial speed of the successful tests with the controlled vehicle with respect to the passive vehicle. Again, the higher speed demonstrates the controller benefits in terms of enhanced vehicle handling qualities and active safety.

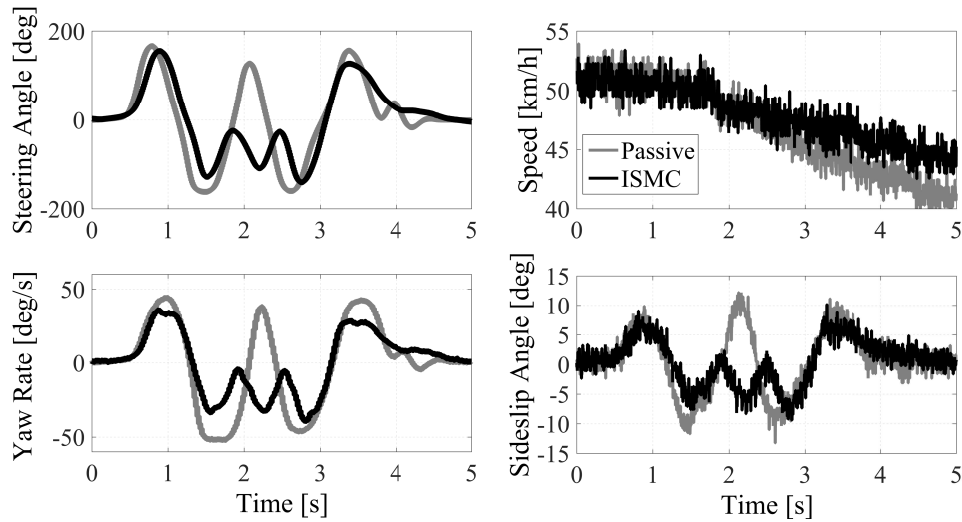


Figure 2.28 $\delta(t)$, $r(t)$ and $\beta(t)$ for the passive and active (in Normal mode) vehicles during an obstacle avoidance maneuver from an initial $V = 51.5$ km/h

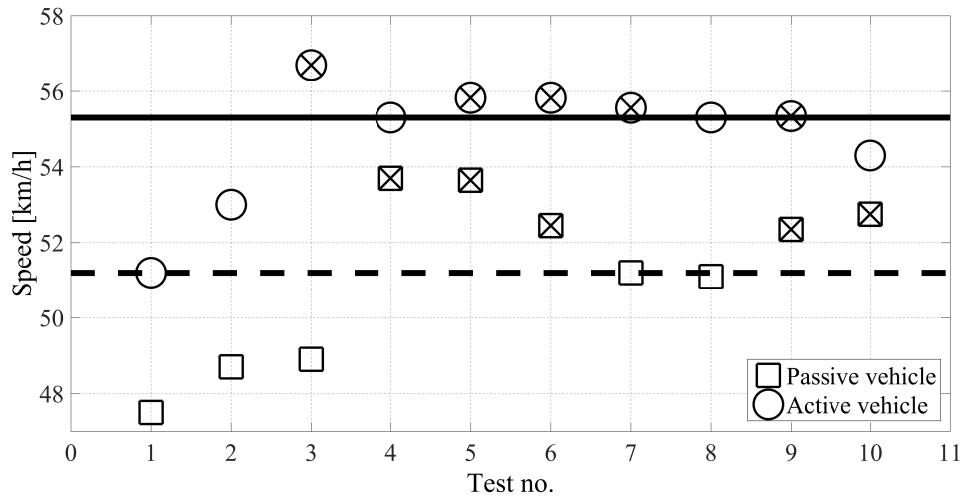


Figure 2.29 Distribution of the successful (indicated by the blank symbols) and unsuccessful indicated by 'x' tests for the passive and active vehicles (in Normal mode), during obstacle avoidance maneuvers

2.6 Sideslip Angle Estimation Analysis

The TV control designed in section 2.3 and implemented in section 2.5 requires as input driver commands (steering angle δ , accelerator x_a and brake x_b pedal position) and variables characteristic of vehicle dynamics (a_x , a_y , r , V , μ and β) that can be measured if specific sensors are available as it happens for the FEV demonstrator in Fig. 2.6. In common FEV and conventional vehicles it is usually not present a sensor for the sideslip angle β and especially for friction coefficient μ so that they require a feasible and robust real-time estimation. In the present section a theoretical state estimator is explained

and analyzed for a future and practical implementation of the TV control strategy here proposed. A brief introduction on the extended Kalman filter (EKF) is presented followed by its application to the estimation of β for sideslip angle control.

One note to be kept in mind is that an accurate estimation of the friction coefficient μ is not needed since it could lead to a wrong evaluation of r_{ref} in extreme conditions (tires saturation limits) thus causing high values of sideslip angle that can be recovered by the sideslip angle control as seen in section 2.4.2.

2.6.1 Extended Kalman Filter Theory

The Kalman filter [124–126] general objective is to find the estimation of a linear stochastic discrete-time controlled system's states $\mathbf{x} \in \mathbb{R}^n$. Furthermore, the *extended* Kalman Filter (EKF) can be also applied to non-linear systems through an idea similar to Taylor series approximation: the estimation procedure is linearized around current estimate through the partial derivatives calculation thus computing the estimation even in presence of non-linearities.

Let's assume that the system can be described by the non-linear stochastic difference equation:

$$\mathbf{x}_k = \mathbf{f}(\mathbf{x}_{k-1}, \mathbf{u}_{k-1}, \mathbf{w}_{k-1}) \quad (2.49)$$

with the measurement vector $\mathbf{y}_k \in \mathbb{R}^m$

$$\mathbf{y}_k = \mathbf{h}(\mathbf{x}_k, \mathbf{v}_k) \quad (2.50)$$

where \mathbf{w}_k and \mathbf{v}_k are respectively the process and the measurement zero-mean white noises with normal probability distribution $p(\mathbf{w}) \sim N(0, \mathbf{Q})$ and $p(\mathbf{v}) \sim N(0, \mathbf{R})$. One approximation of the system can be expressed as:

$$\begin{cases} \tilde{\mathbf{x}}_k &= \mathbf{f}(\hat{\mathbf{x}}_{k-1}, \mathbf{u}_{k-1}, \mathbf{0}) \\ \tilde{\mathbf{y}}_k &= \mathbf{h}(\tilde{\mathbf{x}}_k, \mathbf{0}) \end{cases} \quad (2.51)$$

where $\hat{\mathbf{x}}_k$ is some *a posteriori* estimation of state \mathbf{x}_k at step k . The first step of EKF is the linearization of system Eqs. 2.49 and 2.50 around the approximation states $\tilde{\mathbf{x}}_k$ and $\tilde{\mathbf{y}}_k$:

$$\begin{cases} \mathbf{x}_k &\approx \tilde{\mathbf{x}}_k + \mathbf{A}(\mathbf{x}_{k-1} - \hat{\mathbf{x}}_{k-1}) + \mathbf{W}\mathbf{w}_{k-1} \\ \mathbf{y}_k &\approx \tilde{\mathbf{y}}_k + \mathbf{H}(\mathbf{x}_k - \tilde{\mathbf{x}}_k) + \mathbf{V}\mathbf{v}_k \end{cases} \quad (2.52)$$

where \mathbf{A} , \mathbf{W} are the Jacobian matrix of partial derivatives of \mathbf{f} with respect to \mathbf{x} and \mathbf{w} meanwhile \mathbf{H} , \mathbf{V} are the Jacobian matrix of partial derivatives of \mathbf{h} with respect to \mathbf{x} and \mathbf{v} :

$$\begin{aligned}\mathbf{A}(i, j) &= \frac{\partial \mathbf{f}(i)}{\partial \mathbf{x}(j)}(\hat{\mathbf{x}}_{k-1}, u_{k-1}, 0) \\ \mathbf{W}(i, j) &= \frac{\partial \mathbf{f}(i)}{\partial \mathbf{w}(j)}(\hat{\mathbf{x}}_{k-1}, u_{k-1}, 0) \\ \mathbf{H}(i, j) &= \frac{\partial \mathbf{h}(i)}{\partial \mathbf{x}(j)}(\tilde{\mathbf{x}}_k, 0) \\ \mathbf{V}(i, j) &= \frac{\partial \mathbf{h}(i)}{\partial \mathbf{v}(j)}(\tilde{\mathbf{x}}_k, 0)\end{aligned}\tag{2.53}$$

Note that matrices \mathbf{A} , \mathbf{W} , \mathbf{H} and \mathbf{V} changes for each time step k , even it is not indicated for simplicity. The prediction error is defined as:

$$\tilde{\mathbf{e}}_{\mathbf{x}_k} \equiv \mathbf{x}_k - \tilde{\mathbf{x}}_k \tag{2.54}$$

meanwhile the measurement residual:

$$\tilde{\mathbf{e}}_{\mathbf{y}_k} \equiv \mathbf{y}_k - \tilde{\mathbf{y}}_k \tag{2.55}$$

thus obtaining equations related to the *error process*:

$$\tilde{\mathbf{e}}_{\mathbf{x}_k} \approx \mathbf{A}(\mathbf{x}_{k-1} - \hat{\mathbf{x}}_{k-1}) + \epsilon_k \tag{2.56}$$

$$\tilde{\mathbf{e}}_{\mathbf{y}_k} \approx \mathbf{H}\tilde{\mathbf{e}}_{\mathbf{x}_k} + \eta_k \tag{2.57}$$

where ϵ_k and η_k are two independent variables with zero mean and covariance matrices \mathbf{WQW}^T and \mathbf{VRV}^T . Equations 2.56 and 2.57 are linear approximation of original non-linear process expressed by Eqs. 2.49 and 2.50 thus allowing the application of discrete linear Kalman filter theory according to which an *a posteriori* estimation of $\tilde{\mathbf{e}}_{\mathbf{x}_k}$, defined as $\hat{\mathbf{e}}_k = \mathbf{x}_k - \hat{\mathbf{x}}_k$, is calculated as a linear combination of of an *a priori* estimate $\hat{\mathbf{e}}_k^-$ (which is here supposed to be zero) and measurement residual $\tilde{\mathbf{e}}_{\mathbf{y}_k}$:

$$\hat{\mathbf{e}}_k = \hat{\mathbf{e}}_k^- + \mathbf{K}_k \tilde{\mathbf{e}}_{\mathbf{y}_k} = \mathbf{K}_k \tilde{\mathbf{e}}_{\mathbf{y}_k} \tag{2.58}$$

where the matrix \mathbf{K}_k is the *Kalman gain* that minimizes the *a posteriori* error covariance $\mathbf{P}_k = \mathbf{E}[(\mathbf{x}_k - \hat{\mathbf{x}}_k)(\mathbf{x}_k - \hat{\mathbf{x}}_k)^T]$. A possible solution to the minimization problem is provided

by [124, 127, 128] where the following result is obtained:

$$\mathbf{K}_k = \frac{\mathbf{P}_k^- \mathbf{H}_k^T}{\mathbf{H}_k \mathbf{P}_k^- \mathbf{H}_k^T + \mathbf{V}_k \mathbf{R}_k \mathbf{V}_k^T} \quad (2.59)$$

where $\mathbf{P}_k^- = \mathbf{E}[(\mathbf{x}_k - \mathbf{x}_k^-)(\mathbf{x}_k - \mathbf{x}_k^-)^T]$ is the *a priori* error covariance matrix which is calculated as:

$$\mathbf{P}_k^- = \mathbf{A}_k \mathbf{P}_{k-1} \mathbf{A}_k^T + \mathbf{W}_k \mathbf{Q}_{k-1} \mathbf{W}_k^T \quad (2.60)$$

The *a posteriori* error estimation $\hat{\mathbf{e}}_k$ is finally adopted for evaluating the *a posteriori* state estimation $\hat{\mathbf{x}}_k$:

$$\hat{\mathbf{x}}_k = \tilde{\mathbf{x}}_k + \hat{\mathbf{e}}_k = \tilde{\mathbf{x}}_k + \mathbf{K}_k \tilde{\mathbf{e}}_{y_k} = \tilde{\mathbf{x}}_k + \mathbf{K}_k (\mathbf{y}_k - \tilde{\mathbf{y}}_k) \quad (2.61)$$

When the measurement error covariance \mathbf{R} approaches zero, the gain \mathbf{K}_k approaches \mathbf{H}^{-1} thus considering the actual measurement \mathbf{y}_k more reliable than predicted estimation $\tilde{\mathbf{x}}_k$. Viceversa, when the *a priori* estimate error covariance \mathbf{P}_k^- approaches zero, the gain \mathbf{K}_k approaches zero thus assuming that the predicted estimation $\tilde{\mathbf{x}}_k$ is trusted more than the actual measurement \mathbf{y}_k . The Kalman filter estimates a system by using a form of feedback control: the filter estimates the system states at some time and then obtains feedback in the form of (noisy) measurements. Equations for the Kalman filter fall into two groups: *Prediction phase* equations and the *Measurement phase* equations. The complete set of equations for EKF is reported in Fig. 2.30 where the *Prediction phase* and the *Measurement phase* are shown. During the Prediction phase, all states and

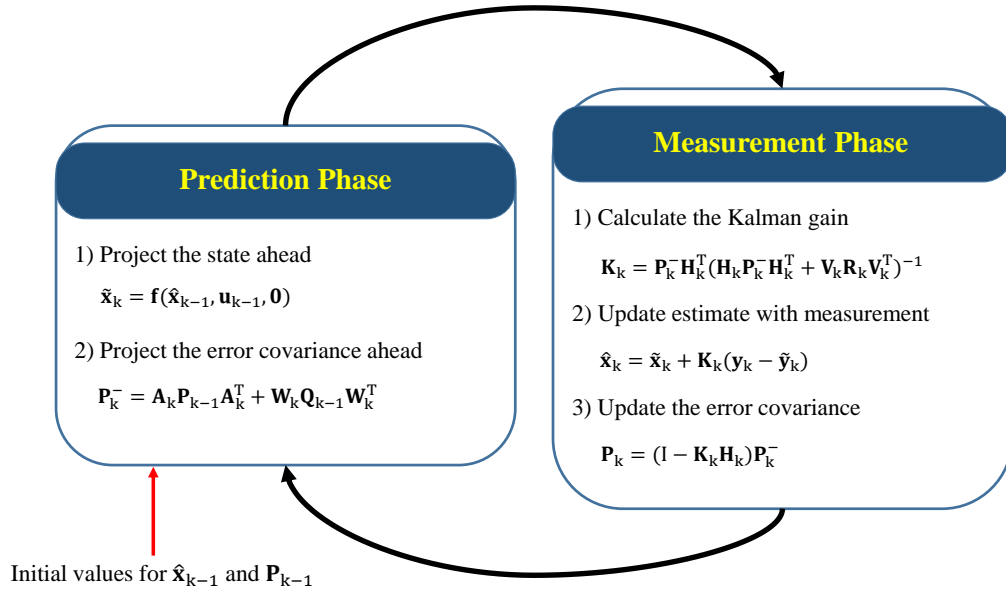


Figure 2.30 Extended Kalman Filter iterative scheme

covariance error estimates are projected forward from the previous time step $k - 1$ to the current one k to obtain the *a priori* estimates. The Measurement phase corrects the states and covariance error estimates with the measurements y_k to obtain an improved *a posteriori* estimate.

2.6.2 Sideslip angle estimation using EKF and Integral solution

The EKF equations are here adapted for the specific case of sideslip angle estimation. Lateral dynamics equations from single-track model are expressed by:

$$\begin{cases} F_{y,F} + F_{y,R} = mV(r + \dot{\beta}) \\ F_{y,F}a - F_{y,R}b + M_{z,TV} = J_z \dot{r} \\ \dot{\mu} = 0 \end{cases} \quad (2.62)$$

where $F_{y,F/R}$ are respectively total front and total rear lateral forces, $M_{z,TV}$ the external yaw moment generated by torque vectoring, V the vehicle speed, r the vehicle yaw rate, β the vehicle sideslip angle, m and J_z its mass and inertia moment and a and b the front and rear semi-wheelbase. Lateral forces $F_{y,F/R}$ are analytical evaluated through the non-linear brush model formulation:

$$F_{y,F/R} = \begin{cases} -\mu F_{z,F/R} 3\vartheta_{y,F/R} \tan \alpha_{F/R} (1 - |\vartheta_{y,F/R} \tan \alpha_{F/R}| + \frac{1}{3\vartheta_{y,F/R}^2 \tan^2 \alpha_{F/R}}) & \text{if } \alpha_{F/R} \leq \alpha_{sl,F/R} \\ -\mu F_{z,F/R} \text{sign}(\alpha_{F/R}) & \text{if } \alpha_{F/R} > \alpha_{sl,F/R} \end{cases} \quad (2.63)$$

where $F_{z,F/R}$ are the front/rear normal forces, $\alpha_{F/R}$ the front/rear axle slip angles and:

$$\vartheta_{y,F/R} = \frac{2c_p l_p^2}{3\mu F_{z,F/R}}, \quad \alpha_{sl,F/R} = \tan^{-1} \frac{1}{\vartheta_{y,F/R}} \quad (2.64)$$

where c_p and l_p the nominal values of respectively wheel cornering stiffens and half-length of tire contact patch. Front/rear axle equivalent slip angles $\alpha_{F/R}$ are given by:

$$\begin{cases} \alpha_F = -\delta_w + \beta + ra/V \\ \alpha_R = \beta - rb/V \end{cases} \quad (2.65)$$

where δ_w is the steering angle at wheel. In order to apply the EKF equations, lateral forces have to be linearized as function of the tire slip angle, vertical load and friction

coefficient:

$$F_{y,F/R} = F_y(\alpha_0, F_{z,0}, \mu_0) + \frac{\partial F_y}{\partial \alpha}(\alpha - \alpha_0) + \frac{\partial F_y}{\partial F_z}(F_z - F_{z,0}) + \frac{\partial F_y}{\partial \mu}(\mu - \mu_0) \quad (2.66)$$

By considering the discretized representation of Eq. 2.62 ($\dot{\mathbf{x}} \approx \frac{\mathbf{x}(k+1) - \mathbf{x}(k)}{\Delta t}$), the system dynamics can be described by:

$$\begin{cases} \mathbf{x}_{k+1} = \mathbf{A}_k \mathbf{x}_k + \mathbf{B}_k \mathbf{u}_k + \mathbf{E}_{x,k} + W w_k \\ \mathbf{y}_k = \mathbf{H}_k \mathbf{x}_k + \mathbf{D}_k \mathbf{u}_k + V v_k \end{cases} \quad (2.67)$$

with $\mathbf{x} = [\beta, r, \mu]^T$, $\mathbf{u} = [\delta_w, F_{z,F}, F_{z,R}]^T$ and $\mathbf{y} = [r, a_y]^T$.

Matrices \mathbf{A}_k , \mathbf{B}_k , $\mathbf{E}_{x,k}$, \mathbf{H}_k and \mathbf{D}_k have the following expression:

$$\mathbf{A}_k = \begin{bmatrix} \frac{1}{mV} \left(\frac{\partial F_{y,F}}{\partial \alpha} + \frac{\partial F_{y,R}}{\partial \alpha} \right) \Delta t + 1 & \frac{1}{mV} \left(\frac{a}{V} \frac{\partial F_{y,F}}{\partial \alpha} - \frac{b}{V} \frac{\partial F_{y,R}}{\partial \alpha} \right) \Delta t & \frac{1}{mV} \left(\frac{\partial F_{y,F}}{\partial \mu} + \frac{\partial F_{y,R}}{\partial \mu} \right) \Delta t \\ \frac{1}{J_z} \left(a \frac{\partial F_{y,F}}{\partial \alpha} - b \frac{\partial F_{y,R}}{\partial \alpha} \right) \Delta t & \frac{1}{J_z} \left(\frac{a^2}{V} \frac{\partial F_{y,F}}{\partial \alpha} + \frac{b^2}{V} \frac{\partial F_{y,R}}{\partial \alpha} \right) \Delta t + 1 & \frac{1}{J_z} \left(a \frac{\partial F_{y,F}}{\partial \mu} - b \frac{\partial F_{y,R}}{\partial \mu} \right) \Delta t \\ 0 & 0 & 1 \end{bmatrix} \quad (2.68)$$

$$\mathbf{B}_k = \begin{bmatrix} -\frac{1}{mV} \frac{\partial F_{y,F}}{\partial \alpha} \Delta t & \frac{1}{mV} \frac{\partial F_{y,F}}{\partial F_z} \Delta t & \frac{1}{mV} \frac{\partial F_{y,R}}{\partial F_z} \Delta t \\ -\frac{a}{J_z} \frac{\partial F_{y,F}}{\partial \alpha} \Delta t & \frac{a}{J_z} \frac{\partial F_{y,F}}{\partial F_z} \Delta t & -\frac{b}{J_z} \frac{\partial F_{y,R}}{\partial F_z} \Delta t \\ 0 & 0 & 0 \end{bmatrix} \quad (2.69)$$

$$\mathbf{E}_{x,k} = \begin{bmatrix} \Delta t e_1 \\ \Delta t e_2 \\ 0 \end{bmatrix} \quad (2.70)$$

where

$$\begin{aligned} e_1 &= \frac{1}{mV} \left(F_y(\alpha_0, F_{z,0}, \mu_0) - \frac{\partial F_{y,F}}{\partial \alpha} \alpha_0 - \frac{\partial F_{y,R}}{\partial \alpha} \alpha_0 - \frac{\partial F_{y,F}}{\partial F_z} F_{z,0} - \frac{\partial F_{y,R}}{\partial F_z} F_{z,0} + \right. \\ &\quad \left. - \frac{\partial F_{y,F}}{\partial \mu} \mu_0 - \frac{\partial F_{y,R}}{\partial \mu} \mu_0 \right) \\ e_2 &= \frac{1}{J_z} \left(a F_{y,F}(\alpha_0, F_{z,0}, \mu_0) - b F_{y,R}(\alpha_0, F_{z,0}, \mu_0) - a \frac{\partial F_{y,F}}{\partial \alpha} \alpha_0 + b \frac{\partial F_{y,R}}{\partial \alpha} \alpha_0 + \right. \\ &\quad \left. - a \frac{\partial F_{y,F}}{\partial F_z} F_{z,0} + b \frac{\partial F_{y,R}}{\partial F_z} F_{z,0} - a \frac{\partial F_{y,F}}{\partial \mu} \mu_0 + b \frac{\partial F_{y,R}}{\partial \mu} \mu_0 + M_{z,TV} \right) \end{aligned}$$

$$\mathbf{H}_k = \begin{bmatrix} 0 & 1 & 0 \\ \frac{1}{m} \left(\frac{\partial F_{y,F}}{\partial \alpha} + \frac{\partial F_{y,R}}{\partial \alpha} \right) & \frac{1}{m} \left(\frac{a}{V} \frac{\partial F_{y,F}}{\partial \alpha} - \frac{b}{V} \frac{\partial F_{y,R}}{\partial \alpha} \right) + V & \frac{1}{m} \left(\frac{\partial F_{y,F}}{\partial \mu} + \frac{\partial F_{y,R}}{\partial \mu} \right) \end{bmatrix} \quad (2.71)$$

$$\mathbf{D}_k = \begin{bmatrix} 0 & 0 & 0 \\ -\frac{1}{m} \frac{\partial F_{y,F}}{\partial \alpha} & \frac{1}{m} \frac{\partial F_{y,F}}{\partial F_z} & \frac{1}{m} \frac{\partial F_{y,R}}{\partial F_z} \end{bmatrix} \quad (2.72)$$

Finally, EKF prediction equation can be evaluated:

$$\tilde{\mathbf{x}}_k = \mathbf{x}_{k-1} + \Delta t \begin{bmatrix} \frac{1}{mV} (F_{y,F}|_{k-1} + F_{y,R}|_{k-1}) - r_{k-1} \\ \frac{1}{J_z} (a F_{y,F}|_{k-1} - b F_{y,R}|_{k-1} + M_{z,TV}|_{k-1}) \\ 0 \end{bmatrix} \quad (2.73)$$

with *a priori* estimate error covariance:

$$\mathbf{P}_k^- = \mathbf{A}_k \mathbf{P}_{k-1} \mathbf{A}_k^T + \mathbf{W}_k \mathbf{Q}_{k-1} \mathbf{W}_k^T \quad (2.74)$$

Meanwhile the EKF measurement equation is defined as:

$$\hat{\mathbf{x}}_k = \tilde{\mathbf{x}}_k + \mathbf{K}_k (\mathbf{y}_k - \mathbf{H}_k \tilde{\mathbf{x}}_k - \mathbf{D}_k \mathbf{u}_k) \quad (2.75)$$

with Kalman gain:

$$\mathbf{K}_k = \frac{\mathbf{P}_k^- \mathbf{H}_k^T}{\mathbf{H}_k \mathbf{P}_k^- \mathbf{H}_k^T + \mathbf{V}_k \mathbf{R}_k \mathbf{V}_k^T} \quad (2.76)$$

and *a posteriori* estimate error covariance:

$$\mathbf{P}_k = (\mathbf{I} - \mathbf{K}_k \mathbf{H}_k) \mathbf{P}_k^- \quad (2.77)$$

The estimate value of sideslip angle $\hat{\beta}_k$ is finally obtained by:

$$\hat{\beta}_k = [1 \ 0 \ 0] * \hat{\mathbf{x}}_k \quad (2.78)$$

EKF equations provides a satisfactory states estimation when the vehicle lateral behavior is well described by the single-track model that is for low values of sideslip angle β . A second strategy for β estimation, called *Integral Solution*, is thus combined with the EKF when the absolute value of sideslip angle overpasses a specific threshold (i.e. $\beta_{TH} = 8$ deg):

$$\hat{\beta}_k = \beta_{TH} + \int_{\beta_{TH}}^{+\infty} \left(\frac{a_y}{V} - r \right) dt \quad (2.79)$$

In order to experimentally validate the sideslip angle estimation, EKF algorithm has been run in post-processing by receiving as input experimental values of V , a_y , a_x , r , $M_{z,TV}$, δ_w and comparing its output with the sideslip angle sensor installed on-board by selecting a diagonal configurations for Q and R matrices and by considering a_y and r measurements more reliable than the system model (more weight on R matrix elements with respect Q matrix ones). Longitudinal acceleration a_x is used for evaluating the vertical load on front and rear axle:

$$\begin{cases} F_{z,F} = \frac{mgb}{a+b} - \frac{ma_x H_{CG}}{a+b} \\ F_{z,R} = \frac{mga}{a+b} + \frac{ma_x H_{CG}}{a+b} \end{cases} \quad (2.80)$$

where H_{CG} is the center of gravity height. The following results are obtained by post processing experimental data recorded during a step steer maneuver of 100 deg steering angle at 100 km/h executed in sport mode and reported in Figs. 2.31 and 2.32. The

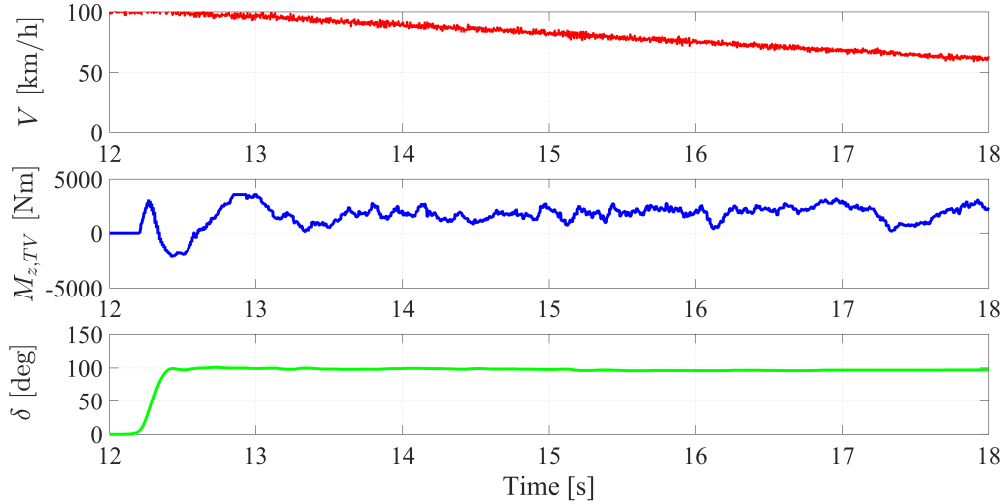


Figure 2.31 Vehicle speed V , torque vectoring yaw moment $M_{z,TV}$ and steering wheel angle δ during a step steer maneuver of 100 deg steering angle at 100 km/h executed in sport mode

sideslip angle estimation is obtained by choosing different weights on R diagonal elements thus analyzing the importance of r (weight on first diagonal element) and a_y (weight on second diagonal element) measurements when compared to experimental value recorded by sideslip angle sensor. Fig. 2.33 shows that the a_y measurements must be trusted more than r one in estimating the sideslip angle though EKF formulation.

Finally, the effect of *Integral solution* when absolute value of sideslip angle is greater than the threshold $\beta_{TH} = 8$ deg is reported in Fig. 2.34 during a step steer maneuver of 100 deg steering angle at 100 km/h executed in enhanced sport mode (thus triggering

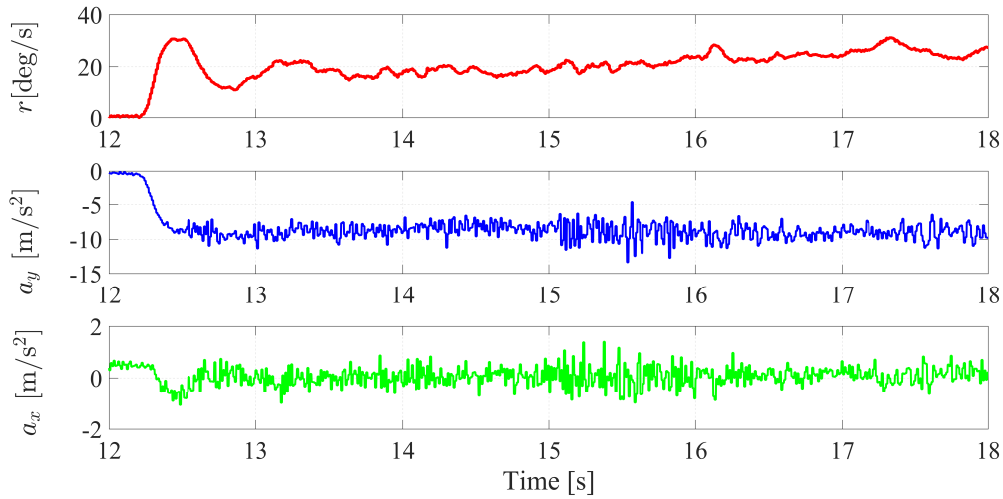


Figure 2.32 Vehicle yaw rate r , lateral acceleration a_y and longitudinal acceleration a_x during a step steer maneuver of 100 deg steering angle at 100 km/h executed in sport mode

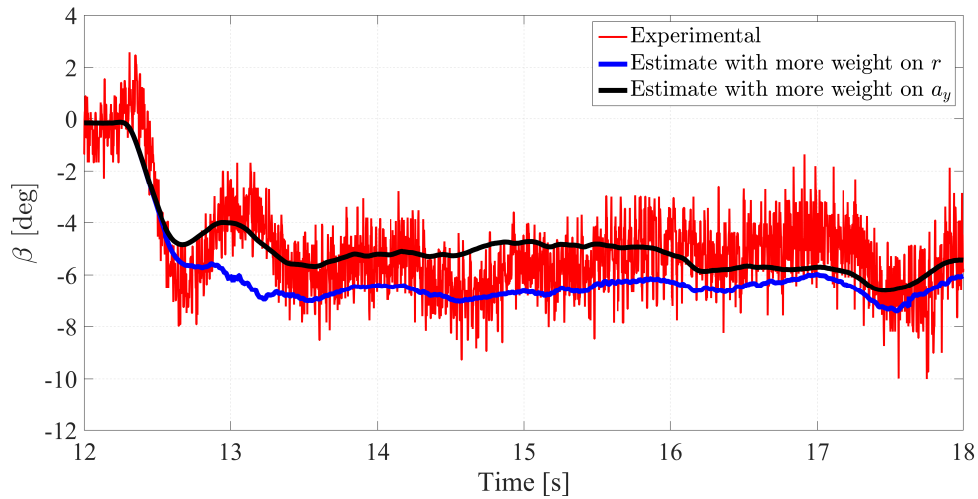


Figure 2.33 Experimental and estimate of sideslip angle β for different selection of matrix R elements

high values of sideslip angle): the figure also highlights the benefit introduced by integral solution when EKF is no more reliable for estimating the sideslip angle.

2.7 Conclusions

The research activity discussed an integral sliding mode control formulation for the concurrent control of yaw rate and sideslip angle on a four-wheel-drive electric vehicle.

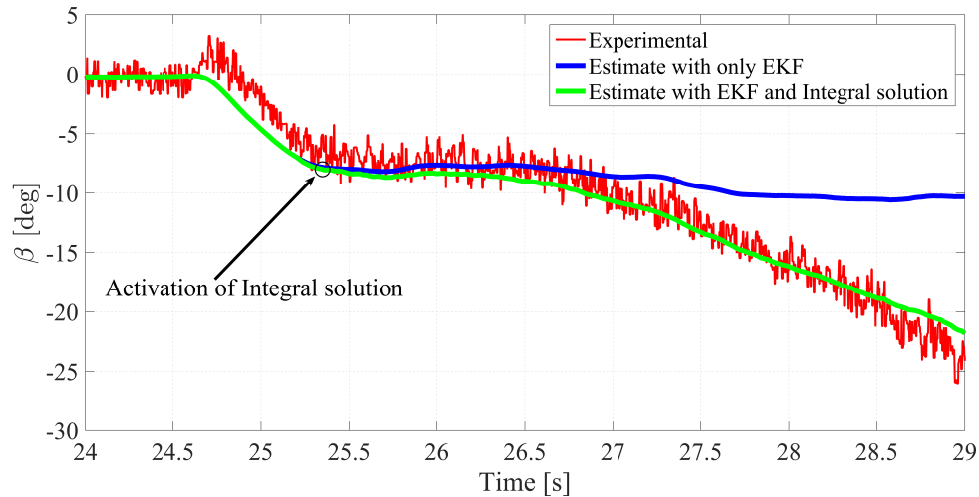


Figure 2.34 Experimental and estimate of sideslip angle β during a step steer maneuver of 100 deg steering angle at 100 km/h executed in enhanced sport mode

The comprehensive set of experimental results in steady-state and transient conditions yields the following conclusions:

- the continuous actuation of yaw rate control allows very different understeer characteristics for the same vehicle, depending on the selected driving mode
- the ISM control formulation as a perturbation compensator significantly enhances the controller tracking performance in transient conditions compared to a linear quadratic regulator with augmented states
- the Enhanced Sport mode allows to purposely induce high values of sideslip angle through the yaw rate controller, and to effectively limit them through the sideslip contribution
- the sideslip yaw moment contribution is introduced to control vehicle response in extreme conditions, such as those induced by the Enhanced Sport mode or by an overestimation of the tire-road friction coefficient. For all these conditions, the proposed sideslip controller is effective in limiting the sideslip angle to a pre-specified threshold. Despite from the theoretical viewpoint the system with simultaneous yaw rate and sideslip control is functionally uncontrollable, desirable performance of the sideslip controller can be achieved via appropriate setting of the respective weights in the LQR and ISM control designs.
- experimental tests show the real efficacy of the torque vectoring controller proposed and its reliability with low tire-road friction coefficients is proved through simulation results with an experimentally validated model

- the simple formulation and tunability of the control structure, without the need for a feedforward contribution, facilitates its industrial implementation on real vehicles
- an Extended Kalman Filter (EKF) formulation is described for future implementation where no sideslip angle sensors are available on-board and an integral solution is presented when sideslip angle reaches high values (i.e. enhanced sport mode). EKF and Integral solution are verified in post processing by considering experimental data as input for estimation process.

Chapter 3

Integration of Powertrain & Brake System Controls

3.1 Introduction

Transmission systems represent a key component in the driveline of conventional passenger vehicles since they are the mechanical link that drives energy from the source (engine) to the road through wheel contacts. They are usually classified in manual and non-manual transmissions whether gear shifting is performed respectively by the driver or by an actuation system controlled by a strategy designed for specific targets (performances, comfort or efficiency) [66, 129]. In Manual Transmissions, the gear shifting dynamics is managed by the clutch for disengaging the engine from gearbox and by the synchronizer for synchronizing the relative speed between the shafts [130, 131]. Non-manual transmissions can be further classified in Continuously Variable Transmissions (CVT), Automatic Transmissions (AT), Automated Manual Transmissions (AMT) and Dual Clutch Transmissions (DCT). CVT are designed for making available an infinite number of gear ratios by adopting a steel belt or chain thus achieving benefits from the point of view of performance and fuel economy [66, 132–134]. In AT the gear shifting is regulated by the presence of a torque converter and the gear selection is carried out by band brakes and multi-disk clutches [135, 136]. An important contribute in non-manual transmissions field is represented by Automated Manual Transmissions and Dual Clutch Transmissions: AMT have the same transmission architecture of MT with the difference that the gear shifting is executed by hydraulic or electromechanical actuator systems [137–142]; DCT have introduced a new architectures that generally consists of two clutches and two different primary shafts [143–147] (for further information see section 3.2). DCTs have been conceived for reducing the so called *torque*

gap ([137, 140, 148]) that usually arises in MT as a consequence of disengagement of the engine from the gearbox during gear shifting. The ATs mechanical architecture allows avoiding the torque interruption during a gearshifts but with the disadvantage of reducing the transmission efficiency (when the converter is slipping) with respect to MT, AMT and DCT where dry clutches are used to this aim. A counterpart effect of adopting high efficiency components in MT, AMT and DCT is that they suffer from NVH issues especially during low speed and torques maneuvers: the presence of gear backlashes together with extremely low mechanical losses can provoke undesirable noises and vibrations when the torque applied to the transmission changes its sign due to external or internal disturbances [149–152] (for further information see section 3.3).

The intent of the research presented in this chapter is to explore the potentiality of reducing noise and vibration of a vehicle transmission thanks to powertrain control integration with active braking system. Even in literature, the two systems are normally studied separately, each with its own objectives, without considering the potential benefits deriving from their integration. Only recently, carmakers are taking advantage of these systems cooperation when developing new active system concerning vehicle speed control. Let consider as an example the Adaptive Cruise Control system: last versions of this active system use automatic braking feature to adjust the car speed with the aim of maintaining a preset distance from the vehicle ahead. On the contrary, the possibility to reduce transmission noise and vibration thanks to powertrain control integration with active braking system has not been explored yet by the scientific community. In [153] a method and a device for determining and dampening juddering vibrations caused by a clutch in a drivetrain of a conventional motor vehicle is introduced. The strategy comprises the following tasks: vibration detection through a torque sensor (not included in conventional powertrain systems) placed inside the clutch, vibration amplitude determination and clutch position control for compensating torque fluctuations of drivetrain. A similar concept is proposed in [154], where the engagement pressure of a clutch in an automatic transmission is controlled with the aim of reducing stationary vibration of the vehicle and engagement and disengagement shock. According to the proposed control method, the clutch begins to slip when the strain between the drive system and the vehicle body reaches a selected value. The strain can be evaluated using one of the following sensors: a displacement sensor, a torque sensor at the output shaft of the transmission, or a sensor to measure the stress at the engine mountings. A methodology for reducing the vibration amplitude caused by clutch grabbing phenomena is shown in patent [155]. A control and regulation system can actuate different motor vehicle active devices (such as the clutch, the service brake, the electromagnetic retarder, the synchronizer and the internal combustion engine) with the aim of generating a compensatory vibration with the same or a similar frequency and a phase offset in relation

to the vibration acting in a disturbing manner. This active vibration control method requires accurate tracking performance at least up to the maximum frequency of the disturbance. A driveline preloading effect, produced by an electric motor, is considered in [156] aiming at minimizing jerks and vibrations caused by backlashes in the driveline. The control system is able to detect an imminent change in load and to react before this new loading condition is applied to the driveline. More specifically, the control system selects the shape, height and duration of a torque pulse that the electric motor must generate to take up the backlash in the driveline before the load from the drive engine is actually changed. If the pulse is properly selected, the driveline will be preloaded thus avoiding jerks and oscillations in the system. The electric motor can be coupled to the engine (directly or with a transmission) or can be positioned elsewhere in the driveline after the engine, e.g. close to the gearbox. The invention in [157] deals with a rattling noise avoidance control for a hybrid vehicle: it can be applied if the engine operating point and the driver reference torque fall within a rattling noise producing range. The control device is supposed to be mounted on a vehicle including an internal combustion engine, a first rotating electric machine for generating electric power and a second rotating electric machine that transmits a driving force to the wheel.

A new methodology is introduced in the following chapter based on a coordinate usage of powertrain and active braking system controls with the aim of improving NVH transmission performance when the vehicle undergoes critical low speed/torque maneuvers. The invention idea, described also in [158, 159], is to preload transmission components through the application of an additional engine torque and proportionally a braking torque (independently from driver intervention on brake pedal) when NVH excitations are detected in advance. It must be noted that the proposed strategy is based on an open loop torque controller which is, differently from [155], enough to guarantee the immunity to the disturbances regardless of their point of application. It is also proved that a normal production braking system with Electronic Stability Control (ESC) can be used to generate the required braking torque since they are able to generate brake pressure build-up through a motor pump regardless of the driver action on the brake pedal. There are many versions of active braking systems, providing different degrees of braking support. Different control strategies have been proposed in the past for achieving improved braking performance of vehicles during emergency scenarios [160–165]: in case an emergency is detected, the control system applies additional brake pressure in order to enhance the promptness of the braking system. In the last years, active braking systems have been re-evaluated to be integrated into the design of global chassis control strategies thus not limiting their task to emergency braking maneuvers (i.e. ABS, ESC as mentioned before). In this new scenario, the braking system is exploited for following a reference pressure in order to accomplish high level control

targets (i.e. collision avoidance) thus moving the control effort from slip ratio to brake caliper pressures. Another important application of braking pressure control is also found in Electro-Hydraulic Braking (EHB) design, which is the key feature of stability control and regenerative braking system for hybrid and electric vehicles [166, 167]. This pressure control is usually related with the application of linear solenoid valves, which are suitable for the task but also quite expensive and not available in conventional internal combustion engine driven cars. A conventional ABS/ESP unit includes a hydraulic pressure modulator with on/off digital valves normally used for slip control and not for the continuous control of the braking pressure inside the calipers. In [168, 169] a detailed electro-mechanical model of an on/off solenoid valve used to regulate brake pressure is presented; due to the valves discontinuous characteristic, PWM is often used to drive both hydraulic [170–172] and high-speed pneumatic [173] valves. The second part of the chapter proposes a new control strategy of a normal-production ABS unit in order to continuously track a reference pressure required for preloading the transmission components. In the literature review, some papers about a continuous pressure following control can be found:

- [174] presents a continuous pressure control based on sliding mode where the on/off valves are modeled as a second order dynamic system;
- in [169] an open-loop controller is designed and the output of the control is the current of the On/Off digital valves;
- in [172] a PI control has been developed using standard feedback linearization techniques on a nonlinear validated model;
- in EHB applications [166, 167], proportional solenoid valves are used for the pressure following control;

Differently from other literature works, the pressure following controller here presented is designed from an experiments-based description of brake pressure dynamics. Since ABS valves dynamics is highly nonlinear and characterized by uncertainties, experiments on a Hardware-In-the Loop (HIL) Brake System Test bench have been carried out to build an experimental model of ABS on/off valves specifically used for the design of a Feed-Forward (FF) and Proportional Integral (PI) control logic based on PWM regulation of conventional on/off digital valves (described also by the author in [175, 176]).

The chapter is structured as follows: in section 3.2 a brief overview of Dual Clutch Transmissions architectures and operating description is presented; section 3.3 is focused on NVH sources that can trigger vibrations or noises in a DCT; in section 3.4 the high level part of control strategy for enhancing NVH performance is explained with simulation

results meanwhile the low level logic about braking system actuation and control is described in section 3.5; finally section 3.6 shows some experimental results from HIL test bench to validate the efficacy of control logic and section 3.7 reports some final conclusions and future recommendations.

3.2 Overview of Dual Clutch Transmissions

In recent years, vehicle fuel economy and passenger comfort has becoming a key factor in transmission design and development. In this contest, Dual Clutch Transmissions (DCT) started to take root in automotive industry due to their feature of keeping the power flow between engine and wheels during the gear shift and avoiding the so called 'torque gap': this usually occurs in MT transmissions when the driver disengages the clutch to allow the gear shifting thus interrupting the vehicle traction.

DCT architecture appears for the first time as a concept idea for heavy commercial vehicles, but a first real implementation arises for racing cars developments: the control quality of the systems was not sufficiently suitable for serial production until 2003. The key idea is to develop a transmission system which is able to achieve high efficiency values typical of AMT/MT and shift-ability/comfort features characteristic of AT.

The solution proposed by DCT lies in its architecture which is characterized by the presence of two clutches, two primary shafts (one with odd gears and one with even gears) and eventually two secondary shafts (where synchronizers are mounted) which engage on the same differential ring (dotted gray line in Fig. 3.1): two parallel power flows are thus generated between the engine and driven wheels.

As an example, assume that the clutch $K1$ is fully close so that the engine torque is transferred to the wheel through the first gear engagement between primary shaft $P1$ and secondary shaft SI , as indicated by the blue path in Fig. 3.1. If the second gear is preselected (with clutch $K2$ fully open) on secondary shaft SS , a certain amount of power (red path) is absorbed from the differential to sustain the dragged path (primary shaft $P2$ and secondary shaft SS) rotations. This strategy allows a proactive engagements of the second gear before the driver or the controller logic requests an up-shift from the first to the second gear. In this configuration, the second gear is already engaged and the synchronization process is obtained through a suitable and precise slip control of both clutches $K1$ and $K2$ ([177]). It is of interest noting that the synchronisers are not mounted between two consecutive gears, as in traditional MT, since the pre-selection of the next gear occurs when the present gear is still engaged and transmitting torque to the wheels. From a kinematic point of view, gear shifting of a dual clutch transmission

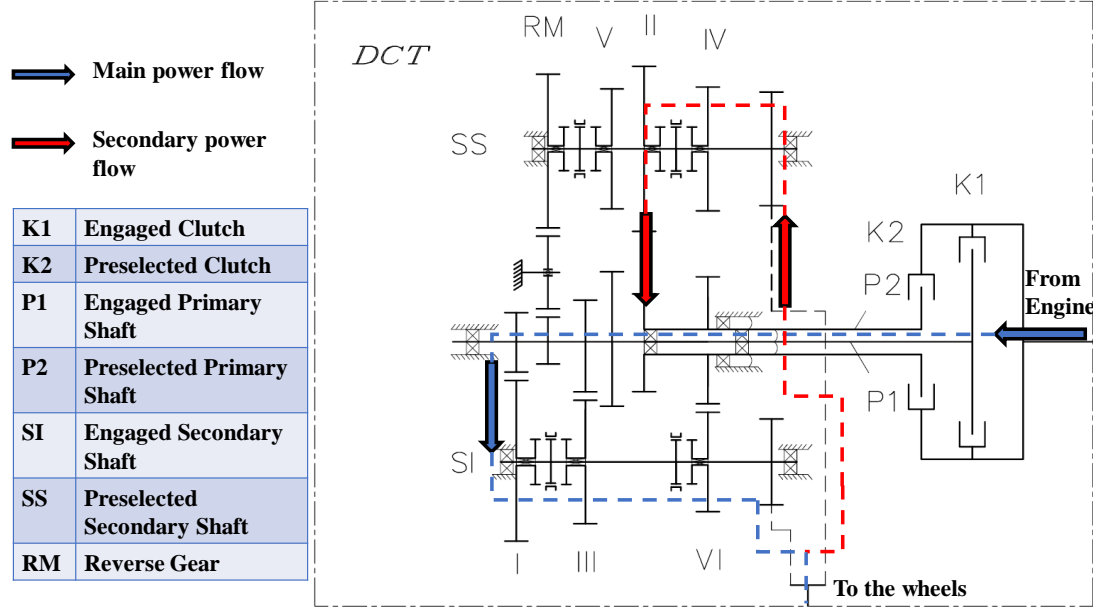


Figure 3.1 General scheme of a DCT with two secondary shafts architecture and power flow representation

is similar to that of a clutch-to-clutch shift in a conventional automatic transmission (AT). However, the two types of transmissions show different dynamic characteristics since AT are equipped with torque converters that dampen shift transients. Dynamic performance of DCT and the relating driver perceptions strongly depend on the control system whose main task is to generate the reference signals both for synchronisers and clutches. DCT architecture is able to provide a better dynamics behavior with respect MT one by ensuring a better performance in acceleration and a more comfortable drivability as a consequence of the continuous torque transmission during gear shifting. In contrast to these positive aspects, DCT systems are more complicated, both in mechanical components and in the control effort for clutches control. Furthermore, the presence of two clutches and of a greater number of bearings leads to a reduced efficiency with respect to MT or AMT gearboxes; however, their efficiency is still better if compared to automatic transmissions with torque converters and continuously variable transmissions (CVT). An important characteristic of DCT is that two different gear ratios are engaged at the same time: the TCU must avoid the concurrent lock of the two clutches in order to prevent damages to the gearbox.

3.3 NVH Issues

Dual Clutch Transmissions show high efficiency properties (for example with respect to automatic transmissions) and avoid the interruption of the power flow from the engine to the wheels during shifting maneuvers (powershift). These advantages are achieved with the expenses of increased complexity, due to the introduction of a second clutch and two primary-secondary shafts, with the consequent increment of gears.

All mechanical transmissions based on ordinary gear trains and adopting synchronizers to perform gear engagement (MT, AMT and DCT), have the highest levels of energy efficiency but suffer from NVH (Noise, Vibration and Harshness) issues especially during low speed maneuvers, when a very low level of torque is transferred from the prime mover to the wheels: gear backlashes can cause some undesired noises when the transmission is not enough preloaded. This usually happens when the torque transmitted by the engine is sufficient to move the vehicle at constant low speed leaving the transmission particularly sensitive to disturbances. During these scenarios typical of everyday urban driving situations, external disturbances coming from the road (i.e. speed-bump or bumpy road) or internal disturbances coming from the engine (i.e. tip out maneuvers) can provoke a sudden contact force inversion between gears thus causing teeth impacts and noise generation (clonk and rattle). A greater torque transmitted from the engine to the wheels led to a bigger preload effect inside the transmission which becomes less sensitive to disturbances.

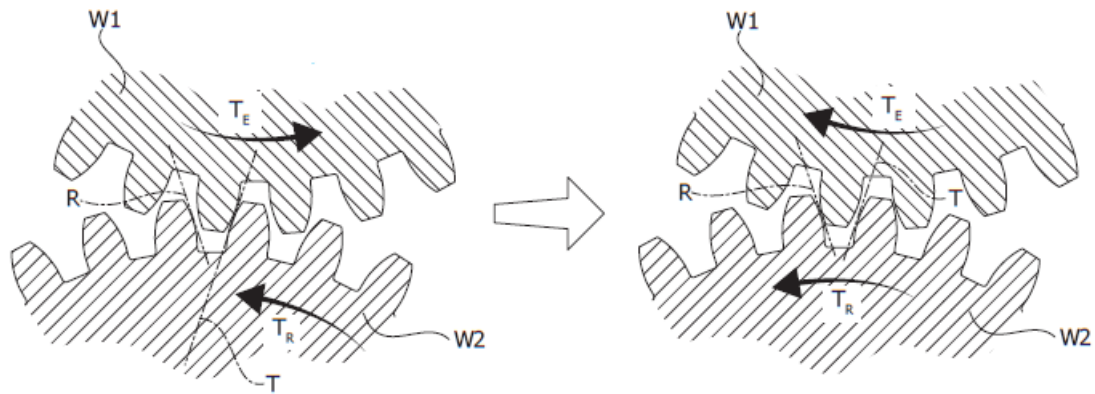


Figure 3.2 Gear Impact

It is noteworthy that this problem is particularly evident in all transmissions designed for high efficiency which are characterized by extremely low mechanical losses: the presence of internal non-negligible friction torques provide a contact-condition between rotating parts even in absence (or with a low level) of mechanical power transmitted through the gearbox. This means that the cost for having a high efficient transmissions

is the reduction of damping, and so the friction losses between rotating parts, thus increasing disturbances sensitivity.

Among transmissions typologies, the automatic ones are definitely less influenced by noise issues during maneuvers at low speed due to the presence of a torque converter providing a filtering effect of noises sources. However, they present lower efficiencies and a dynamic behavior that doesn't match desired driver performances, especially for European market. From this point of view, manual transmissions with one or two clutches are preferred for their dynamical and shifting performances with the counterpart of being more influenced by noises and vibrations. In particular, Dual Clutch Transmissions present an active branch where the power flows from the engine to the wheels (first clutch close) and a passive branch not engaged (second clutch open) which also represents a weak point in terms of NVH.

3.3.1 NVH Excitations

NVH excitations can be categorized between internal and external triggers depending on the origin of the disturbance: if it comes from the road then it is considered an external trigger, otherwise, e.g. if due to the driver's action, it is classified as an internal one. In order to better visualize the problem, two different maneuvers are here presented to be representative of the NVH issues for a classic DCT transmission by considering internal and external excitations:

1. tip-out maneuver: instantaneous release of the gas pedal
2. speed-bump maneuver: speed bump crossing at low speed (lower than 10 km/h)

Internal Trigger - Tip-out maneuver

This is a classic urban scenario where the driver is forced to push and release the gas pedal as a consequence to a traffic queue. When the gas pedal is released (tip-out), the driver requested engine torque fall down instantaneously to zero thus drastically reducing the load on the transmission. The following plots are obtained by using an experimentally validated vehicle model whose main features are:

- front wheel drive medium car data;
- only longitudinal vehicle dynamics is modeled (no lateral dynamics);

- 6-speed DCT lumped parameter model including rotational backlashes, gears contact stiffness, inertia of components and an accurate description of power losses inside the gearbox (bearings, seals, oil drags), see [151] for more details;
- infinitely stiff powertrain mounting system, see e.g. [178] for the effect of powertrain mounts compliance on torsional transmission dynamics;
- transient nonlinear Pacejka tire model [179].

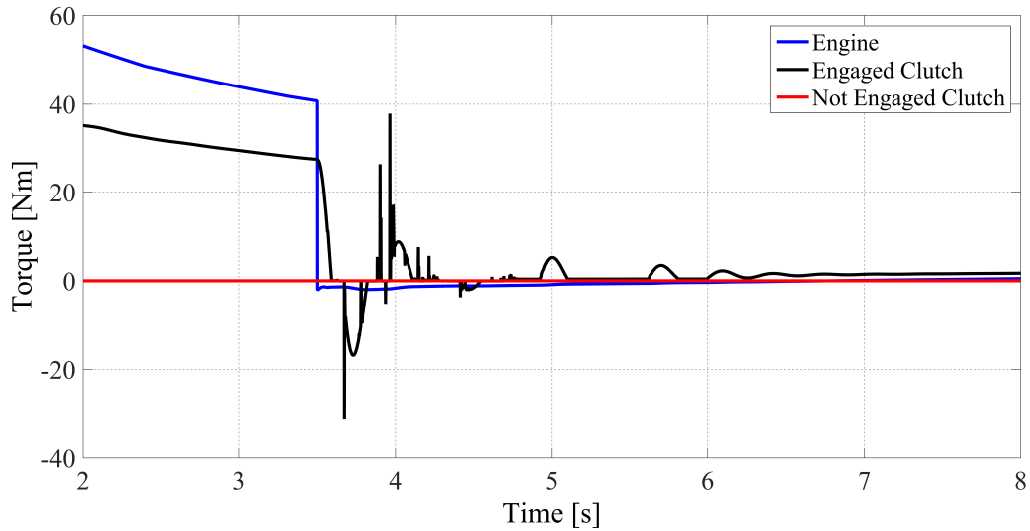


Figure 3.3 Tip-out maneuver: engine & clutches torques

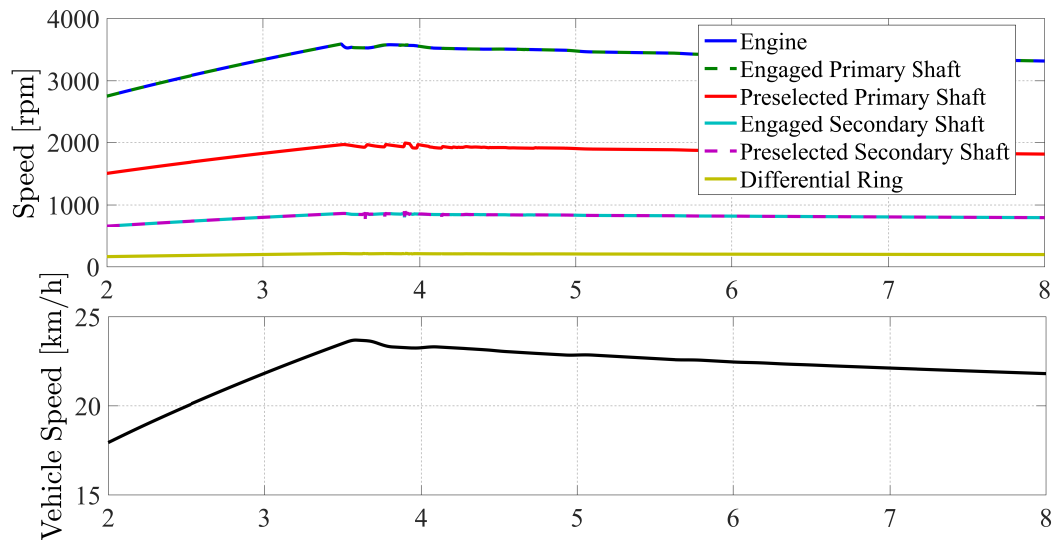


Figure 3.4 Tip-out maneuver: vehicle and transmission speeds

The maneuver simulated in Figs. 3.3 and 3.4 describes a vehicle initially accelerating with first gear engaged and second gear preselected; then the driver instantaneously

releases the gas pedal after 3.5 seconds: the engine torque is abruptly cut-off thus leading to an inversion of gear teeth contact surface with consequent noises and vibration inside the transmission. The kinematic variable $\Delta\vartheta$ has been introduced for evaluating the contact flank of gear teeth; these variables are usually adopted for the angular positions difference between driving and driven gears and between gears and their correspondent synchronizer teeth.

In the first case, the angular positions difference is relative to the driving shaft through the specific gear ratio:

$$\Delta\vartheta_i = \vartheta_{i,P} - \tau_i \vartheta_{i,S}$$

where $\vartheta_{i,P}$ is the angular position of i_{th} primary shaft gear, $\vartheta_{i,S}$ is the angular position of i_{th} secondary shaft gear and τ_i their correspondent gear ratio.

In the second case, the angular positions difference is between the gear engaged or preselected and its correspondent pinion shaft:

$$\Delta\vartheta_{syn,i} = \vartheta_{i,n} - \vartheta_{pin,n}$$

where $\vartheta_{i,n}$ is the angular position of i_{th} gear placed on n_{th} shaft and $\vartheta_{pin,n}$ is the angular position of correspondent n_{th} shaft.

A positive value of $\Delta\vartheta$ means a gears contact on the the "active" teeth surface (when the power flows from the engine to the wheels) and, viceversa, a negative value of it means a gears contact on the "passive" teeth surface (when the power flows from the wheels to the engine). A null value of $\Delta\vartheta$ represents a condition where gear teeth is placed between the "active" and "passive" surfaces, with no contact occurring.

Fig. 3.5 shows that a change of teeth contact surfaces happens when the engine torque is reduced to zero thus provoking teeth oscillations and consequently noises. The first evident aspect is that $\Delta\vartheta$ is positive for the engaged shaft since the power flows through it from the engine to the wheels and part of that is absorbed by the preselected shaft (negative value of $\Delta\vartheta$) through the differentials which represents a mechanical node. Moreover, higher frequency vibrations characterize the preselected shaft since the second clutch is not engaged to the engine: oscillations generated on the engaged shaft are amplified on the preselected one.

In the last plot of Fig. 3.5, similar conclusions can be drawn for the final gear engagement of both shafts with the differential ring and for gear backlashes inside the differential gearbox. In particular, the angular displacement inside the differential box is indicated with:

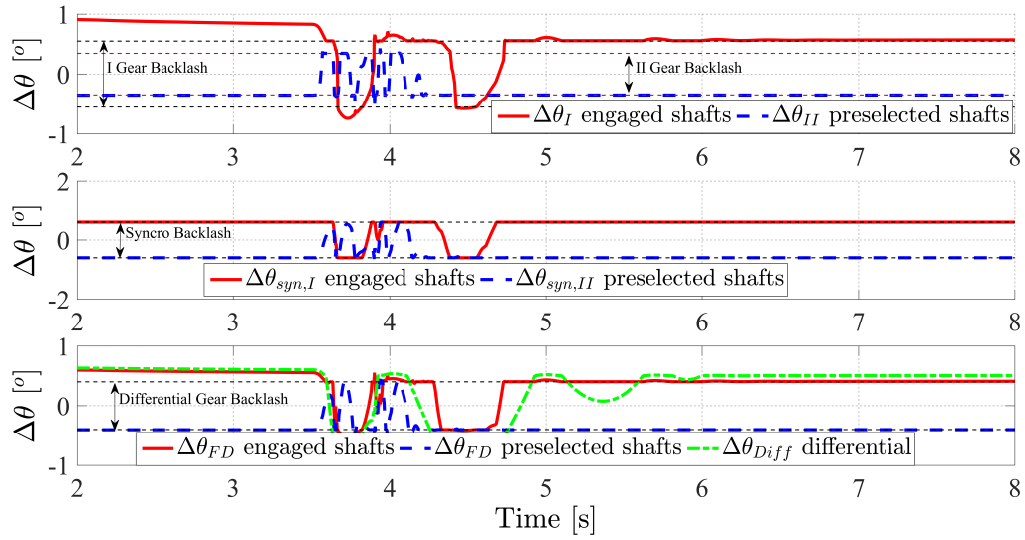


Figure 3.5 Tip-out maneuver: Angular Position Differences $\Delta\theta$; I: First gears - II: Second gears - FD: Final Drive gears - Diff: Differential gears

$$\Delta\theta_{Diff} = \vartheta_{DC} - \vartheta_{sun}$$

where ϑ_{DC} is the differential ring angular position and ϑ_{sun} is the sun gear angular position.

External Trigger - Speed-bump maneuver

An alternative source of disturbance that triggers transmission vibrations can come from a variation of the resistance torque induced by road irregularities like the speed bump analyzed in this section. If the vehicle is moving at low constant speed while crossing the speed bump, it will undergo a longitudinal acceleration variation as indicated in Fig. 3.6.

During the hill-up side of the bumper the vehicle speed is reduced (if the engine torque imposed by the driver is constant) while speed is recovered during the hill-down side of the bumper. Due to the low vehicle speed, the torque required by the engine is extremely small (less than 10 Nm) thus allowing the wheel torque load to invert transmission gears contact flank especially on the preselected shaft.

The following plots, obtained by using the same simulation model adopted in the previous section, show the results during speed-bump crossing maneuver when the vehicle is traveling at a constant speed of 7 km/h (engine torque constant during the whole maneuver).

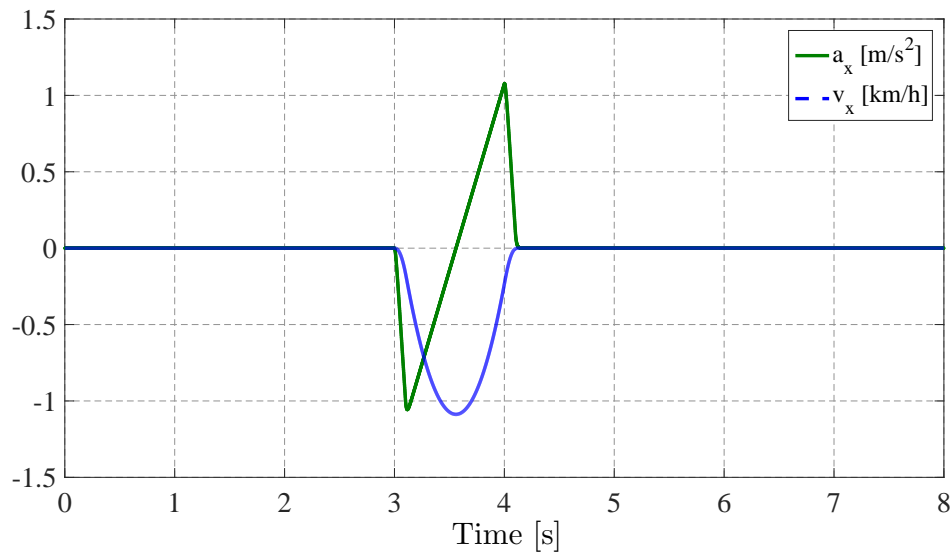


Figure 3.6 Speed-bump maneuver: disturbance longitudinal acceleration and speed

The disturbance coming from the bumper modifies the vehicle speed of less than 1 km/h but it is sufficient to trigger gears teeth hitting as indicated in Fig. 3.8.

Before the speed-bump crossing, an engine torque of about 3 Nm is required for keeping constant the vehicle speed but it is not high enough to guarantee a sufficient preload to the transmission shafts. It is noticeable that also in this case, gear teeth change their contact surfaces thus triggering oscillations as particularly evident on the preselected shaft.

3.4 Braking System Integration: High Level Logic

Previous sections have shown two examples of possible NVH excitations inside a DCT transmission with the conclusion that whether the disturbance comes from engine or wheel transmission side, a common solution can be proposed: primary and secondary transmission shafts have a non negligible stiffness so that a torque transmitted from the engine to the wheels provoke a deformation which can better tighten the rotational parts to each other. This has the same effect of a spring preload in order to compress always the spring even in presence of an external force/disturbance. The "preload effect" on the transmission can prevent the gears to change the contact flank during torque transients. Based on this principle, a preload on transmission shafts can be obtained by controlling the braking wheel torque together with the engine torque. The control intervention must be as smooth as possible and such that the driver doesn't feel the control action: the desired braking torque needs to be compensated by increasing engine torque in order to

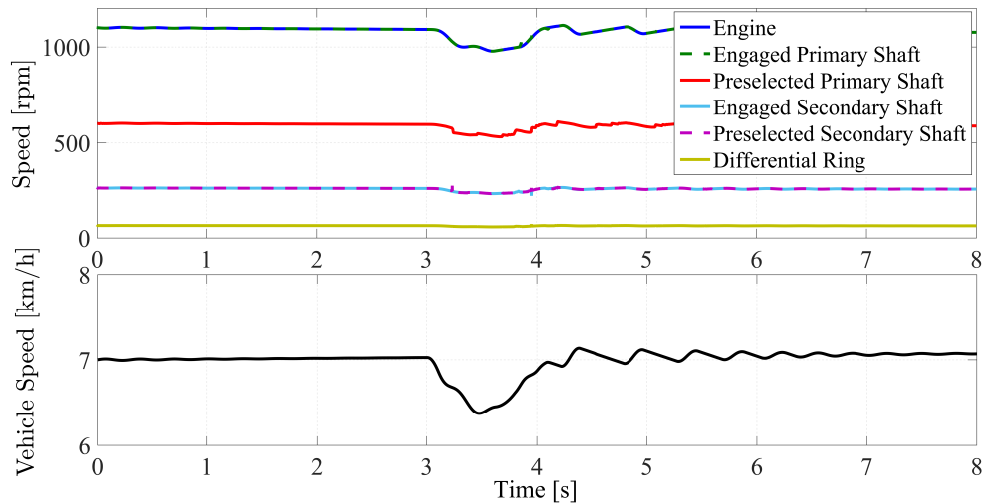


Figure 3.7 Speed-bump maneuver: vehicle and transmission speeds

keep the longitudinal speed unchanged.

The controller strategy, represented by the general scheme of Fig. 3.9 can be described with two phases:

1. proactive detection of NVH sources through the use of sensors or estimation techniques (High level control).
2. activation of braking system, together with engine control, for generating a torsional preload (Low level control)

3.4.1 Detection of NVH Sources

The first phase must be always promptly actuated in order to allow brake and engine control enough time to preload the transmission and avoid noise generation.

In the case of disturbances coming from the road, the detection of irregularities (i.e. speed-bump) must be evaluated before the driven axle cross it by adopting optical sensors or 3D laser scan systems able to map the field and recognize the disturbance with enough resolution. A noteworthy case is the rear-wheel drive powertrain configuration since the disturbance can be detected by specific sensors mounted on the front non-driven axle: a front suspension position transducer, an accelerometer and a good estimation of vehicle speed could provide enough information to the powertrain and brake control unit to promptly react on the rear axle (this concept will be verified through future investigations).

As regard noises internal excitations (i.e. sudden reduction of engine torque during Tip-Out maneuvers), their prediction is easier since it can exploit DCT gear shift algorithms

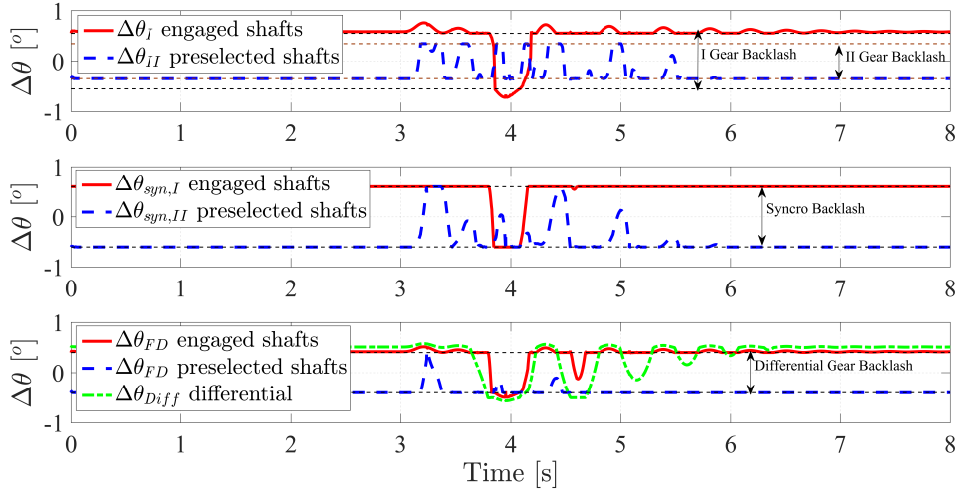


Figure 3.8 Speed-bump maneuver: angular position differences $\Delta\theta$; I: First gears - II: Second gears - FD: Final Drive gears - Diff: Differential gears

already implemented in the control unit; gears preselection on the non-engaged shaft is already based on driver behavior prediction. Signals measured by other on-board sensors related to the vehicle dynamics, such as longitudinal acceleration or wheel speed sensors used by ABS logic, can be further adopted in combination with the transmission control unit.

For other NVH excitations not described here but which can trigger gear oscillations because of a low engine torque value, the controller activation can depend on a threshold torque value $T_{Diff,min}$ applied to the differential ring that must be calibrated based on the desired noise immunity level: if the torque applied to the differential is lower than $T_{Diff,min}$, for example due to a reduction of the torque transmitted by the engaged clutch, the braking system is activated. To avoid the addition of a sensor for measuring the torque applied to the differential ring, the brake intervention condition can be evaluated as follow:

$$T_{K1}\tau_{K1} + T_{K2}\tau_{K2} < T_{Diff,min} \quad (3.1)$$

where T_{K1} is the torque transmitted by the engaged clutch, T_{K2} is the torque transmitted by the other clutch and τ_{K1} , τ_{K2} are the correspondent total gear ratio from the clutch to the differential ring. When Eq. 3.1 is satisfied, a desired brake torque is required:

$$T_{B,req} = MAX(0, T_{Diff,min} - (T_{K1}\tau_{K1} + T_{K2}\tau_{K2})) \quad (3.2)$$

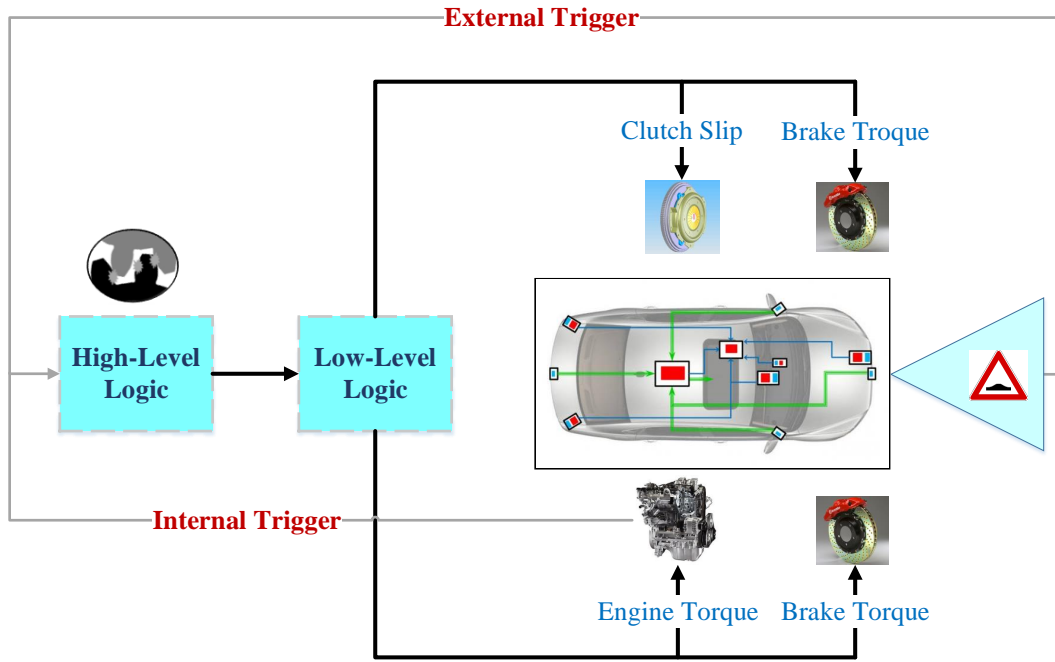


Figure 3.9 Controller Strategy for Noises Reduction

where $T_{B,req}$ represents the desired braking torque to preload the transmission. As mentioned before, the control action shouldn't modify the vehicle speed in order to avoid the driver perception of it: for this reason the torque T_{K1} must be incremented through the engine control or the clutch actuation:

$$\Delta T_{K1} = T_B / (\eta_T \tau_{K1}) - (T_{K2} \tau_{K2}) / \tau_{K1} \quad (3.3)$$

where T_B is the current wheel brake torque and η_T is the transmission efficiency.

3.4.2 Simulation concept proof

In order to demonstrate the efficacy of the methodology described in the previous section, the Tip-Out and Speed-Bump maneuvers are simulated by applying to the front axle a brake torque.

Fig. 3.10 shows that a constant braking torque of 200 Nm is applied three seconds before the release of gas pedal which is compensated by an increment of engine torque calculated by Eq. 3.3: when the gas pedal is released, there is still a residual engine torque

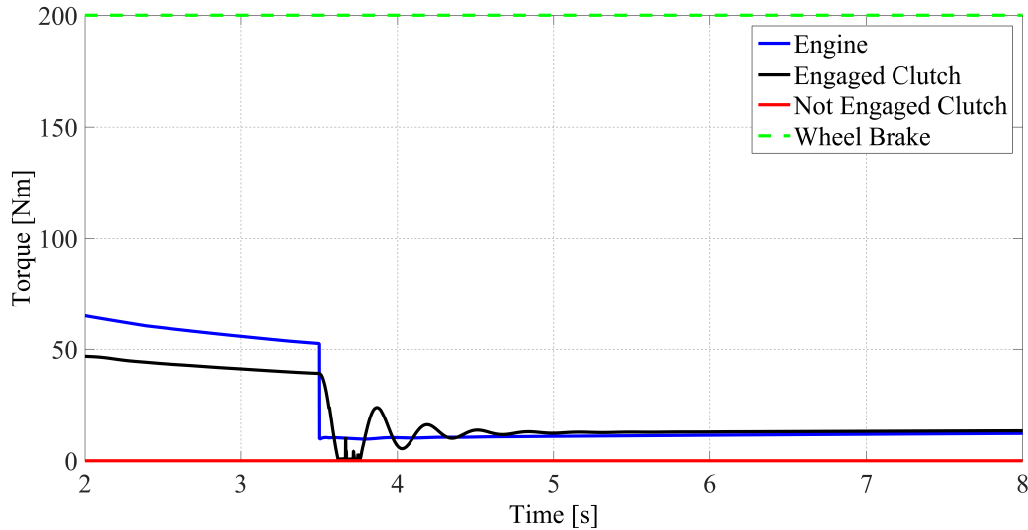


Figure 3.10 Tip-out maneuver: Torques applied to the Transmission

for compensating the braking torque and keep unchanged the vehicle speed with respect the passive configuration.

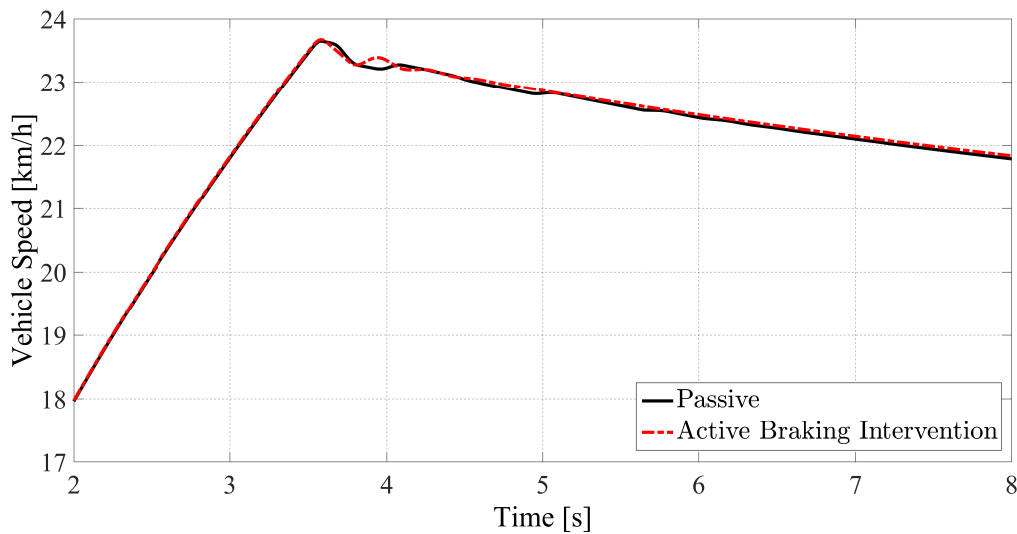


Figure 3.11 Tip-out maneuver: Vehicle Speed for Passive and Active configuration

As highlighted in Fig. 3.11, the speed of the vehicle (active) is kept as close as possible to the passive (without a noise reduction controller) vehicle since the driver should only appreciate the noise reduction without any changes to the conventional longitudinal dynamic behavior. The only drawback of the controller is the fuel consumption used for keeping unaltered the passive vehicle speed: a feasible calibration of braking action is required for a better tradeoff between noises rejection performance and energy consumption.

In order to appreciate the effect of braking intervention in terms of noises reduction, the angular position differences between rotational parts are proposed in the following plots by distinguishing between the engaged and the preselected shafts.

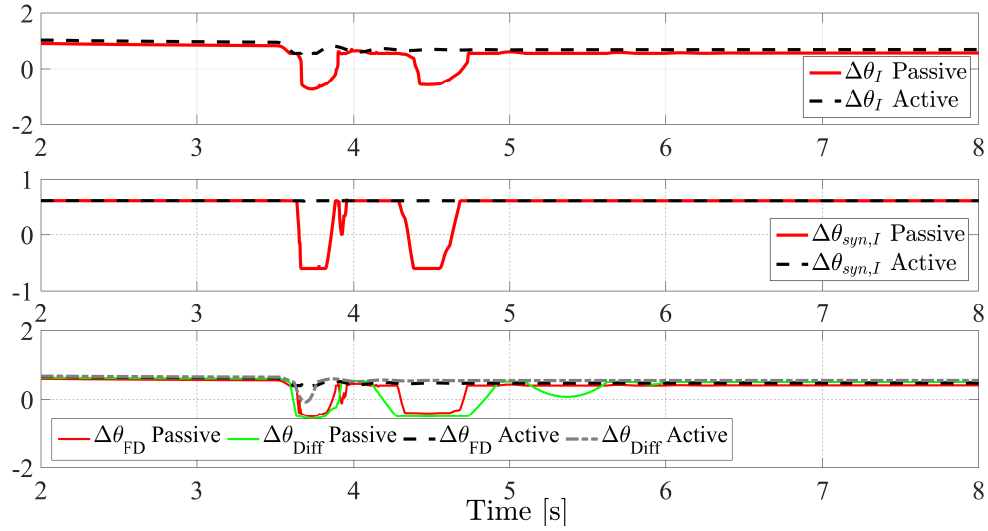


Figure 3.12 Tip-out maneuver: $\Delta\theta$ on the engaged shaft for active and passive configurations; I: First gears - II: Second gears - FD: Final Drive gears - Diff: Differential gears

Fig. 3.12 clearly proves the efficacy of the braking integration for transmission noises rejections on the engaged shaft: the combination of the brake action together with engine torque compensation guarantees a sufficient preload effect between rotational parts thus avoiding oscillations inside their backlashes. Moreover, the effect of braking action on the preselected shaft is described by the Fig. 3.13.

It is evident that the braking intervention is effective for mitigating oscillations between rotational parts even if some changes of teeth flank are still present on the preselected shaft (Fig. 3.13). Furthermore, $\Delta\theta$ on the preselected shaft is negative which means that the power flows in opposite direction with respect the engaged shaft. The main reason is because part of the power from the engine to the wheel (through the engaged shaft) is used to drive also the preselected shaft which is disengaged from the engine. A further solution is to couple the brake intervention with the second clutch (here indicated with K2) slip control in order to guarantee a sufficient preload effect on both transmission shafts. As an example, the K2 clutch slip is controlled in order to have a torque of 2 Nm transmitted on the preselected shaft and a torque calculated by Eq. 3.3 transmitted on the engaged shaft.

Fig. 3.14 proves what was stated before: based on Eq. 3.3, part of engine torque is removed from the engaged shaft and applied to the preselected one thus increasing its preload effect. This is also quite evident from the modification of the gear teeth

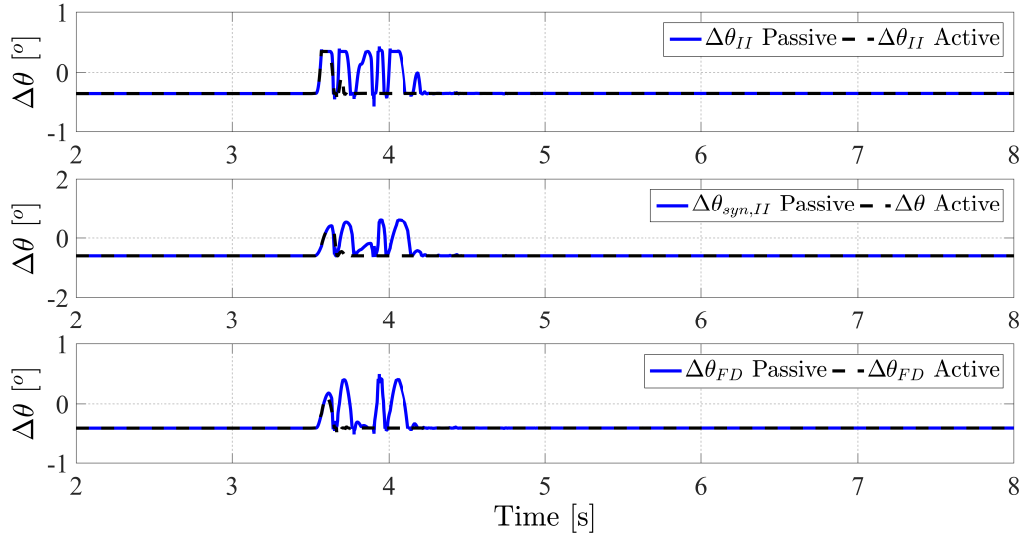


Figure 3.13 Tip-out maneuver: $\Delta\theta$ on the preselected shaft for active and passive configurations; I: First gears - II: Second gears - FD: Final Drive gears

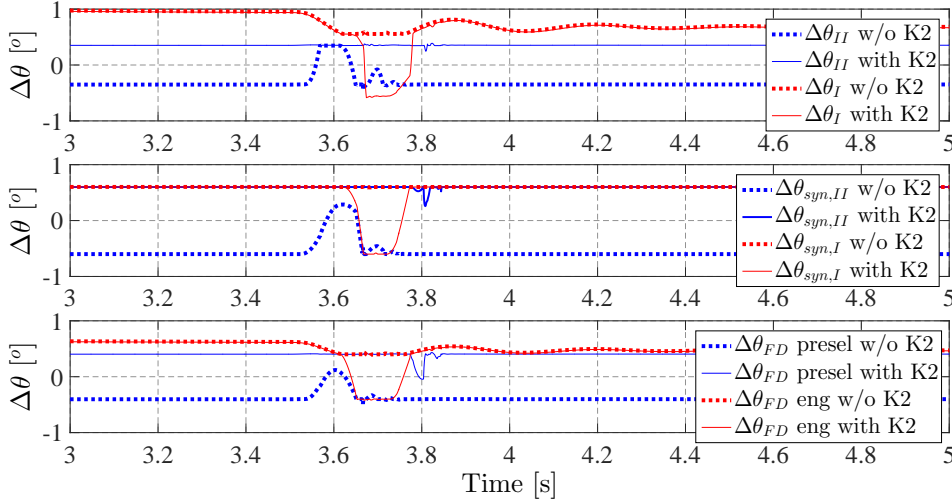


Figure 3.14 Tip-out maneuver: $\Delta\theta$ for Brake Intervention with and without K2 clutch slip control; I: First gears - II: Second gears - FD: Final Drive gears

contact surfaces: the $\Delta\theta$ becomes positive in the case of clutches position control thus implying that even the preselected shaft is driven by the engine. This second solution (brake and K2 slip controls) changes the torque distribution between the engaged and preselected shaft, and in particular it reduces the torque transmitted from the engaged shaft, as indicated in Eq. 3.3, thus reducing the preload effect on it. For this reason, the selection of torque transmitted by the K2 clutch requires a further calibration in order to have the desired noise reduction level on both transmission drivelines. Finally, the conclusion about the Tip-Out maneuver is that a brake intervention, without clutch control, is enough to guarantee a total oscillations rejection effect on the engaged shaft

and a partial benefit on the preselected shaft; a further degree of control can be provided by K2 clutch regulation with the aim at obtaining the same noise rejection level on the whole transmission but it requires a more advanced calibration of torques transmitted by not-engaged clutch.

A similar description is shown for the Speed-Bump maneuver and simulation results are here summarized:

- brake intervention when the bumper is detected, with no longitudinal dynamic perturbation and same constant speed (Fig. 3.15)

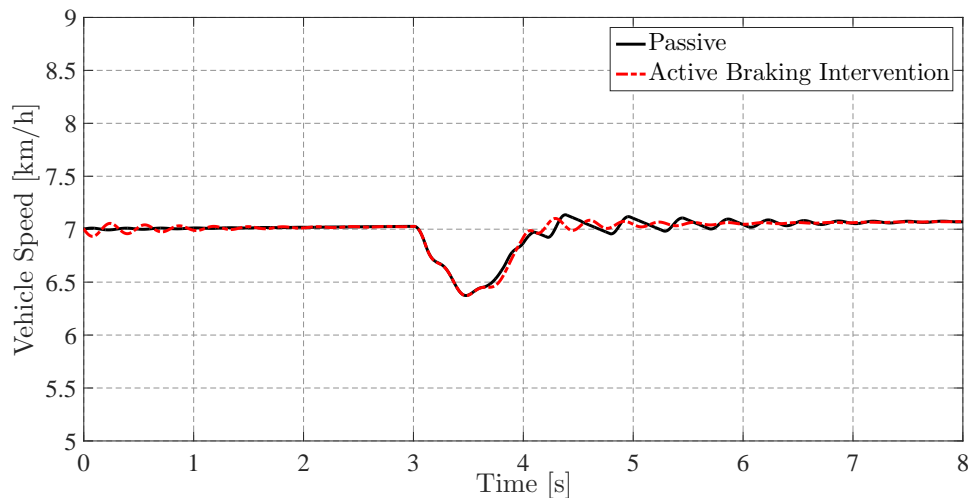


Figure 3.15 Speed-Bump maneuver: vehicle speed for passive and active configurations

- brake torque control is able to provide a total oscillations rejection on the engaged shaft (Fig. 3.16)
- brake torque control is able to provide a partial oscillations rejection on the preselected shaft (Fig. 3.17)
- brake torque and not-engaged K2 clutch slip control is able to provide a global oscillations rejection inside the whole transmission (Fig. 3.18)

Finally, the simulation results obtained with the Tip-Out and Speed-Bump maneuvers have shown the efficacy of a combined engine and brake torque control on the oscillations reduction between rotational components of engaged shaft, preselected shaft and differential gears. Furthermore, a feasible control of K2 clutch slip coupled with the brake intervention can improve the noises rejection level on the preselected shaft. The following section will discuss the low level control logic to obtain the desired noise reduction level inside the powertrain.

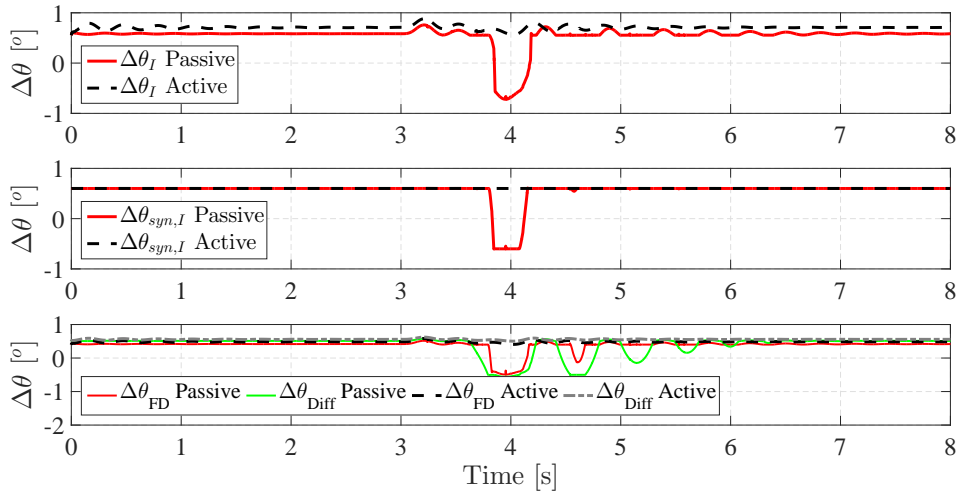


Figure 3.16 Speed-Bump maneuver: $\Delta\theta$ on the engaged shaft for active and passive configurations; I: First gears - II: Second gears - FD: Final Drive gears - Diff: Differential gears

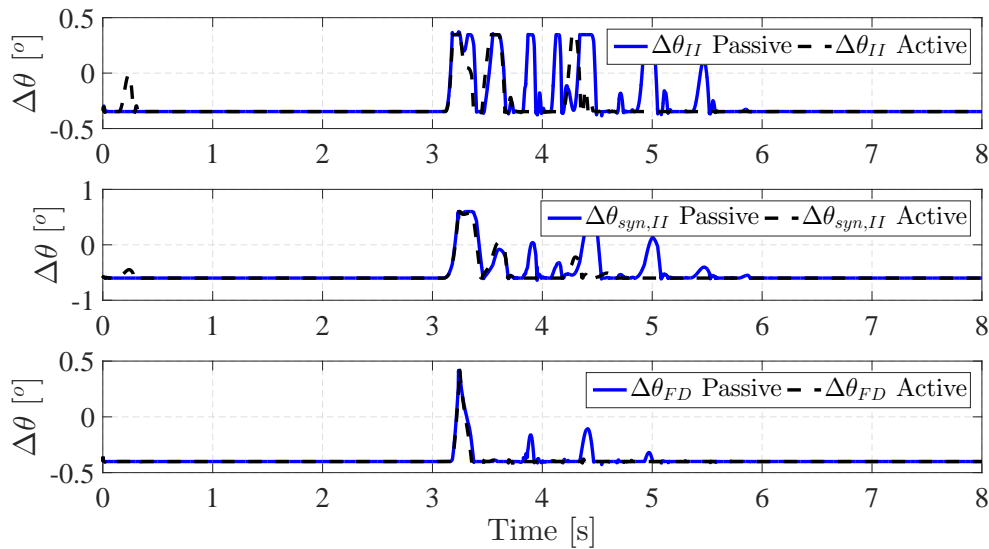


Figure 3.17 Speed-Bump maneuver: $\Delta\theta$ on the preselected shaft for active and passive configurations; I: First gears - II: Second gears - FD: Final Drive gears

3.5 Braking System Intervention: Low Level Logic

When the NVH excitation is detected and brake torque $T_{B,req}$ with engine compensation are calculated, the brake and powertrain systems must be actuated to provide the desired torsional preload effect. Three different actuation interventions can be used for the noise reduction control strategy:

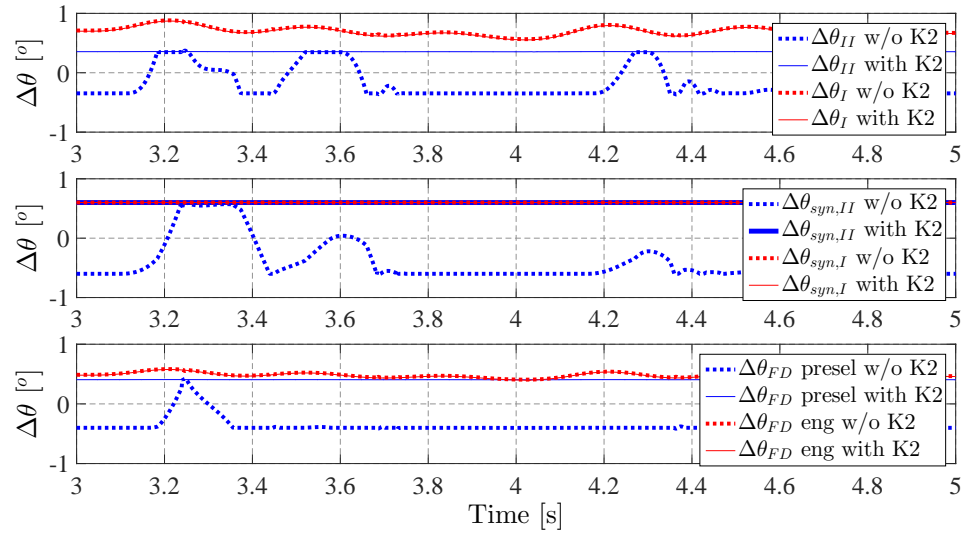


Figure 3.18 Speed-Bump maneuver: $\Delta\theta$ for brake intervention with and without K2 clutch slip control; I: First gears - II: Second gears - FD: Final Drive gears

- ABS/ESC actuation for brake caliper pressure control in order to obtain a brake torque on the driven wheel axle: brake torque intervention must be the same between right and left wheels for avoiding an undesired turning effect.
- actuation of the clutch related to the preselected shaft in order to constraint it from engine side and let be the brake intervention as effective as on the engaged shaft.
- intervention of engine control unit to modify the engine torque in order to compensate the speed reduction due to the previous two interventions.

The second intervention aims to generate a torsional preload on the preselected shaft since it introduces an alternative power flow from the engine to the wheels. The first two interventions represent dissipative contributions which require an increment of input power from the engine side (third intervention) thus restoring the longitudinal dynamic equilibrium reached before the control action.

The low level controller needs the intervention of three independent actuators by means the engine, the transmission (for clutch axial position) and the braking systems. Among these systems, the last one is the most critical from the point of view of a continuous control logic design; the hardware already mounted on conventional passenger cars allows an easy and fast implementation of clutch position and engine torque controls but the regulation of the wheel braking torque is not so automatic even because the ABS/ESC systems are designed to be active only during emergency situations. Moreover, ABS/ESC controls is not intended to have a desired brake torque but to achieve the max wheel slip ratio to reduce the braking distance: this task doesn't require a continuous

control of brake caliper pressure (and so brake torque), thus limiting the hydraulic hardware to on-off digital valves for regulating oil flow rate inside calipers. The following sections propose a method to characterize the dynamic behavior of a normal production hydraulic brake system through experiments on a hardware-in-the-loop (HIL) test bench for both modeling and control tasks. The activity is relative to analyze, model and control ABS/ESC digital valves, aiming at obtaining reference tracking and disturbance-rejection performance similar to that achievable when using pressure proportional valves.

The first section is focused on the development of a mathematical model which emulates the pressure dynamics inside brake caliper when ABS/ESC inlet valves, outlet valves and motor-pump are controlled by a digital or PWM signal. The model takes into account some inherent non-linearities of these systems, e.g. the variation of fluid bulk modulus with pressure while inlet and outlet valves together with the relay box are modeled as second order systems with variable gains. The HIL test rig is used for both parameters identification and model validation, which will be used for control strategy development. The last section deals with the design of a non-linear brake caliper pressure controller for a conventional ABS/ESC system and the experimental validation of its tracking performances. The control strategy is based on a Feedforward (FF) and a Proportional Integral (PI) controller through a Pulse Width Modulation (PWM) with constant frequency and variable Duty Cycle (DC).

3.5.1 Braking Test Rig

The HIL test rig shown in Fig. 3.19 includes a hydraulic braking system composed of a tandem master cylinder (TMC), a customized ABS/ESC hydraulic unit and four brake calipers located on non-rotating disks. A hydraulic power unit using a double effect cylinder with flow proportional valve emulates the brake pedal action. The ECU of ABS/ESC system is customized to get a direct command to the motor-pump and to each single valve by means of digital control signals. Valves and motor-pump solenoids are powered by a 12 V DC line through solid state relays, one for each of the twelve valves and one for the motor-pump. Relays control signals can be equal to 5 V (relay 'On') or 0 V (relay 'Off') according to TTL logic levels.

The bench is equipped with a set of sensors necessary for monitoring and control:

- 8 pressure sensors: one for each brake caliper (4), one for each TMC chamber (2) and one for each brake pedal cylinder chamber (2)
- 1 potentiometer for double-effect hydraulic cylinder rod position.

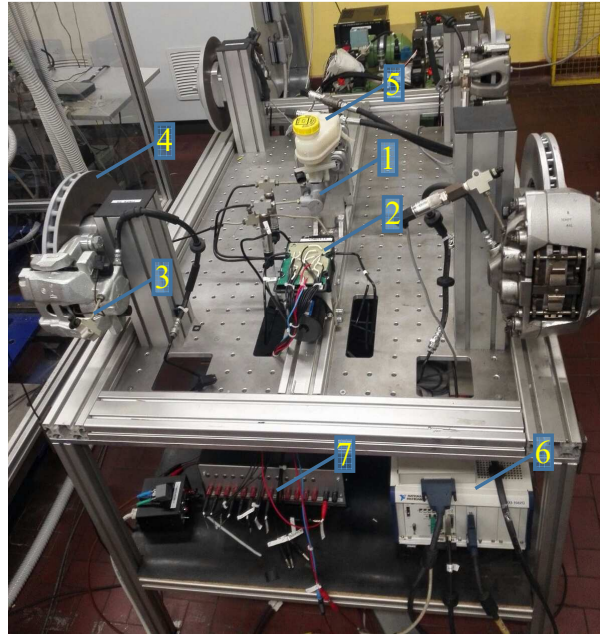


Figure 3.19 HIL Test Rig 1-TMC 2-customized ESC 3-Brake caliper 4-Brake disk 5-oil tank 6-Data Acquisition System 7-Relay Box

A model of the hydraulic system was developed in Matlab[®]/Simulink[®] while a real time system manages the data acquisition process and the deployment of the system model together with its control logic. In particular, experiments are handled by using:

- NI Labview[®] Real-Time for data acquisition and system identification processes
- NI Veristand[®] NI for control and hardware-in-the-loop tasks

The real time system enables to send control signals to each valve and motor-pump by using a digital board together with the relays-box.

In this configuration, a model of the system based on experimental data has been realized in order to evaluate its accuracy with respect to the real system and/or to design suitable control logic.

3.5.2 Hydraulic system model

The simplified scheme of hydraulic circuit composed by the TMC, inlet and outlet valves and front/rear brake calipers is represented in Fig. 3.20. The hydraulic connections

between the two TMC chambers with the four calipers is typical of a 'X' scheme, where the first chamber delivers oil to Front Left (FL) and Rear Right (RR) calipers meanwhile the second chamber delivers oil to Front Right (FR) and Rear Left (RL) calipers. Since the paper is concentrated on the pressure dynamics inside one brake caliper (i.e. RR brake caliper), the FR-RL hydraulic behavior is represented by an equivalent hydraulic circuit.

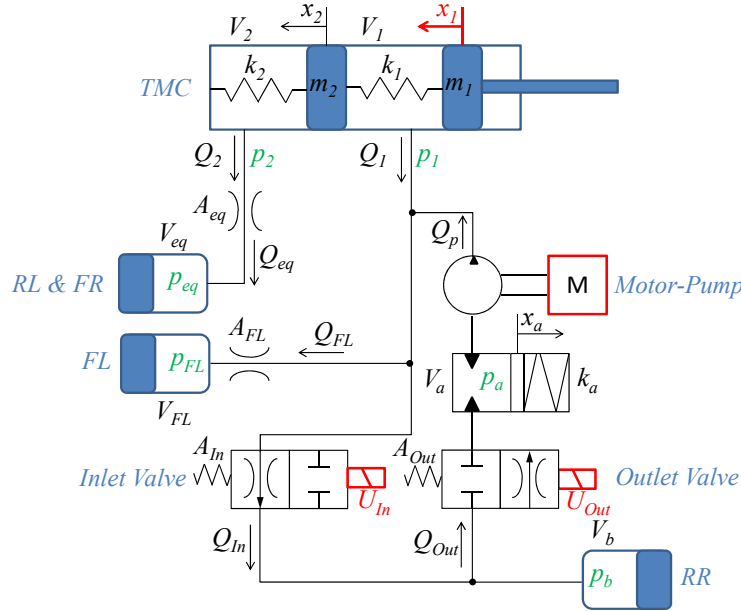


Figure 3.20 Representation of ABS/ESC hydraulic circuit with input (red) and output (green)

The TMC axial dynamics can be described as a 2 d.o.f (displacements x_1 and x_2) system but since x_1 represents an input, a unique equation is sufficient to describe the motion of the system:

$$m_2 \ddot{x}_2 + F_{f2} \text{sgn} \dot{x}_2 - b_1 (\dot{x}_1 - \dot{x}_2) + b_2 \dot{x}_2 - k_1 (x_1 - x_2) + k_2 x_2 = (p_1 - p_2) S \quad (3.4)$$

where k_i is the stiffness of the i_{th} spring, m_i the mass of i_{th} element, b_i the oil viscous damping coefficient of the i_{th} chamber, F_{f2} the Coulomb friction coefficient, S the hydraulic cylinder surface and p_i the pressure inside the i_{th} chamber of TMC.

The spring hydraulic accumulator is modeled as a 1 d.o.f (piston displacement x_a) dynamic system:

$$m_a \ddot{x}_a + b_a \dot{x}_a + F_{fa} \text{sign} \dot{x}_a + k_a x_a = p_a S_a \quad (3.5)$$

where k_a , m_a , b_a , F_{fa} , S_a and p_a are respectively the stiffness, mass, viscous damping coefficient, Coulomb friction coefficient, cylinder surface and oil pressure in the spring accumulator.

The two ports of the TMC and each valve orifice can be considered as hydraulic resistances, so flow rates Q can be calculated respectively as :

$$\left\{ \begin{array}{lcl} Q_{In} & = & c_{q,In} A_{In} \sqrt{\frac{2|p_1 - p_b|}{\rho}} \operatorname{sgn}(p_1 - p_b) \\ Q_{Out} & = & c_{q,Out} A_{Out} \sqrt{\frac{2|p_b - p_a|}{\rho}} \operatorname{sgn}(p_b - p_a) \\ Q_{FL} & = & c_{q,FL} A_{FL} \sqrt{\frac{2|p_1 - p_{FL}|}{\rho}} \operatorname{sgn}(p_1 - p_{FL}) \\ Q_{eq} = Q_2 & = & c_{q,eq} A_{eq} \sqrt{\frac{2|p_2 - p_{eq}|}{\rho}} \operatorname{sgn}(p_2 - p_{eq}) \\ Q_1 & = & Q_{In} + Q_{FL} - Q_p \end{array} \right. \quad (3.6)$$

where Q_i is the flow rate through the i_{th} element and A_i the flow area of the i_{th} component (see Fig. 3.20). The flow coefficient $c_{q,i}$ depends on the pressure drop Δp across the hydraulic resistance:

$$c_{q,i} = c_{q,max} \tanh\left(2 \frac{\lambda}{\lambda_{cr}}\right) \quad (3.7)$$

$$\lambda = \frac{h_d}{\nu} \sqrt{\frac{2|\Delta p|}{\rho}} \quad (3.8)$$

where h_d is the hydraulic diameter, ν the kinematic viscosity, ρ the oil density, $c_{q,max}$ the maximum value of the flow coefficient at which it asymptotically approaches for $\lambda \gg \lambda_{cr}$; λ_{cr} is the critical flow number at which transition from laminar to turbulent flows occurs.

The 2 TMC chambers are modeled as variable volume hydraulic capacities, while brake calipers as fixed volume capacities by means of the following equation:

$$\frac{dp_i}{dt} = \frac{\beta_i}{V_i} (\pm Q_i - \dot{V}_i) \quad (3.9)$$

where $i = 1, 2, FL, eq$ and flow rate is positive when it flows inside the volume V_i . β is the bulk modulus of hydraulic fluid and it is considered a function of pressure p_i :

$$\beta_i = \beta_n \frac{1 + \alpha \left(\frac{p_{atm}}{p_{atm} + p_i}\right)^{1/n}}{1 + \alpha \frac{(p_{atm})^{1/n}}{n(p_{atm} + p_i)^{\frac{n+1}{n}}} \beta_n} \quad (3.10)$$

where α is the relative gas content at atmospheric pressure p_{atm} , β_n is the pure liquid bulk modulus and n is the gas-specific heat ratio.

Similarly, the dynamics of brake caliper pressure p_b and spring accumulator pressure p_a are respectively evaluated by :

$$\frac{dp_b}{dt} = \frac{\beta_b}{V_b}(Q_{In} - Q_{Out} - \dot{V}_b) \quad (3.11)$$

$$\frac{dp_a}{dt} = \frac{\beta_a}{V_a}(Q_{Out} - Q_p - \dot{V}_a) \quad (3.12)$$

The TMC chambers may change their volumes due to the displacements of the two pistons:

$$V_2 = V_{20} - Sx_2 \quad (3.13)$$

$$V_1 = V_{10} + S(x_2 - x_1) \quad (3.14)$$

with V_{10} and V_{20} respectively the initial value of the first and second chamber of the TMC when no forces are applied.

The variation of volumes V_{FL}, V_{eq} and V_b , are neglected, i.e.: $\dot{V}_{FL} \approx 0, \dot{V}_{eq} \approx 0, \dot{V}_b \approx 0$ (fixed volume hydraulic chambers).

Volumes V_{eq} , V_{FL} and flow areas A_{eq} , A_{FL} are related to V_b and A_{In} by the following equations:

$$\begin{cases} V_{FL} = q_{FL} V_b \\ V_{eq} = V_{FL} + V_b \\ A_{FL} = A_{In} \\ A_{eq} = 2A_{In} \end{cases} \quad (3.15)$$

where coefficient q_{FL} represents the proportional relation between front hydraulic cylinders volume and rear one.

The flow rate generated by the pump Q_p is influenced by the spring accumulator pressure p_a since when the intake pressure is too low the motor-pump is unable to deliver any flow rate:

$$Q_p = Q_{ss}[1 - e^{-3p_a/p_{th}}] \quad (3.16)$$

where Q_{ss} is the steady-state value of flow rate delivered by motor-pump and p_{th} represents the pressure threshold at which the flow rate drops to zero.

Finally, inlet and outlet valves dynamics are modeled with a cascade series of time delays and a second-order transfer functions with non constant static gain which is a function of PWM DC of input signal:

$$\frac{A_i(s)}{U(s)} = \frac{G_s}{\frac{s^2}{\sigma_n^2} + \frac{2\zeta s}{\sigma_n} + 1} \quad (3.17)$$

where s is the Laplace variable, A_i the effective inlet/outlet flow area, U is the input solenoids valve (Voltage), G_s is the static gain, σ_n is the system natural frequency and ζ is its damping ratio.

The model inputs for the model are the position of TMC rod x_1 (which represents the brake pedal position in a common passenger car) together with the command signal for inlet, outlet valves and motor-pump while the outputs are the pressures of each brake calipers, the pressures of the two TMC chambers and x_2 .

Model Parameters identification

All the parameters introduced by equations 3.3- 3.17 and reported in table 3.1 have been either measured, extracted from technical specifications or experimentally estimated.

Masses m_2 , m_a spring stiffness k_2, k_a and cylinder surfaces S , S_a have been measured from the technical drawings. Oil density ρ and kinematic viscosity ν have been derived from DOT 4 brake fluid properties; The parameters characterizing the oil flow through an orifice like maximum flow coefficient $c_{q,max}$, and critical flow number λ_{cr} are reported in table 3.1. These coefficients are supposed constant and not subjected to parameter identification.

The Bulk modulus variations are modeled with the non-linear relation described by Eq. 3.10. β_n and α are identified in order to describe the non-linear dependence by oil pressure of bulk modulus which heavily influences pressure dynamics: in Fig. 3.21 the effect of a step change of the inlet control signal, from fully closed to fully open, considering a null initial brake pressure is shown. In the meanwhile TMC rods moves from the initial position to a final steady state position. Different values of β_n and α are tested in simulation in order to find optimal values to match the experimental trend (reported in table 3.1). All experimental pressure trends measured by sensors have been filtered with a digital zero-phase filter characterized by a cut-off frequency of 50 Hz in order to better highlight the comparison with simulation results where high frequency contents are not modeled.

Eq. 3.9 states that pressure derivative depends on volume V_i , and on total flow rate Q_i entering or exiting the volume V_i . Effective values of valves flow area A_i and chambers volume V_{i0} , V_i together with unknown damping coefficients b_2, b_a and friction forces F_{f2}, F_{fa} have been experimentally identified through the following tests: the starting

Table 3.1 Model parameters for break pressure dynamic non-linear model

Symbol	Description	Value
A_{In}	Inlet valve flow Area	0.29 mm^2
A_{Out}	Outlet valve flow Area	0.59 mm^2
b_1, b_2	TMC viscous damping coefficient	100 Nms/rad
b_a	Accumulator damping coefficient	85 Nms/rad
$c_{q,max}$	Max Flow Coefficient	0.7
F_{f2}	TMC Friction Force	14 N
F_{fa}	Accumulator Friction Force	0 N
k_1	First Spring Stiffness	2222.2 N/m
k_2	Second Spring Stiffness	4000 N/m
k_a	Accumulator Spring Stiffness	35 N/m
m_2	Second TMC Mass	40 g
m_a	Accumulator Mass	10 g
n	Gas specific heat ratio	1.4
p_{th}	Pressure threshold for Pump Flow Rate	0.6 bar
Q_{ss}	Pump Flow Rate	0.26 l/min
S	TMC Thrust Surface	5.07 cm^2
S_a	Accumulator Thrust Surface	2.54 cm^2
V_{10}	First TMC Volume Chamber	18.8 cm^3
V_{20}	Second TMC Volume Chamber	12.5 cm^3
V_b	Brake Volume	338.9 cm^3
α	Relative gas content at atmospheric pressure	0.02
β_n	Pure Liquid Bulk Modulus	27000 bar
ζ	Damping ratio of electro-mechanics valve	35 %
λ_{cr}	critical flow number	100
ρ	Oil Density	1070 kg/m^3
σ_n	Natural frequency of electro-mechanics valve	251 rad/s
ν	Kinematic viscosity	$100e^{-6} \text{ kg/(ms)}$

steady-state condition is when the TMC rod is pushed until TMC pressures p_1 , p_2 reach a desired initial values (i.e. 130 bar) with inlet valves completely open and outlet valves completely closed (which represents their normal configuration). From this initial condition, the RR inlet valve is closed and the RR outlet valve is opened together with the

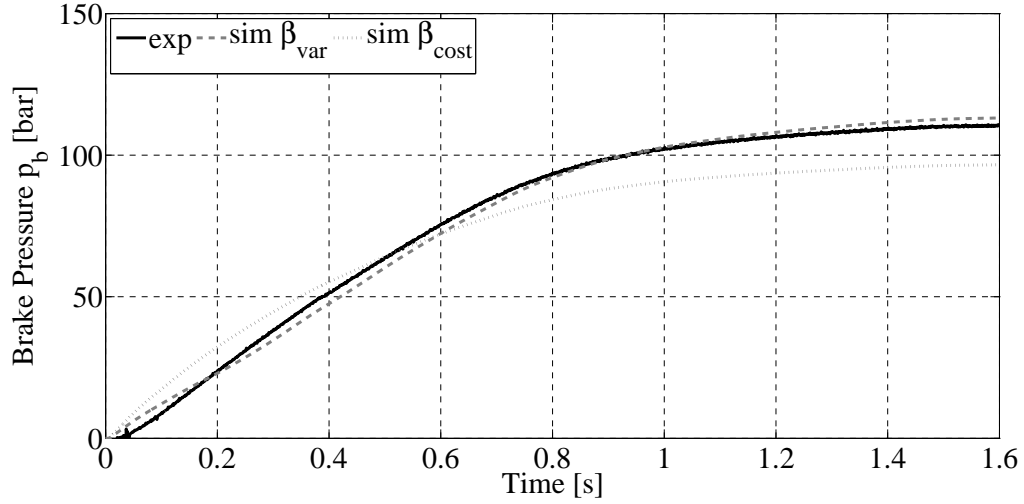


Figure 3.21 Influence of Bulk modulus on brake pressure trend: experimental (solid black line) vs simulation with constant β (dotted gray line) and with non-linear β (dashed gray line)

activation of the motor-pump, thus emptying the RR brake caliper (falling phase). Once all pressures have stabilized, the outlet valve is closed with the motor-pump switched off and the inlet valve is opened, thus filling the RR brake caliper (raising phase).

The 'raising phase' is used to identify volumes V_b , V_{FL} , V_{eq} of each brake caliper, initial TMC volumes V_{01} , V_{02} and flow areas A_{In} , A_{FL} , A_{eq} . By a curve-fitting procedure between the time history of simulated pressures p_1 , p_2 , p_{eq} , p_{FL} and p_b and their experimental values, it has been possible to identify the parameters V_b , q_{FL} , A_{In} , V_{01} and V_{02} . Fig. 3.22 shows the comparison between experimental data and simulation results considering the best combination of unknown parameters. Volumes V_b and V_{0i} influence the steady-state values at which all pressures tend after an initial transient phase which is mainly characterized by A_{In} .

Effective values of unknown damping coefficient b_2 and friction force F_{f2} cannot be easily identified from experimental data since position x_2 is not measured. Reasonable values are chosen for simulations and a post-processing analysis of their influence on pressure dynamics is reported in Fig. 3.23 where it is possible to understand how b_2 influences the transient behavior while F_{f2} affects the steady-state value of TMC and brake pressures. More specifically, an increase of b_2 causes a larger transient pressure difference between the two TMC chambers and a slower response of inlet valve without affecting steady-state behavior. An increase of F_{f2} provokes a steady-state pressure difference between the two TMC chambers without modifying considerably the valve transient phase.

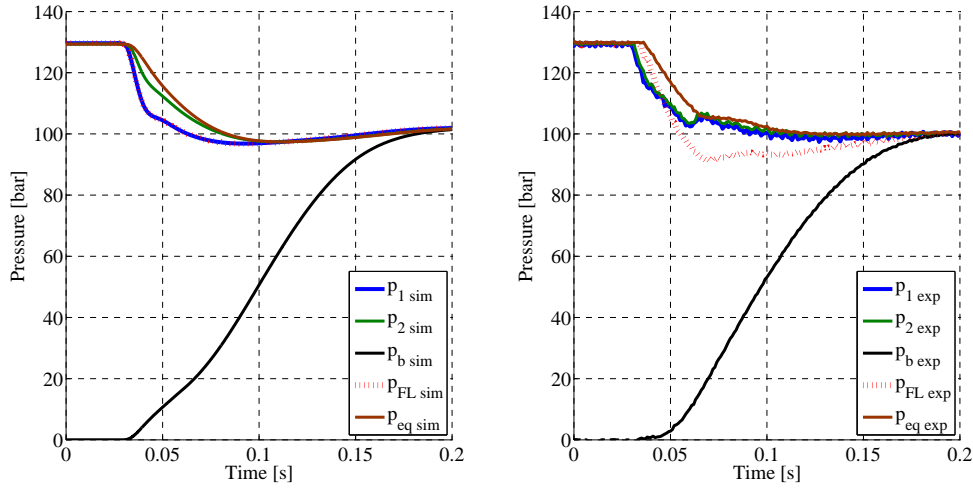


Figure 3.22 'Raising phase': 1= 1° chamber TMC, 2= 2° chamber TMC, b= Rear Right caliper, FL= Front Left caliper, eq= equivalent Front Right+Rear Left caliper, exp=experimental, sim=simulation

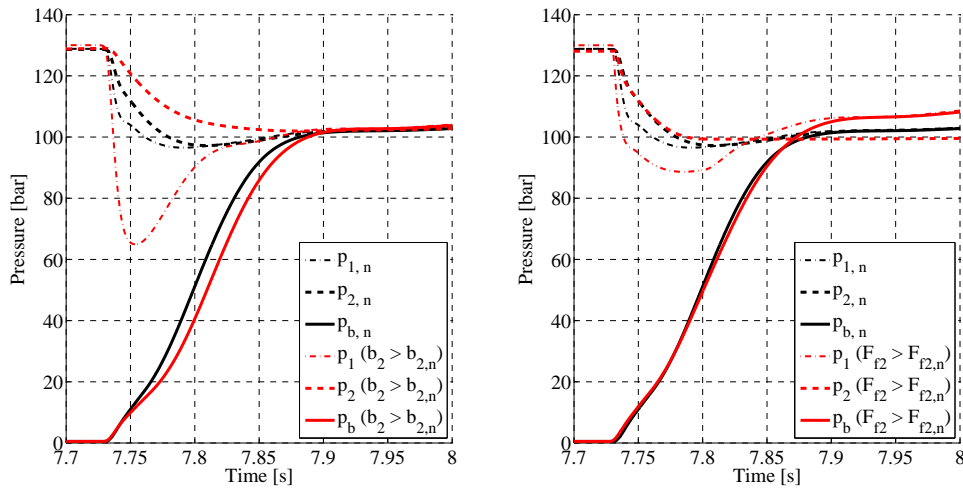


Figure 3.23 Sensitivity analysis on b_2 and F_{f2} : 1= 1st TMC chamber, 2= 2nd TMC chamber, b= Rear Right caliper, n = nominal condition

The 'falling phase' is used to identify remaining parameters characterizing the pressure dynamics inside the discharge hydraulic branch composed by the outlet valve, the spring accumulator and the motor-pump. Q_{ss} , p_{th} and A_{Out} have been identified through a curve fitting procedure between experimental and simulated pressures as shown in Fig. 3.24:

Q_{ss} is strictly related to the TMC pressure gradients while the flow area A_{Out} influences both brake and accumulator pressure gradients. After 0.3 seconds, the flow rate delivered by the motor-pump decrease from Q_{ss} to 0 because accumulator pressure is

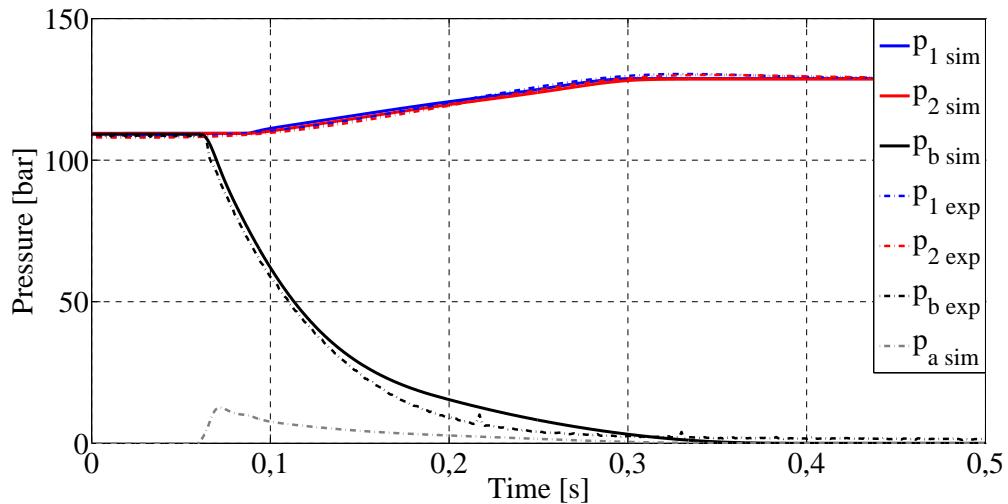


Figure 3.24 'Falling phase': 1= 1st TMC chamber, 2= 2nd TMC chamber, b= Rear Right caliper, a= accumulator, exp=experimental, sim= simulation

too low: it is important to underline the effect of one way valve inside the discharge branch which prevents oil to flow-back to the brake caliper.

Inlet and outlet valves can be controlled by applying a digital ON/OFF voltage command to their solenoids through the relay box. An overall analysis about valves dynamical behavior has been carried out by applying a PWM signal to their solenoids in order to identify transient and steady state characteristics.

Fig. 3.25 refers to the non-linear behavior of inlet valve when a PWM voltage command with frequency of 900 Hz and different Duty Cycle (DC) is applied to its solenoid.

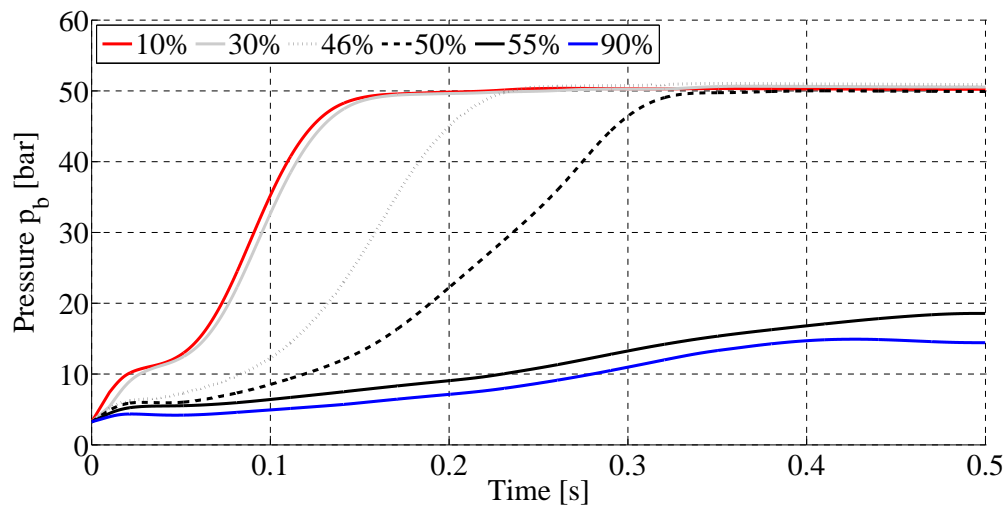


Figure 3.25 Effect of PWM Duty Cycle on pressure trend in the brake caliper: the inlet valve is controlled via a constant frequency and variable Duty Cycle

It is possible to observe a clear dependence of the pressure gradient on the Duty Cycle. This behavior represents the transformation from the PWM digital command to the effective flow area A_i through the relay box and electro-valves. This electro-mechanical system is characterized by saturation in both directions: for a DC lower than 30% the valve behaves as a fully open one and for DC greater than 55% the valve works as a fully closed one. Based on this consideration, inlet and outlet valves can be modeled with second-order transfer functions with a non constant static gain as indicated in Eq. 3.17. The dynamic parameters σ_n and ζ are roughly derived through a curve-fitting procedure between the simulated pressure trend and the experimental results for a specific DC, as indicated in Fig. 3.26. The figure also makes clear the effect of the PWM frequency on the pressure ripple: while the outlet valve PWM frequency of 50 Hz is close to its natural frequency amplifying pressure oscillations, the high value of inlet valve modulation frequency of 900 Hz is very well attenuated due to the mechanical low pass filtering effect involved by the valve dynamics.

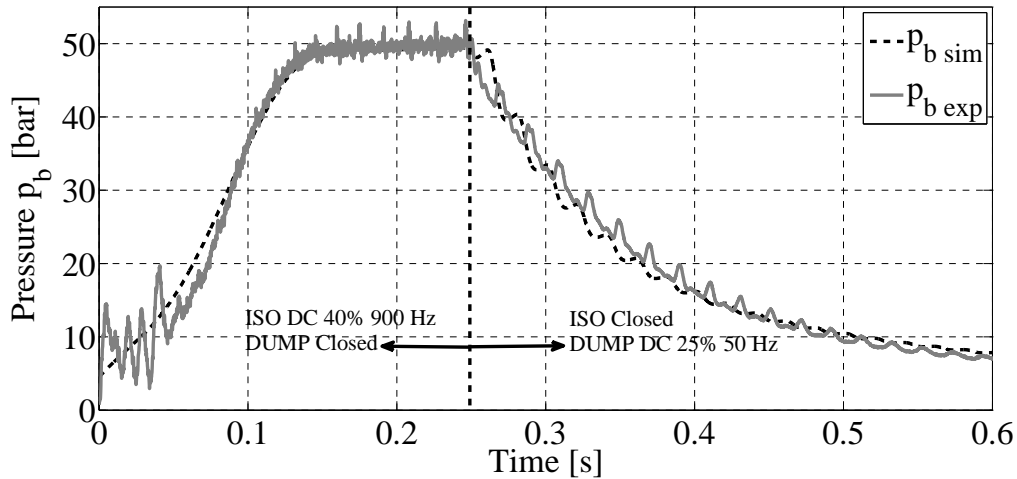


Figure 3.26 Raising and falling phases by applying a PWM signal of 40% DC and modulation frequency of 900 Hz to the inlet valve and a PWM signal of 25% DC on 50 Hz to the outlet valve

The variable static gain G_s , which takes into account all the unmodeled nonlinearities, e.g. introduced by the relay box and electro-mechanics behavior of valves, is identified from experimental curve-fitting all over the effective DC range (e.g. from 30% to 55% for the inlet valve) finally getting the non-linear static behavior between DC and effective flow area A_i shown in Fig. 3.27. The inlet valve gain shows a monotonically decreasing trend which has a clear physical meaning since it states that when Duty Cycle increases the inlet valve behaves as closed valve. On the other hand, the outlet valve gain is characterized by an increasing trend followed, after the maximum, by a decreasing trend and thus showing a different behavior from inlet valve, also because of the motor-pump presence.

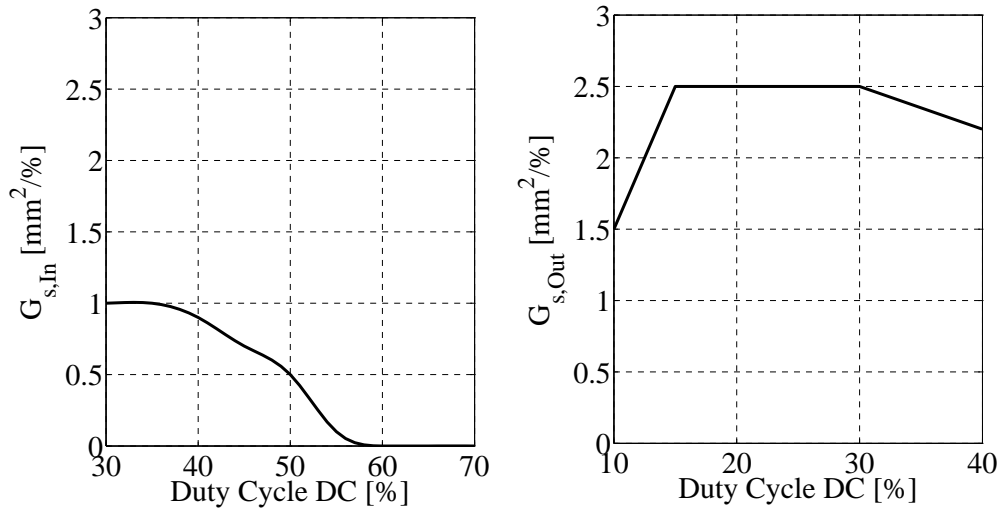


Figure 3.27 Static Gain G_s for both inlet (left) and outlet (right) valve

Model Validation

This last section presents the experimental validation of the non-linear model by applying the same time-histories used during specific experimental test in order to compare simulated brake pressure behavior with the pressure measured by sensors. Two different time-histories are chosen to be as close as possible to real operating conditions of vehicle braking system:

- Normal production ABS emergency wheel anti-lock control strategy
- PWM signal with variable Duty Cycle for both inlet and outlet valves

In the first case, both test rig and non-linear model receive the same input coming from a real emergency braking maneuver where the system is activated in order to avoid wheel locking. An example of valves activation is reported in Fig. 3.28 (activation of outlet valve always comes together with motor-pump to empty brake calipers) together with the comparison of brake caliper pressures obtained during simulation and from test rig sensors. A proper tuning of the inlet valve static gain, focused on low pressures, has led to a good estimation in that range: the RMS value of the error between simulation and experimental data in the time range shown in Fig. 3.28 is 1.5 bar.

A more specific test is elaborated for evaluating valves dynamic response to a PWM signal with a constant frequency and variable Duty Cycle. The time history is chosen in order to cover the whole range where Duty Cycle is effective on the pressure gradient as described in the previous section. The simulation has been carried out by adding to both valves input commands a time delay equal to the sampling period (0.02 s) used during

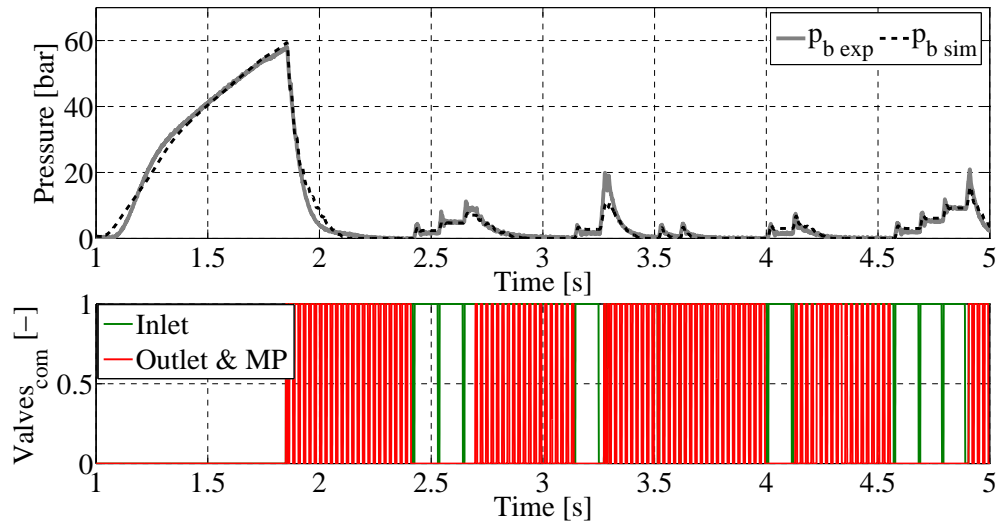


Figure 3.28 Experimental validation of non-linear model during ABS emergency braking under extremely low road friction conditions: b= Rear Right caliper, exp=experimental, sim=simulation

experimental test. Contrary to the other tests, where the sampling frequency is 10 kHz, in this case (frequency of 50 Hz) the time delay due to the sampling period cannot be neglected. Fig. 3.29 reports the experimental validation showing a good match between experimental and simulated brake pressure (RMS error is 3.5 bar), especially during the activation of inlet valve.

The RMS value of the error between experimental and simulation data is lower in the case of ABS emergency test than the PWM signal test due to a lower mean value (10 bar and 35 bar respectively).

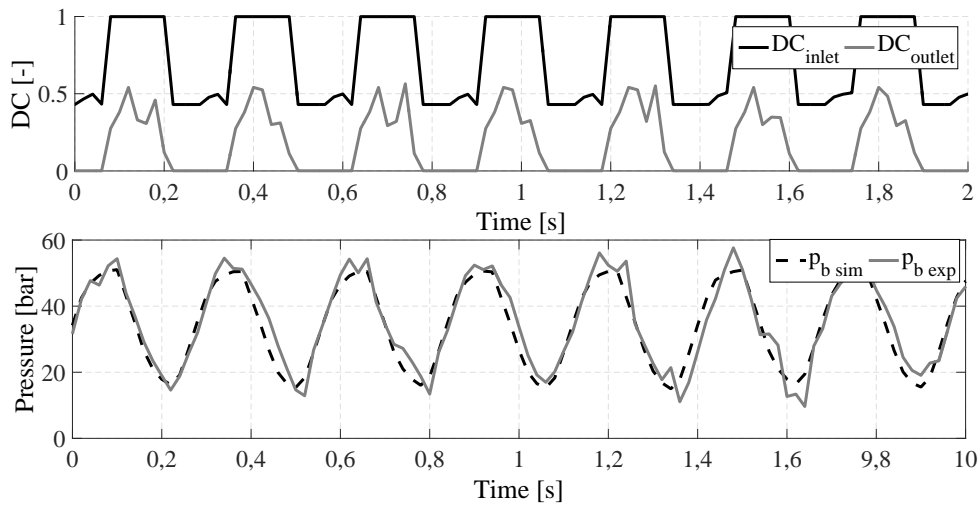


Figure 3.29 Experimental Validation of Non-Linear Model under a PWM signal excitation: b= Rear Right caliper, exp=experimental, sim= simulation

3.5.3 Pressure control design

This section deals with the design of a brake caliper pressure controller for a conventional ABS/ESC system and the experimental validation of its tracking performances. The analysis of the hydraulic plant, carried out in previous section, is here utilized to develop the control algorithm for ABS digital electro-hydraulic valves.

The control strategy is based on a Feedforward (FF) and a Proportional Integral (PI) controller through a Pulse Width Modulation (PWM) with constant frequency and variable Duty Cycle (DC). FF contribution requires modeling the nonlinear open-loop system behavior which has been experimentally identified and described through 2-D maps: the inputs are the DC applied to the electro-valves and the pressure drop across their orifice, while the output is the pressure gradient in the brake caliper. These maps, obtained for inlet and outlet valves, are used to set the FF term. Finally a PI controller is designed to reject external disturbances and compensate for model uncertainties.

The same brake system test rig, previously described, is used for building inverse maps and validating the proposed control logic. Different reference pressure profiles are used to experimentally verify the control tracking performances.

Valves Dynamics Behavior

Brake pressure inside calipers can be modulated through the activation of Inlet and Outlet valves. A generic scheme for the 'raising' phase (when brake pressure p_b increases) controlled by the Inlet valve and the 'falling phase' (when brake pressure p_b decreases) managed by the presence of Outlet valve and motor-pump is shown in Fig. 3.30.

From Eq. 3.6 and 3.12 brake pressure gradient \dot{p}_b is described by the following generic equation:

$$\dot{p}_b = \frac{\beta}{V_b}(Q_{In} - Q_{Out}) \quad (3.18)$$

where V_b is the volume of brake caliper, β is the oil bulk modulus and Q_{In} , Q_{Out} are the flow rates respectively through Inlet and Outlet valves that are expressed by:

$$\begin{cases} Q_{In} &= c_{q,In} A_{In} \sqrt{\frac{2|p_T - p_b|}{\rho}} \operatorname{sgn}(p_T - p_b) \\ Q_{Out} &= c_{q,Out} A_{Out} \sqrt{\frac{2|p_b - p_a|}{\rho}} \operatorname{sgn}(p_b - p_a) \end{cases} \quad (3.19)$$

where c_q is the flow coefficient, ρ the oil density, p_T the pressure inside one of the TMC chambers, p_a the spring accumulator pressure and A_{In} , A_{Out} Inlet and Outlet

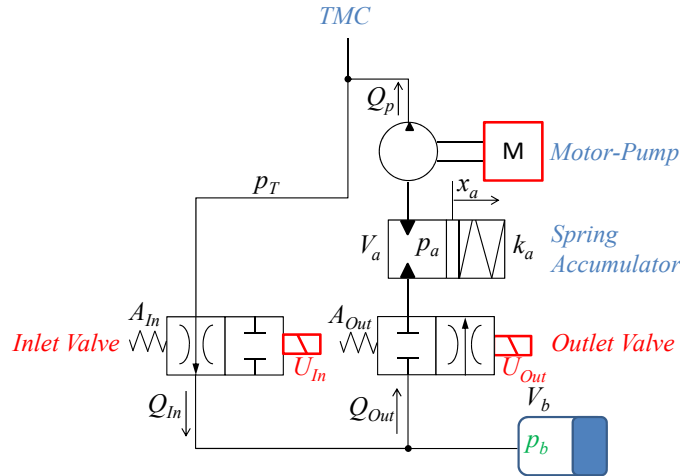


Figure 3.30 Hydraulic scheme for the raising and falling phase in a brake caliper including Inlet/Outlet valves, Motor-pump and Spring accumulator.

nominal flow areas. Under the hypothesis that the two valves cannot be simultaneously open, when Inlet valve is activated (raising phase) Q_{Out} is null while when Outlet valve is open (falling phase) Q_{In} is equal to zero.

From eqs. (3.18) and (3.19), it is evident that the brake pressure depends on flow areas and on pressure drop across the two valves.

Inlet valve behavior is described considering as inputs:

- Inlet pressure drop $\Delta p_{In} = p_T - p_b$
- flow area A_{In}

and as output:

- brake calipers pressure gradient \dot{p}_b

Also Outlet valve can be represented considering as inputs:

- Outlet pressure drop $\Delta p_{Out} = p_b - p_a$
- flow area A_{Out}

and as output:

- brake calipers pressure gradient \dot{p}_b

In this last case, the spring accumulator guarantees a reference pressure for the suction port of the motor-pump. Accumulator pressure p_a is not measured by a sensor but, as highlighted in the model simulation results, it is reasonable to approximate the pressure drop across the Outlet valve with the brake pressure p_b alone.

Hence a possible strategy to control the brake pressure gradient is to modulate the valve command thus regulating their flow areas. Since electrovalves are designed to receive a digital command, the generation of a PWM signal as input voltage is a solution to modify in a continuous way their flow area. Meanwhile, pressure drops across valves can be considered as an external disturbances from the control point of view, that are measured on the test bench through sensors placed in the TMC and inside each brake calipers.

A PWM signal is described by a frequency and a Duty Cycle that is the percentage of a modulation period during which the signal is active. By fixing the PWM frequency, the DC is used to change the effective flow area and so to regulate the flow rate going inside/outside the brake caliper thus controlling brake pressure.

Valves characterization

The test rig used for valves characterization is shown in Fig. 3.19, where a normal production hydraulic brake system is controlled by a customized ABS/ESC electronic unit to command directly Inlet and Outlet electrovalves together with the motor-pump. A PWM signal is chosen to command Inlet and Outlet valves meanwhile the motor-pump is activated with an On-Off logic. Calipers brake pressure and TMC pressures are here considered measurable and available feedback for the proposed pressure controller.

A more refined analysis of the valves can be achieved through a semi-empirical model by involving experimental maps to describe their dynamics. An experimental test is carried out to analyze valves response to a PWM signal: starting from a steady-state condition where all valves are in their normal configuration (normally open for Inlet and normally close for Outlet) and brake pressure p_b is equal to TMC pressures, the brake caliper it is emptied by applying a PWM signal with a certain frequency and DC to the Outlet valve (together with the activation of the motor-pump) while the Inlet valve is kept closed; when brake pressure p_b falls below a specific software selectable threshold, i.e. 5 bar, the Inlet valve is excited with a PWM signal in order to increase brake pressure while Outlet valve is closed and motor-pump is switched off. This cycle of 'falling' and 'raising' phases is repeated when the brake pressure has reached again the TMC pressure.

An example of a data acquisition is presented in Fig. 3.31 where different duty cycles are

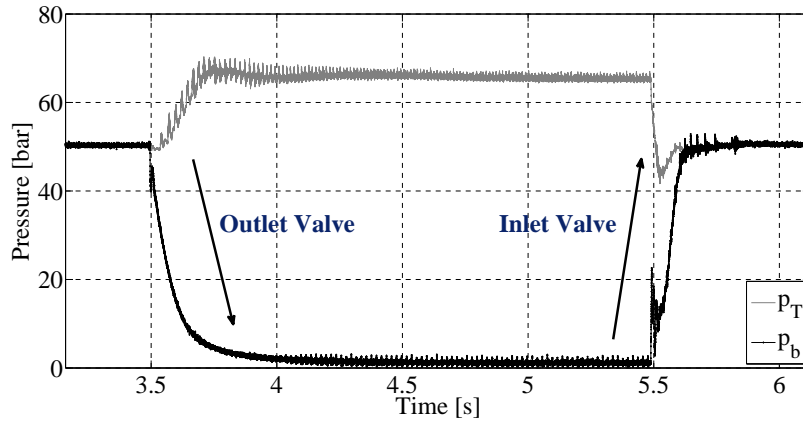


Figure 3.31 Data Acquisition with a sample time of 0.1 ms of TMC (p_T) and Brake (p_b) pressures

imposed for Inlet (30%) and Outlet (55%) valves with the same PWM frequency of 900 Hz.

The figure also shows how valves activation influences the brake and TMC pressures since their variation has a direct effect on the flow rate (and so on the gradient of brake pressure). The correlation between PWM command and valves behavior will be fully described by experimental maps obtained by choosing a suitable value of PWM frequency and a DC range within which brake pressure gradient is controllable.

PWM Frequency selection

Starting from a preliminary test, a PWM command with a constant duty cycle and different frequencies (range between 50 and 900 Hz) is applied to both valves in order to choose a suitable frequency for the control strategy. By exciting the Inlet valve with a PWM command characterized by a DC of 30% and a frequency of 100 Hz, lower with respect to Fig. 3.31, a different behavior can be observed as shown in Fig. 3.32: a PWM frequency smaller than 900 Hz leads to significant pressure oscillations.

PWM frequency directly influences brake pressure ripples so it can be selected in order to reduce oscillations and to improve pressure controllability. The Root Mean Square (RMS) of the difference between raw and filtered signal (zero-phase digital filter with a cut-off frequency of 15 Hz) is used to correlate the ripple pressure to the PWM frequency:

$$P_{RMS} = \sqrt{\frac{\sum_{i=1}^n (p_{bi} - p_{bfi})^2}{n}} \quad (3.20)$$

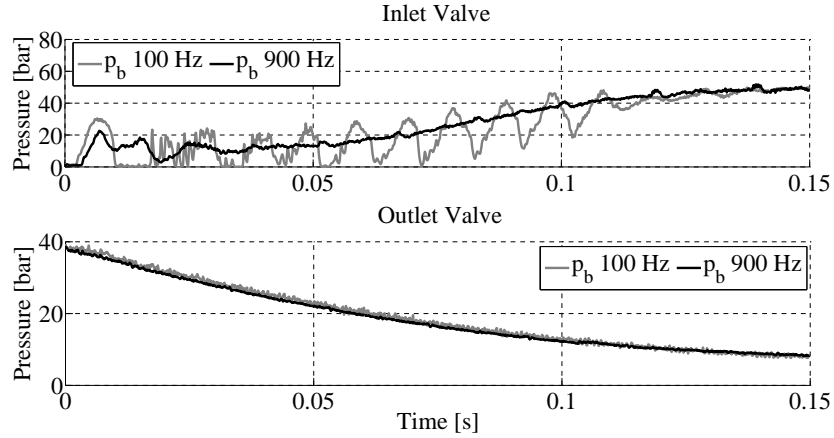


Figure 3.32 PWM signal with different frequencies for both Inlet (DC=30%) and Outlet Valves (DC=70%), p_b = Brake Pressure

where P_{bi} is the raw pressure and P_{bfi} its value filtered at time t_i . Fig. 3.33 shows that the pressure ripple for Inlet valve decreases with the PWM frequency and after 500 Hz this trend is settled. This means that a high frequency could lead to a better solution in terms of controllability by cutting off the PWM frequency content which is a disturbance for pressure control.

Outlet valve shows a decreasing trend similar to the Inlet one, with a noticeable difference in terms of RMS amplitude range: it is less influenced by PWM modulation frequency than Inlet valve, as visible in Fig. 3.33. This behavior can be explained considering that the pressure oscillations in the outlet branch are influenced both by PWM frequency content and by the motor-pump which is not present in the inlet branch. Consequently the motor-pump can be considered as a flow-rate regulator which modifies the pressure oscillations caused by the PWM command.

Finally PWM frequencies of 900 Hz and 50 Hz are chosen for Inlet and Outlet valves respectively, aiming at obtaining the minimum pressure ripple according to Fig. 3.33. Since the brake pressure dynamics is minimally affected by the outlet valve PWM frequency, the selection of this parameter for the outlet valve is aimed at obtaining the max DC range which is effective during pressure control as it will be seen in next section.

DC range: Open-loop Maps

The relation between DC and pressure gradient is not linear and it is limited within a certain range beyond which the duty cycle no longer affects the pressure dynamics. A first step refers to the search for a duty cycle range to achieve a good sensitivity in terms of controllability within minimum and maximum DC. A gradual variation of the duty cycle is applied to each valve (by keeping PWM frequency as indicated in the

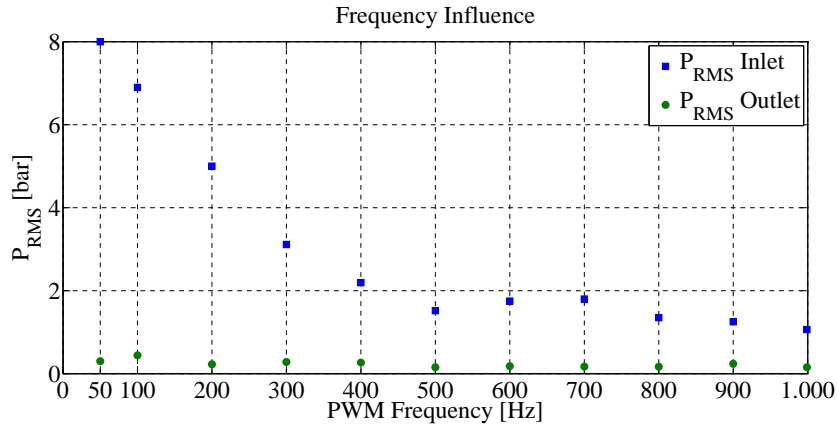


Figure 3.33 PWM frequency influence on brake pressure ripple for both Inlet (blue) and Outlet (green) valves

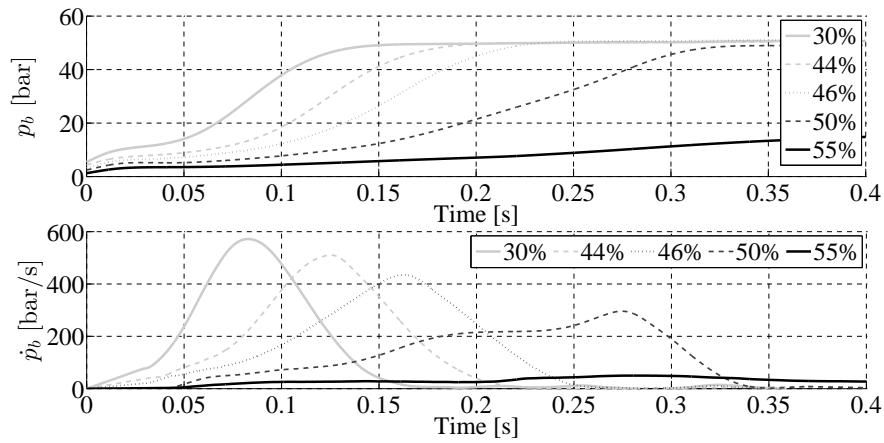


Figure 3.34 Brake pressure (up) and its gradient (down) vs time for different values of DC (Inlet valve)

previous section) in order to build up the open-loop maps describing the experimental relationship between input (DC) and output (p_b).

By considering the Inlet valve (normally open), the pressure gradient decreases with increasing DC until the valve is not able to further increase pressure because the opening time is too short, as it happens when a DC of 55% is imposed with a nominal frequency of 900 Hz (Fig. 3.34). If DC is larger than 55%, pressure cannot be increased up to TMC pressure thus representing maximum limit for Inlet valve. DC minimum limit can be evaluated from the same experimental data when the valve behaves as a fully open one (a lower DC is ineffective), thus getting a complete information about valves open-loop behavior.

Fig. 3.34 indicates that for a fixed DC, pressure gradient is not constant since it depends also on the pressure drop across the valve $\Delta p_{In} = p_T - p_b$, which is measurable

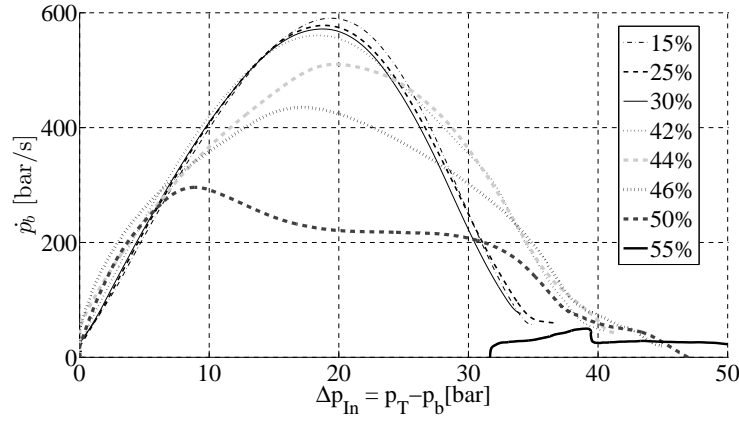


Figure 3.35 Inlet Open-Loop map: pressure gradient vs pressure drop across Inlet valve for different value of DC

on the test rig. Therefore, an experimental relationship between pressure gradient \dot{p}_b , pressure drop Δp_{In} and DC is obtained, which constitutes the open-loop map of Inlet valve (Fig. 3.35).

The 'bell' shape in Fig. 3.35 can be divided into three sections: the increasing section, the peak point and decreasing section. The increasing section and peak point show an almost inversely proportional trend with respect the DC: the pressure gradient in brake caliper decreases consequently to a reduction of the inlet valve effective flow area due to an increase of DC.

The behavior of the system corresponding to the decreasing section cannot be explained in the same way, due to the saturation limit imposed by the TMC pressure (without this limit, the decreasing section would not be present): it is not intuitive to figure out how the DC influences the pressure gradient. It is of interest noting that in the DC operative range there exists a progressive modulation of pressure gradient with respect to DC, thus becoming a feasible controllable variable.

Figures 3.34 and 3.35 clearly show the upper and lower limits of duty cycle range for the Inlet valve; under the lower limit, a packing effect of the curves occurs: pressure gradient is no more influenced by DC (the same behavior of a fully open valve) and a transition occurs between the active (where a variation of DC provokes a variation of pressure gradient) and the passive region (where pressure gradient is not influenced anymore by the DC): this transition modifies the 'bell' shape, causing an intersection of the curves in the decreasing section. In Fig. 3.35 can be seen that DC of 15%, 25% and 30% have the same bell shape meanwhile a DC of 42% has a shape which is a sort of composition of 30% and 44% DC curves.

Similarly, the Outlet open-loop map is built selecting the appropriate duty cycle range between upper and lower limits, considering that the outlet valve is normally closed

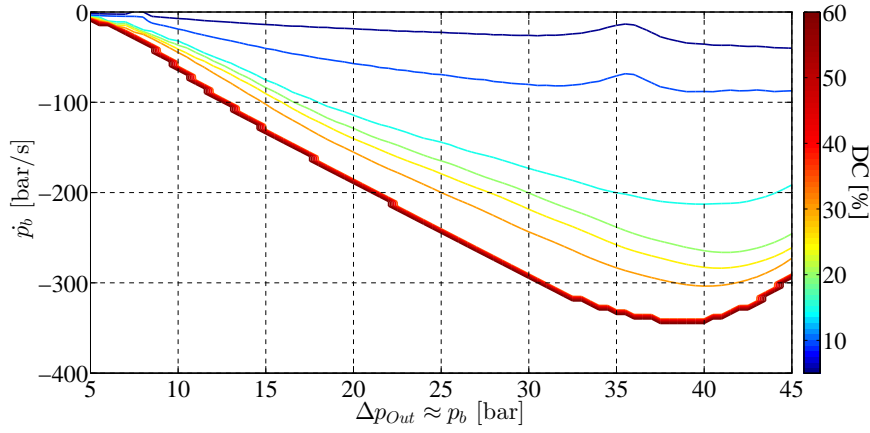


Figure 3.36 Outlet Open-Loop map: pressure gradient vs pressure drop across Outlet valve for different value of DC

(when DC is too low the valve behaves as a fully close one) and that the pressure drop across the valve, $\Delta p_{Out} = p_b - p_a$, is approximated with the brake pressure p_b (neglecting the influence of spring accumulator). The open-loop map obtained for the Outlet valve is reported in Fig. 3.36.

Control logic design

A non-linear FeedForward (FF) plus a Proportional Integral (PI) controller is designed for continuously tracking a reference pressure which can be generated, for example, by the high-level control logic aiming at a transmission noise reduction. In order to design the controller structure and to figure out its performance enhancement, a linearization around a nominal equilibrium point is required. Equilibrium points can be found just starting from dynamic equations that describe brake pressure behavior for both inlet and outlet valves in Eq. 3.18, 3.19:

$$\dot{p}_{b,In}(p_b, A_{In}, p_T) = \frac{\beta}{V_b} c_q A_{In}(DC_{In}, \Delta p_{In}) \sqrt{\frac{2\Delta p_{In}}{\rho}} \quad (3.21)$$

$$\dot{p}_{b,Out}(p_b, A_{Out}) = -\frac{\beta}{V_b} c_q A_{Out}(DC_{Out}, p_b) \sqrt{\frac{2p_b}{\rho}} \quad (3.22)$$

where A_{In} and A_{Out} depends on DC and pressure drop across each valve. Steady-state occurs when $\dot{p}_b = 0$: a trivial solution is obtained when $p_{T,n} = p_{b,n}$ for Inlet hydraulic branch and $p_{b,n} = 0$ for Outlet hydraulic branch.

A more interesting steady-state condition is reached when $A_{In,n} = 0$ ($DC_n = 100\%$)

$\forall \Delta p_{In,n} = (p_T - p_b)_n$ for Inlet valve and $A_{Outlet,n} = 0$ ($DC_n = 0\%$) $\forall p_{b,n}$ for Outlet valve. This means that any value of brake pressure p_b represents a stable configuration when $A_{Out,n} = 0$ and $A_{In,n} = 0$.

Since pressure gradient in equations Eq. 3.21 and Eq. 3.22 is a function of two variables (DC and Δp), the following linear relations are obtained respectively for Inlet and Outlet hydraulic branches, by linearizing around nominal equilibrium points:

$$\begin{aligned} \dot{p}_{b,In} &= \left. \frac{\partial \dot{p}_{b,In}}{\partial DC_{In}} \right|_n (DC_{In} - DC_{In,n}) + \left. \frac{\partial \dot{p}_{b,In}}{\partial \Delta p_{In}} \right|_n (\Delta p_{In} - \Delta p_{In,n}) = \\ &= k_{DC,In}(DC_{In} - DC_{In,n}) + k_{\Delta,In}(\Delta p_{In} - \Delta p_{In,n}) \end{aligned} \quad (3.23)$$

$$\begin{aligned} \dot{p}_{b,Out} &= - \left. \frac{\partial \dot{p}_{b,Out}}{\partial DC_{Out}} \right|_n (DC_{Out} - DC_{Out,n}) + \left. \frac{\partial \dot{p}_{b,Out}}{\partial p_b} \right|_n (p_b - p_{b,n}) = \\ &= k_{DC,Out}(DC_{Out} - DC_{Out,n}) + k_{\Delta,Out}(p_b - p_{b,n}) \end{aligned} \quad (3.24)$$

Eq. 3.23 and 3.24 state that brake pressure gradient is influenced by DC of valve input signal and pressure drop across valves through four coefficients $k_{DC,In}$, $k_{DC,Out}$, $k_{\Delta,In}$ and $k_{\Delta,Out}$. These two relations, neglecting the constant terms, can be grouped in a unique general formulation for both inlet and outlet valves:

$$\dot{p}_b = k_{DC}DC + k_{\Delta}\Delta p = k_{DC}DC + k_{\Delta}p_T - k_{\Delta}p_b \quad (3.25)$$

where $DC = DC_{In}$ for inlet valve, $DC = -DC_{Out}$, $k_{\Delta}p_T = 0$ for outlet valve and k_{DC}, k_{Δ} are linearization coefficients related to nominal equilibrium points.

By applying Laplace transform to Eq. 3.25, it is possible to derive the transfer function between output p_b and input (DC, p_T):

$$p_b(s) = \frac{k_{DC}}{s + k_{\Delta}} DC(s) + \frac{k_{\Delta}}{s + k_{\Delta}} p_T(s) \quad (3.26)$$

where s is the Laplace variable and DC is the controlled input p_T represents a measurable disturbance. The poles of transfer function (3.26) depend on coefficient k_{Δ} which states the relation between \dot{p}_b and the pressure drop across each valve and it is expressed by the gradient of open-loop maps when DC is fixed to a constant value. For both inlet and outlet valves k_{Δ} changes from positive (stability region) to negative (instability region) values: by looking the Inlet open-loop map (Fig. 3.35), for high pressure drops (right side of the map with a negative k_{Δ}), an increase in pressure causes an increase of pressure gradient, making the linearized system unstable. On the other hand, for low pressure

drops (left side of the map with a positive k_Δ), the system shows a stable behavior. The Control logic used to stabilize the system and to track the reference brake pressure is composed of two different contributions:

- a non-linear FeedForward (FF) part which is based on dynamics system inversion of the open-loop behavior;
- a Proportional-Integrative (PI) part which aims to reject noise and to compensate for model parameters uncertainties not considered in the FF contribution.

Feed Forward Controller A FF contribution is built by considering the dynamics of brake pressure gradient: it works to track the gradient of the reference pressure. Theoretically speaking, this is obtained inverting Eq. 3.25:

$$DC_{FF} = \frac{\dot{p}_r - k_\Delta(p_T - p_b)}{k_{DC}} \quad (3.27)$$

where \dot{p}_r is the gradient of the reference brake pressure. Since gains k_Δ and k_{DC} are not constant in the real system, dynamics inversion can be easily achieved by inverting experimental open loop maps $\dot{p} = f(DC, \Delta p)$ to inverse maps $DC = f(\dot{p}, \Delta p)$ through a post-processing procedure consisting of two phases:

1. Original maps discretization & interpolation: each pressure gradient trend in Fig. 3.34 and Fig. 3.36 has a different x-axis (pressure drop across valves) discretization, thus requiring a suitable standardization which is obtained by fixing a common abscissa distribution. Consequently, a linear interpolation is carried out to create a common x-axis discretization and to fill original open-loop maps where experimental values are not available, providing more data for the following inversion step.
2. Maps inversion: for each pressure drop Δp there exists an experimental correlation between pressure gradient and duty cycle: hence a simple vector inversion is performed as shown in Fig. 3.37

Finally, Fig. 3.38 and 3.39 illustrate the inverse maps for Inlet and Outlet valves, respectively.

It is important to highlight that DC_{FF} is not a traditional open-loop feedforward since inverse maps use as input feedback from the plant, the actual pressure drop across valves measured by sensors whose effect will be clarified in the next subsection.

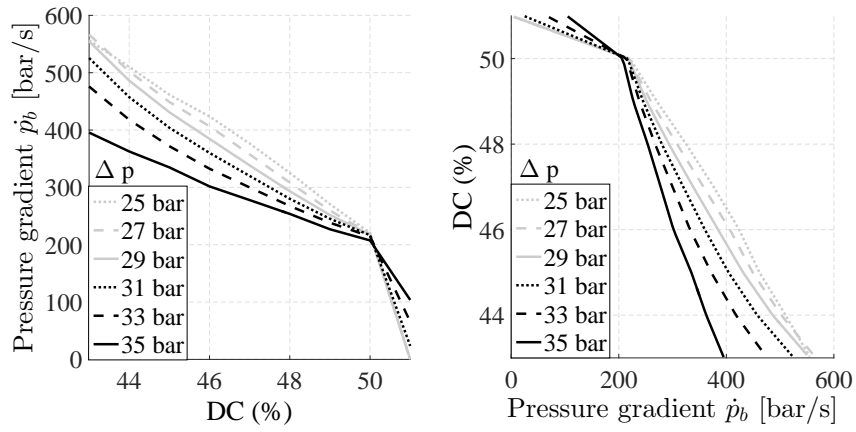


Figure 3.37 Conversion from open-loop map (left) to inverse map (right) for different values of pressure drop across Inlet valve

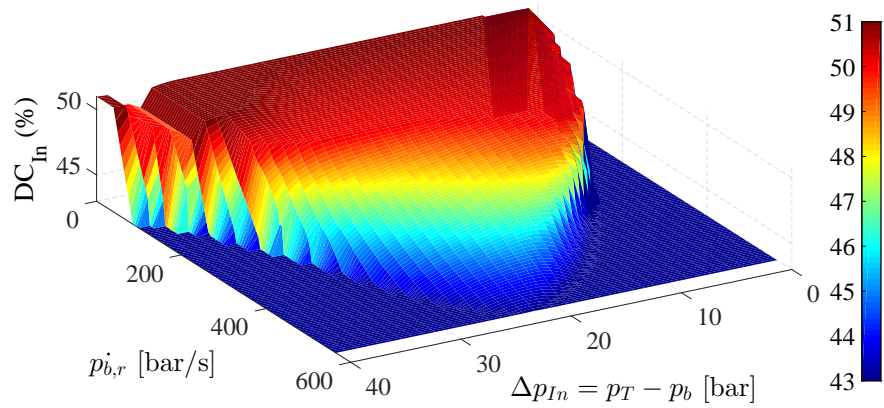


Figure 3.38 Inlet Inverse map: DC vs reference pressure gradient and pressure drop across Inlet valve

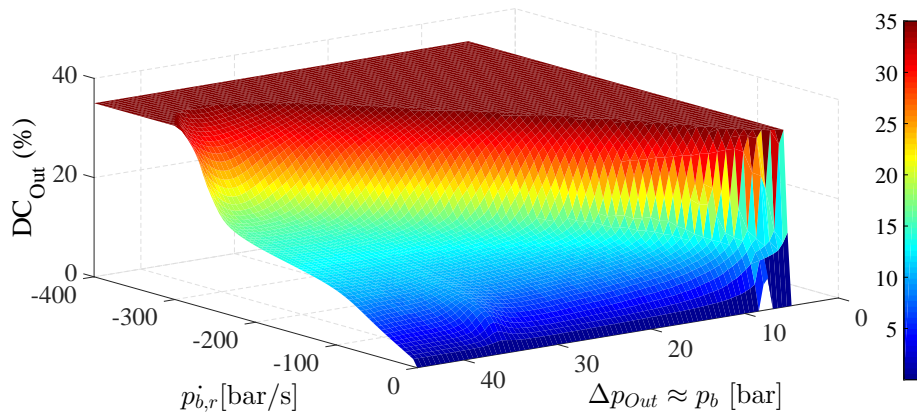


Figure 3.39 Outlet Inverse map: DC vs reference pressure gradient and pressure drop across Outlet valve

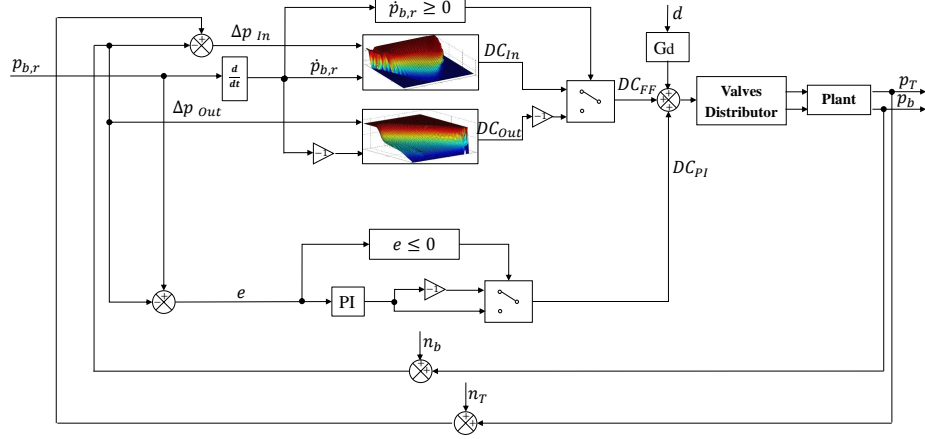


Figure 3.40 Block diagram of FF + PI control strategy

Proportional Integrative Controller Open-loop maps are obtained from experimental data, so they are obviously affected by uncertainties. In order to reduce their impact on the control strategy and to better track the reference brake pressure, a PI controller on the error between p_b and $p_{b,r}$ is designed.

In order to understand the PI effects on the closed loop system shown in Fig. 3.40, a not measurable disturbance d is added to the control output $u_c = DC_{FF} + DC_{PI}$ and sensor noises n_b , n_T are considered respectively for both TMC and brake pressures.

Pressure gradient equation express in Eq. 3.25 is modified as:

$$\dot{p}_b = k_{DC}DC + k_{\Delta}p_T - k_{\Delta}p_b + G_d(s)d \quad (3.28)$$

By considering the Laplace transform of Eq. 3.28, a new transfer function of the disturbed plant is obtained:

$$p_b(s) = \frac{k_{DC}}{s + k_{\Delta}}DC(s) + \frac{k_{\Delta}}{s + k_{\Delta}}p_T(s) + \frac{G_d(s)}{s + k_{\Delta}}d(s) \quad (3.29)$$

The closed loop transfer function from $p_{b,r}$ to p_b can be derived considering the controller equations $DC(s)$

$$DC(s) = DC_{PI}(s) + DC_{FF}(s) = (K_{Pr} + \frac{K_{In}}{s})e(s) + DC_{FF}(s) \quad (3.30)$$

where $e(s) = p_{b,r} - p_b - n_b$, K_{Pr} is the proportional gain, K_{In} is the integral gain and DC_{FF} is the DC from inverse maps. Finally, the relation between the output $p_b(s)$ and the input $p_{b,r}(s), p_T(s), d(s), n_b(s)$ is calculated by substituting Eq. 3.30 in Eq. 3.29:

$$\begin{aligned} p_b(s) \left(1 + K_{Pr} \frac{k_{DC}}{s + k_{\Delta}} + \frac{K_{In}}{s} \frac{k_{DC}}{s + k_{\Delta}} \right) &= \left(K_{Pr} \frac{k_{DC}}{s + k_{\Delta}} + \frac{K_{In}}{s} \frac{k_{DC}}{s + k_{\Delta}} \right) p_{b,r}(s) + \\ &+ \left(\frac{k_{DC}}{s + k_{\Delta}} DC_{FF}(s) \right) + \left(\frac{k_{\Delta}}{s + k_{\Delta}} \right) p_T(s) + \left(\frac{G_d(s)}{s + k_{\Delta}} \right) d(s) + \\ &- \left(K_{Pr} \frac{k_{DC}}{s + k_{\Delta}} + \frac{K_{In}}{s} \frac{k_{DC}}{s + k_{\Delta}} \right) n_b(s) \end{aligned} \quad (3.31)$$

Without considering the effect of $DC_{FF}(s)$, this equation shows how PI gains can modify the closed loop transfer function between $p_b(s)$ and $p_{b,r}(s)$. On the other hand, DC_{FF} derives from inversion of the nominal open-loop dynamic behavior, see Eq. 3.27 hence Laplace transform is:

$$DC_{FF}(s) = \frac{s}{k_{DC}} p_{b,r}(s) - \frac{k_{\Delta}}{k_{DC}} p_T(s) - \frac{k_{\Delta}}{k_{DC}} n_T(s) + \frac{k_{\Delta}}{k_{DC}} p_b(s) + \frac{k_{\Delta}}{k_{DC}} n_b(s) \quad (3.32)$$

by substituting Eq. 3.32 in Eq. 3.31 it yields:

$$\begin{aligned} p_b(s) &= p_{b,r}(s) - \left(\frac{(k_{DC}K_{Pr} + k_{\Delta})s + k_{DC}K_{In}}{s^2 + k_{DC}K_{Pr}s + k_{DC}K_{In}} \right) n_b(s) + \\ &- \left(\frac{k_{\Delta}s}{s^2 + k_{DC}K_{Pr}s + k_{DC}K_{In}} \right) n_T(s) + \left(\frac{G_d(s)s}{s^2 + k_{DC}K_{Pr}s + k_{DC}K_{In}} \right) d(s) \end{aligned} \quad (3.33)$$

and in terms of tracking error $e(s)$:

$$\begin{aligned} e(s) &= \left(\frac{k_{\Delta}s - s^2}{s^2 + 2\zeta\omega_n s + \omega_n^2} \right) n_b(s) + \left(\frac{k_{\Delta}s}{s^2 + 2\zeta\omega_n s + \omega_n^2} \right) n_T(s) + \\ &- \left(\frac{G_d(s)s}{s^2 + 2\zeta\omega_n s + \omega_n^2} \right) d(s) \end{aligned} \quad (3.34)$$

where

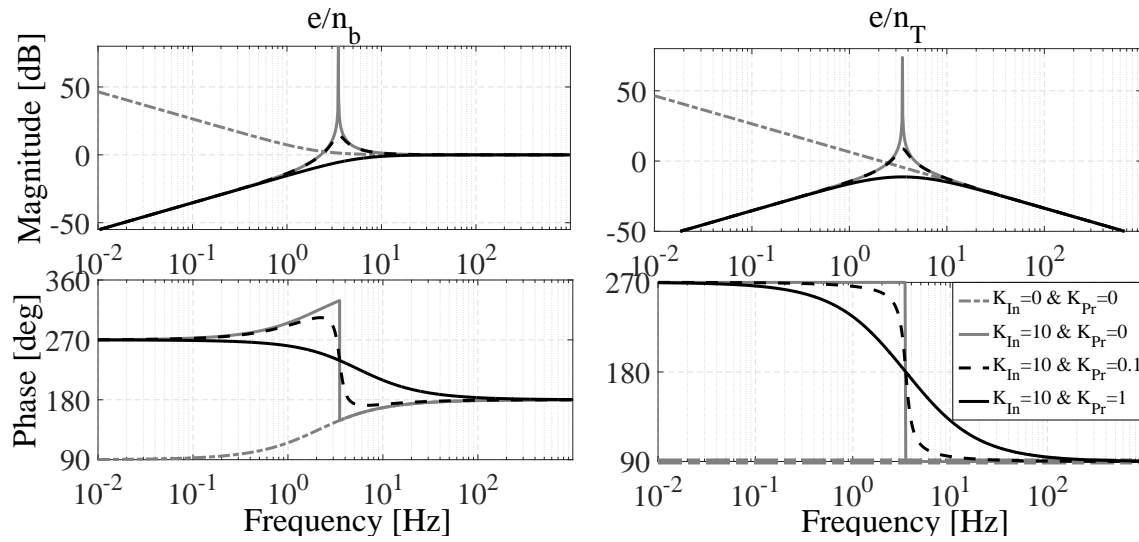


Figure 3.41 Bode plots for transfer functions $\frac{e(s)}{n_b(s)}$ (left) and $\frac{e(s)}{n_T(s)}$ (right)

$$\begin{aligned}\omega_n &= \sqrt{k_{DC}K_{In}} \\ \zeta &= \frac{K_{Pr}}{2} \sqrt{\frac{k_{DC}}{K_{In}}}\end{aligned}\quad (3.35)$$

Non-linear FF is able to improve control tracking performance ($\frac{p_b(s)}{p_{b,r}(s)} = 1$) and reject the measurable disturbance p_T , but it is not able to reject unmeasurable disturbances like d and sensor noises like n_T, n_b . The intervention of the PI control is able to modify the poles of transfer functions $\frac{e(s)}{n_b(s)}$, $\frac{e(s)}{n_T(s)}$ and $\frac{e(s)}{d(s)}$ thus enhancing robustness against uncertainties and external disturbances. Considering firstly the transfer function $\frac{e(s)}{n_T(s)}$, without a PI controller ($K_{Pr} = 0$ and $K_{In} = 0$) only one pole in zero is present: in the low frequency range, TMC pressure sensor noises can negatively affect error between brake pressure and its reference value. The presence of proportional and integral gains can change the position of close-loop poles: by considering a fixed value of k_Δ and k_{DC} , bode plots of $\frac{e(s)}{n_T(s)}$ and $\frac{e(s)}{n_b(s)}$ for different values of K_{Pr} and K_{In} are compared in Fig. 3.41. Integral gain modify the Bode plot magnitude on the low frequency region and implies a resonance amplitude peak which can be reduced by the proportional gain. Eq. 3.34: proportional gain influences damping factor (ζ) since integral gain is selected to modify natural frequency (ω_n).

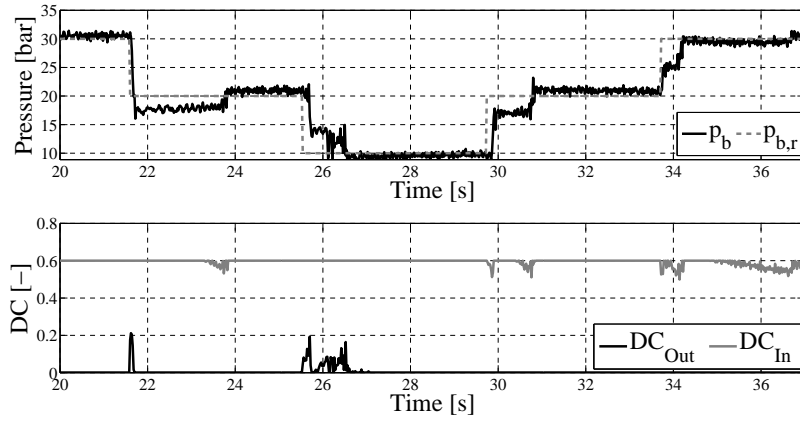


Figure 3.42 System response to a sequence of step changes of the reference pressure (dashed gray)

Experimental Results

This last section shows the experimental results obtained applying the proposed controller to the physical system on the braking test rig. The update rate of the controller set during the experiments is 50 Hz. This limitation is due to the PWM frequency selected for the outlet valve (50 Hz): the electronic instrumentation used for controlling/monitoring the braking system is not able to generate a PWM signal with a frequency lower than the sampling rate of the controller. System responses to three different stimulus profiles are proposed, in order to show the accuracy and efficacy of the proposed controller.

Step response Starting from $K_{Pr} = 1$, $K_{In} = 10$ as optimal values in Fig. 3.41, a sequence of constant steps is imposed to the reference pressure signal in order to validate PI gains.

Fig. 3.42 shows the closed-loop system response, where reference pressure is tracked quite precisely. In this first experiment, FF term intervenes only in the time interval between one step and the following ($\dot{p}_{b,r} \neq 0$), since the required pressure gradient is null when the reference pressure is constant.

It is of interest observing that when brake pressure reaches the reference value, both valves stay closed keeping the pressure equal to its reference value. The lower subplot of Fig. 3.42 shows valves DC in their control operative range: the Inlet DC saturates at 60%, since it behaves as a fully closed valve for larger DC.

Triangle wave excitation A second experiment is performed by imposing a triangle wave signal to the reference pressure. This experiment allows evaluating the FF contribution, i.e. how inverse maps work in response to a constant reference pressure gradient

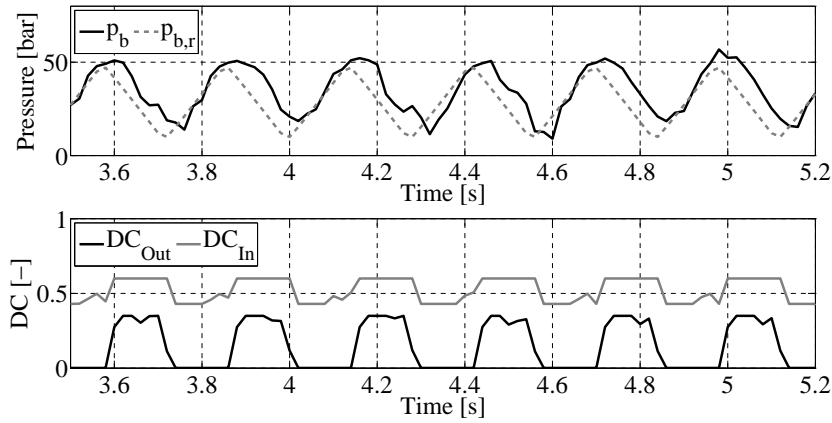


Figure 3.43 System response to a triangle wave reference pressure (dashed gray)

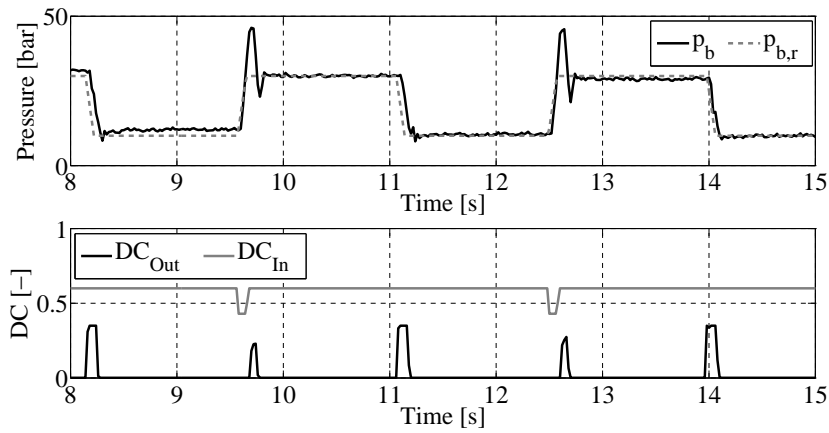


Figure 3.44 System response to a trapezoidal wave reference pressure (dashed gray)

(the PI control is disabled during this test). The response is plotted in Fig. 3.43: even though the measured pressure does not closely match the reference, due to the absence of the linear feedback controller, its gradient closely resemble the 300 bar/s imposed by the wave. The lower chart highlights the activation of both valves in their respective DC operative range: DC values are obtained by entering the inverse maps with $\dot{p} = \pm 300$ bar/s.

Trapezoidal excitation Finally, a trapezoidal excitation allows appreciating the intervention of both FF and PI terms.

Fig. 3.44 proves that the use of inverse maps integrated with a PI controller leads to noticeable improvement in following the reference pressure. PI contribution has the double effect of controlling brake pressure when $\dot{p} = 0$ without adopting FF inverse maps (switching between Inlet and Outlet valve in order to keep constant the brake pressure) and to rejects external disturbances when FF is activated ($\dot{p} \neq 0$). The overshoot visible in

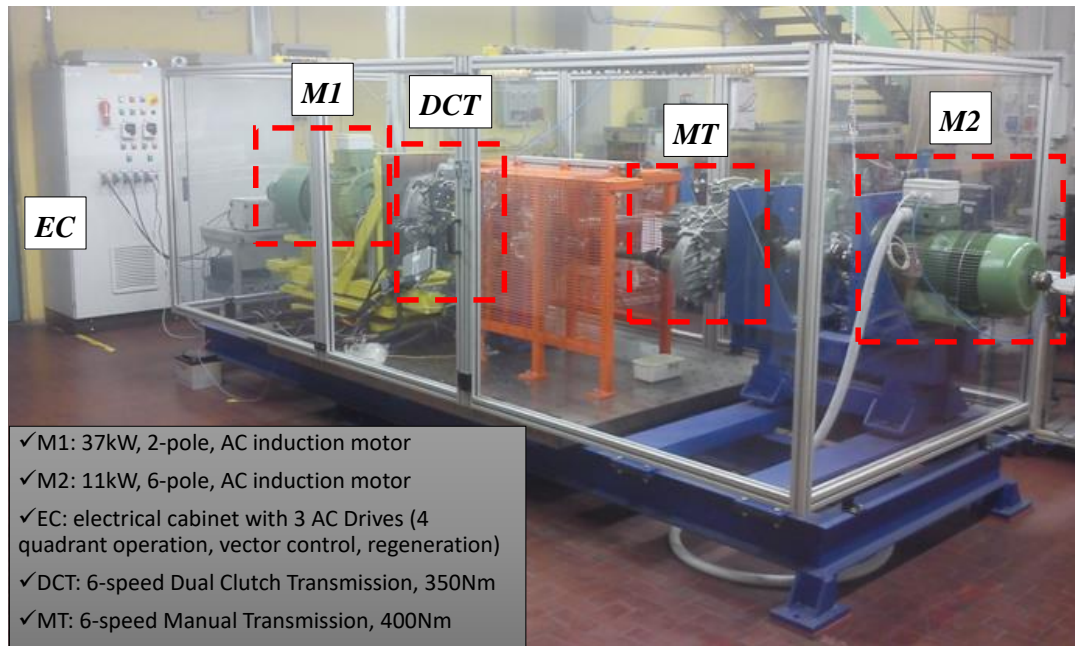


Figure 3.45 Transmission Test Rig at Politecnico di Torino

figure could be limited by adopting a faster control loop rate; unfortunately, as previously stated, the experimental system does not allow to further increase this parameter (the limit is 50 Hz).

3.6 Experimental Analysis of NVH Reduction Control Strategy

In previous two sections the braking intervention logic is studied and designed in order to achieve a desired noise rejection level inside the transmission. Moreover, the braking test rig has been introduced and used for pressure following control strategy by using conventional ABS/ESC hydraulic components. The object of the present section is to describe the transmission test rig and to show the efficacy of braking intervention logic by applying a brake pressure to a caliper mounted on the output of the DCT.

3.6.1 Transmission Test Rig

The transmission test rig located at Politecnico di Torino is shown in Fig. 3.45.

Main components of the test rig are:

- Three-phase induction electric motor M1 with 37 KW

- Three-phase induction electric motor M2 with 11 KW
- Electric Cabinet (EC) with 3 AC drives
- 6-speed Manual Transmission with max torque of 400Nm
- 6-speed Dual Clutch Transmission with max torque of 350Nm

Electric motor M1 is used to simulate the Internal Combustion Engine static behavior meanwhile M2 emulates the vehicle load (aerodynamic and rolling resistance, the road slope, and the vehicle inertial effects). The EC unit is composed by three different drivers for electric power management and regeneration among electric motors and building electric grid. The EC unit software is also able to set up and tune speed or torque control for each electric motor. The 6-speed MT is introduced just for torque/speed range extension between two electric motors, i.e. to amplify the torque delivered by M1. The 6-speed DCT is the mechanical system observed for the NVH analysis whose kinematic and dynamic behavior is described in [143]. The DCT differential is locked since the test rig is used only for longitudinal dynamics.

The test bench is equipped with many sensors for monitoring the dynamic state of the transmission system. For torsional vibration analysis, the most relevant sensors are (see Fig. 3.46):

- three incremental encoders for measuring M1 (1024 pulses per revolution), M2 (3600 pulses per revolution) and DCT differential (9000 pulses per revolution) angular speeds (respectively EM1, EM2 and ED)
- three torque-meter sensor for measuring M1 and M2 output shaft (T_1 with ± 500 Nm and T_2 with ± 230 Nm) torques and half-shaft torque (T_{HS} with ± 2500 Nm)
- ten inductive pick-ups for measuring DCT gears angular speeds: first mass of DMF (Dual Mass Flywheel), two primary shafts, two secondary shafts, differential ring and I, II, III, IV gears
- two sensors for measuring oil temperature inside DCT

Fig. 3.46 also shows the data acquisition layout for both monitoring and controlling the test bench. Four workstations are installed, each one with a specific task:

1. PC1 is used for communicating with electric motor drives through Control Techniques® (CT) softwares, e.g. setting the speed or torque control mode, tuning PID controller gains, monitoring the voltage/current within cabinets and fault diagnosis

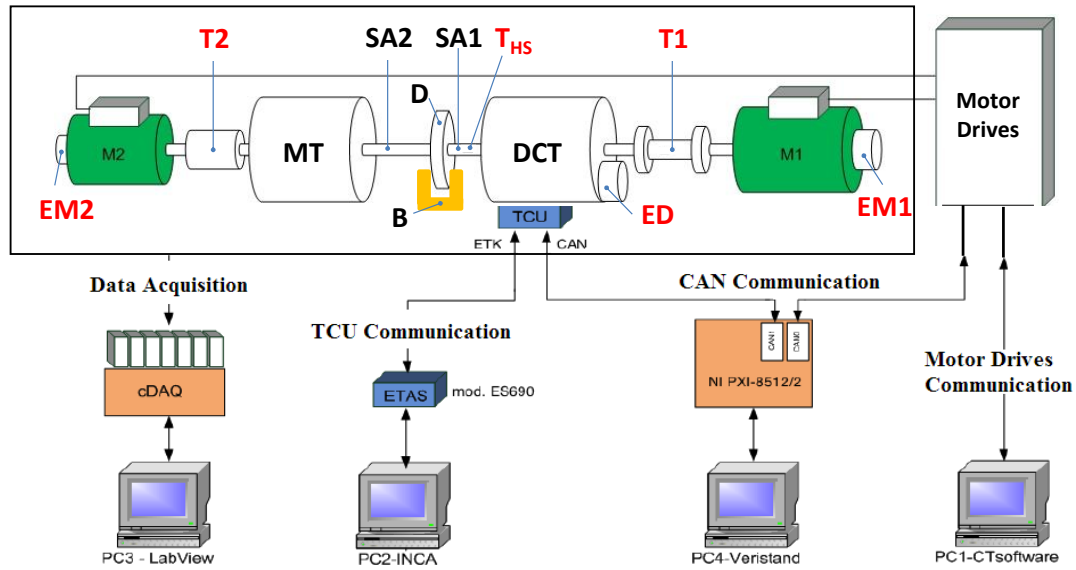


Figure 3.46 Transmission test bench layout. M1, M2: electric motors; EM1, EM2, ED: speed sensors (encoders); T1, T2, T_{HS} : torque sensors; B: disk (D) brake; SA1, SA2: half shafts.

2. PC2 is connected to the DCT control unit (TCU) through ETK communication: gear selection and clutches engagements are managed by INCA[®] software
3. all sensors are connected to a National Instruments (NI) Compact DAQ (cDAQ) and the data is collected only for analysis purposes through NI Labview[®] software installed on PC3
4. the HIL configuration is set up through a NI PXI by interfacing with NI Veristand[®] software installed on PC4

The HIL test rig is conceived with the purpose of reproducing typical maneuvers representative of the real usage of the DCT on a passenger car. This target is achieved through the implementation of a simulation model running and communicating in real time with the sensors and actuators installed on the test rig. One HIL configuration is shown in Fig. 3.47 where the motor M1 is controlled in torque to simulate the static behavior of an internal combustion engine and the motor M2 is controlled in speed for emulating the load applied to the driven axle.

Some further examples of test benches sharing a similar HIL technology are also reported in [180–182]. However, HIL configurations are not the only purpose of the test rig. The good controllability in terms of torque and angular speed of both motors M1 and M2 together with high resolution speed sensors allow the generation of standard

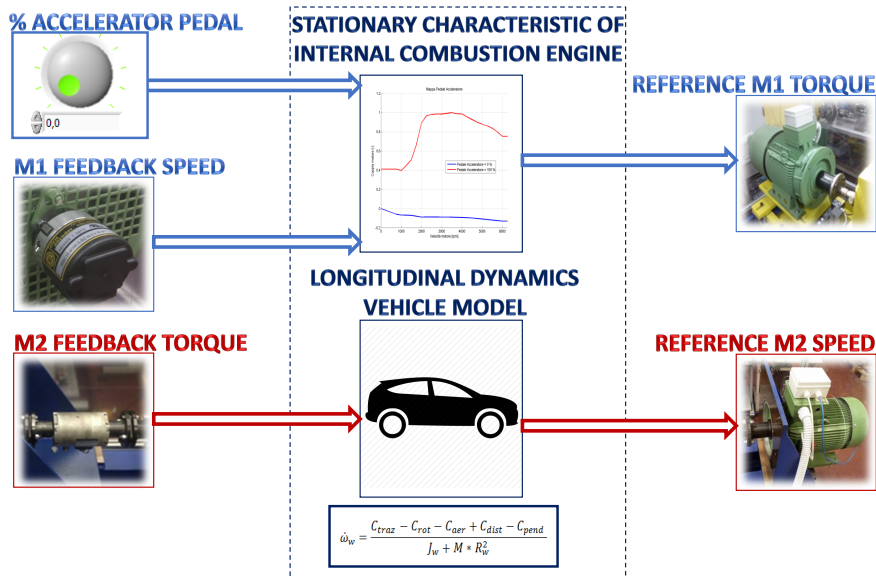


Figure 3.47 Example of HIL configuration for longitudinal dynamics analysis.

(e.g. step, sine wave or chirp) or custom stimulus profiles for the torsional excitation of the system thus accurately monitoring the dynamical system response. The next section is focused on torsional vibration analysis when a brake pressure or torque controller is applied.

3.6.2 Experimental Validation

The test bench previously introduced has been adopted in order to replicate realistic scenarios during which the transmission is supposed to be subjected to NVH issues. The motor with higher power (37 kW) has been used to emulate the static behavior of a conventional internal combustion engine meanwhile the second motor (11 kW) has been controlled in order to replace vehicle external road disturbances (i.e. speed-bump).

Two different experimental scenarios are here considered in order to validate the noise reduction control strategy presented in previous sections:

- Speed-Bump crossing at constant speed
- Tip-Out maneuver

The transmission test rig has been set up in the following configuration:

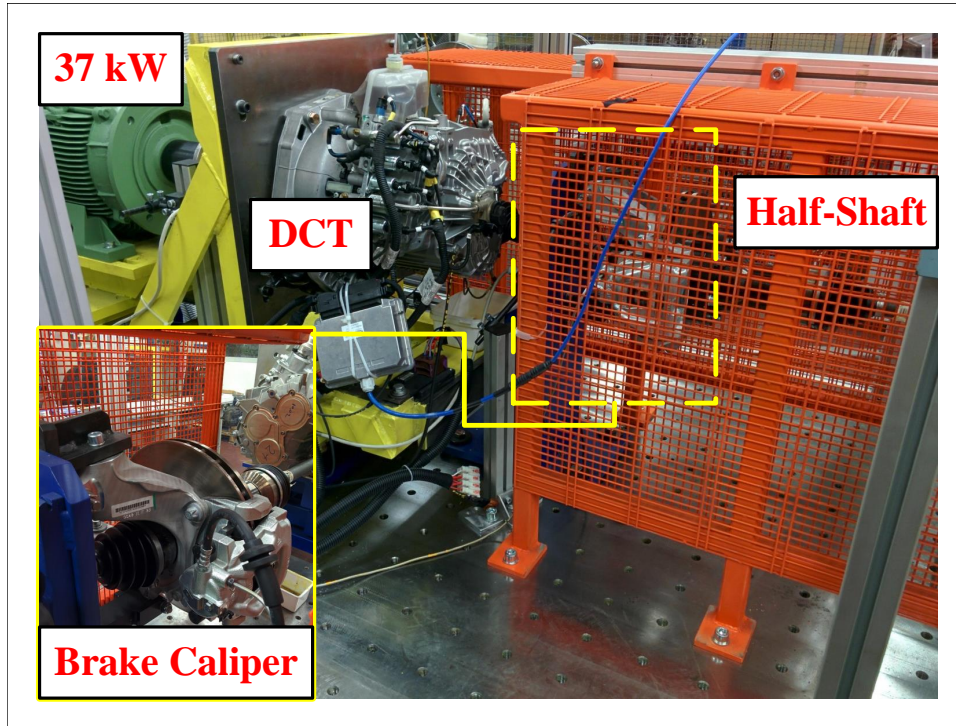


Figure 3.48 DCT Test Rig: zoom on the brake caliper mounting

- the 37 kW motor is controlled in torque in order to guarantee an engine torque sufficient for keeping the vehicle speed at 7 km/h
- the 11 kW motor is controlled in speed in order to have an acceleration profile identified by Fig. 3.6 which emulates the presence of a speed-bump disturbance
- the manual transmission is engaged in second gear
- the DCT is set up with the first gear engaged and the second gear preselected

Moreover, the braking test rig has been configured as follow:

- the front right brake caliper has been placed on the output output shaft of the transmission test rig in order to apply the desired braking torque (Fig. 3.48)
- the remaining three brake calipers are kept in their original position on the brake test rig
- the pressure following control logic previously described is used for controlling ABS digital valves related to the front right caliper
- the remaining ABS digital valves have been kept on their nominal position (Inlet valves open and Outlet valves close)

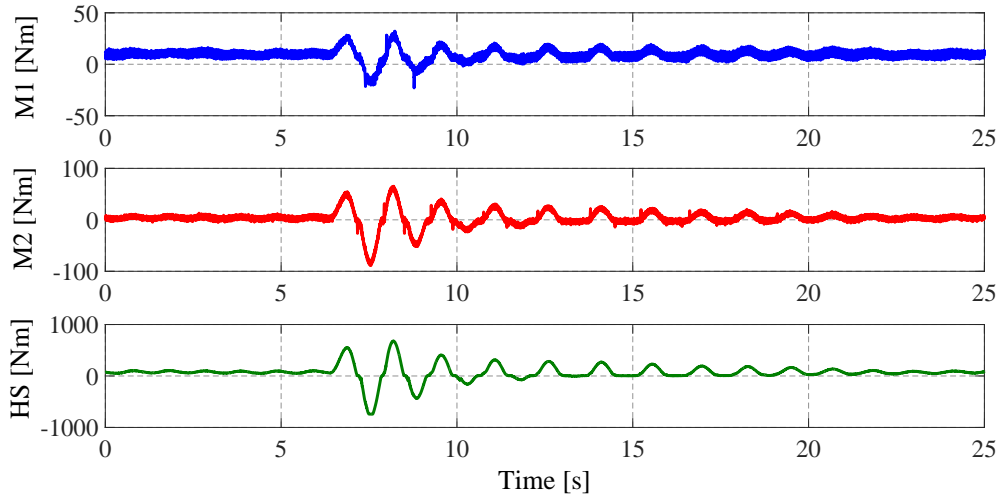


Figure 3.49 Speed-Bump crossing: M1 - torque applied by 37 kW motor; M2 - torque applied by 11 kW motor; HS - Half shaft torque

Speed-Bump crossing

The first experimental test emulates the crossing of speed-bump when the vehicle is supposed to travel at constant speed (7 km/h). The torque applied by the two electric motors and the measured half-shaft torque are shown in Fig. 3.49. The speed-bump disturbance is triggered 6 s after the beginning of the test. The half shaft torque represents a good indication for detecting the presence of noise since the inversion of its sign causes the inversion of the working flank of the teeth, thus originating impacts.

Fig. 3.50 also reports the angular speed of the transmission components: the motor M2 controller is able to follow the speed profile (black line) which accounts for the disturbance imposed by the speed bumper; after twelve seconds the disturbance is distinguished but some oscillations are still evident in all speed profiles. By adopting the same notations used for simulation results of section 3.4.2, the rotational components $\Delta\vartheta$ are plotted in the following Fig. 3.51 and Fig. 3.52. The sign inversion of both M1 and half-shaft torques provokes the sign inversion of $\Delta\vartheta$ thus triggering the generation of internal noises. All $\Delta\vartheta$ values starts from null values since the pick-up sensors measure a relative position, but from Fig. 3.51 it is possible to notice that gears teeth change their contact surface due to the presence of internal backlashes; in particular, the $\Delta\vartheta_{syn,i}$ between the gear and secondary shaft angular position is more marked and protracted, probably due to larger backlashes values. Moreover, the oscillations of $\Delta\vartheta$ on the preselected shaft are slightly reduced if compared with the engaged shaft one; this behavior may be due to a reduced level of oscillations inside the differentials which represents the mechanical node between the two shafts.

The controller strategy presented in section 3.5.3 is adopted for the front right caliper

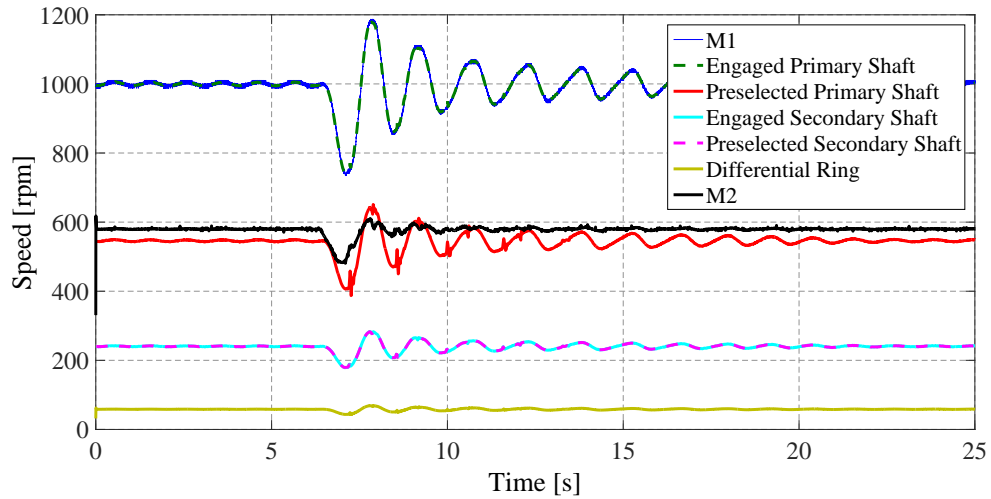
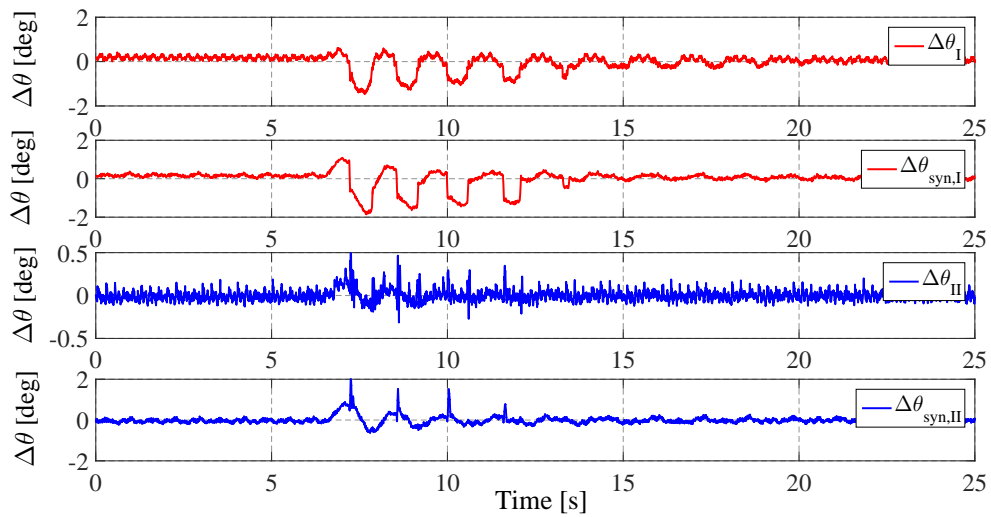


Figure 3.50 Speed-Bump crossing: transmission and motor speeds

Figure 3.51 Speed-Bump crossing: $\Delta\theta$ on the engaged and preselected shafts

in order to control its braking pressure; two different pressure levels (8 bar and 16 bar) are selected and set up as reference values for the controller. In order to recover the dissipative effect imposed by the wheel braking effect and to supply the desired torsional preload, the M1 reference torque is properly increased as indicated in Eq. 3.3 and shown in Fig. 3.53. The half-shaft torque is measured before the application of the braking torque so it increases proportionally with the engine torque. From the other side, M2 torque is almost constant since it is measured downstream the brake caliper so that the brake torque is stationary compensated by the increased M1 (engine) torque: this ensures that if the pressure control logic would be applied to a real scenario, the longitudinal vehicle dynamic will be kept equal to the configuration without control action. Fig. 3.54 shows the $\Delta\theta$ values for the engaged and preselected shafts when a

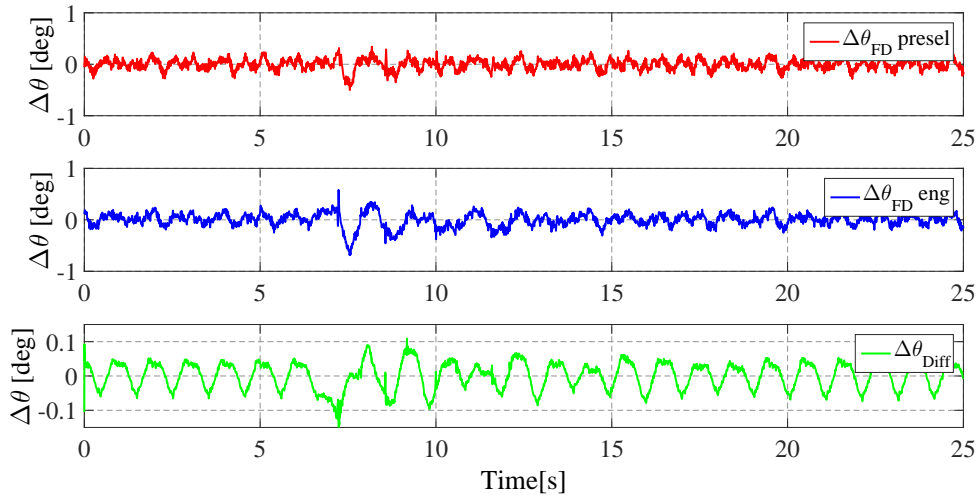
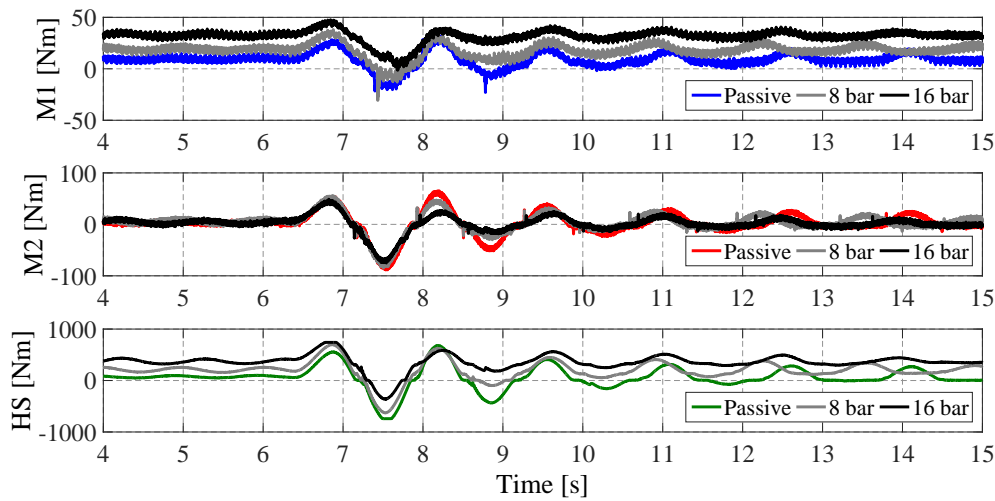
Figure 3.52 Speed-Bump crossing: $\Delta\theta$ inside the differential

Figure 3.53 Speed-Bump crossing with different braking pressures: M1 - torque applied by 37 kW motor; M2 - torque applied by 11 kW motor; HS - Half shaft torque

braking pressure is applied to the output of the transmission: an important oscillations reduction is measured for the engaged shaft especially with the application of a braking pressure of 16 bar (which corresponds to almost 300 Nm of front axle braking torque). The same positive effect is not obtained for the noise reduction on the preselected shaft which seems not sensitive to the brake pressure variations. As mentioned for the simulation results, the preselected shaft is characterized by a low value of preload effect imposed by only friction/damping losses since it is decoupled from the engine.

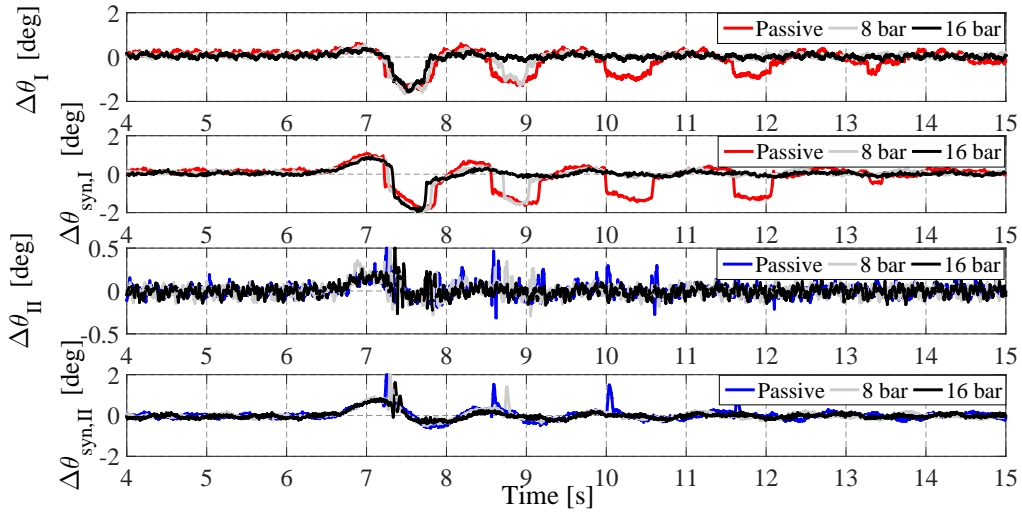


Figure 3.54 Speed-Bump crossing with different braking pressures: $\Delta\theta$ on the engaged and preselected shafts

Tip-Out Maneuver

As final validation test, a Tip-Out maneuver is experimented with an initial constant vehicle speed of 7 km/h: the reference torque imposed on the M1 electric motor falls down instantaneously to a null value. In this way, the torque applied to the transmission changes dynamically its sign thus triggering gears teeth impacts. The brake torque application on the transmission output shaft is counterbalanced by an increasing of engine torque in order to keep the same static wheel torque and so to avoid any longitudinal dynamic modification and to give the desired torsional preload. Fig. 3.55 shows that M2 torque is stationary kept unaltered with the application of a brake torque thus avoiding the driver perception of any controller intervention. For a complete test description, internal transmission speeds are reported in Fig. 3.56 for both passive and controlled vehicles. The angular speed of the differential ring and the electric motor M2 are kept at the same values with and without the controller action. The brake application has a damping effect on all transmission speeds thus reducing internal vibrations level.

A similar analysis can be carried out by plotting $\Delta\theta$ for both engaged and preselected shafts, as indicated in Fig. 3.57. The preload effect introduced by the brake wheel torque and engine torque has a positive influence in terms of gears oscillations as evident from $\Delta\theta$ on the engaged shaft where there is a visible noise rejection, meanwhile the same positive effect is less marked but still present on the preselected shaft.

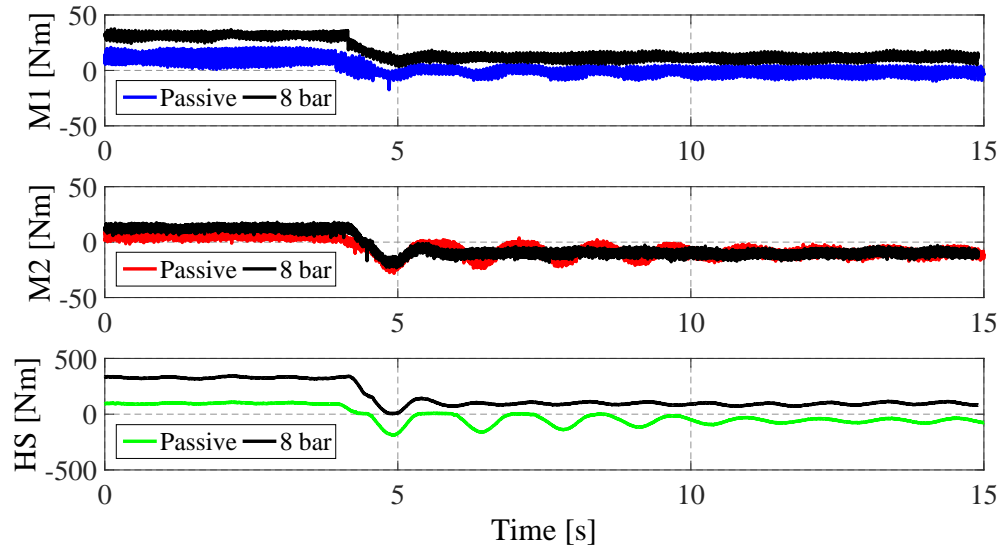


Figure 3.55 Tip-Out Maneuver with and without the control action (brake pressure of 8 bar): M1 - torque applied by 37 kW motor; M2 - torque applied by 11 kW motor; HS - Half shaft torque

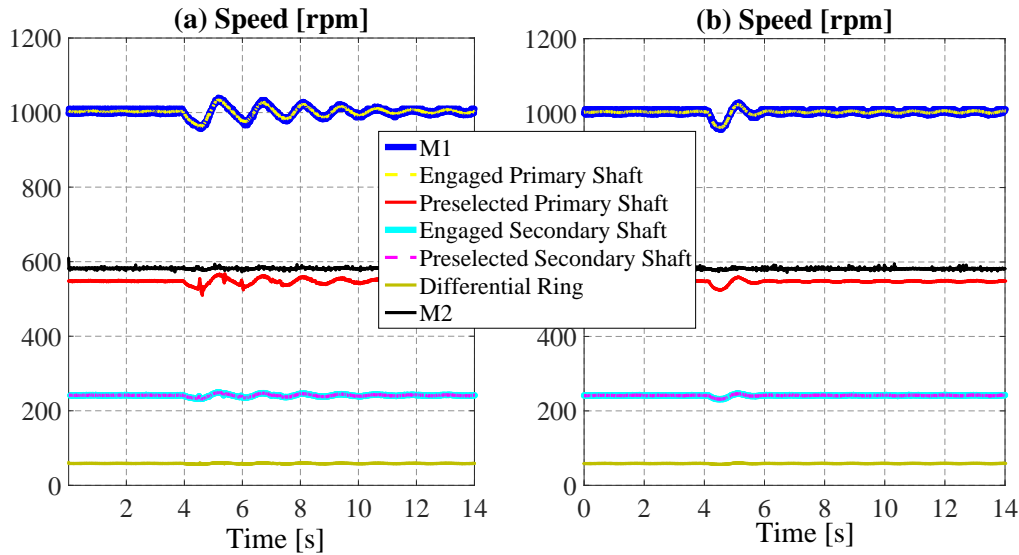


Figure 3.56 Tip-Out Maneuver without (a) and with (b) the control action (brake pressure of 8 bar): transmission speeds

3.7 Conclusions

Recent research activities discussed in the present chapter demonstrate the wide potential of powertrain and active braking control integration from transmission NVH perspective: a brake pressure control strategy, integrated with a powertrain control to compensate its longitudinal dynamic modification, is able to reduce the noise level inside the transmission. The larger the brake pressure, the greater is the noise level reduc-

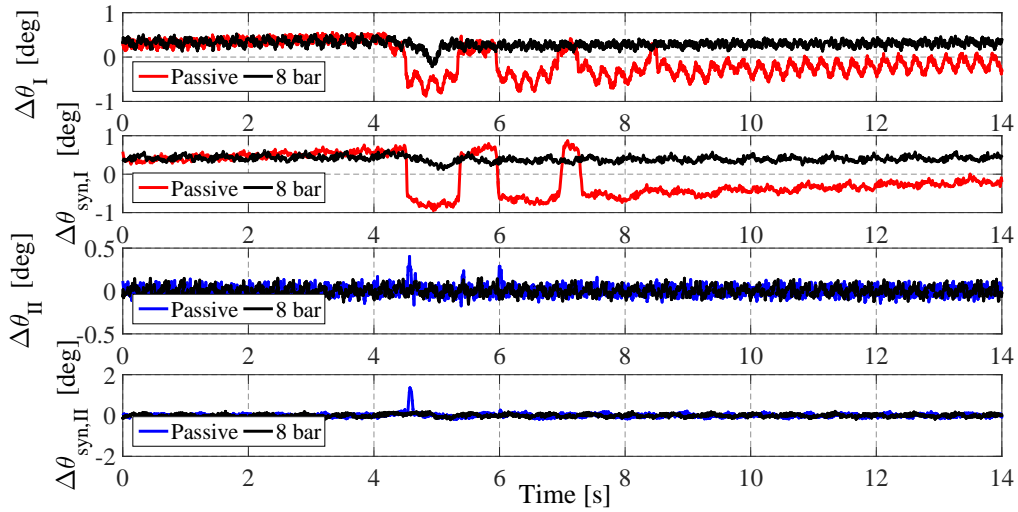


Figure 3.57 Tip-Out Maneuver without (a) and with (b) the control action (brake pressure of 8 bar): $\Delta\theta$ on the engaged and preselected shafts

tion inside the transmission, with the drawback of higher fuel consumption with respect to the configuration without control strategy. In particular, this strategy is more effective for the engaged than the preselected shaft due to a different preload: the engaged shaft is directly affected by the preload effect imposed by the brake control strategy, while the preselected shaft cannot be preloaded as much as on the other one thus showing a lower benefit. For this reason, a further calibration on driver noises perception must be carried out in order to optimize the energy consumption for getting the desired NVH performances. Moreover, a control logic that activates the clutch of the unloaded transmission path in combination with the brakes has also the potentiality to reduce noise and vibrations from the gearbox. The research activity also proves that even a simple pressure following control logic can be designed by using conventional braking systems and its efficacy is demonstrated through specific experimental test on HIL test rig.

Future studies will be concentrated on the high level control logic improvement for proactive detection of a critical event through on-board sensors or estimators in order to allow brake and powertrain control enough time to preload the transmission and prevent noise generation.

Conclusions and Recommendation for Future Works

In the present doctoral dissertation several solutions for passenger vehicle active systems design and integration are discussed and implemented for practical case scenarios. Automation, handling, safety and comfort are the objectives achieved by controller strategies presented in each chapter by activating or combining conventional and innovative vehicle actuators. The first chapter introduces the autonomous driving topic by converting a conventional passenger car into an autonomous vehicle through the installation of drive-by-wire technology. In particular, an automated driving system is studied and implemented for path tracking and collision avoidance purposes. Different control logic are designed and compared during specific experimental maneuvers, demonstrating their efficacy in following a reference path even in presence of static obstacles. The activity shows how a simple design methodology is successfully applicable for autonomous driving or automated steering adopted for conventional vehicles. A possible drawback of the proposed solution comes from the safety-comfort point of view, since the performance task (i.e. following a specific trajectory and keeping as low as possible the lateral deviation) may lead to undesirable yaw rate and sideslip angle oscillations. Consequently, the effect of a concurrent yaw rate and sideslip angle controller is presented in the second chapter where a torque vectoring strategy for fully electric vehicles is analyzed. The steering angle imposed by the driver (or eventually from an automated steering control) is considered as a 'disturbance' from the point of view of TV strategy, and the handling task (here identified by the desired understeer characteristic achievement) is pursued by taking into account the safety margin (sideslip angle control) in the design process. The TV strategy is finally experimentally validated and tuned by flashing it on a FEV demonstrator through the execution of aggressive and realistic maneuvers positively judged by a professional driver. It is also proved that a concurrent yaw rate and sideslip angle control can be implemented in real case scenario thus demonstrating the importance of introducing a properly designed sideslip angle control for safety purposes. Further analysis may consist in evaluating the TV

strategy by introducing in the controller loop a sideslip angle estimator (instead of a sensor usually not available in a passenger vehicle); a possible solution is presented at the end of the chapter. Future investigations are necessary for improving the low level TV strategy where the torque of each electric motor must be properly controlled to achieve the desired yaw moment (calculated from the reference understeer characteristic): some related activities have been discussed by some authors by coupling a wheel slip controller when tires reach their saturation limits or by integrating an optimization algorithm from the efficiency viewpoint. The TV strategy is designed and implemented for a fully electric vehicle since it represents one of the most flexible solution, but it can be applied also for conventional or hybrid vehicles by introducing specific devices in the driveline (e.g., torque vectoring differentials). The presence of the driveline may negatively affect the TV strategy since it introduces a mechanical delay not present in a FEV architecture; a second important drawback is related to the torque inversion that may be requested by the logic, thus leading to undesirable effects from the comfort point of view, causing noises and vibrations. This aspect is analyzed and studied in the last part of the dissertation, where noise and vibration generation is observed for a dual clutch transmission when a wheel torque sign change occurs. NVH issues are specifically evident for high efficiency transmissions where gears or synchronizer backlashes can be recovered in presence of wheel torque inversion due to external (from road side) or internal disturbances (from engine control side or TV torque requests). An innovative methodology for reducing noise inside the transmission, without modifying the desired longitudinal dynamics, is introduced by integrating the intervention of a conventional braking system not usually adopted for transmission NVH purposes. Brake calipers pressure following strategy is designed and implemented by exploiting the hardware conventionally available on-board (digital on-off electro-valves originally thought for ABS/ESC control logic). Controller strategy efficacy is proved on a HIL test rig where a real brake and DCT hardware is installed and the effect of a brake pressure control on transmission NVH is shown. This represents only the first step for an innovative idea which has not been explored by other authors; successful results encourage for further improvements especially for the high level part of the strategy where the NVH sources have to be identified in order to guarantee a proactive activation of the braking system and of the engine torque.

In conclusions, the present dissertation has introduced novelty and innovative concepts by integrating different vehicle systems also providing new ideas and methodologies for further development in the field of vehicle dynamics control.

Bibliography

- [1] G Genta and L Morello. The automotive chassis: Volume 2: System design (mechanical engineering series), 2009.
- [2] Leonardo De Novellis, Aldo Sorniotti, and Patrick Gruber. Wheel torque distribution criteria for electric vehicles with torque-vectoring differentials. *IEEE Transactions on Vehicular Technology*, 63(4):1593–1602, 2014.
- [3] Qian Lu, Pierangelo Gentile, Antonio Tota, Aldo Sorniotti, Patrick Gruber, Fabio Costamagna, and Jasper De Smet. Enhancing vehicle cornering limit through sideslip and yaw rate control. *Mechanical Systems and Signal Processing*, 75:455–472, 2016.
- [4] Tommaso Goggia, Aldo Sorniotti, Leonardo De Novellis, Antonella Ferrara, Patrick Gruber, Johan Theunissen, Dirk Steenbeke, Bernhard Knauder, and Josef Zehetner. Integral sliding mode for the torque-vectoring control of fully electric vehicles: Theoretical design and experimental assessment. *IEEE Transactions on Vehicular Technology*, 64(5):1701–1715, 2015.
- [5] SAE On-Road Automated Vehicle Standards Committee et al. Taxonomy and definitions for terms related to on-road motor vehicle automated driving systems, 2014.
- [6] Michael Regan and Kristie Young. *Use of manual speed alerting and cruise control devices by drivers in New South Wales*. Number 219. 2004.
- [7] Susanne Schleicher, Christhard Gelau, et al. The influence of cruise control and adaptive cruise control on driving behaviour—a driving simulator study. *Accident Analysis & Prevention*, 43(3):1134–1139, 2011.
- [8] T Watanabe, N Kishimoto, K Hayafune, K Yamada, and N Maede. Development of an intelligent cruise control system. In *Steps Forward. Intelligent Transport Systems World Congress*, number Volume 3, 1995.
- [9] Rajesh Rajamani. *Vehicle dynamics and control*. Springer Science & Business Media, 2011.
- [10] Gianpiero Mastinu and Manfred Ploechl. *Road and off-road vehicle system dynamics handbook*. CRC Press, 2014.
- [11] Pamela I Labuhn and William J Chundrlik Jr. Adaptive cruise control, October 3 1995. US Patent 5,454,442.

- [12] C Grover, I Knight, F Okoro, I Simmons, G Couper, P Massie, B Smith, et al. Automated emergency brake systems: Technical requirements, costs and benefits. *Automated emergency brake systems: technical requirements, costs and benefits*, 1(1):1–109, 2013.
- [13] Martin Distner, Mattias Bengtsson, Thomas Broberg, and Lotta Jakobsson. City safety—a system addressing rear-end collisions at low speeds. In *Proc. 21st International Technical Conference on the Enhanced Safety of Vehicles*, number 09-0371, 2009.
- [14] John A Michon. A critical view of driver behavior models: what do we know, what should we do? In *Human behavior and traffic safety*, pages 485–524. Springer, 1985.
- [15] TJ Gordon and Mathias Lidberg. Automated driving and autonomous functions on road vehicles. *Vehicle System Dynamics*, 53(7):958–994, 2015.
- [16] Ola Dahl and Lars Nielsen. Torque-limited path following by online trajectory time scaling. *IEEE Transactions on Robotics and Automation*, 6(5):554–561, 1990.
- [17] Lionel Lapierre, Rene Zapata, and Pascal Lepinay. Combined path-following and obstacle avoidance control of a wheeled robot. *The International Journal of Robotics Research*, 26(4):361–375, 2007.
- [18] Diederik Verscheure, Bram Demeulenaere, Jan Swevers, Joris De Schutter, and Moritz Diehl. Time-optimal path tracking for robots: A convex optimization approach. *IEEE Transactions on Automatic Control*, 54(10):2318–2327, 2009.
- [19] Charles C MacAdam. Application of an optimal preview control for simulation of closed-loop automobile driving. *IEEE Transactions on Systems, Man, and Cybernetics*, 11(6):393–399, 1981.
- [20] RS Sharp, DANIELE Casanova, and P Symonds. A mathematical model for driver steering control, with design, tuning and performance results. *Vehicle System Dynamics*, 33(5):289–326, 2000.
- [21] Robin S Sharp. Driver steering control and a new perspective on car handling qualities. *Proceedings of the Institution of Mechanical Engineers, Part C: Journal of Mechanical Engineering Science*, 219(10):1041–1051, 2005.
- [22] R Oshima, E Kikuchi, M Kimura, and S Matsumoto. Control system for automobile driving. In *Proceedings of the Tokyo IFAC Symposium*, pages 347–357, 1965.
- [23] Robert E Fenton and Robert J Mayhan. Automated highway studies at the ohio state university-an overview. *IEEE transactions on Vehicular Technology*, 40(1):100–113, 1991.
- [24] Aldo Sorniotti, Phil Barber, and Stefano De Pinto. Path tracking for automated driving: A tutorial on control system formulations and ongoing research. In *Automated Driving*, pages 71–140. Springer, 2017.
- [25] R Craig Coulter. Implementation of the pure pursuit path tracking algorithm. Technical report, DTIC Document, 1992.

- [26] Jarrod M Snider et al. Automatic steering methods for autonomous automobile path tracking. *Robotics Institute, Pittsburgh, PA, Tech. Rep. CMU-RITR-09-08*, 2009.
- [27] Sebastian Thrun, Mike Montemerlo, Hendrik Dahlkamp, David Stavens, Andrei Aron, James Diebel, Philip Fong, John Gale, Morgan Halpenny, Gabriel Hoffmann, et al. Stanley: The robot that won the darpa grand challenge. In *The 2005 DARPA Grand Challenge*, pages 1–43. Springer, 2007.
- [28] Sadayuki Tsugawa. An overview on control algorithms for automated highway systems. In *Intelligent Transportation Systems, 1999. Proceedings. 1999 IEEE/IEEE/JSAI International Conference on*, pages 234–239. IEEE, 1999.
- [29] Hiroshi Mouri and Hiroyuki Furusho. Automatic path tracking using linear quadratic control theory. In *Intelligent Transportation System, 1997. ITSC'97., IEEE Conference on*, pages 948–953. IEEE, 1997.
- [30] Jürgen Guldner, Han-Shue Tan, and Satyajit Patwardhan. Analysis of automatic steering control for highway vehicles with look-down lateral reference systems. *Vehicle System Dynamics*, 26(4):243–269, 1996.
- [31] Hideaki Inoue, H Mouri, H Sato, A Asaoka, and S Ueda. Technologies of nissan's ahs test vehicle. In *3rd ITS World Congress*, 1996.
- [32] Jürgen Ackermann, Jürgen Guldner, Wolfgang Sienel, Reinhold Steinhauser, and Vadim I Utkin. Linear and nonlinear controller design for robust automatic steering. *IEEE Transactions on Control Systems Technology*, 3(1):132–143, 1995.
- [33] Jürgen Ackermann. *Robust control: the parameter space approach*. Springer Science & Business Media, 2012.
- [34] Jürgen Guldner, Wolfgang Sienel, Han-Shue Tan, Jürgen Ackermann, Satyajit Patwardhan, and Tilman Bunte. Robust automatic steering control for look-down reference systems with front and rear sensors. *IEEE transactions on control systems technology*, 7(1):2–11, 1999.
- [35] Mümin Tolga Emirler, Haoan Wang, Bilin Aksun Güvenç, and Levent Güvenç. Automated robust path following control based on calculation of lateral deviation and yaw angle error. In *ASME 2015 Dynamic Systems and Control Conference*, pages V003T50A009–V003T50A009. American Society of Mechanical Engineers, 2015.
- [36] Vito Cerone, A Chinu, and D Regruto. Experimental results in vision-based lane keeping for highway vehicles. In *American Control Conference, 2002. Proceedings of the 2002*, volume 2, pages 869–874. IEEE, 2002.
- [37] Huei Peng and Masayoshi Tomizuka. Optimal preview control for vehicle lateral guidance. *California Partners for Advanced Transit and Highways (PATH)*, 1991.
- [38] JK Hedrick, Masayoshi Tomizuka, and P Varaiya. Control issues in automated highway systems. *IEEE Control Systems*, 14(6):21–32, 1994.
- [39] Huei Peng, Masayoshi Tomizuka, et al. Preview control for vehicle lateral guidance in highway automation. *TRANSACTIONS-AMERICAN SOCIETY OF MECHANICAL ENGINEERS JOURNAL OF DYNAMIC SYSTEMS MEASUREMENT AND CONTROL*, 115:679–679, 1993.

- [40] Toshihiro Hiraoka, Osamu Nishihara, and Hiromitsu Kumamoto. Automatic path-tracking controller of a four-wheel steering vehicle. *Vehicle System Dynamics*, 47(10):1205–1227, 2009.
- [41] Gilles Tagne, Reine Talj, and Ali Charara. Higher-order sliding mode control for lateral dynamics of autonomous vehicles, with experimental validation. In *Intelligent Vehicles Symposium (IV)*, 2013 IEEE, pages 678–683. IEEE, 2013.
- [42] Pushkar Hingwe and Masayoshi Tomizuka. Experimental evaluation of a chatter free sliding mode control for lateral control in ahs. In *American Control Conference, 1997. Proceedings of the 1997*, volume 5, pages 3365–3369. IEEE, 1997.
- [43] Hocine Imine and Tarek Madani. Sliding-mode control for automated lane guidance of heavy vehicle. *International Journal of Robust and Nonlinear Control*, 23(1):67–76, 2013.
- [44] C Hatipoglu, Keith Redmill, and Umit Ozguner. Steering and lane change: A working system. In *Intelligent Transportation System, 1997. ITSC'97., IEEE Conference on*, pages 272–277. IEEE, 1997.
- [45] Anthony B Will and STANISLAW H Z AK. Modelling and control of an automated vehicle. *Vehicle System Dynamics*, 27(3):131–155, 1997.
- [46] Richard T O'Brien, Pablo A Iglesias, and Thomas J Urban. Vehicle lateral control for automated highway systems. *IEEE Transactions on Control Systems Technology*, 4(3):266–273, 1996.
- [47] Salim Hima, Benoit Lusseti, Benoit Vanholme, Sebastien Glaser, and Said Mammar. Trajectory tracking for highly automated passenger vehicles. *IFAC Proceedings Volumes*, 44(1):12958–12963, 2011.
- [48] DH Shin and BY Joo. Design of a vision-based autonomous path-tracking control system and experimental validation. *Proceedings of the Institution of Mechanical Engineers, Part D: Journal of Automobile Engineering*, 224(7):849–864, 2010.
- [49] José Eugenio Naranjo, Carlos González, Ricardo García, Teresa De Pedro, and Rodolfo E Haber. Power-steering control architecture for automatic driving. *IEEE Transactions on Intelligent Transportation Systems*, 6(4):406–415, 2005.
- [50] Jun Ni and Jibin Hu. Dynamics control of autonomous vehicle at driving limits and experiment on an autonomous formula racing car. *Mechanical Systems and Signal Processing*, 90:154–174, 2017.
- [51] Krisada Kritayakirana and J Christian Gerdes. Autonomous vehicle control at the limits of handling. *International Journal of Vehicle Autonomous Systems*, 10(4):271–296, 2012.
- [52] Nitin R Kapania and J Christian Gerdes. Design of a feedback-feedforward steering controller for accurate path tracking and stability at the limits of handling. *Vehicle System Dynamics*, 53(12):1687–1704, 2015.
- [53] Guodong Yin, Jianghu Li, Xianjian Jin, Chentong Bian, and Nan Chen. Integration of motion planning and model-predictive-control-based control system for autonomous electric vehicles. *Transport*, 30(3):353–360, 2015.

- [54] Rachid Attia, Rodolfo Orjuela, and Michel Basset. Combined longitudinal and lateral control for automated vehicle guidance. *Vehicle System Dynamics*, 52(2):261–279, 2014.
- [55] Yiqi Gao, Andrew Gray, H Eric Tseng, and Francesco Borrelli. A tube-based robust nonlinear predictive control approach to semiautonomous ground vehicles. *Vehicle System Dynamics*, 52(6):802–823, 2014.
- [56] Jie Ji, Amir Khajepour, William Melek, and Yanjun Huang. Path planning and tracking for vehicle collision avoidance based on model predictive control with multi-constraints. *IEEE Transactions on Vehicular Technology*, 2016.
- [57] Mengyin Fu, Kai Zhang, Yi Yang, Hao Zhu, and Meiling Wang. Collision-free and kinematically feasible path planning along a reference path for autonomous vehicle. In *Intelligent Vehicles Symposium (IV), 2015 IEEE*, pages 907–912. IEEE, 2015.
- [58] Keonyup Chu, Minchae Lee, and Myoungho Sunwoo. Local path planning for off-road autonomous driving with avoidance of static obstacles. *IEEE Transactions on Intelligent Transportation Systems*, 13(4):1599–1616, 2012.
- [59] Sean Quinlan and Oussama Khatib. Elastic bands: Connecting path planning and control. In *Robotics and Automation, 1993. Proceedings., 1993 IEEE International Conference on*, pages 802–807. IEEE, 1993.
- [60] Öncü Ararat and Bilin Aksun Güvenç. Development of a collision avoidance algorithm using elastic band theory. *IFAC Proceedings Volumes*, 41(2):8520–8525, 2008.
- [61] Dataspeed inc. Last accessed 15 February 2017.
- [62] Delphi electronically scanning radar. Last accessed 15 February 2017.
- [63] Velodyne lidar. Last accessed 15 February 2017.
- [64] Mobileye camera development kit. Last accessed 15 February 2017.
- [65] OXTS xnav. Last accessed 15 February 2017.
- [66] Giancarlo Genta and Lorenzo Morello. *The automotive chassis*, volume 1. Springer, 2009.
- [67] William F Milliken and Douglas L Milliken. *Race car vehicle dynamics*, volume 400. Society of Automotive Engineers Warrendale, 1995.
- [68] A Lienard and MH Chipart. On the sign of the real part of the roots of algebraic equations. *J. Math. Pares. Appl.*, 6(10):291–346, 1914.
- [69] RA Frazer and WJ Duncan. On the criteria for the stability of small motions. *Proceedings of the Royal Society of London. Series A, Containing Papers of a Mathematical and Physical Character*, 124(795):642–654, 1929.
- [70] Katsuhiko Ogata. *Discrete-time control systems*, volume 2. Prentice Hall Englewood Cliffs, NJ, 1995.

- [71] Yuri Shtessel, Christopher Edwards, Leonid Fridman, and Arie Levant. *Sliding mode control and observation*. Springer, 2014.
- [72] Vadim Utkin, Jürgen Guldner, and Jingxin Shi. *Sliding mode control in electro-mechanical systems*, volume 34. CRC press, 2009.
- [73] Vadim Utkin and Jingxin Shi. Integral sliding mode in systems operating under uncertainty conditions. In *Decision and Control, 1996., Proceedings of the 35th IEEE Conference on*, volume 4, pages 4591–4596. IEEE, 1996.
- [74] CC Chan and KT Chau. *Modern electric vehicle technology*, volume 47. Oxford University Press on Demand, 2001.
- [75] Kaoru Sawase, Yuichi Ushiroda, and Takami Miura. Left-right torque vectoring technology as the core of super all wheel control (s-awc). *Mitsubishi Motors Technical Review*, 18:16–23, 2006.
- [76] Massimo Canale, Lorenzo Fagiano, Mario Milanese, and P Borodani. Robust vehicle yaw control using an active differential and imc techniques. *Control Engineering Practice*, 15(8):923–941, 2007.
- [77] Leonardo De Novellis, Aldo Sorniotti, Patrick Gruber, Javier Orus, Jose-Manuel Rodriguez Fortun, Johan Theunissen, and Jasper De Smet. Direct yaw moment control actuated through electric drivetrains and friction brakes: Theoretical design and experimental assessment. *Mechatronics*, 26:1–15, 2015.
- [78] Leonardo De Novellis, Aldo Sorniotti, and Patrick Gruber. Driving modes for designing the cornering response of fully electric vehicles with multiple motors. *Mechanical Systems and Signal Processing*, 64:1–15, 2015.
- [79] David A Crolla and Dongpu Cao. The impact of hybrid and electric powertrains on vehicle dynamics, control systems and energy regeneration. *Vehicle system dynamics*, 50(sup1):95–109, 2012.
- [80] Leonardo De Novellis, Aldo Sorniotti, Patrick Gruber, Leo Shead, Valentin Ivanov, and Kristian Hoeppeing. Torque vectoring for electric vehicles with individually controlled motors: state-of-the-art and future developments. In *26th Electric Vehicle Symposium 2012*, 2012.
- [81] Yasuji Shibahata, K Shimada, and T Tomari. Improvement of vehicle maneuverability by direct yaw moment control. *Vehicle System Dynamics*, 22(5-6):465–481, 1993.
- [82] Kazuhiko Shimada and Yasuji Shibahata. Comparison of three active chassis control methods for stabilizing yaw moments. Technical report, SAE Technical Paper, 1994.
- [83] WJ Manning and DA Crolla. A review of yaw rate and sideslip controllers for passenger vehicles. *Transactions of the Institute of Measurement and Control*, 29(2):117–135, 2007.
- [84] Hui Zhang and Junmin Wang. Vehicle lateral dynamics control through afs/dyc and robust gain-scheduling approach. *IEEE Transactions on Vehicular Technology*, 65(1):489–494, 2016.

- [85] Riccardo Marino and Stefano Scalzi. Asymptotic sideslip angle and yaw rate decoupling control in four-wheel steering vehicles. *Vehicle System Dynamics*, 48(9):999–1019, 2010.
- [86] Shuibo Zheng, Houjun Tang, Zhengzhi Han, and Yong Zhang. Controller design for vehicle stability enhancement. *Control Engineering Practice*, 14(12):1413–1421, 2006.
- [87] Cong Geng, Lotfi Mostefai, Mouloud Denai, and Yoichi Hori. Direct yaw-moment control of an in-wheel-motored electric vehicle based on body slip angle fuzzy observer. *IEEE Transactions on Industrial Electronics*, 56(5):1411–1419, 2009.
- [88] Motoki Shino and Masao Nagai. Yaw-moment control of electric vehicle for improving handling and stability. *JSAE review*, 22(4):473–480, 2001.
- [89] Lu Xiong, Zhuoping Yu, Yang Wang, Chen Yang, and Yufeng Meng. Vehicle dynamics control of four in-wheel motor drive electric vehicle using gain scheduling based on tyre cornering stiffness estimation. *Vehicle system dynamics*, 50(6):831–846, 2012.
- [90] Massimo Canale, Lorenzo Fagiano, Antonella Ferrara, and Claudio Vecchio. Vehicle yaw control via second-order sliding-mode technique. *IEEE Transactions on Industrial Electronics*, 55(11):3908–3916, 2008.
- [91] Masato Abe, Yoshio Kano, Kazuasa Suzuki, Yasuji Shibahata, and Yoshimi Furukawa. Side-slip control to stabilize vehicle lateral motion by direct yaw moment. *JSAE review*, 22(4):413–419, 2001.
- [92] Daniel Rubin and Shai Arogeti. Vehicle yaw stability control using rear active differential via sliding mode control methods. In *Control & Automation (MED), 2013 21st Mediterranean Conference on*, pages 317–322. IEEE, 2013.
- [93] R Tchamna and I Youn. Yaw rate and side-slip control considering vehicle longitudinal dynamics. *International Journal of Automotive Technology*, 14(1):53–60, 2013.
- [94] Hongtian Zhang and Jinzhu Zhang. Yaw torque control of electric vehicle stability. In *2012 IEEE 6th International Conference on Information and Automation for Sustainability*, pages 318–322. IEEE, 2012.
- [95] DV Thang Truong, Martin Meywerk, and Winfried Tomaske. Torque vectoring for rear axle using adaptive sliding mode control. In *Control, Automation and Information Sciences (ICCAIS), 2013 International Conference on*, pages 328–333. IEEE, 2013.
- [96] Houyu Yu, Miaohua Huang, and Zhenliang Zhang. Direct yaw-moment hinfinity control of motor-wheel driving electric vehicle. In *2013 IEEE Vehicle Power and Propulsion Conference (VPPC)*, pages 1–5. IEEE, 2013.
- [97] Vito Cerone, Mario Milanese, and Diego Regruto. Yaw stability control design through a mixed-sensitivity approach. *IEEE Transactions on Control Systems Technology*, 17(5):1096–1104, 2009.

- [98] Gerd Kaiser. *Torque Vectoring-Linear Parameter-Varying Control for an Electric Vehicle*. Verlag Dr. Hut München, 2015.
- [99] Kanghyun Nam, Hiroshi Fujimoto, and Yoichi Hori. Advanced motion control of electric vehicles based on robust lateral tire force control via active front steering. *IEEE/ASME Transactions on Mechatronics*, 19(1):289–299, 2014.
- [100] Paolo Falcone, Francesco Borrelli, Jahan Asgari, Hongtei Eric Tseng, and Davor Hrovat. Predictive active steering control for autonomous vehicle systems. *IEEE Transactions on control systems technology*, 15(3):566–580, 2007.
- [101] Giovanni Palmieri, Miroslav Barić, Luigi Glielmo, and Francesco Borrelli. Robust vehicle lateral stabilisation via set-based methods for uncertain piecewise affine systems. *Vehicle System Dynamics*, 50(6):861–882, 2012.
- [102] Pongsathorn Raksincharoensak, Takuya Mizushima, and Masao Nagai. Direct yaw moment control system based on driver behaviour recognition. *Vehicle System Dynamics*, 46(S1):911–921, 2008.
- [103] F Assadian and M Hancock. A comparison of yaw stability control strategies for the active differential. In *Proceedings of the IEEE International Symposium on Industrial Electronics, 2005. ISIE 2005.*, volume 1, pages 373–378. IEEE, 2005.
- [104] Leonardo De Novellis, Aldo Sorniotti, Patrick Gruber, and Andrew Pennycott. Comparison of feedback control techniques for torque-vectoring control of fully electric vehicles. *IEEE Transactions on Vehicular Technology*, 63(8):3612–3623, 2014.
- [105] Andy Wong, Dhanaraja Kasinathan, Amir Khajepour, Shih-Ken Chen, and Bakhtiar Litkouhi. Integrated torque vectoring and power management framework for electric vehicles. *Control Engineering Practice*, 48:22–36, 2016.
- [106] Zhibin Shuai, Hui Zhang, Junmin Wang, Jianqiu Li, and Minggao Ouyang. Lateral motion control for four-wheel-independent-drive electric vehicles using optimal torque allocation and dynamic message priority scheduling. *Control Engineering Practice*, 24:55–66, 2014.
- [107] Leonardo De Novellis, Aldo Sorniotti, and Patrick Gruber. Design and comparison of the handling performance of different electric vehicle layouts. *Proceedings of the Institution of Mechanical Engineers, Part D: Journal of Automobile Engineering*, 228(2):218–232, 2014.
- [108] Sigurd Skogestad and Ian Postlethwaite. *Multivariable feedback control: analysis and design*, volume 2. Wiley New York, 2007.
- [109] Laura R Ray. Nonlinear tire force estimation and road friction identification: Simulation and experiments. *Automatica*, 33(10):1819–1833, 1997.
- [110] Guillaume Baffet, Ali Charara, and Joanny Stéphant. Sideslip angle, lateral tire force and road friction estimation in simulations and experiments. In *Computer Aided Control System Design, 2006 IEEE International Conference on Control Applications, 2006 IEEE International Symposium on Intelligent Control, 2006 IEEE*, pages 903–908. IEEE, 2006.

- [111] Yan Chen and Junmin Wang. Design and experimental evaluations on energy efficient control allocation methods for overactuated electric vehicles: Longitudinal motion case. *IEEE/ASME Transactions on Mechatronics*, 19(2):538–548, 2014.
- [112] Arash M Dizqah, Basilio Lenzo, Aldo Sorniotti, Patrick Gruber, Saber Fallah, and Jasper De Smet. A fast and parametric torque distribution strategy for four-wheel-drive energy-efficient electric vehicles. *IEEE Transactions on Industrial Electronics*, 63(7):4367–4376, 2016.
- [113] Masato Abe. A theoretical analysis on vehicle cornering behaviors in acceleration and in braking. *Vehicle System Dynamics*, 15(sup1):1–14, 1986.
- [114] Eric Ostertag. *Mono-and multivariable control and estimation: linear, quadratic and LMI methods*, volume 2. Springer Science & Business Media, 2011.
- [115] C Bohn and DP Atherton. An analysis package comparing pid anti-windup strategies. *IEEE Control Systems Magazine*, 15(2):34–40, 1995.
- [116] Xin-lan Li, Jong-Gyu Park, and Hwi-Beom Shin. Comparison and evaluation of anti-windup pi controllers. *Journal of Power Electronics*, 11(1):45–50, 2011.
- [117] Daniel J Stilwell and Wilson J Rugh. Interpolation of observer state feedback controllers for gain scheduling. *IEEE transactions on automatic control*, 44(6):1225–1229, 1999.
- [118] Qian Lu, Aldo Sorniotti, Patrick Gruber, Johan Theunissen, and Jasper De Smet. H_∞ loop shaping for the torque-vectoring control of electric vehicles: Theoretical design and experimental assessment. *Mechatronics*, 35:32–43, 2016.
- [119] Tommaso Goggia, Aldo Sorniotti, Leonardo De Novellis, Antonella Ferrara, Andrew Pennycott, Patrick Gruber, and Ilhan Yunus. Integral sliding mode for the yaw moment control of four-wheel-drive fully electric vehicles with in-wheel motors. *International Journal of Powertrains*, 4(4):388–419, 2015.
- [120] Makoto Yokoyama, Gyu-Nam Kim, and Masahiko Tsuchiya. Integral sliding mode control with anti-windup compensation and its application to a power assist system. *Journal of Vibration and Control*, 16(4):503–512, 2010.
- [121] e-vectoorc, 2014. Last accessed 5 June 2015.
- [122] i-compose, 2016. Last accessed 5 June 2015.
- [123] Passenger cars – Test track for a severe lane-change manoeuvre – Part 2: Obstacle avoidance. Standard, International Organization for Standardization, 2011.
- [124] Robert Grover Brown and Patrick YC Hwang. Introduction to random signals and applied kalman filtering: with matlab exercises and solutions. *Introduction to random signals and applied Kalman filtering: with MATLAB exercises and solutions*, by Brown, Robert Grover.; Hwang, Patrick YC New York: Wiley, c1997., 1997.
- [125] Greg Welch and Gary Bishop. An introduction to the kalman filter. 1995.
- [126] Rudolph Emil Kalman et al. A new approach to linear filtering and prediction problems. *Journal of basic Engineering*, 82(1):35–45, 1960.

- [127] Oliver Louis Robert Jacobs. Introduction to control theory. 1974.
- [128] Peter S Maybeck. *Stochastic models, estimation, and control*, volume 3. Academic press, 1982.
- [129] Harald Naunheimer, Bernd Bertsche, Joachim Ryborz, and Wolfgang Novak. *Automotive transmissions: Fundamentals, selection, design and application*. Springer Science & Business Media, 2010.
- [130] Yen-Chen Liu and Ching-Huan Tseng. Simulation and analysis of synchronisation and engagement on manual transmission gearbox. *International journal of vehicle design*, 43(1-4):200–220, 2007.
- [131] Michael A Kluger and Denis M Long. An overview of current automatic, manual and continuously variable transmission efficiencies and their projected future improvements. Technical report, SAE Technical Paper, 1999.
- [132] Nilabh Srivastava and Imtiaz Haque. A review on belt and chain continuously variable transmissions (cvt): Dynamics and control. *Mechanism and machine theory*, 44(1):19–41, 2009.
- [133] Tejinder Singh and Satish S Nair. A mathematical review and comparison of continuously variable transmissions. Technical report, SAE Technical Paper, 1992.
- [134] G Mantriota. Power split continuously variable transmission systems with high efficiency. *Proceedings of the Institution of Mechanical Engineers, Part D: Journal of Automobile Engineering*, 215(3):357–358, 2001.
- [135] Joško Deur, Jahan Asgari, Davor Hrovat, and Petar Kovač. Modeling and analysis of automatic transmission engagement dynamics-linear case. *Journal of dynamic systems, measurement, and control*, 128(2):263–277, 2006.
- [136] Masahiro Hayabuchi, Masaaki Nishida, Satoru Kasuya, Kenji Gotou, and Toshihiko Aoki. Automatic transmission for a vehicle, May 6 2003. US Patent 6,558,287.
- [137] Fabrizio Amisano, Enrico Galvagno, Mauro Velardocchia, and Alessandro Vigliani. Automated manual transmission with a torque gap filler part 1: kinematic analysis and dynamic analysis. *Proceedings of the Institution of Mechanical Engineers, Part D: Journal of Automobile Engineering*, 228(11):1247–1261, 2014.
- [138] Aldo Sorniotti. Torque gap filler for automated manual transmissions: principles for the development of the control algorithm. *SAE International Journal of Engines*, 2(2009-01-0952):925–934, 2009.
- [139] Enrico Galvagno, Mauro Velardocchia, and Alessandro Vigliani. Analysis and simulation of a torque assist automated manual transmission. *Mechanical Systems and Signal Processing*, 25(6):1877–1886, 2011.
- [140] Fabrizio Amisano, Enrico Galvagno, Mauro Velardocchia, and Alessandro Vigliani. Automated manual transmission with a torque gap filler part 2: control and experimental validation. *Proceedings of the Institution of Mechanical Engineers, Part D: Journal of Automobile Engineering*, 228(14):1700–1717, 2014.

- [141] Mauro Velardocchia, Elvio Bonisoli, Enrico Galvagno, Alessandro Vigliani, and A Sorniotti. Efficiency of epicyclic gears in automated manual transmission systems. Technical report, SAE Technical Paper, 2007.
- [142] Gianluca Lucente, Marcello Montanari, and Carlo Rossi. Modelling of an automated manual transmission system. *Mechatronics*, 17(2):73–91, 2007.
- [143] Enrico Galvagno, Mauro Velardocchia, and Alessandro Vigliani. Dynamic and kinematic model of a dual clutch transmission. *Mechanism and Machine Theory*, 46(6):794–805, 2011.
- [144] Manish Kulkarni, Taehyun Shim, and Yi Zhang. Shift dynamics and control of dual-clutch transmissions. *Mechanism and Machine Theory*, 42(2):168–182, 2007.
- [145] Richard G Reed Jr and Jeffrey P Cherry. Method of controlling a transmission having a dual clutch system, October 15 2002. US Patent 6,463,821.
- [146] M Goetz, MC Levesley, and DA Crolla. Dynamics and control of gearshifts on twin-clutch transmission [j]. *Drive System Technique*, 3:007, 2006.
- [147] Yonggang Liu, Datong Qin, Hong Jiang, and Yi Zhang. A systematic model for dynamics and control of dual clutch transmissions. *Journal of Mechanical Design*, 131(6):061012, 2009.
- [148] Mauro Velardocchia, Nicolò D’Alfio, Elvio Bonisoli, Enrico Galvagno, Fabrizio Amisano, and Aldo Sorniotti. Block-oriented models of torque gap filler devices for amt transmissions. Technical report, SAE Technical Paper, 2008.
- [149] MT Menday, Homer Rahnejat, and M Ebrahimi. Clonk: an onomatopoeic response in torsional impact of automotive drivelines. *Proceedings of the Institution of Mechanical Engineers, Part D: Journal of Automobile Engineering*, 213(4):349–357, 1999.
- [150] P Bellomo, N De Vito, C-H Lang, and L Scamardi. In depth study of vehicle powertrains to identify causes of loose components rattle in transmissions. Technical report, SAE Technical Paper, 2002.
- [151] Enrico Galvagno, Guido Ricardo Guercioni, and Alessandro Vigliani. Sensitivity analysis of the design parameters of a dual-clutch transmission focused on nvh performance. Technical report, SAE Technical Paper, 2016.
- [152] Enrico Galvagno, Mauro Velardocchia, and Alessandro Vigliani. Torsional oscillations in automotive transmissions: Experimental analysis and modelling. *Shock and Vibration*, 2016, 2016.
- [153] Peter Herter, Joachim Staudinger, Rainer Petzold, and Franz Bitzer. Method and device for determining and dampening juddering vibrations of a drivetrain, January 8 2013. US Patent 8,352,140.
- [154] Norbert Ramm and Frank Zimmermann. Method and apparatus for controlling engagement and disengagement of the clutch as a function of displacements between engine and vehicle body, August 8 1995. US Patent 5,439,425.

- [155] Matthias Winkel, Thomas Jäger, Rupert Kramer, and Horst Aepker. Method and device for actively reducing clutch grabbings in a motor vehicle, July 8 2008. US Patent 7,396,314.
- [156] Johan Lindström and Krister Fredriksson. Method and arrangement for controlling a drive system, March 22 2005. US Patent 6,870,335.
- [157] Masaru Kogure and Koji Matsuno. Vehicle control device and vehicle control method, July 26 2005. US Patent 6,922,617.
- [158] Giancarlo Osella, Francesco Cimmino, Constantinos Vafidis, Enrico Galvagno, Mauro Velardocchia, Alessandro Vigliani, and Antonio Tota. Procedimento per ridurre la rumorosità di una trasmissione di un autoveicolo, 2016. WO 2016207806 A1, Patent App. PCT/IB2016/053,701.
- [159] Enrico Galvagno, Antonio Tota, Mauro Velardocchia, and Alessandro Vigliani. Enhancing transmission nvh performance through powertrain control integration with active braking system. Technical report, SAE Technical Paper, 2017.
- [160] Georg F Mauer. A fuzzy logic controller for an abs braking system. *IEEE Transactions on Fuzzy Systems*, 3(4):381–388, 1995.
- [161] Cheng Guan and Shuangxia Pan. Adaptive sliding mode control of electro-hydraulic system with nonlinear unknown parameters. *Control Engineering Practice*, 16(11):1275–1284, 2008.
- [162] Amir Poursamad. Adaptive feedback linearization control of antilock braking systems using neural networks. *Mechatronics*, 19(5):767–773, 2009.
- [163] Basanta Kumar Dash and Bidyadhar Subudhi. A fuzzy adaptive sliding mode slip ratio controller of a hev. In *Fuzzy Systems (FUZZ), 2013 IEEE International Conference on*, pages 1–8. IEEE, 2013.
- [164] Damiano Capra, Enrico Galvagno, V Ondrak, B Van Leeuwen, and Alessandro Vigliani. An abs control logic based on wheel force measurement. *Vehicle system dynamics*, 50(12):1779–1796, 2012.
- [165] Andrea Morgando, Mauro Velardocchia, Alessandro Vigliani, BG van Leeuwen, and V Ondrak. An alternative approach to automotive esc based on measured wheel forces. *Vehicle System Dynamics*, 49(12):1855–1871, 2011.
- [166] Dongmei Wu, Haitao Ding, Konghui Guo, and Zhiqiang Wang. Experimental research on the pressure following control of electro-hydraulic braking system. Technical report, SAE Technical Paper, 2014.
- [167] Liang Chu, Liang Yao, Jian Chen, Libo Chao, Jianhua Guo, Yongsheng Zhang, and Minghui Liu. Integrative braking control system for electric vehicles. In *Vehicle Power and Propulsion Conference (VPPC), 2011 IEEE*, pages 1–5. IEEE, 2011.
- [168] Marco Branciforte, Alessandro Meli, Giovanni Muscato, and Domenico Porto. Ann and non-integer order modeling of abs solenoid valves. *IEEE transactions on control systems technology*, 19(3):628–635, 2011.

- [169] Chen Lv, Junzhi Zhang, Yutong Li, Dongsheng Sun, and Ye Yuan. Hardware-in-the-loop simulation of pressure-difference-limiting modulation of the hydraulic brake for regenerative braking control of electric vehicles. *Proceedings of the Institution of Mechanical Engineers, Part D: Journal of Automobile Engineering*, 228(6):649–662, 2014.
- [170] Seongho Choi and Dong-Woo Cho. Control of wheel slip ratio using sliding mode controller with pulse width modulation. *Vehicle System Dynamics*, 32(4-5):267–284, 1999.
- [171] Ming-chin Wu and Ming-chang Shih. Simulated and experimental study of hydraulic anti-lock braking system using sliding-mode pwm control. *Mechatronics*, 13(4):331–351, 2003.
- [172] Humair Raza, Zhigang Xu, Bingen Yang, and Petros A Ioannou. Modeling and control design for a computer-controlled brake system. *IEEE transactions on control systems technology*, 5(3):279–296, 1997.
- [173] Jianqiang Wang, Bo Yang, Shengbo Li, Dezhaio Zhang, and Keqiang Li. Pneumatic electronic braking assistance system using high-speed valves. In *Vehicular Electronics and Safety (ICVES), 2010 IEEE International Conference on*, pages 59–64. IEEE, 2010.
- [174] Kyongsu Yi and Jintai Chung. Nonlinear brake control for vehicle cw/ca systems. *IEEE/ASME transactions on mechatronics*, 6(1):17–25, 2001.
- [175] Antonio Tota, Enrico Galvagno, Mauro Velardocchia, and Ale Vigliani. Passenger car active braking system: Model and experimental validation (part I). *Proceedings of the Institution of Mechanical Engineers, Part C: Journal of Mechanical Engineering Science*, 2017.
- [176] Antonio Tota, Enrico Galvagno, Mauro Velardocchia, and Alessandro Vigliani. Passenger car active braking system: pressure control design and experimental results (part II). *Proceedings of the Institution of Mechanical Engineers, Part C: Journal of Mechanical Engineering Science*, 2017.
- [177] Sooyoung Kim, Jiwon Oh, and Seibum Choi. Gear shift control of a dual-clutch transmission using optimal control allocation. *Mechanism and Machine Theory*, 113:109–125, 2017.
- [178] Enrico Galvagno, Pablo Gutierrez, Mauro Velardocchia, and Alessandro Vigliani. A theoretical investigation of the influence of powertrain mounts on transmission torsional dynamics. Technical report, SAE Technical Paper, 2017.
- [179] Hans Pacejka. *Tire and vehicle dynamics*. Elsevier, 2005.
- [180] Alexandre Schalch Mendes and Pablo Siqueira Meirelles. Application of the hardware-in-the-loop technique to an elastomeric torsional vibration damper. *SAE International Journal of Engines*, 6(2013-01-9044):2004–2014, 2013.
- [181] Aldo Sorniotti, Nicolò D’Alfio, Enrico Galvagno, Andrea Morgando, and Fabrizio Amisano. Hardware-in-the-loop testing of automotive control systems. Technical report, SAE Technical Paper, 2006.

-
- [182] Giovanni Bracco, Ermanno Giorcelli, Giuliana Mattiazzo, Vincenzo Orlando, and Mattia Rafferio. Hardware-in-the-loop test rig for the iswec wave energy system. *Mechatronics*, 25:11–17, 2015.